The Pennsylvania State University
The Graduate School
College of Engineering

AN INVESTIGATION OF COUPLED ATMOSPHERIC TURBULENCE AND SHIP AIRWAKES FOR HELICOPTER-SHIP DYNAMIC INTERFACE SIMULATIONS

A Dissertation in
Aerospace Engineering
by
Regis Santos Thedin

Submitted in Partial Fulfillment
of the Requirements
for the Degree of

Doctor of Philosophy

December 2019

The dissertation of Regis Santos Thedin was reviewed and approved* by the following:

Sven Schmitz
Associate Professor of Aerospace Engineering
Dissertation Advisor
Chair of Committee

Joseph F. Horn
Professor of Aerospace Engineering

Michel P. Kinzel
Assistant Professor of Mechanical Engineering, University of Central Florida

Xiaofeng Liu
Associate Professor of Civil and Environmental Engineering

Amy Pritchett
Department Head of Aerospace Engineering

*Signatures are on file in the Graduate School.

Abstract

The dynamic interface between a ship and a helicopter is a complex, hazardous environment, demanding high levels of pilot workload. In modeling & simulation of such environment for pilot training purposes, high levels of fidelity are required on the airwake module. The objectives of this research effort are two-fold. The first one is to analyze in details the effects of the turbulence present in the atmospheric boundary layer (ABL) on ships and the resulting airwake. The other objective is to use airwake data saved from the numerical simulations as external disturbances to a helicopter model in order to quantify an increase in pilot workload. Two different types of inflow are investigated: unsteady ABL and steady ABL. Unsteady cases are executed in OpenFOAM, are representatives of an actual stability state and include realistic features such as coherent structures. Steady ABL cases are executed in OVERFLOW and represent an appropriate velocity profile, but do not include any freestream turbulence. Uniform inflow cases are also executed on both codes as baseline cases. The SFS2 ship geometry is used and it is modeled by the immersed boundary method within OpenFOAM, while body-fitted overset grids are used in OVERFLOW. Pilot workload is quantified by a frequency-domain analysis of the energy associated with the usage of the input sticks.

Initially, neutral cases with two levels of shear are investigated and compared to uniform inflow solutions. Analysis of velocity distributions along probe lines at the deck revealed that the presence of an ABL modifies the recirculation region and delays the reattachment point. Different levels of shear yield different characteristics. For airwakes modified by unsteady ABL inflow, spectral analysis at locations near the ship's flight deck indicated that higher energy content at frequencies above 3 Hz, with better agreement to Kolmogorov's $-5/3$ cascade, have been captured. Increased content has also been observed in the 0.1–0.3 Hz range. This energy cascade matches in situ experiments. Spectral content on the uniform inflow cases fails to match content above 3 Hz, which are also not usually captured in standard CFD simulations. The airwakes related to ABL inflows were not related to each other by a common factor, indicating that these solutions are not scalable, differently than what is usually observed for uniform inflows.

Next, two hover locations outside of the airwake are considered, subject only to the turbulence present in the inflow — in at an altitude of 20 ft and another at 80 ft. The ABL turbulence had a substantial effect on the vehicle, resulting in significantly more disturbances, considerably more power fluctuations, and fluctuations on the vehicle's attitudes. While this was observed on both cases, it was much more prominent in the

high altitude case. The fluctuations were reflected on the stick usage, and thus pilot workload. The uniform inflow case barely exerted any effect and had comparable results to a scenario where only Pitt-Peters inflow model is used (no external disturbances). Analysis of the energy related to the stick usage showed that substantially more energy was found for the ABL case across all of the frequency range investigated for high altitude case, and a lower increase for the lower altitude case, found in the range of approximately 0.1–0.6 Hz. These results suggested that the large length-scale eddies that are present in the atmosphere seems to affect the vehicle and the pilot workload.

Lastly, two hover locations at the flight deck have been investigated. The vehicle was subject to the highly turbulent air shedding off the superstructure and chimney. Comparisons between steady ABL, unsteady ABL, and uniform inflow are made. One hover location is within the highly separated region, and another is slightly higher. The second location represents a mix of the pure unsteady ABL flow and airwake turbulence. These locations were selected in order to check whether or not the effects from the atmospheric turbulence observed previously would apply here. For the unsteady ABL case, the results indicated that when the airwake turbulence dominates, an increase in the energy associated with frequencies in the range of 0.1–0.3 Hz has been observed. For frequencies above 0.5 Hz, not many differences are observed at the energy associated with the stick use. However, one of the main findings of this work is that when the aircraft was hovering only 10 ft higher, in a flowfield that was a mix of airwake and atmospheric turbulence, the energy associated with the unsteady ABL was higher than that associated with the uniform inflow for all of the 0.2–2 Hz spectrum. Now, with respect to the OVERFLOW's steady ABL case, no appreciable differences have been captured, in neither of the hover locations. The steady ABL approach did not affect the vehicle nearly as much as the unsteady ABL did. In fact, the uniform inflow consistently exhibited higher energy (although very small) than that seen under the steady ABL. The steady ABL did not add any relevant information.

The results indicate that when the aircraft is flying at a location that is subject to more of the atmospheric eddies, the vehicle tends to react to the unsteadiness present, which represents additional pilot workload. This is especially relevant for a ship with a flat deck (similar to the LHA class). If the vehicle is solely in the wake of the superstructure, no relevant differences were observed. The lower fidelity approach of modeling the ABL as a steady ABL did not add any relevant pilot workload for the SFS2 with zero wind-over-deck case investigate.

Table of Contents

List of Figures

List of Tables

List of Symbols

Roman

b	Ship beam width, m
c_p	Specific heat capacity, J/(kg K)
F	Body force, N/m^3
g	Gravity, m/s^2
H_h	Superstructure height, m
L	Obukhov length, m
I	Moments of inertia, slug ft^2
k	Turbulent kinetic energy, m^2/s^2
p	Pressure, Pa
$\tilde{p}$	Modified pressure, Pa
p_0	Standard reference pressure, Pa
p, q, r	Angular velocity components of fuselage in body axis, rad/s
Pr	Prandtl number
q, $\theta' w'$	Potential temperature flux, K m/s
q_s	Potential temperature flux at the surface, K m/s
Re_L	Reynolds number based on the ship length
T	Absolute Temperature, K
u_i, u,v,w	Velocity components, m/s

U	Velocity magnitude, m/s
$\boldsymbol{U}$	Immersed body velocity, m/s
U_∞	Freestream velocity, m/s
x, y, z	Position coordinates in space, m
u_*	Friction velocity, m/s
w_*	Convective velocity, m/s
z	Height, m
$\hat{z}$	Non-dimensional height
z_0	Aerodynamic surface roughness, m

Greek

β	Immersed body
$\partial\beta$	Immersed body boundary
η	Location of immersed body
$\mathcal{P}$	Production of turbulent kinetic energy, m^2/s^3
κ	von Karman constant
ρ	Density, kg/m^3]
ρ_0	Reference density, kg/m^3
θ	Potential Temperature, K
θ_0	Reference potential temperature, K
τ	Stress tensor, m^2/s^2
τ_*	Eddy turnover time, s
ν	Kinematic molecular viscosity, m^2/s
ν_t	Kinematic eddy viscosity, m^2/s
Ω_f	Region occupied by the fluid
ϕ, θ, ψ	Euler angles (roll, pitch, yaw, respectively), rad

Acronyms

ABL	Atmospheric boundary-layer
CFD	Computational fluid dynamics
CPF	Canadian Patrol Frigate
DES	Detached eddy simulation
DDES	Delayed detached eddy simulation
IBM	Immersed boundary method
LES	Large eddy simulations
LHA	Landing helicopter assault
NSWCCD	Naval Surface Warfare Center Carderock Division
NRC	National Research Center (of Canada)
PIV	Particle image velocimetry
PSD	Power spectral density
RANS	Reynolds-averaged Navier-Stokes
SFS2	Simple frigate shape 2
SHOL	Ship-helicopter operating limits
SGS	Sub-grid scale
SST	Shear-stress transport
SR	Stretching ratio
WOD	Wind-over-deck

Subscripts

col	collective
lat	lateral cyclic
lon	longitudinal cyclic
ped	pedals
ref	At reference point

Other

$\overline{\cdot}$	Mean (time-averaged) quantity
$\cdot\,'$	Fluctuating quantity
$\langle\,\cdot\,\rangle$	Horizontally-averaged quantity
$\dot{}$	First derivative in time
$\ddot{}$	Second derivative in time

Line Styles

The line styles and colors listed below are consistent throughout this document.

Related to OpenFOAM uniform inflow scenarios

Related to OVERFLOW uniform inflow scenarios

Related to OpenFOAM unsteady ABL scenarios

Related to OVERFLOW steady ABL scenarios

, , , Evolution of a certain characteristic, parametric study

Acknowledgments

First and foremost, I'd like to thank my advisor, Dr. Sven Schmitz, for the support and trust in me throughout these years. To the many meetings, fruitful discussions, guidance, and encouragement — thank you.

I wish to thank my dissertation committee members, Drs. Joe Horn, Mike Kinzel, and Xiaofeng Liu, for their time and expertise. I had the opportunity to interact closely with each one of them in different aspects of this research, and not only during the official examinations. Their support and guidance are greatly appreciated.

I'm also thankful to Dr. Scott Murman for hosting me at the Advanced Supercomputing Division at NASA Ames. Access to OVERFLOW and the computing hours on the Pleiades supercomputer are greatly appreciated. Thanks are also extended to his group members and Dr. William Chan for the help with overset grids.

I would like to express my gratitude towards Kirk Heller for all of the support and assistance provided. From the hundreds of emails exchanged, all the way to the many hours spent down at his office debugging InfiniBand issues and contemplating why some cocoa6 nodes refused to work properly, Kirk helped in many steps along the way for this thesis to get done.

Throughout these years, I've had the support from a few different friends, at different times. I'm grateful for these people for their friendship, support, and sometimes just being there to listen to my complaints about life. I would like to sincerely thank Ahmad Haidar, Amanda Hermann, Amandeep Premi, Bernardo Vieira, Ethan Corle, Hannah Young, Ilker Topcuoglu, Michel Feinstein, Rafael Basilio, Tenzin Choephel, Tanmay Marthur, and Umberto Saetti. Special thanks to Samantha English for her unfailing support and understanding, especially towards the end.

Thanks to the many past and present friends at 144 Hammond for the welcoming environment. For the many moments of joy and, more often than not, insightful discussions about research, life, and everything in between.

To my family, for their love, support, and encouragement.

This research was supported by the Government under Agreement No. W911W6-17-2-0003. The U.S. Government is authorized to reproduce and distribute reprints for Government purposes notwithstanding any copyright notation thereon. The views and conclusions contained in this document are those of the authors and should not be interpreted as representing the official policies, either expressed or implied, of the Aviation Development Directorate or the U.S. Government.

Dedication

To my parents, for all they taught me.

"The answer, my friend,
is blowin' in the wind."

Bob Dylan

Chapter 1 | Introduction

The operation of rotorcraft in the vicinity of ships continues to present a number of technical challenges. The aircraft limits are specified in terms of pilot workload, margins, landing gear loads, ship motion, limited landing area, controls, power, visibility, among other aspects [13]. Figure 1.1 shows some of these issues. The interaction of helicopter rotors and vortices shed in the airwake behind the ship is hazardous and difficult to predict. During a landing operation, for instance, the aerodynamic loading of the rotor can be considerably altered by the passage of an eddy or a region of crossflow [14], increasing the pilot workload. The presence of a ship superstructure results in a modified airflow with recirculating zones, bounded by shear layers that emanate from the sharp edges. Such flow features vary greatly in size and frequency, thus resulting in regions of steep velocity gradients and high turbulence intensity levels [15]. The ship airwake is a complex unsteady phenomenon and its prediction through modeling and simulation is not a trivial task.

(a)

(b)

(c)

Figure 1.1: Some of the limits encountered in shipboard operation of rotorcraft: Strong airwake modification due to superstructure size, substantial ship motion, and limited landing site. (a) SH-60 Seahawk approaching Royal Netherlands Navy HNLMS Johan de Witt; (b) Westland Lynx on the flight deck of HMS Birmingham (from [16]); (c) SH-60 Seahawk approaching USS Jarrett FFG-33.

Ship airwakes are, therefore, an important factor for handling qualities, and thus subsequent performance of a helicopter during a shipboard launch or recovery operation. Operational limits of a rotorcraft are usually determined by the Ship-Helicopter Operating Limits (SHOL). SHOL define the boundaries of safe operation of a particular ship/helicopter combination in terms of wind speed and direction. Wind direction is commonly known as wind-over-deck (WOD) in maritime terminology and is specified as *red* for winds coming from the port side of the ship and *green* for those coming from the starboard side. The SHOL of an aircraft and ship combination are usually given as a chart, illustrated in Fig. 1.2.

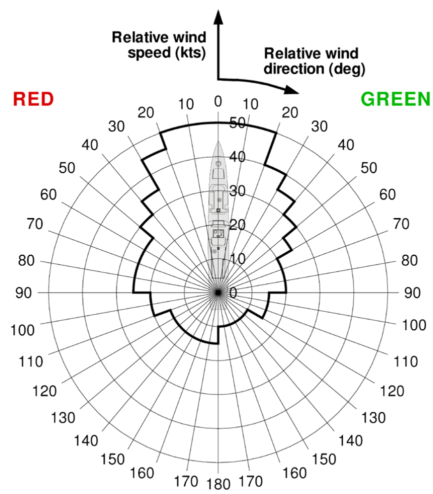

Figure 1.2: Typical Ship-Helicopter Operating Limits (SHOL) diagram. Radial coordinate represents wind speed and angular coordinate the wind direction. Figure from [17].

Ship-Helicopter Operating Limits are derived by a series of sea-trials and can involve hundreds of landings, since several directions and conditions have to be evaluated [18]. As one can expect, this process is costly and risky, since the aircraft is being pushed to its limits, with increased pilot workload and degradation of the handling qualities of the vehicle. There is also the issue of suitable conditions for testing a specific scenario not being found within a certain period of time devoted for testing, thus resulting in a limited testing of the SHOL envelope.

The possibility of using modeling and simulation of the *dynamic interface* to improve sea-trials and even replace some of them is appealing. Hodge et al. [19] define the dynamic interface as the environment around the ship characterized by increased levels of turbulence, degraded visual cues, and a restricted and moving landing site; and the “dynamic” word reflects the unsteady nature of the conditions faced by both the pilot and the helicopter when operating in close proximity to the ship’s flight deck and superstructure. High-fidelity simulation models of the dynamic interface have the benefit of providing controllable and reproducible scenarios, in addition to being safer and reduce costs significantly. Such simulation models are useful for a range of tasks such as the investigation of dynamic interface behavior of ships at design stage; further prediction and expansion of the SHOL for current and future aircraft/ship combinations; pilot training, including conditions of extreme workload; and possible identification of potential hazards.

Pilot workload refers to the effort it takes for a human pilot to perform a specified flight operation. In the present context, it represents being able to correctly apply the necessary inputs to the pedals, lateral and longitudinal cyclic, and collective in order to maneuver the vehicle. Considerably higher levels of pilot workload may be required in a dynamic interface environment, especially in the presence of wind, ship motion, and low visibility [18].

In order to develop practical design and training simulation tools, the associated fidelity requirements for the model have to be evaluated. It is necessary to identify critical flow physics that need to be modeled and considered from those that are superfluous. Fidelity requirements for simulators are discussed in detail by Wilkinson et al. [10]. It is pointed out that for flight envelope testing, high levels of fidelity are required for the airwake and aerodynamic models. Also, according to Zan [13], the accurate representation of the unsteady air disturbances due to airwake turbulence is an important aspect in the task of replicating workload levels experienced by pilots at sea. This is proving to be a particularly challenging aspect of dynamic interface modeling [20]. A given modeling strategy needs to be able to reproduce the energy associated with the relevant frequency range that is observed on in situ experiments and that will be experienced by the pilot, thus giving the model a higher level of fidelity.

In the light of identifying critical flow physics, some physical phenomena have not been thoroughly analyzed. One such phenomenon is the interaction of the ship airwake with details of the atmospheric conditions and the turbulent atmospheric boundary layer (ABL). Crozon et al. [21] mention that the ship airwake is a combination of the wind and ship motion and is influenced by the ABL and any element of the ship superstructure. Although several authors highlight the importance of including atmospheric effects [13, 20, 22–26], fully-resolved and coupled ABL interaction with the ship airwake has not yet been investigated.

Atmospheric boundary layers are characterized as highly turbulent, three-dimensional boundary layers that are not readily obtained or approximated. Previous work has considered logarithmic or power-law profiles to represent the ABL, which more correctly estimate the mean velocity; however, such an approach ignores the geostrophic winds and large-scale structures inherent to the atmospheric surface layer. In the lowest part of the atmosphere, the turbulence length scale is relatively small, in such a way that the effects of the disturbances on a helicopter are severe [27]. Fully-resolved ABL data and atmospheric implications are an important research branch in the wind energy community due to its effects. For example, the wake of wind turbines and performance of entire wind farms can be modified when immersed in ABL flow, as opposed to the trivial modeling of the incoming wind as a constant, uniform inflow [7, 28].

In this work, fundamental differences of ship airwakes when submerged in a uniform inflow vs. resolved ABL inflow are investigated. This work also studies how the modified wake affects flight handling qualities of a helicopter. What is important and needs to be included in dynamic interface modeling tools is also discussed. Coupled simulations composed of atmospheric turbulence-modified airwake and flight dynamics of an UH-60 representative helicopter are presented and discussed.

A review of the state-of-the-art of ship airwake modeling for dynamic interface simulation is presented in the next section, including models of the ABL. Works that involved helicopter models are also reviewed. The approaches, conclusions, and limitations of several research efforts will be discussed. The challenges and motivation for the current work are presented in the subsequent section. Lastly, objectives of the current work are established and discussed in detail.

1.1 Review of Previous Work

Several authors have investigated SHOL expansion efforts through dynamic interface modeling. As discussed, the airwake model represents one of the most complex components of a dynamic interface simulation. It is considered the most significant technical challenge according to Wilkinson et al. [29], who in a collaborative fashion, laid out standards for modeling and simulation efforts of the dynamic interface (especially the airwake component).

The collaborative effort was carried out under the auspices of The Technical Cooperation Program (TTCP), where researchers from the USA, UK [29], Canada [30, 31], and Australia [32] agreed on a simple frigate-like shape to be used in numerical and experimental studies. This would allow more direct comparison between experiments and models of different levels of fidelity and cost, facilitating the dissemination of best-practices amongst the dynamic interface modeling community. The mentioned shape is known as the Simple Frigate Shape (SFS), introduced in the work of Wilkinson et al. [29]. Its successor, with more realistic features, is known as SFS2 (see Fig. 1.3).

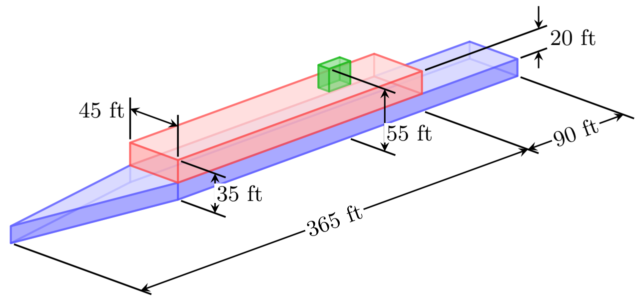

Figure 1.3: The ship geometry used in this work, the Simple Frigate Shape 2 (SFS2). The hull is noted in blue, the superstructure in red, and the chimney in green. The original SFS geometry does not include the pointed bow. The flight deck is the region above the hull, aft the superstructure.

The full-scale SFS2 model is sized after the FFG-8 frigate (USS McInerney), which was 453 ft long and 45 ft wide (see Fig. 1.4). Interestingly, SH-60B helicopters operated from this ship, making an investigation of a representative of the UH-60 helicopter over the SFS2 a realistic dynamic interface investigation.

Figure 1.4: The FFG-8 frigate, USS McInerney. The full scale SFS2 model resembles the dimensions of the USS McInerney, which is 453 ft long and 45 ft wide. Photos: `navsource.org`.

Figure 1.5 shows some topology features of the flow over a ship, focusing primarily on the flight deck region. As can be seen, with the superstructure acting as a bluff body and arranged in a backward-facing step fashion, the flowfield is dominated by vortices, recirculation zones, and flow separation and re-attachment.

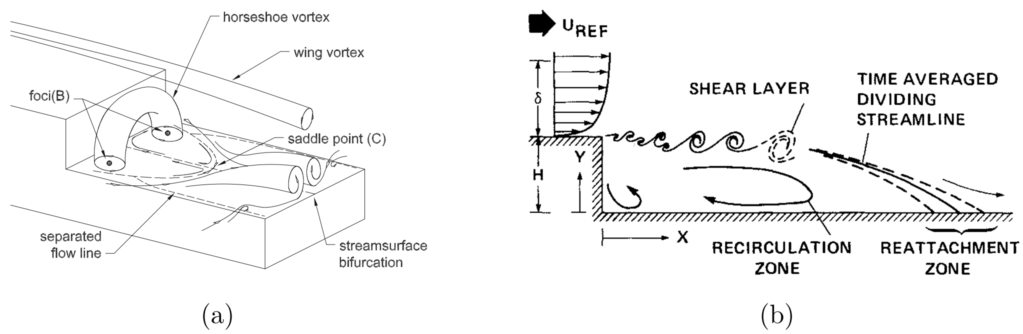

Figure 1.5: Complexity of the airwake flow topology aft a backward-facing step. (a) Figure from Tinney et al. [33]; (b) Figure from Driver et al. [34].

The goal of the research efforts outlined next is to understand the unsteady behavior of the airwake downstream of a ship, in order to more realistically account for the airwake in a dynamic interface simulation. The review of previous work starts by discussing experimental wind tunnel efforts, followed by some experiments conducted at-sea. Lastly, computational efforts are discussed, alongside coupled helicopter-ship investigations.

1.1.1 Wind Tunnel Experimental Efforts

Wind tunnel experiments have become a valuable asset for validation studies of computational fluid dynamics (CFD) models. Wind tunnel experiments, however, have two main limitations. The first is due to the size of real ships and the size of wind tunnel test sections. Wind tunnel models are generally in the 1:100 scale range, which makes full-scale Reynolds number unattainable. The second is that unsteady flow features that are of moderate frequency at full scale, are at a much higher frequency at wind tunnel scales [1], and these unsteady features are often those of most concern to the pilot. Acknowledging this fact, wind tunnel results are still a relevant tool to validate CFD studies and provide insight into missing features and/or the inability of CFD to capture certain flow features.

In 1998, before the agreement of the SFS shape, Zan et al. [35] conducted experiments on the Canadian Patrol Frigate (CPF) ship. The experiment included the effects of an

ABL by placing a set of rods upstream the model. This study served to compare early CFD work on ship airwakes, especially those that attempt a modeled ABL (for instance, Syms [36]).

Upon international agreement on the simple ship geometry to carry out both experimental and computational research, Zan and Cheney [30, 31] from the National Research Council of Canada (NRC) performed a series of tests on the SFS geometry. Data were collected at the 2×3 m closed-circuit wind tunnel from the Aerodynamic Laboratory of the NRC. They investigated the flow topology on a 1:60 scale model using oil and pressure taps, whilst the wake was examined by means of smoke visualization. Turbulence statistics and mean velocity data were obtained for several different locations (bow and flight deck region). The results presented were used for validation of early computational efforts.

Yet another wind tunnel study has been conducted by the NRC of Canada by Lee [37] in 2003. Off-body flowfield was measured by hot-film anemometry on a 1:100 scale model of the SFS2 in the same wind tunnel, see Fig. 1.6. Mean velocity and turbulence statistics metrics were obtained at several different deck locations and heights. Long data acquisition periods also allowed for derivation of accurate velocity spectra. A boundary-layer suction mechanism was used to ensure uniform inflow to the model; thus no ABL effects have been modeled or considered. This study served as a basis for CFD validation by many authors, as will be shown later. The present work also uses data from this experiment for comparisons with the obtained numerical results.

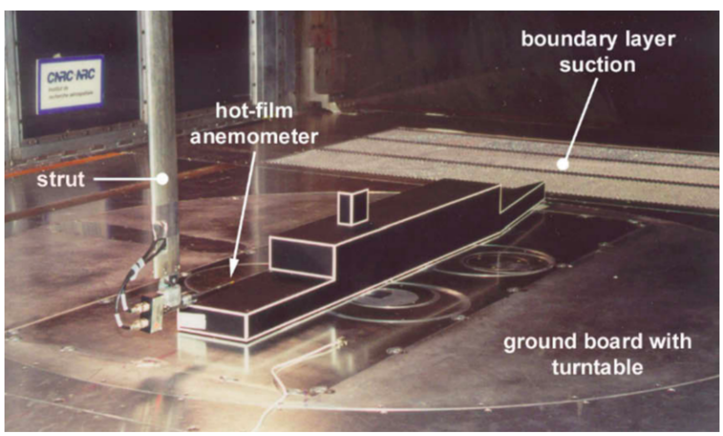

Figure 1.6: SFS2 model inside the NRC wind tunnel. Image from [20].

More recently, in 2015, uniform-inflow wind tunnel data were acquired by the Naval Surface Warfare Center Carderock Division (NSWCCD), a division of the U.S. Navy [38].

The NSWCCD 8' × 10' ft subsonic wind tunnel is a general-purpose, continuous-flow, closed-circuit facility. The experiment investigated and quantified impacts of Reynolds number, blockage, and wall effects on wind loads and airwake in the context of experimental practices. This experiment is of great interest to the current work as the effort studied a range of conditions useful for validation. Specifically, the experiments investigated a number of different conditions resulting in different Reynolds numbers with respect to the ship length. Particularly, they investigated a few SFS2 scale-models, a number of wind speeds, and relative wind heading. These experiments collected velocity data for several points in the aft portion of the ship, above the flight deck. Results from this experiment are used for the initial model validation and further comparisons presented in chapter 5. Although an ABL has been included in part of the experiments, only loads on the ship have been measured and compared with respect to the inclusion of the ABL. Figure 1.7 shows pictures of the experiment.

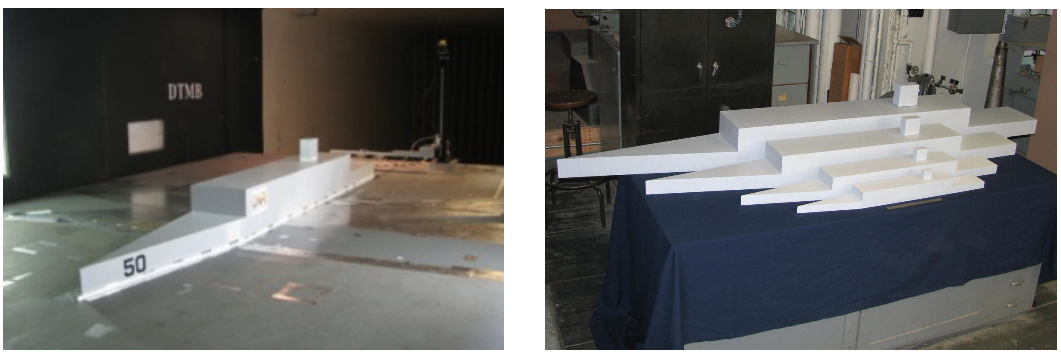

(a) (b)

Figure 1.7: SFS2 placed in the NSWCCD wind tunnel and a few different models investigated in the experiment. Figures from Rosenfeld et al. [38].

Regarding the inclusion of a helicopter, Nacakli and Landman [39] investigated a 1:50 model of the SFS geometry with a focus on identifying the rotor thrust coefficient and the interactions between the rotor downwash and the ship airwake at WOD 0 degrees. Particle Image Velocimetry (PIV) technique was used, first on the airwake alone, then later on the helicopter alone, and lastly, both effects coupled. The separation allowed better understanding of the physics involved. The rotor was represented by a 4-bladed propeller. The goal of this work was to investigate ground effects on a ship deck coupled with an airwake. It was found that the unsteadiness present in the recirculating region of the airwake increases the power required, whilst the proximity to the ground (ground effect) reduces it. A balance can be achieved depending where, with respect to the recirculating region, the helicopter is flying. The more into the recirculating region, the higher the power required; the further away, the lower the power needed (considering a constant height so the ground effect can be considered constant).

The studies outlined in this section, although not large in number, provided validation data for several of the computational efforts presented next. Some of these works attempted to model an ABL, but it remains a challenge to simulate a realistic turbulent inflow in a laboratory setting. To the best of the author's knowledge, only one facility in the U.S. provides proper treatment for wind tunnel-generated *atmospheric* turbulence — it is located at the University of New Hampshire [40].

Some other experimental efforts were not used in this work mostly due to the geometry chosen, but they represent important experimental studies to the ship airwake and dynamic interface field. For instance, Lee and Zan [41, 42] explored the airwake on the CPF with a 4-bladed rotor nearby. The investigation focused on unsteady loads measurements. Work performed at Naval Air System Command (NAVAIR), such as that of Rajagopalan et al. [43] and Silva et al. [44], investigated a Landing Helicopter Assault-class ship (LHA) with models of the V-22 and CH-46, looking at airwakes and loads by means of PIV. Kääriä et al. [45] investigated effects of aerodynamic design changes to the superstructure in wind tunnel experiments, in an attempt to reduce the impact of the airwake on helicopter operations. It was shown that some modifications were positive, but overall noted that the unsteady aerodynamic loading caused by the airwake has a significant impact on pilot workload.

In 2016, Rahimpour & Oshkai [46] studied the effects of both uniform inflow and ABL inflow on a Canadian vessel using PIV. They created an ABL in a wind tunnel setting by using spires and concluded that the ABL promoted the development of higher turbulent velocity fluctuations over the landing deck, and noted that it "can lead to increase in the workload of the pilots". The highest levels of turbulence intensity were observed in a 60 degrees WOD case. The spatial structure of the airwake was found to depend on the inflow conditions (mostly the wind-over-deck).

Recently, in 2018, Buchholz et al. [47] performed dye visualization experiments on the Office of Naval Research (ONR) Tumblehome geometry. The study focused on the identification of flow structures and their relationship with Reynolds number. Some images of the obtained flowfield are shown in Fig. 1.8. Another study from the same research group, by Dooley et al. [48], compared the experimental airwakes with computational simulations.

Lastly, in 2019, Watson et al. [49] investigated experimentally the unsteady airwake of the HMW Queen Elizabeth Aircraft carrier. The study was focused on the experimental

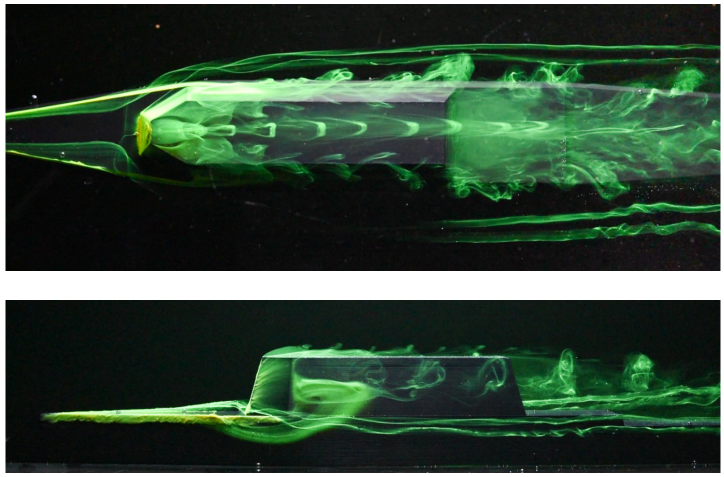

Figure 1.8: Dye visualization experiment of the ONR Tumblehome geometry at Reynolds of 32,000. Figures from [47].

techniques for data sampling in a water-tunnel setting and in providing data for the companion numerical study [50], which will be discussed later.

1.1.2 In situ Experimental Efforts

In situ experiments are invaluable tools for validation of both computational studies and wind tunnel investigations. Not many high quality in situ experiments have been carried out. Such experiments have several challenges, including, but not limited to:

- They are expensive and time consuming;
- Sometimes require modification of the ship used;
- They will rarely be performed on a real carrier due to prohibitive logistics;
- It is impossible to instrument all locations at the same time without one anemometer influencing the airwake seen by the other;
- Sonic anemometers, commonly used for measurements, are capable of providing the three velocity components, but are often limited in temporal resolution, resulting in averages over a measurement volume that is larger than the smallest eddies in the flow;
- It is impossible to control the weather so the exact desirable conditions are unlikely to be encountered;

- The WOD angle and magnitude will not remain constant and, on top of that, a large range of wind speeds and directions are a challenge to obtain at sea;
- There is ship motion naturally included and that effect has to be filtered in some way if it is not a desirable feature;
- Atmospheric turbulence effects are always naturally included, which is the main advantage over wind tunnel experiments; however, its isolate assessment is extremely difficult [2]. It would require simultaneous measurements at several different elevations, and in locations considerably upstream the ship.

With that said, below is outlined some of the experiments conducted at-sea[1].

In a computational work by Polsky and Bruner [1], data obtained in situ was used for comparisons. The ship used is a LHA-class Navy ship that is approximately 820 ft in length (see Fig. 1.9). Both on the CFD and the experimental side, data were sampled at 20 Hz for two minutes and spectral analysis was carried out. The full-scale experimental data are non-stationary due to changes in the ambient wind over the recording period that naturally includes the ABL. It was found that when adding Menter's Shear Stress Transport (SST) boundary-layer turbulence model on the CFD, the solution matches well the content related to the lowest frequency captured but damps out any higher-frequency content. The over-damping is attributed to the added dissipation by the SST model to an already dissipative model used for the sub-grid scale quantities, monotone integrated LES (MILES). This issue will be further discussed when laying the motivations of this work. The increased energy content of the high-frequency range may be due to atmospheric turbulence effects.

Another in situ experimental work was carried out by Brownell et al. [2] in 2012. They used three-component ultrasonic anemometers to collect airwake data on the YP676 patrol craft, a 108 ft long research vessel (detailed description of the in situ experiment is provided in Metzger [51]) — see Fig. 1.10. This data has been used in the computational work of Snyder et al. [24] in 2013 which will be described later. Data were collected for headwind and the mean velocity field showed a clear structure of the flow, dominated by the recirculation region near the flight deck. They found significant anisotropy in the wake, both within the main vortex and in the far field. Reynolds stresses are presented and a peak in the shear component has been observed in the recirculating region, whilst the streamwise normal stress is found to increase with height in the domain investigated. The effects of the atmospheric boundary layer are discussed in detail and the challenges

[1]The terms *at-sea* and in situ are used interchangeably throughout this work.

Figure 1.9: Picture from the experiments conducted at sea by Polsky and Bruner [1] on a LHA-class ship. The picture shows four anemometers masts on the deck.

associated with the measurement and quantification of ABL effects in situ are also given, such as scaling and repeatability metrics. It was found that the ABL indeed affects flow unsteadiness. When discussing comparisons with wind tunnel experiments, it is acknowledged that most of the disagreement comes from the lack of realistic inflow in wind tunnels.

Figure 1.10: Pictures from experiments conducted at sea by Brownell et al. [2]. The YP676 patrol craft and the modified flight deck, including a backward-facing step. Note the anemometer.

In 2016, Kang et al. [52] conducted in situ experiments on the same YP676 U.S. Naval Academy ship. The goal of the study was to gather data using ultrasonic anemometers mounted above the aft flight deck, and compare with CFD and wind tunnel investigations. The CFD simulations were carried out using Cobalt, whilst the wind tunnel was conducted at a 4%-scale model of same ship. The Reynolds number of all three approaches were closely matched. Investigated were a headwind and 15 degrees green WOD. It was found that (i) flow structures are quite different in the two WOD angles investigated; and (ii) in general, all three approaches show large-scale recirculation motion in the ship's hangar. It is noted that there are non-negligible differences between the simulation and wind tunnel compared to the in situ measurement. In situ measurements capture energy content that followed Kolmogorov's $-5/3$ slope in all of the domain showed (0.04 to 10 Hz); however, CFD data are not given for comparison. It is important to see in this work that in situ atmospheric turbulence data indeed follows the $-5/3$ slope. The deviations observed in the wind tunnel and CFD are attributed to the "possible interaction between the wake flow and incoming turbulent boundary layers", since in situ, the YP676 is fully submerged in a turbulent ABL. The authors conclude stating that it is "very important to quantify the profiles of the turbulent ABLs".

All of the in situ experimental work discussed in this section pointed out the influence of the ABL on the airwake. Next, computational investigations from the literature are reviewed.

1.1.3 Airwake Modeling Computational Efforts

Several past work of airwake and atmospheric turbulence modeling attempts are reviewed next. A complete review of all studies on such topics would be quite lengthy and almost impossible to do justice to, thus this survey is not intended to be complete. Instead, focus is given to the more relevant and recent work that is of interest to the current research, especially those carried out on the SFS2 geometry. Before the 2000's, due to computing power limitations, most of the airwake work consisted of steady-state solutions. This review starts in the early 2000's, when most of the work published investigated time-resolved unsteady airwake characteristics. Only the relevant steady-state investigations are cited. Works such as the one by Polsky [1] (2002) has started the trend of time-accurate CFD due to its proven increased fidelity. An attempt has been made to keep this review in chronological order as much as possible.

Starting in 2000, an early work by Reddy et al. [32] presented steady-state solutions of the airwake over the SFS geometry. The CFD code Fluent with structured grids and k–ϵ turbulence model was used. A range of different low to moderate WOD angles have been investigated and compared with experimental data. Prominent flow features such as recirculation zones and strong vortex fields have been identified, especially in the operating region of a helicopter.

Advani and Wilkinson [18], in 2001, discuss dynamic interface modeling and simulation issues in the context of the Joint Shipboard Helicopter Integration Process (JSHIP). The goal of the program was to develop a process to predict WOD envelopes using piloted simulation. The helicopter flight dynamics model used was based on GENHEL [53] and the airwake model was produced using CFD solutions by means of an unstructured solver. Inflow conditions were uniform (i.e., no ABL was considered) and the airwake was not influenced by either ship motion or the helicopter rotor.

Polsky [1], in 2002, used the unstructured-grid CFD solver Cobalt to investigate the airwake problem on a LHA-class ship. The uniform-inflow unsteady simulations presented are at full-scale Reynolds number and an attempt has been made to identify Reynolds independent airwakes. It was found that the general structure of the flow of a ship airwake remains very similar at Reynolds on the order of 10^5, but only a scaling factor of 2 has been investigated (confirming previous findings by the same author [54] and similar recent sudy by Buchholz et al. (2018) [47], where Reynolds independency has also been found). Uniform-inflow CFD solutions have been compared to uniform-inflow wind tunnel data and good agreement has been observed. The same computational solutions have been compared to data obtained at-sea, and power spectral density (PSD) plots were used for comparisons. The CFD, however, was not able to capture high-frequency content correctly. This has been one of the main issues with CFD solutions when comparing with at-sea data and this aspect will be returned to later. In the same work, it was also found that steady-state solutions do not always give the same results as time-averaged time-resolving solutions, and also that steady-state results do not compare nearly as well to experiments as time-averaged time-resolving results (which was also highlighted in a later work by Syms [36]).

In 2002, Wakefield et al. [16] also investigated the flow over the SFS geometry using a steady-state solver. Large-scale flow features and general trends of flow separation and reattachment have been captured, although they are not as accurate as the experimental results from Cheney et al. [30] used for comparison. A helicopter rotor was incorporated into the simulation by means of extra terms in the momentum equations. A blade element approach was used, and their approach is similar to an actuator disk model. Hover over the flight deck and 40-knot forward-flight cases were considered. Power and control parameters were analyzed. It was found that the airwake substantially modifies the local flow experienced by the helicopter, thus resulting in different power requirements depending on the headwind and proximity to the deck. Increased collective pitch was necessary under certain conditions, which increased the power requirements. Neither piloted simulation nor pilot workload have been assessed but it was pointed out that enough stick control was crucial under certain conditions, which means an increase in pilot workload is very likely.

In 2003/2005, Lee et al. [55, 56] also preformed unsteady simulations of the airwake past a LHA-class ship using the PUMA2 code, one-way coupled with GENHEL for the helicopter's dynamics representation. The airwake included a gust penetration model in an attempt to model the effects of a 3D ship airwake on the helicopter flight dynamics. In these efforts, the focus was on the optimal control model of a human pilot, under the task of approaching and landing on the ship deck. It is emphasized that time varying effects seem to have a "significant impact on pilot control activity".

Syms [36], in 2004, also considered a modeled logarithmic profile. He used the solver CFD–ACE in a Reynolds-averaged Navier-Stokes (RANS) mode, employing the k–ω model for closure. Using a steady-state solver, it was difficult to maintain the ABL profile due to incorrect momentum dissipation and subsequent boundary-layer thickness reduction in lower portions of the ABL. His results are compared with wind tunnel experiments on the CPF ship that included the ABL (work by Zan et al. [35] discussed earlier). General agreement is found but drawbacks are attributed to the incapability of capturing unsteady features with a steady-state solver. It is suggested that a time-resolving approach is used as a steady-state code is inappropriate to capture the unsteady airwake, since a RANS solution does not necessarily represent the time-average of an unsteady flow.

In 2006, Roper et al. [57] performed steady-state simulations for a wide range of WOD conditions using Fluent. Turbulence models investigated were the standard k–ω and realizable k–ϵ. The airwake was saved for later to be used as lookup tables in FLIGHTLAB, a flight simulation environment. In this approach, the wake was not modified by the presence of the helicopter and the same, steady wake has been used during the flight simulation trials. Increased workload has been observed in trials with a former Royal Navy pilot, and a typical SHOL for the SFS2 and a Lynx-like helicopter has been developed. Yesilel et al. [58] also investigated different turbulence models within a steady-state and an unsteady solver, using both CFX and Fluent CFD codes. His results were compared with those of Roper but limited improvements were shown.

Keller et al. [59], in 2007, explored the airwake problem on the LHA-class ships, using a hybrid methodology with an octree-Cartesian Euler solver that solves the inviscid flow equations, while preserving the vorticity transport in a time-accurate fashion. The goal of this effort was to develop offline databases to be used in one-way coupled fashion of simulated flight. This work, like many others, captured general flow features and trends, but was unable to capture high-frequency content. The drawback is "believed to be a result of neglecting viscous effects", but atmospheric turbulence is also pointed out as being present for at-sea data, even though it was not modeled or considered in the CFD.

In 2008, Syms [60] used the lattice Boltzmann method to perform time-accurate uniform-inflow simulations using the PowerFLOW solver on both the SFS and SFS2 geometries. The flow topology and root mean square velocities captured in the simulations compared well with uniform-inflow wind tunnel data for low to moderate WOD angles. Small errors in the position of the shear layer emanating from the hangar roof were found, and the simulation appeared to have less dissipation than the wind tunnel experiment, but overall good agreement was found and general flow features were matched.

Zhang et al. [61] investigated the same SFS2 airwake problem using Cobalt with uniform inflow, in 2009. The general trends were also matched with respect to wind tunnel data. Also shown were frequency spectra with a drop in resolved quantities (i.e., not following Kolmogorov's $-5/3$ slope), though following what was observed in the uniform-inflow wind tunnel experiment.

Forrest et al. [20], in 2010, investigated unsteady ship airwakes on the SFS2 using a Detached Eddy Simulation (DES) framework in Fluent, with the k–ω turbulence model. The CFD was able to capture most of the flow features present in the wind tunnel experiment used for validation, from Lee [37]. PSD plots showed agreement in all of the frequency range investigated (10^{-2} to 10^{1} Hz), in comparison to uniform-inflow wind tunnel data (which does not include any modeled effect of a real-world turbulent ABL). This work was one of the first to investigate, although not in detail, effects of an ABL. A modeled logarithmic profile was used, neglecting the impact of increased freestream turbulence and any temperature-related effects. Comparisons were made for a very limited number of data points and it is acknowledged that it is difficult to draw any conclusions about data agreement. Comparing their approximate ABL results with at-sea data, they concluded that the airwake turbulence has been reduced because low heights experience lower freestream velocities compared to a uniform inflow case. In addition, they recommended that ship airwake computations for flight simulation purposes should include an ABL to improve fidelity, identifying the airwake turbulent fluctuations to be sensitive to the inlet boundary condition, that is, uniform inflow vs. ABL inflow. They also concluded that the "shear layer separation and vortex formation from sharp edges is the dominant mechanics for turbulence generation over the flight deck". The airwake from green 45 degrees contains turbulence with larger time and length scales. Forrest et al. results on the ABL is consistent with Polsky [23], who investigated beam winds on ships and found that in such cases modeling an ABL is essential for predicting full-scale ship airwake flowfield (especially in beam winds). Polsky's study compared CFD with data obtained at-sea.

In 2013, Snyder et al. [24] compared their uniform inflow CFD solutions with the in situ data from Brownell et al. [2] as well as uniform-inflow wind tunnel experiment of the same ship geometry. General trends were captured but significant velocity magnitude differences were observed. The differences were identified as being due to the lack of an ABL model in both CFD and wind tunnel solutions. Once again, it was emphasized the importance of including an ABL profile in ship airwake simulations.

Van Muijden et al. [62], in 2013, compared Large Eddy Simulation (LES) and hybrid RANS/LES approaches on a different ship geometry (although also simple). They used the solver ENFLOW, with the k–ω turbulence model for closure. It was concluded that the hybrid approach provides solutions that are in general closer to experimental results. Only uniform inflow was investigated. The CFD solutions were used as an offline database for a helicopter dynamics simulator, and the approach used to feed the data was discussed. For the unsteady solution (hybrid approach), the time-resolved data were decomposed into steady-state modes by means of proper orthogonal decomposition (POD) and fed to the simulator. The fidelity of the piloted simulation depended on the number of modes the system's memory could handle, ultimately limiting the reconstruction procedure of the decomposed modes by the POD method.

In 2014, Quon et al. [26] used the SFS2 geometry to investigate a hybrid Unsteady Reynolds-Averaged Navier-Stokes (URANS) and vorticity transport methodology, similar to Keller [59], in 2007. They used the FUN3D/VorTran-M solver. Their solutions have been compared to uniform-inflow wind tunnel results by Rosenfeld et al. [38] and general trends at the flight deck region were captured. They acknowledge that the turbulent fluctuations from the ABL modify the freestream mean flow but no ABL has been considered.

Kelly et al. [63] (2016) investigated a modeled ABL on the UK's Queen Elizabeth Class aircraft carrier and compared with uniform-inflow water tunnel data, but the effect of the ABL by itself is not detailed. Fluent was used for the analysis, within a Delayed DES (DDES) framework with SST k–ω model for turbulence closure. The inflow was modeled by a logarithmic approximation, which is more realistic than a power-law profile, as it takes into account other parameters such as the aerodynamic surface roughness (taken in this case to be 0.001 m) and the friction velocity. The simulations presented are of the order of 120 million cells and were executed for 30 s of simulated time, which required a wall-clock time of about 30 days on 128 processors. Their results are compared with a water tunnel test currently being conducted by the same research group, and acoustic doppler velocimeter (ADV) results compare well with the computational findings.

More recently, a study by Dooley et al. [48] (2019) used a modeled turbulence approach of Mann [64] to represent the ABL. The effort was focused on the coupled effects of wave, ship motion, and ABL. It was concluded that the presence of the ABL resulted in an increase in turbulence over the flight deck, and extra vertical fluctuations provided additional diffusion which effectively "‘smoothed" the profiles obtained at the flight deck.

Watson et al. [50] performed DDES around the Queen Elizabeth Class aircraft carrier, comparing the data with the companion experimental study mentioned before [49]. The conclusions were that the full-scale CFD solution matched within 5% the velocities of the scale experiment. A steady ABL was considered in the full-scale CFD, but little differences were observed between a full-scale with ABL and 1:200 scale without ABL. This effort did not focus on ABL aspects, and little discussion about the ABL is presented.

A trend can be observed in the computational studies presented here. In early efforts, no ABL has been considered. With the availability of in situ experiments, CFD researchers acknowledged that a uniform inflow solution is not able to capture all real-world effects. Generally speaking, several efforts started to investigate the influence of a modeled ABL profile. Modeling such profiles has the advantage of negligible increased computational cost to the CFD model; however, it is limited to an appropriate velocity profile and thus does not capture all the physics involved.

Some of the work discussed above already included models of the flight dynamics of a helicopter, although the focus was on the airwake component of the dynamic interface. Next, some work in which a greater attention is given to the helicopter modeling are discussed.

1.1.4 Coupled Flight Dynamics and Airwake Computational Efforts

Due to increasing computational power, piloted simulation of the dynamic interface has become increasingly more complex and realistic. In the late 90's [29] and early 2000's [18], the most promising approach to include airwake in the simulation was to use look-up tables produced using an airwake model. In recent years, more complex and realistic approaches have been investigated. Some of them are reviewed in this section.

Adding a helicopter to the airwake adds complexity to the problem: the main rotor, tail rotor, and fuselage all influence the wake itself. There is also the interaction of the rotor with the flight deck. It is an inherently coupled problem. Generally speaking, coupling between a flight simulation code and CFD can be classified into two major categories: one-way and two-way coupling. In one-way coupling, the flight dynamics receives information about the flowfield from the CFD, but it does not send information back. In other words, the CFD does not account for the presence of the rotor. In two-way coupling methods, on the other hand, the information is passed back. This way, both codes run at the same time and the CFD takes into account the helicopter features that alter the flowfield. This method is also known as 'fully-coupled'.

Crozon et al. [21], in 2014, investigated in great detail helicopter rotors coupled with ship airwakes, using the CPF and a model of the Sea King helicopter. Two strategies were used: (i) steady-state calculations and actuator disk model of the rotor, and; (ii) URANS with k–ω and blade-resolving representation of the rotor. The importance of coupling effects on the wake and rotor inflow when operating close to the ship is stressed, and thus an "invalidity" of superposition methods is mentioned. Predictions of the rotor thrust compare well with experimental data. Findings include the difference in rotor loading between forward flight and near-deck operation. No ABL has been considered. Finally, as expected, resolving the blades yielded better predictions, although with higher computational costs.

In 2015, Forsythe et al. [65] coupled the ship airwake to the helicopter flight controls, though without atmospheric turbulence. They used the CREATE-AV Kestrel CFD code for the airwake and the U.S. Navy's code CASTLE for flight dynamics calculations. One- and two-way coupling were investigated. The coupled framework was not real-time-capable and thus included a pilot model. The helicopter main rotor has been modeled by an actuator disk model. Promising results were achieved.

In 2016, Rajmohan et al. [66] used a vortex particle method coupled with CFD to study the airwake of the SFS2 and rotor interaction. A case of a helicopter in proximity of the SFS2 flight deck was investigated using two-way coupling, with OpenFOAM on the airwake side and FLIGHTLAB on the flight dynamics side. No ABL was included in this work, and the Spalart–Allmaras model was used for closure. Again, general good agreement with wind tunnel results by the NRC of Canada was observed. Frequency characteristics analysis of the airwake was carried out for a sampling period of 15 s at 100 Hz. The simulation showed good agreement in the range of 1 to 5 Hz. At higher frequencies, there is a sharp drop in resolved content attributed to excessive RANS dissipation. The wind tunnel results used for comparison also have the sharp drop in the energy content at higher frequencies. In their UH-60A coupled simulations, results have shown non-linear unsteady interactions between the ship airwake and rotor wake, and these characteristics changed with the position of the rotor with respect to the ship deck.

In 2016, Polsky et al. [67] described an airwake analysis tool developed at NAVAIR. It relies on CFD for the airwake model and real-time aircraft flight dynamics models. The tool has been used for both rotary-wing and fixed-wing aircraft. On the airwake modeling side, both uniform inflow and modeled ABL were investigated in a URANS framework in Cobalt. The ABL profile has been generated using a power-law function, resulting in a steady profile. A uniform inflow profile has been superimposed to the ABL profile to account for the ship velocity; this approach of modeling the ABL improved results substantially with respect to a no-ABL case (the power-law profile without the uniform inflow superimposed was not discussed). The final tool has integrated flight dynamics in a one-way coupling fashion. Emphasis has also been given to developing a user-friendly graphical interface. It was emphasized that for a helicopter hovering near the deck, the airwake produced by the aircraft can have a significant effect on the surroundings, including the ship airwake. Thus, similarly to Crozon [21], it is pointed out that one-way coupling should be used with caution.

Oruc et al. [68] (2017) investigated coupled CFD and flight dynamics in hovering and forward-flight cases, without considering the ABL. Hovering included partial ground effect, sloped terrain, near a wall, and near ship. It was found that using fully-coupled simulations instead of an inflow model resulted in more fluctuations in the helicopter dynamics due to rotor/terrain interactions. In forward-flight acceleration cases, the coupled simulations were able to reproduce recirculation and ground vortex features present in experiments. The rotor was modeled by the actuator disk model. Real-time two-way coupling has been achieved by the same authors [69].

In 2019, Sharma et al. [70] investigated the flow over the SFS2 and a helicopter performing an approach trajectory using HeliUM 2 flight dynamics code. It was found that the vehicle response required additional control effort when subject to non-zero WOD as opposed to aligned wind. This is consistent with findings from [55]. Even greater control effort was required when the model included the fuselage, empennage, and tail rotor. Asymmetry of results was also reported, this time from a controls perspective.

Several other works in the literature have investigated computational approaches to ship airwake modeling and coupling flight dynamics. In general, in airwake-only investigations, all of them captured the main flow features when comparing to wind tunnel results and they do not usually include any ABL effect. When coupling, the addition of the helicopter by itself is the challenge, and thus no ABL effects tend to be considered.

This review finishes by quoting Brownell's in situ work [2] regarding the importance of the ABL: "Wind-tunnel data alone cannot be used to validate CFD, especially considering potential issues with recreating the atmospheric boundary layer". ABLs should be included in numerical studies and comparisons with data obtained at-sea should be made.

1.2 Motivations

In the review of previous airwake modeling efforts, several of the drawbacks of commonly used approaches have been identified and discussed. The deficiencies can be broadly summarized as the lack of realistic atmospheric turbulence effects in computational studies. At most, a low-order model has been used. As discussed, there are many studies that support the need to better understand the impact of a realistic ABL on dynamic interface modeling.

Dynamic interface simulation is challenging due to the several subsystems that need to be considered and coupled for a realistic model. For instance, in flight envelope testing, differently from a pilot training simulation, the model must also operate realistically at the edges of the envelope. In this case, high levels of fidelity are required for the airwake and aerodynamic models [10]. The airwake, though, is dependent on a number of factors, including ambient atmospheric winds, sea state, ship geometry, and ship motion. Furthermore, the impact of the airwake on the helicopter is a function of its size, weight, geometry, flight control system, and rotor design. The lack of realistic ABL turbulence in the current state-of-the-art modeling and simulation strategies are the motivations for the current work. In this section, the specific motivations are described in more detail.

1.2.1 A Problem of Many Scales

Considering a real-world scenario of a helicopter landing on a moving aircraft carrier, it is not difficult to realize the broad range of time- and length-scales present and in constant interaction. For instance, turbulent eddies present in the atmospheric boundary layer have length scales that can span many orders of magnitude. Not all length- and time-scales are relevant for the problem considered, but those that span from tens to hundreds of meters are likely to be important.

When adding an actual ship with its major components, and a helicopter, the range of scales increases greatly. In reality, scales from the large atmospheric fronts, all the way to the rotor airfoil boundary layer are present. The associated time-scale also spans many orders of magnitude.

The presence of the wide range of scales is one of the challenges in performing a fully-resolved simulation of a helicopter flying in the wake of a ship subject to realistic atmospheric inflow. This issue is illustrated in Table 1.1.

Table 1.1: Scale requirements in coupled atmospheric turbulence, ship airwakes, and helicopter aerodynamics.

	Length scale (m)	**Velocity Scale (m/s)**	**Time scale (s)**
Airfoil boundary layer	0.001	100	0.00001
Airfoil	0.1	100	0.001
Rotor	10	10	1
Ship	100	10	10
Large-scale atmospheric eddies	100	1	100

In this work, not all scales are realized. Some of the reasons for that are (i) it is clearly prohibitively expensive; (ii) not all scales are relevant for the problem; (iii) no helicopter rotor will be resolved in this work, such that some of the small length scales would not be present anyway. This research project aims in understanding the effect of large and small scale atmospheric eddies on a ship and the subsequent effect on a vehicle. The complexity of the interaction of the atmospheric eddies with those shed off from a ship and its interaction when at the same time- and length-scale are one of the motivations of this work and the goal is to resolve such scales and explore their interaction.

1.2.2 Unsteady Effects Due to Atmosphere Turbulence

Another motivation can be simply stated as the desire to capture the unsteady atmospheric effects. A simplified cartoon that illustrates the unsteady aerodynamic loads seen by the rotor blades is shown in Fig.1.11. Similarly, Leishman [71], when discussing sources of unsteady aerodynamic forcing terms at a blade element level, points out the unsteady vertical gusts which atmospheric disturbances are part of, contribute to the unsteady loading on rotors (Fig. 1.12). In fact, the unsteady airwake, when modified by atmospheric inflow turbulence, exhibits a more disturbed vertical velocity field. Therefore, unsteadiness present in the atmosphere is likely to have an effect on the handling qualities of a helicopter.

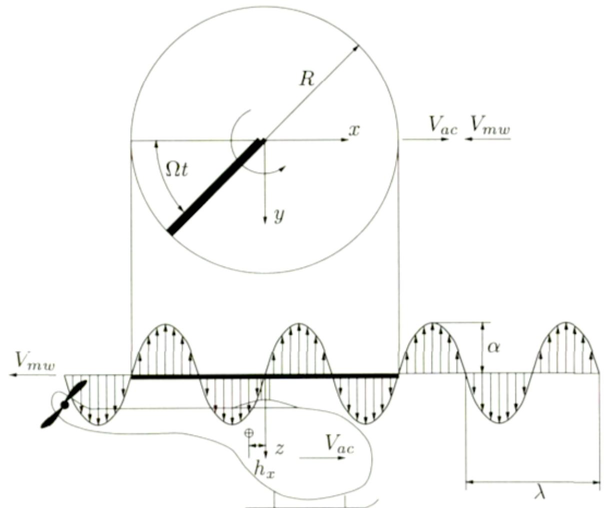

Figure 1.11: Simplified atmospheric turbulence effect on the rotor. Figure from van Gool [27].

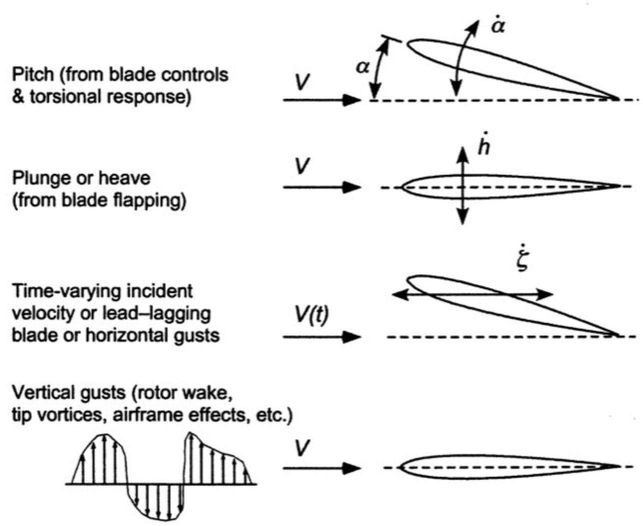

Figure 1.12: Unsteady aerodynamic sources at a blade element level. Atmospheric effects are included in unsteady vertical gusts. Figure from Leishman [71].

The importance of atmospheric effects has been discussed by Gool [27] in 1997, who investigated in great levels of detail the influence of atmospheric turbulence on the handling characteristics of a helicopter. Thorough for its time, the work consisted of one-way coupled simulations, where the helicopter only sampled the velocity field generated by the atmosphere. The atmosphere has been modeled by a stochastic model. It was concluded that several dynamic aspects of the vehicle are influenced by an atmospheric model, such as the statistics of the helicopter response and turbulence, as well as the dynamic stall response. It is also mentioned that space-fixed and one-dimensional turbulence approximations are not adequate for predicting blade flap response to turbulence.

As indicated by several efforts reviewed in the previous section, including atmospheric effects is important. The atmospheric velocity vector varies with space, time, local weather condition, and ground roughness, all of which are not trivial to describe mathematically and create a simple model. In other words, realistic atmospheric turbulence is not readily obtained or approximated. In particular, synthetic turbulence models of the atmosphere have difficulty predicting flows in which are dominated by buoyancy. The so-called steady (or modeled) profiles from the literature do not include the inherent turbulence present in the ABL. In this work, the *resolved* aspect of the atmospheric turbulence field is investigated.

By immersing the SFS2 in a resolved ABL inflow, it is possible to study the fundamental differences present in the airwake in comparison to a simple uniform-inflow model of the incoming wind. In other words, the interaction of the ship airwake with the atmospheric conditions results in complex physical phenomena, that have not been thoroughly analyzed yet. Several authors highlight the importance of including atmospheric effects [13, 20, 22–25, 52, 63], solutions of resolved ABL coupled with ship airwakes have not been investigated. Crozon et al. [21] mention that the ship airwake is a combination of the wind and ship motion and is influenced by the ABL and any element of the boat superstructure. It is known that the inclusion of a planetary boundary layer changes not only velocity magnitudes but also the appearance and location of many dominant flow structures [2].

1.2.3 Power Spectral Density and Energy Content

The study by Polsky [1] mentioned earlier presented PSD plots comparing uniform-inflow CFD solutions with data obtained at-sea. Lower-frequency content is captured, as acknowledged in the paper, but the CFD fails to capture the correct content at frequencies higher than about 3 Hz — see Fig. 1.13. A drop occurs in the content resolved by the CFD, indicating that it no longer follows Kolmogorov's $-5/3$ slope. The work of Wilkinson et al. [10], which discusses fidelity requirements, also presents a similar plot to illustrate airwake requirements for dynamic interface testing. The results of these studies will be shown later when a spectral analysis is performed on different points of the airwake, since a comparison will be readily possible. In the case of Wilkinson, regarding the CFD-resolved airwake model, it is mentioned that the airwake "should be accurately modeled in the frequency range that impacts most on pilot's workload" — and the range mentioned is 0.2 to 2 Hz.

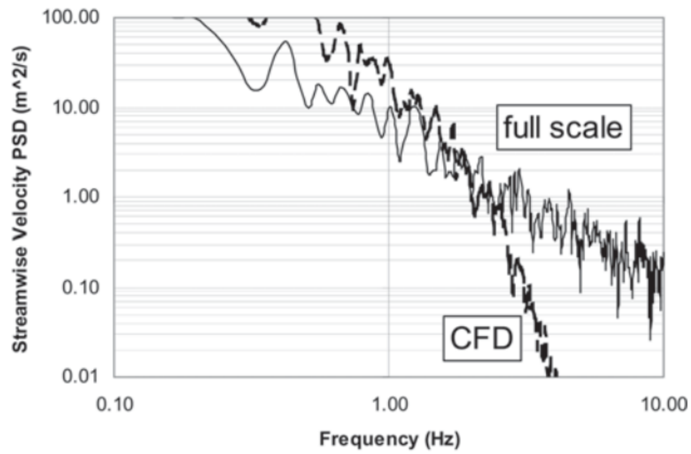

Figure 1.13: Typical velocity spectra from data collected at a real carrier, in comparison with typical CFD calculation. Note the drop in resolved content at higher frequencies that usually happens in typical CFD calculations. Figure from [13], with data from Polsky [1].

With that said, it has been argued that the frequency bandwidth that has the greatest effect on pilot workload is approximately 0.2 to 2 Hz by not only Wilkinson [10], but several other sources [2,13,45,72]. All of these efforts cite the original work of McRuer [73], from 1994. Several computational works then focused on only accurately matching this frequency bandwidth. All of the computational efforts discussed earlier that present energy spectra [1, 10, 59, 61, 66] either (i) fail to match high-frequency content when compared to in situ data; or (ii) present a substantial drop in resolved content, that no longer follows $-5/3$ (and when compared to wind tunnel results, good agreement is acknowledged).

Little attention has been given to frequencies outside this range. When developing solution methods that have the end goal of being used in training simulators, it is desired that a given modeling strategy is able to reproduce the energy frequency spectra seen for in situ experiments and that will be experienced by the pilot, thus giving the model a higher level of fidelity. Although there is a bigger question of what bandwidth should be captured, it is important to understand the effects of the frequencies that are not far from the 0.2–2 Hz range given. No work has been found in which frequencies from the CFD matched what is observed in situ. Therefore, another motivation of this work is to try to reproduce a broader range of frequencies. Although higher frequencies such as 20 or 30 Hz may be well into the vibratory modes of the vehicles, the same cannot be said about frequencies between 3 and 4 Hz, for instance. As will be shown later in chapter 5, under an unsteady ABL inflow, a broader range has been matched with respect to the $-5/3$ turbulence cascade slope observed at sea.

1.2.4 Time Accuracy

In order to achieve high levels of fidelity of both the airwake and the actual ambient atmospheric turbulence, it is essential to resolve the flowfield in a time-accurate fashion. Also, in order to investigate the unsteady phenomena that occurs in an airwake, it is evident that a time-resolved dataset is necessary. Although the time accuracy motivation aspect is closely related to the 'unsteady effects' listed previously, it is given here as a separate motivating factor. The reason to do so is to highlight that several authors [1, 36, 74] mention that steady-state RANS solution may not match a time-average of an unsteady solution.

Furthermore, the atmospheric turbulence is also highly unsteady. Resolving the unsteady features of the ABL is common practice within the wind energy community [7,75], where, for example, time-varying effects have consequences on wind turbine blade fatigue and overall turbine efficiency.

In a numerical solver setting, Polsky [1] mentions that steady-state results do not compare nearly as well to experiments as the time-averaged results of time-accurate simulations. The differences are most likely attributable to the fact that steady-state solutions are obtained using local time-stepping, which are physically correct only when fully converged. An unsteady flow, however, never achieves convergence in the sense of small residuals.

Given the findings from the literature and the fact that in order to capture the atmospheric turbulence a time-accurate simulation is necessary, time accuracy is considered another motivation of this work.

1.2.5 Coupled Physics

In this work, as it will be discussed shortly in the objectives section, the dynamic interface modeling problem is investigated further in order to quantify the effects of an ABL-modified airwake on a dynamic system. In the dynamic interface problem, such a system is a helicopter operating in the vicinity of the ship.

Therefore, another motivation of this work comes from the importance of two-way coupled approaches when simulating the flight dynamics of a helicopter flying in the airwake of a ship. Polsky et al. [67], Crozon et al. [21] and Oruc et al. [68, 76] highlight the importance of two-way approaches for realistic physics when flying or maneuvering in the airwake. In addition, effects of complex terrain and/or complex structures in the vicinity of the helicopter wake are difficult to predict. Both the performance and handling qualities of a vehicle can be substantially influenced by the presence of such features [68].

It is acknowledged that fully-coupled physics are not performed in this present study. However, a quest for a fully-coupled model is indeed one of the motivations of this work. This present research effort contributes to further the understanding of the atmospheric effects in a dynamic interface setting, and the goal is to eventually be able to perform a fully-coupled investigation.

1.3 Objectives and Scope of Current Work

Given the previous discussion of the motivation for this research, the objectives and scope of the paper are now presented. This research is part of a larger effort to evaluate the fidelity requirements for dynamic interface simulation. The current dissertation focuses on the details of the atmospheric boundary layer and its effect on a dynamic interface simulation.

In this work, high-fidelity numerical simulations are executed in both OpenFOAM and OVERFLOW in order to understand what is relevant in a turbulent atmospheric inflow. Hence, to develop practical design and training tools, it is necessary to identify critical and superfluous flow physics for ship airwake and helicopter interactions. Airwake models should capture all relevant time and length scales from the ABL that affect the vehicle response and pilot input. It is anticipated that coupled simulations of a piloted helicopter in a turbulence-resolving ABL is useful in understanding the importance of the relevant time and length scales.

The objective of this work is twofold and can be summarized as follows: (i) investigate and identify the fundamental changes in the flow characteristics of a ship airwake that is modified by realistic atmospheric turbulence; and (ii) perform coupled helicopter dynamics simulations using ABL-modified CFD data and determine pilot workload subject to the different inflows, in special unsteady ABL inflow.

Determining whether flow features such as high turbulence intensity and steep velocity gradients present in shear layers have adverse effects on the operations of the aircraft is not possible without considering actual vehicle characteristics [67]. In this work, a representative of the UH-60A helicopter model will be used. For the ship geometry, the SFS2 will be used. Although there are no in situ results on a ship geometry created for research purposes, matching in situ results for the energy content at different locations of the wake is one of the goals. Results will be presented in which Kolmogorov's cascade has been captured for a longer frequency range than previous studies (e.g. Fig. 1.13 for instance).

While the focus of this work is on the study of the resolved turbulence, attention is also given to the "steady ABL" profile that is frequently mentioned in the literature. The idea is that such profile contains the appropriate velocity gradient, but not the freestream turbulence. It is a scenario in which an instantaneous snapshot of the flow upstream the ship is, by definition, the same as the time-averaged one.

The modeling and simulation of the dynamics interface discussed throughout this dissertation are defined to include non-piloted, non-real-time activities. To fully resolve an atmospheric velocity field and to maintain its accurate representation, a large domain is required, thus it comes at a substantial computational cost. In fact, computational efficiency, good parallel scaling, and the likes are not explicitly explored in this work. While every effort is made in order to make proper use of the resources available, since the objective is not to develop a tool for routine engineering use, most of the simulations executed are very expensive. Actually, most of them takes between 3 to 6 days to complete, sometime on 600-1000 cores. It is acknowledged that such computational requirements remain high for a dynamic interface tool. The present work's primary scope is to develop a physical understanding, putting computational efficiency as a subsequent effort.

This work also aims in motivating future research, particularly within the area of reduced-order models. Reduced-order modeling approaches such as proper orthogonal decomposition (POD) [77], or spectral POD (SPOD), pose as feasible approaches to successfully perform real-time flight simulation while accounting for realistic atmospheric effects. Recently, POD has been applied to a ship airwake problem [78]; however, the analysis did not include an ABL. Such work represents one of the first attempts in using reduced-order modeling on ship airwakes, alongside the studied by van Muijden mentioned before [62].

The goal of this work is not to provide an exhaustive study on the effects of different parameters in modeling an ABL and their effects on the ship airwake. While convective ABL cases are considered in validation efforts, only neutral cases are executed with the coupled ship and flight dynamics. The work is an initial exploration into the effects of unsteady atmospheric freestream turbulence on ship airwakes, thus canonical neutral atmospheric stability states have been considered. The results presented here help further understanding on complex physical interactions between the atmospheric boundary layer and ship airwake, and the effects of the resulting flowfield into a helicopter. This is done in an effort to support and provide insight for the development of lower order and/or less expensive engineering tools.

1.4 Concluding Remarks

The problem investigated in this work involves multiple disciplines and requires the use of concepts, tools, and ideas from different areas. The disciplines that are most relevant to this work are meteorology, numerical methods, computer science, and helicopter aerodynamics and dynamics. For instance, the physical processes that occur in the lowest part of the atmosphere need to be understood, as well as the numerical aspects related to the computational modeling of such processes. Due to the size of the numerical problems, efficient use of large computational resources are required. Finally, the interaction of the ship airwake with the turbulence present in the freestream needs to be considered in a helicopter flight dynamics setting, alongside an analysis of the possible effects on a pilot and the associated workload.

It is not within the scope of this work to address the details of each of these disciplines. The goal of this project, however, is to develop an understanding of the atmospheric effects in ship airwakes for practical applications of dynamic interface modeling and simulation. In order to contribute towards the bigger objective, while some disciplines are investigated in more depth than others, an appropriate attention is given to all of them and how they interact with each other within the developed analysis tool.

An attempt is made to provide the essential background of concepts utilized in this work, although the main focus is on the numerical solution of the ABL and the effects on a helicopter. The remainder of this dissertation is organized as follows:

- In chapter 2, theoretical aspects pertinent to the ABL are discussed, alongside the similarity theory and considerations of theoretical curves to represent the mean wind speed;
- Chapter 3 provides a description of the computational setup used to solve the ABL and validation efforts are presented and discussed;

- In chapter 4, numerical aspects pertinent to the inclusion of the SFS2 model are discussed. A description of OVERFLOW and the steady ABL profile is also given in this chapter;

- Chapter 5 presents comparisons between the turbulent airwake obtained by using the different inflows and levels of fidelity for the ABL model;

- Chapter 6 describes the coupling methodology and the results obtained with the one-way coupled flight dynamics code;

- Finally, in chapter 7, the conclusions, contributions, and suggestions for future research are laid out.

Chapter 2 The Atmospheric Boundary Layer

Boundary layer meteorology and the atmospheric boundary layer are extremely rich and broad research areas. It is usually studied in depth by meteorologists and it has applications in several areas of engineering. In this chapter, some aspects of the atmospheric boundary layer that are pertinent to this work will be discussed. For a more in-depth discussion, the interested reader is referred to the work of Stull, which covers the topic with a slightly different perspective in each of his books — references [79–81] — and that of Wyngaard [5]. The theoretical content presented in this chapter is based on these references.

2.1 Overview

The bottom 0–200 m to 0–4 km of the troposphere is called the atmospheric boundary layer (ABL). It is a region that is often turbulent and varies in thickness in space and time. This layer is usually topped by a stronger variation in temperature. The ABL is sometimes referred to as the planetary boundary layer. The behavior of such layer is directly influenced by the contact with the Earth's surface, which slows the wind due to surface drag, changes temperature depending on the time of the day and season, and modifies moisture and pollutant concentrations. The turbulence within the ABL is generated and maintained by two forces: wind shear and buoyancy. Figure 2.1 illustrates the atmospheric boundary layer.

The ABL experiences a diurnal cycle of temperature, wind, humidity, and pollution variations in response to the varying surface fluxes. Due to this constant cycling nature, the ABL is turbulent, and the presence of turbulence is one aspect that makes it unique. Above the ABL, the air is usually unmodified by turbulence, and retains the same temperature profile as the standard atmosphere in an ideal scenario. This air present

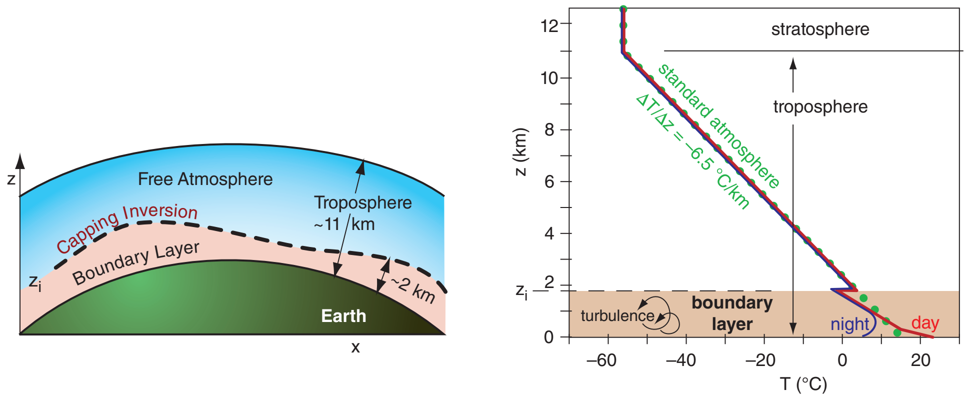

Figure 2.1: The boundary layer within the bottom of the troposphere. The plot on the right shows the standard atmosphere in dotted green and typical temperature profiles during the day and night. Figures from Stull [79].

above the ABL is called the *free atmosphere*.

Within the ABL, air is highly turbulent, and within the free atmosphere, the tropospheric air has little to no turbulence. A result of these layers being adjacent is a sharp temperature increase at the top of the ABL. This zone is very stable due to the inversion of temperature. This temperature increase effectively acts like a cap to the motions and turbulence present in the ABL. The middle of such thin layer is a measure of the depth (height) of ABL, and it is usually denoted by z_i. It is also called the capping inversion. Several parameters such as season, current weather, and time of the day can impact the height of the boundary-layer.

Geostrophic winds are winds due to the pressure gradient and Coriolis forces, with directions parallel to straight isobars with low pressure. Geostrophic winds are the winds present in the free atmosphere, above the capping inversion and are unaffected by drag, shear, and thermal turbulence present in the atmospheric boundary layer.

The bottom 0–20 to 0–200 m of the ABL is called the *surface layer*. In this region, frictional drag, heat conduction, and evaporation from the surface cause substantial variations of wind sped, temperature, and humidity with the height. This layer is also called the constant flux layer because the turbulent fluxes are uniform along the height. This work is interested in the turbulence present in this layer.

In summary, the ABL is a region of highly turbulent, high Reynolds number flow. Its depth varies with time and location. The behavior of this layer is directly influenced by the contact with the planetary surface as it responds quickly to changes in surface heating and temperature, exhibiting strong diurnal variations of winds, temperature, moisture, etc. Because of the heating and cooling cycle, there is a cycle of static stability, which will be discussed next.

2.2 Stability of the Atmosphere

Before a discussion on the stability state of the atmosphere, some key concepts in flow stability are quickly introduced. In this context, flow stability is a characteristic of how a system reacts to small disturbances.

A system is said to be *stable* if the disturbances are damped, whereas if they cause an amplifying response, the system is said to be *unstable*. In a situation where the disturbances neither amplify or dampen, the system is said to be *neutral*. Flow stability is controlled by all processes acting on the flow, such as buoyancy, inertia, wind shear, rotation, etc. Static stability is related to buoyancy and dynamic stability includes both buoyancy and wind shear.

Static stability can quantify instability due to vertical variation of temperature alone. Dynamic stability, on the other hand, can quantify instability due to the combined effects of wind and temperature variations with height. Regarding turbulence, statically stable flows can be dynamically unstable and and can become turbulent if the wind shear is strong enough (if only buoyancy is present, statically stable flows remain laminar). Static stability controls the formation of the ABL and it affects its wind and temperature profiles.

In an atmospheric boundary layer setting, consider a parcel of air forcibly disturbed up or down. When moved, the parcel's temperature could differ from that of its surroundings, thus resulting in buoyant forces. Similarly to the previous discussion, the environment is statically stable if the buoyant forces push the displaced air parcel back to its starting position. The environment is statically unstable if the displaced particle is pushed further away from its starting position, and statically neutral if it remains stationary. Unstable regions are turbulent.

In a practical sense, the standard atmosphere is statically stable, but because of the daily cycle of heating and cooling, there is an associated cycle of stability in the ABL. In practice, there are three distinct conditions:

Unstable condition Associated with light winds and a surface that is warmer than the air (sun-heated surface). Typical of sunny days in fair weather, and can also occur when cold air blows over a warmer surface. Thermals of warm air rise and the layer reaches heights of 200 m to 4 km. Turbulence within this region is vigorous.

Stable condition Associated with light winds and a surface that is cooler than the air. Typically occurs at night in fair weather with clear skies, or when warm air blows over a colder surface. This layer is shallow compared to the unstable cases. Turbulence in this region is weak to non-existent.

Neutral condition Associated with moderate to strong winds, and there is little to no heating or cooling from the surface. Typical of overcast conditions, often associated with bad weather.

Essentially, under neutral conditions, shear is generated by the interaction of the wind with the rough planetary surface. Under unstable conditions, buoyancy forces amplify disturbances in the flow, resulting in turbulence with more vertical motions than a shear-generated case. Lastly, under stable conditions, buoyancy forces damp disturbances in the flow, effectively reducing turbulence. Wind shear dominates neutral and most of the stable ABL, while buoyancy dominates the convective (unstable) ABL. Depending on the forcing mechanism, or, the stability state, the flow patterns and turbulence statistics can be quite different [82]. Individual or collection of roughness elements present in the ground can accentuate a certain stability state.

It is now appropriate to introduce the concept of potential temperature. Potential temperature θ of a parcel of fluid at pressure p is the temperature that the parcel would attain if adiabatically brought to a standard reference pressure p_0 (usually 100 kPa, or 1 atm). For an ideal gas,

$$\theta = T \left(\frac{p_0}{p} \right)^{R/c_p} \tag{2.1}$$

where T is the absolute temperature (in K), R is the gas constant of air, and c_p is the specific heat capacity. Potential temperature is an important quantity because its value is not affected by the rising and sinking of parcels associated with flow over obstacles or large-scale atmospheric turbulence. Consider a figure similar to that shown on the right of Fig. 2.1, but this time with the potential temperature instead of the absolute temperature — this is shown in Fig. 2.2.

Next, Fig. 2.3 illustrates the relationship between the potential temperature gradient and the stability state. Following the previous discussion, a stable condition occurs if the potential temperature increases along the height. An unstable condition is when the potential temperature drops with the height and thus allows thermals of hot air to rise, without the dampening of the buoyant forces observed in unstable cases. In the middle of the two, there is the idealized neutral case, where as discussed, no variations of the

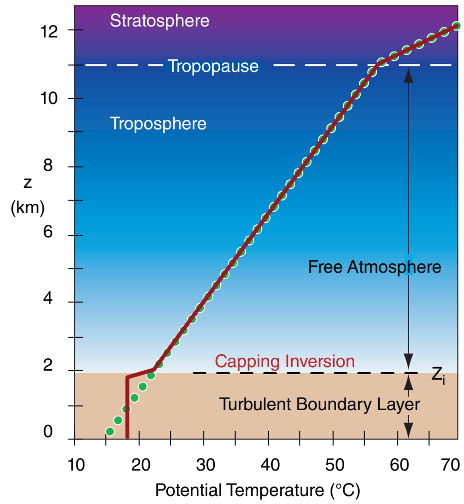

Figure 2.2: The ABL and the free atmosphere heights vs. potential temperature. Standard atmosphere plotted in green, and the red curve shows an idealized potential temperature profile. Figure from Stull [79].

potential temperature are present below the capping inversion.

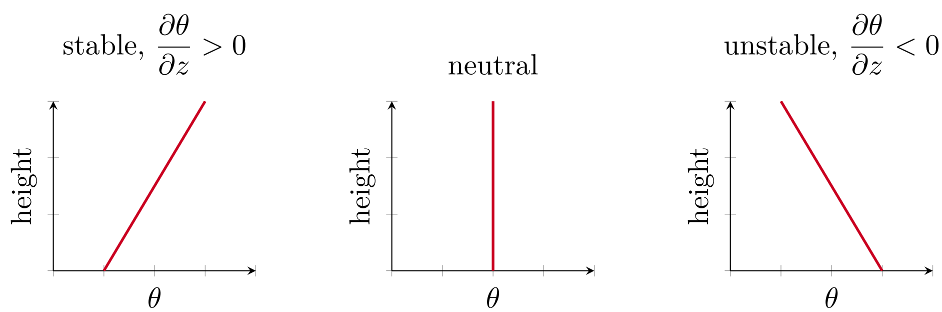

Figure 2.3: Sketch of the distribution of averaged potential temperature along the height for the different stability states.

Figure 2.4 depicts a typical potential temperature and potential temperature flux (sometimes referred to as kinematic flux) for an unstable boundary layer. The heat flux characteristic of an unstable ABL results in an increased potential temperature near the surface, which directly modifies the temperature flux throughout the surface and mixed layers. The value of the potential temperature flux at the bottom is sometimes referred to as surface temperature flux, denoted by q_s. Note the relationship between the unstable condition shown in Fig. 2.3 and the lowest portion of the surface layer shown in Fig. 2.4.

To illustrate these concepts with real data, measurements of potential temperature made by Anderson et al. [3] are shown in Fig. 2.5. Such experiment will be discussed

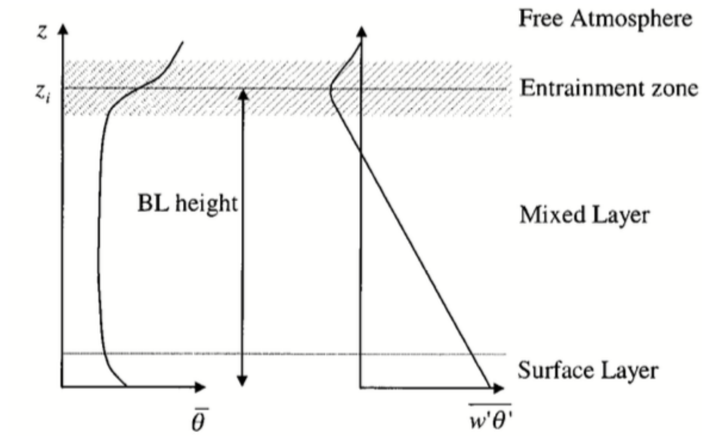

Figure 2.4: Typical shape of vertical profiles of potential temperature θ and its flux $\theta' w'$. Overbars refer to time-averaged quantities. After Stull [79].

in more depth in section 3.3. The data was collected over sea, and the condition was stated to be unstable. Different profiles are related to different sampling windows, but the general $\partial\theta/\partial z$ is consistent across the windows.

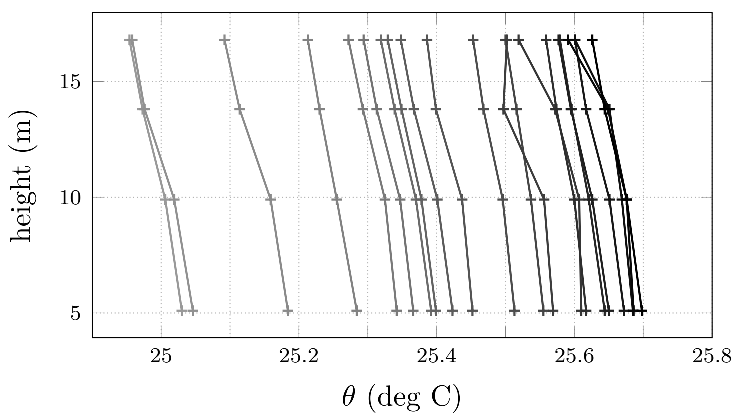

Figure 2.5: Potential temperature values observed at 5 mast positions at-sea for the very bottom of the surface layer during the RED experiment in 2002 [3]. Each profile represents a 30-min average.

There are a lot of details that go into the discussion of the ABL structure and evolution. Some examples are the differences between a day or night profile, or across different seasons. The purpose of this work is to provide a better understanding and the first investigation of the effects of a real ABL on the coupled problem of the ship airwake, and thus preferences are given to the analysis of a neutral condition. It is acknowledged that the flow will be generally less turbulent than that of a convective condition, however, a simpler condition with no buoyancy effects present was preferred.

2.3 Surface Roughness

The aerodynamic surface roughness is defined as the height where the wind speed becomes zero. The 'aerodynamic' aspect is due to the fact that the only way to truly determine such a quantity is by measurements of the wind speed at various heights [81]. The roughness length is not equal to the height of individual roughness elements on the ground, but there is a one-to-one relationship between the roughness elements and the aerodynamic surface roughness. Once the aerodynamic surface roughness length is determined for a particular surface, it does not vary with wind speed, stability, or stress. The surface roughness is an important parameter because, as mentioned, it can further accentuate a certain stability state.

Typical values for the aerodynamic roughness length are presented here using two different classifications. The Davenport-Wireringa classification encompasses different types of landscape and has the associated approximate surface roughness, and it is given in Table 2.1, as reported by Stull [79].

Table 2.1: The Davenport-Wieringa roughness-length z_0 classification. Table presented in Stull [81].

$\mathbf{z_0}$ **(m)**	**Classification**	**Landscape**
0.0002	sea	sea, paved areas, snow-covered flat plain, tide flat, smooth desert
0.005	smooth	beaches, pack ice, morass, snow-covered fields
0.03	open	grass prairie or farm fields, tundra, airports, heather
0.1	roughly open	cultivated area with low crops and occasional obstacles (single bushes)
0.25	rough	high crops, crops of varied height, scattered obstacles such as trees or hedgerows, vineyards
0.5	very rough	mixed farm fields and forest clumps, orchards, scattered buildings
1.0	closed	regular coverage with large-sized obstacles with open spaces roughly equal to obstacle heights, suburban houses, villages, mature forests
≥ 2	chaotic	centers of large towns and cities, irregular forests with scattered clearings

Another classification for the aerodynamic surface roughness, after Garrat [83], Smedman-Hogstrom [84], Kondo and Yamazawa [85], Thompson [86], and Nappo [87], but compiled and presented by Stull [80] is shown in Fig. 2.6.

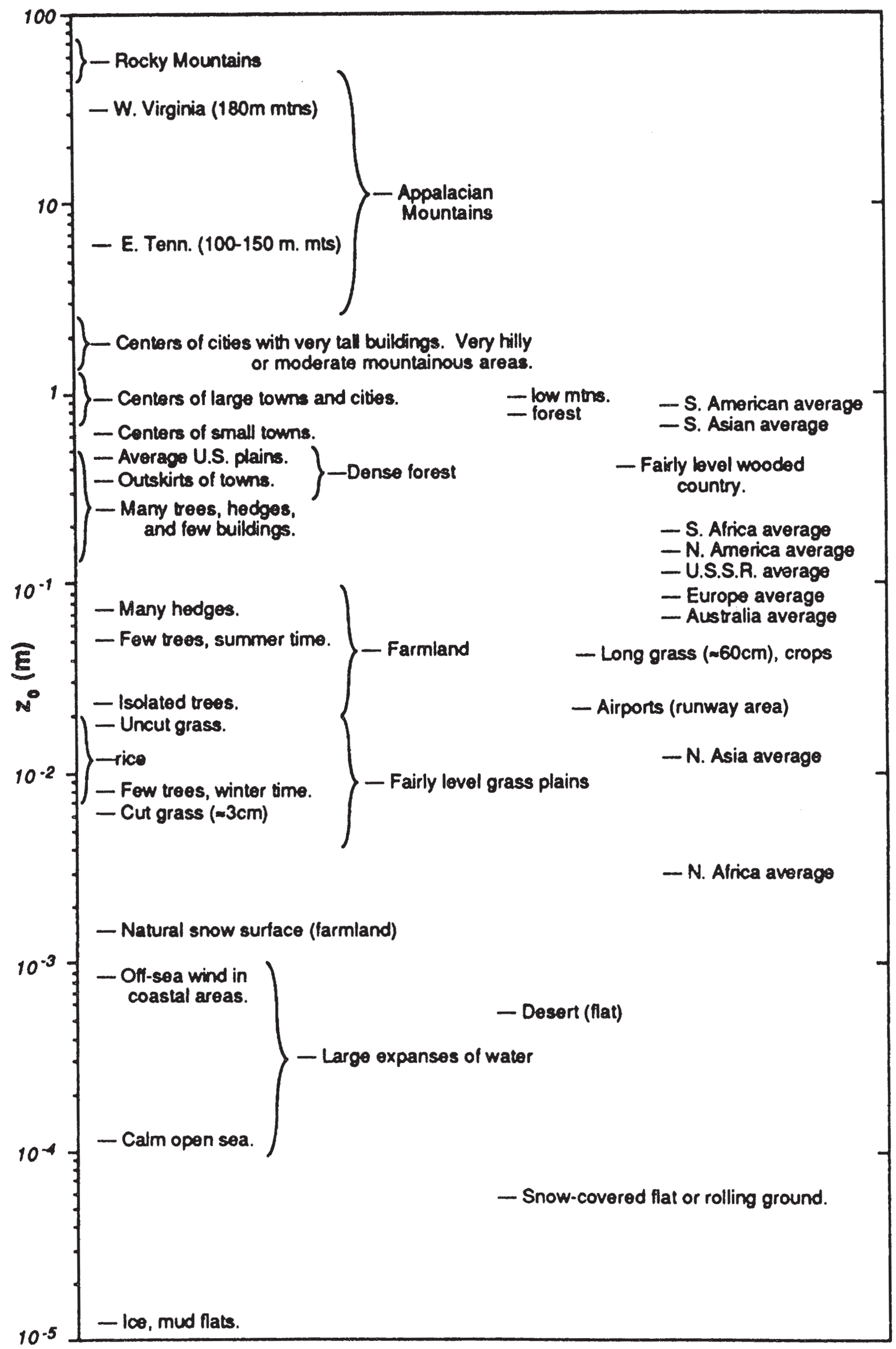

Figure 2.6: Aerodynamic surface roughness lengths for typical terrain types. Figure from Stull.

In numerical models, however, the first grid point off the surface is often higher than the aerodynamic surface roughness value for a given landscape. In those scenarios, a model is important. In situations where the turbulence is generated and maintained by the wind shear near the ground (that is, a more neutral case), the magnitude of the Reynolds stress at the surface becomes an important scaling variable. Only two components of the symmetric stress tensor are important and they are

$$\tau_{xz} = \tau_{zx} = -\rho\overline{u'w'} \tag{2.2}$$

$$\tau_{yz} = \tau_{zy} = -\rho\overline{v'w'} \tag{2.3}$$

where ρ is the density, $U = (u, v, w)$ is the velocity vector and the prime denotes fluctuations around a mean quantity. Based on such relationship, the friction velocity can be defined as

$$u_*^2 = \left(\tau_{xy}^2 + \tau_{yz}^2\right)^{1/2} \ . \tag{2.4}$$

The concepts of friction velocity and stress are important to the model. The next chapter will return to this discussion on modeling the stress terms from Eqs. (2.2) and (2.3).

2.4 Monin-Obukhov Similarity Theory

The wind profile of neutrally stratified ABLs can be represented with relative accuracy by means of a logarithmic analytical equation. However, when stability is considered, the resulting profiles can deviate significantly from the standard neutral logarithmic profile. The Monin-Obukhov similarity theory describes dimensionless parameters across the different stability states, enabling relationships to be derived.

The derivation of the Monin-Obukhov similarity theory was based on dimensional analysis and the Buckingham Pi theory. Sparing several details, the Obukhov length is given by

$$L = -\frac{u_*^3\,\theta_0}{\kappa\, g\, q_s} \tag{2.5}$$

where $q_s = \overline{\theta' w'}$ is the potential temperature flux (or kinematic surface heat flux) at the surface[1], θ_0 is a reference potential temperature (usually 300 K), g is the gravity, and κ is the von Karman constant. L has units of meters and its magnitude is used

[1]Sometimes in the literature a different form of the flux is given, with units of W/m^2. Denoting it by Q, $Q = \rho\, c_p\, q_s$. As can be easily inferred from its definition, q_s has units of K m/s.

to define the stability state of the atmosphere. Essentially, L is negative in unstable conditions ($q_s > 0$), positive in stable conditions ($q_s < 0$), and defined as infinite in neutral conditions ($q_s = 0$). The Obukhov length can be interpreted as the height of the stable surface layer below which shear production of turbulence exceeds buoyant consumption. Table 2.2 lists the stability condition with respect to the value of the Obukhov length L. This quantity is usually not explicitly set in any LES code, but rather is a result of different physical parameters, as its definition suggests.

Table 2.2: Stability state classification with respect to Obukhov length. Units of L given in meters.

Obukhov Length range	**Classification**
$10 < L < 50$	very stable
$50 < L < 200$	stable
$200 < L < 500$	near neutral / stable
$L > 500$ or $L < -500$	neutral
$-500 < L < -200$	near neutral / unstable
$-200 < L < -100$	unstable
$-100 < L < -50$	very unstable

The Obukhov length is used for non-dimensionalization of the height, thus resulting in the quantity z_i/L. $-z_i/L$ is also often given as a classification of the stability state (remember, z_i is the boundary layer height).

The Monin-Obukhov similarity theory describes non-dimensional mean wind speed and temperature in the surface layer as a function of a non-dimensional height for conditions other than neutral. The logarithmic profile, with its derivation rooted in Prandtl's mixing length theory, is not always valid and the idea of the similarity theory is to further generalize this theory for non-neutral conditions. For that, some *universal* functions for the mean wind speed, mean virtual temperature, and mean water vapor mixing ratio are derived. The 'universal' aspect is that such functions are the same in all locally homogeneous, quasi-steady surface layer.

Dimensionless mean wind shear ϕ_m and mean potential temperature gradient ϕ_h can be defined as

$$\phi_m\left(\frac{x}{L}\right) = \frac{\kappa z}{u_*}\frac{\partial \bar{U}}{\partial z} \tag{2.6}$$

$$\phi_h\left(\frac{x}{L}\right) = \frac{\kappa z u_*}{q_s}\frac{\partial \bar{\theta}}{\partial z} \ . \tag{2.7}$$

Such Monin-Obukhov universal functions are shown graphically in Fig. 2.7.

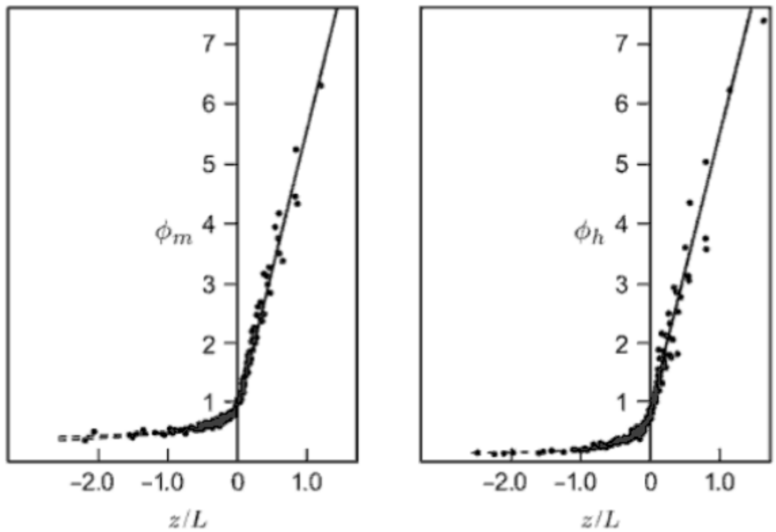

Figure 2.7: The Monin-Obukhov functions for mean wind shear ϕ_m (left) and mean potential temperature gradient ϕ_h (right). Data from the 1968 Kansas experiment [4].

In practice, however, these universal functions need to be determined using experimental data when applying the similarity theory. An advantage of using such parameters is that it is easy to measure mean wind speeds at a variety of heights within the surface layer, but significantly more difficult to measure turbulent correlations like $\overline{u'w'}$. Based on the famous Kansas experiment (Businger et al. [4], and Dyer [88]), equations have been empirically derived. Such equations are not shown here, but they represent the solid curves shown in Fig. 2.7, which are different depending on the sign of z/L. These relationships are also known as the Businger-Dyer relationships.

Integrating the Businger-Dyer relationships, the well-known, general wind speed profile can be obtained

$$\frac{\overline{U}}{u_*} = \frac{1}{\kappa}\left(\ln\left(\frac{z}{z_0}\right) + \psi\left(\frac{z}{L}\right)\right) \tag{2.8}$$

which is general for any stability state. The function $\psi(z/L)$ is zero for neutral conditions, reducing Eq. (2.8) to

$$\frac{\overline{U}}{u_*} = \frac{1}{\kappa}\ln\left(\frac{z}{z_0}\right) \tag{2.9}$$

Function ψ is defined for stable and unstable conditions and it is a function of z/L only. Due to the linearity found in stable conditions, such integration is easy and yields simply $\psi = 4.8z/L$. Under unstable conditions such integration is more complicated and thus curve-fitting and other analytical forms have been proposed over the years. Some of these forms can be found in [5, 80].

Another quantity derived from the Monin-Obukhov similarity theory is the velocity scale used in the analysis of convective (unstable) boundary layers. Again, with dimensional analysis, a convective velocity scale can be derived

$$w_\star = \left(\frac{g}{\theta_0} z_i\, q_s\right)^{1/3} \tag{2.10}$$

This quantity is used to normalize turbulent fluxes profiles in convective boundary layers. Sometimes, the buoyancy velocity scale w_B is used and the relationship between the two scales is such that $w_\star \approx 0.08 w_B$.

In a practical sense, when setting up a numerical simulation, the target stability state is determined by the L (or z_i/L). The surface heating (or temperature flux at the surface) is the obvious choice of a physical boundary condition to use in simulations. It is then convenient to rearrange Eq. (2.5) to be solved for the potential temperature flux:

$$q_s = -\frac{u_*^3 \theta_0}{\kappa\, g\, L} \tag{2.11}$$

where q_s, as mentioned, has units of K m/s. Typical values of q_s measured during the summer is shown in Fig. 2.8.

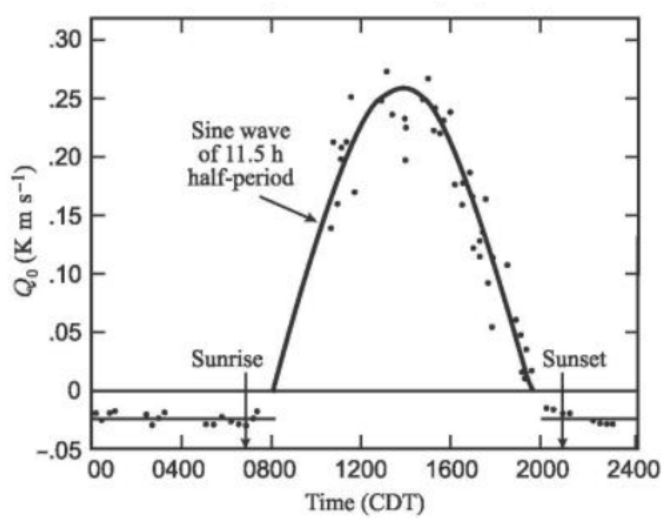

Figure 2.8: Time variation of the surface temperature flux observed in the Kansas experiment [4]. Data collected during mid-summer of 1968, and the scatter is due to day-to-day variations. Figure from [5].

The Monin-Obukhov similarity theory is only valid for cases where the first grid point is higher than 2 to 5 times the height of the roughness elements. In the context of very high resolution LES of the ABL, Basu and Lacser [89] mention that the first grid point should be higher than $50z_0$. Although this condition is easily satisfied in this work, it is important to mention, since the grid scheme used in this work would no longer be valid if an urban landscape (very high surface roughness) were to be considered.

2.5 Analytical Wind Profiles

The similarity theory has an important application to the mean wind profile within the surface layer. The shape of such profile affects much of human life. For instance, structures of buildings, bridges, wind turbine and wind farm designs, wind breaks, and pollutant dispersion are all dependent on the wind speed profile. The variation of the wind along the height is usually logarithmic in the surface layer for neutral conditions. Close to the ground, the frictional drag causes the wind speed to become zero. On the other hand, pressure-gradient forces cause the wind to increase with height. As previously discussed, the height in which the logarithmic curve has zero speed is at the height of the aerodynamic surface roughness, by definition.

By means of dimensional analysis and the Buckingham Pi theory, such logarithmic profile can be obtained, as it was discussed in the previous section. The logarithmic curve from Eq. (2.9) is known to be valid for neutral conditions. For simplicity, consider a coordinate system aligned with the mean wind direction at lower heights, such that $\overline{U} = u$. By doing so, dropping the time-averaged overbar notation, and solving for the wind speed, the well-known logarithmic relationship is obtained

$$u(z) = \frac{u_*}{\kappa} \ln\left(\frac{z}{z_0}\right) \tag{2.12}$$

When plotted in a semi-log plot, the logarithmic relationship of the wind profile in a statically neutral situation is a straight line. Considering the previous discussion of the parameter ψ, for convective and unstable conditions, the wind profile deviates slightly from logarithmic. This is illustrated in Fig. 2.9.

Thus, in a neutral ABL, with the ψ term dropped, considering a reference point, Eq. 2.12 can be written as

$$u(z) = \frac{u_*}{\kappa} \ln\left(\frac{z - z_{\text{ref}}}{z_0}\right) \tag{2.13}$$

Alternatively, Eq. 2.13 can be rearranged to calculate the wind speed at one height

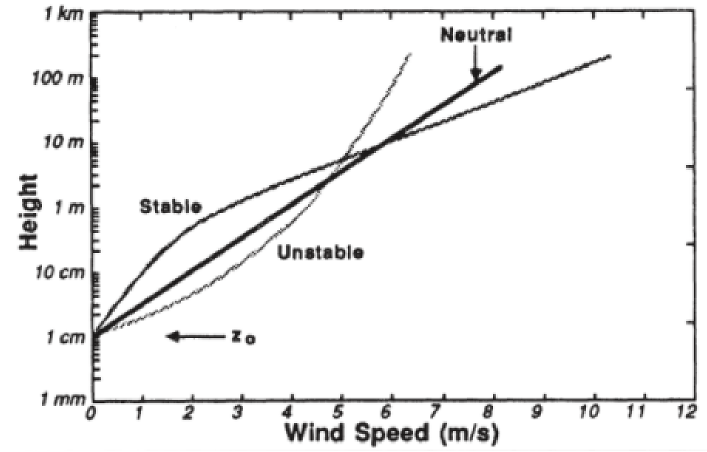

Figure 2.9: Typical wind profiles versus static stability plotted in a semi-log graph. From [80].

given the wind speed at another height

$$u(z_1) = u(z_2)\frac{\ln z_1/z_0}{\ln z_2/z_0} \ . \tag{2.14}$$

Another well-known analytical relationship between the wind speed at a reference height and those at another height is the a power-law wind profile. It reads

$$u(z) = u_{\mathrm{ref}}\left(\frac{z}{z_{\mathrm{ref}}}\right)^{\alpha} \ . \tag{2.15}$$

The exponent α in Eq. (2.15) is generally considered to be 1/7 for wind profiles under neutral conditions.

To understand better how these curves behave, it is useful to perform a quick parametric study. For instance, Fig. 2.10 shows logarithmic profiles with varying surface roughness. It can be noted that starting with very low surface roughness, the logarithmic curve gets closer to the power-law as z_0 increases. When the value of the surface roughness reaches about 0.05–0.06 m, there is a strong agreement between the two profiles. Also interesting to note from the figure is that upon normalization of such profiles, the curves with the same conditions but different wind speed, collapse to the same non-dimensional curve.

Another parameter relevant for a parametric study is the reference point selected. It is evident that the curves cannot be simply shifted in the Cartesian plane. So, given a fixed reference height, the choice of the reference wind speed makes the profile more "stretchy", or rather, it makes the profile show characteristics of high shear. That is

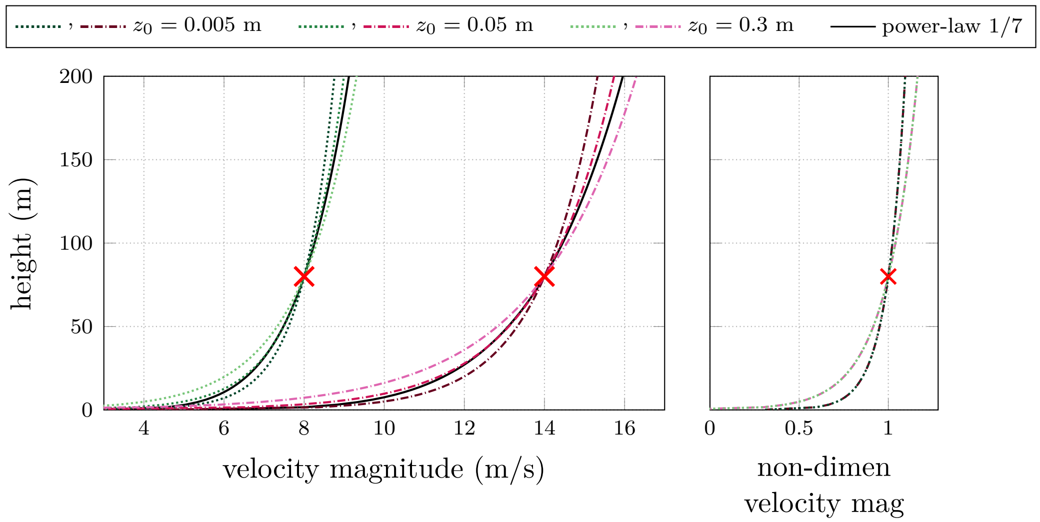

Figure 2.10: Logarithmic curves with varying surface roughness z_0 plotted against a power-law profile with exponent 1/7. Red markers indicate the reference point.

expected, even from a purely intuitive point of view, and the same occurs on a power-law profile. Figure 2.11 illustrates this behavior.

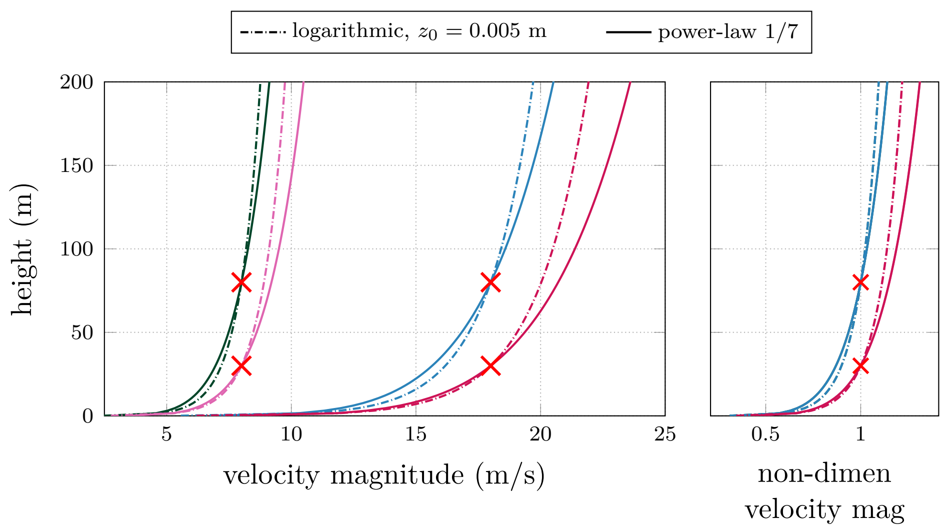

Figure 2.11: Logarithmic curves with varying reference wind speed, plotted against power-law profiles with exponent 1/7 at the same reference point, indicated by the red markers.

Given the same speed and different heights for the reference point, a different level of shear is exhibited in the first 20 or 30 m. It is evident that, since the equation used is the same, once the reference point lies on a curve, it follows the exact same curve. Normalizing the curves by the reference wind speed, yield comparable curves, as expected, with similar behavior to those from Fig. 2.10.

From moderate to high speed winds, the analytical profiles start to diverge at heights much higher than z_{ref}. If the reference point is set higher in an attempt to circumvent this issue, the curves diverge at lower heights as well. So in order to keep the analytical profiles as close as possible, a relatively low reference point should be selected. In the numerical solver used in this work, a reference point is selected in a similar fashion. Therefore, given that one is usually after a comparable analytical curve, it is important to realize that such curves deviate more from one another at either high wind speeds, far away from the reference point, or a combination of both.

2.6 Turbulence

Winds can have properties that are quite variable. The total wind speed is the superposition of three types of flow: *mean wind*, which is relatively constant, but vary slowly over the course of hours; *waves*, which are regular oscillations, often with periods of ten minutes or longer; and *turbulence* which are the irregular, quasi-random, non-linear variations, with much smaller time-scale. In this work, waves are not considered as their time-scale is not relevant.

In many instances, Taylor's hypothesis is used. It is an assumption where the turbulence added by the advection of the turbulent eddies themselves is small. Essentially, the advection of a field of turbulence past a fixed point can be taken to be entirely due to the mean flow. Taylor's hypothesis is also known as frozen turbulence hypothesis. This assumptions is the basis of field experiments where fixed points in space are instrumented. When it comes to numerical results, the frozen turbulence hypothesis is applied to a snapshot of turbulent flow over a large physical domain in order to deduce time-average quantities. Let angle brackets denote space-average, and overbar denote time-average, the hypothesis means that $\langle \mathcal{X} \rangle = \overline{\mathcal{X}}$, where $\mathcal{X}$ is any arbitrary quantity.

Fluctuations, both short and long term, are associated with eddies. Eddies can have many different time and length scales. The superposition of many scales of eddies are what makes up the turbulence, that is embedded into the mean flow. Normally, weather forecasts are made for mean conditions, not turbulence. However, statistics are used to quantify the net effect of turbulent quantities.

Variances σ^2 is an overall statistic of gustiness and can be given, for example, for the vertical velocity w as $\sigma_w^2 = \overline{w'^2}$. The standard deviation σ is defined as the square-root of the variance, and can be interpreted as an average turbulent fluctuation. Larger variance (or standard deviation) or velocity means more intense turbulence.

In this work, comparisons of the turbulence present in the ABL flowfield calculated numerically are made. Standard deviations of the velocity are used for that purpose. Standard deviations σ of the wind speed for an ABL of depth z_i have been empirically found to vary with height for different stability states. The following equations are given by Stull [79] for each velocity component u, v, and w. For a statically stable condition:

$$\sigma_u = 2.2 \cdot u_\star \left(1 - \frac{z}{z_i}\right)^{3/4} \tag{2.16}$$

$$\sigma_v = 2.2 \cdot u_\star \left(1 - \frac{z}{z_i}\right)^{3/4} \tag{2.17}$$

$$\sigma_w = 1.73 \cdot u_\star \left(1 - \frac{z}{z_i}\right)^{3/4} \tag{2.18}$$

For a statically neutral condition,

$$\sigma_u = 22.5 \cdot u_\star \cdot \exp\left(-1.5\frac{z}{z_i}\right) \tag{2.19}$$

$$\sigma_v = 1.6 \cdot u_\star \left(1 - 0.5\frac{z}{z_i}\right) \tag{2.20}$$

$$\sigma_w = 1.25 \cdot u_\star \left(1 - 0.5\frac{z}{z_i}\right) \tag{2.21}$$

And for a statically unstable state,

$$\sigma_u = 0.032 \cdot w_B \left(1 + \left(1 - \frac{z}{z_i}\right)^6\right) \tag{2.22}$$

$$\sigma_v = 0.032 \cdot w_B \tag{2.23}$$

$$\sigma_w = 0.11 \cdot w_B \left(\frac{z}{z_i}\right)^{1/3} \left(1 - 0.8\frac{z}{z_i}\right) \tag{2.24}$$

where, again, $w_B \approx w_*/0.08$ is the buoyancy velocity. These equations are only valid within the ABL (that is, below the boundary-layer height z_i), and when stability is weak enough that turbulence is not suppressed altogether. These equations will be used when comparing results obtained with the solver in section 3.3.

A flow is considered isotropic if the variance on all three components of the velocity are comparable — that is, $\sigma_u^2 \approx \sigma_v^2 \approx \sigma_w^2$. Turbulence, however, is often anisotropic. The turbulence present in the ABL is an example of anisotropic turbulence. Thermals, wind shear, the daily cycle, etc. form coherent structures that contribute to the anisotropy.

2.7 A Note on Marine Atmospheric Boundary Layers

The discussions presented in this work revolve around a boundary layer over land. It is straightforward to visualize the strong temperature gradients in the lowest few millimeters of air present on ABLs over land (think of black asphalt road on a sunny day where the actual surface is hot to the touch, even though the air temperature may be pleasant). At night, cooler environment reverses the direction of the heat flux and thus stable conditions are observed. On ABLs over the ocean[2], however, the characteristics of the heat flux are different due to the physical properties of the water.

While the boundary-layer depth varies quickly over land, over oceans it varies relatively slowly in space and time. Differently than land, the sea surface temperature changes little over a diurnal cycle because of the significant mixing at the top of the ocean. The energy budget behaves differently because turbulence in the water can efficiently transport heat away from the surface and distribute it deeper in the water. The heat capacity of the water is also about 4,000 times larger than that of air, which means it can absorb large amounts of heat from the sun without much change in temperature [80]. In other words, the diurnal cycle of radiation is almost completely balanced by a corresponding diurnal variation of energy transport into the sea. As a consequence, a slowly varying sea surface temperature means a slowly varying forcing into the bottom of the boundary layer.

While the surface roughness is a parameter that can be relatively straightforward to study on an onshore fashion, its study offshore is difficult. In offshore environments, the surface roughness is a function of wave height that depends on the wind speed, which makes separating the effects of wind speed and roughness difficult, if not impossible [7]. In this context, there are waves created by the wind, and additional wind created by the waves (known in the literature as wave-induced wind and wind-induced wave). Churchfield et al. [7] mention that wave height in and around an offshore wind plant, for instance, has yet to be measured.

With respect to experimental observations, direct measurements of turbulent fluxes over the ocean is often a complex task due to platform motion, flow distortion, and effects of sea spray [90]. Because of that, flux profile relationships that relate turbulent fluxes of momentum, head, and moisture/mass to their respective values of velocity, temperature, and water vapor are used. These quantities are of great importance in marine meteorology and oceanographer studies, and in this work, profiles such as temperature and velocity are especially relevant. However, the author did not identify good experimental observations

[2]Often referred to as marine atmospheric boundary layer.

that would provide useful data for the present study. In fact, an example of the challenging environment for data collection will be given in section 3.3, for an experiment conducted off the coast of Hawaii.

Over ocean, the roughness length associated with the ocean wave heights is a known function of the surface stress (or wind speed), as it is given as

$$z_0 = 0.015 \frac{u_*}{g} \ . \tag{2.25}$$

Such relationship is known as Charnock's relation [6]. It says that stronger wind stress creates higher waves, which results in higher surface roughness. Such a relationship can be easily plotted, as shown in Fig. 2.12. The range of values for the aerodynamic surface roughness that are obtained via Eq. (2.25) are within the same range of those observed earlier in Fig. 2.6 and Table 2.1.

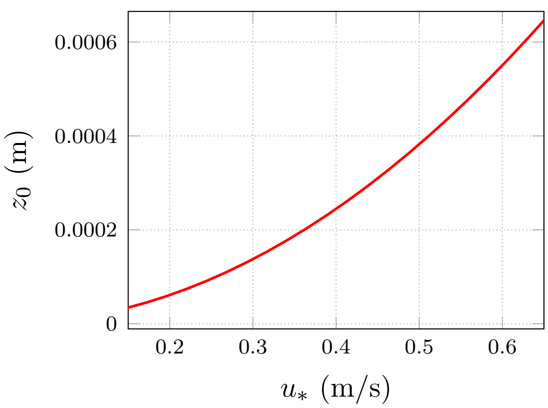

Figure 2.12: Charnock's relation [6] from Eq. (2.25), relating the aerodynamic surface roughness over the ocean and the friction velocity.

When it comes to the stability state, Wyngaard [5] mentions that "the most likely place to find a neutral planetary boundary layer might be the upper ocean", and adds that boundary-layer observations and experimental data collection in the ocean are substantially lagged, mostly due to challenging research environments. Bauer [91], in a reference from 1996, mentions that "day-night difference in stability conditions over water is unlikely to be large, but the influence of air masses will be important".

In conclusion, studies that investigate the marine ABL in detail are not common. Some authors such as Peña et al. [8] mention that the stability over ocean was measured to be "generally unstable", while some as mentioned above say it can be considered as a neutral state. This work discusses the generation and general properties of both convective and neutral scenarios, but selects canonical neutral conditions for further investigations with respect to the coupled problem. The bottom surface, the "sea floor" is represented by a solid surface with the appropriate aerodynamic surface roughness. Such a condition is chosen because it not only represents a simpler and smaller precursor, but it is also a conservative case, representing a relatively low amount of turbulence when compared to convective scenarios with buoyant forces.

2.8 Modeling Strategies and Concluding Remarks

This chapter discussed some theoretical aspects of the atmospheric boundary layer from a meteorological point of view. It is important to understand the physics that are common to such atmospheric events, however, moving forward, focus is given to the computational aspect of solving canonical cases.

Looking at the big picture of the current project, the aim is to obtain realistic atmospheric turbulence and investigate its effects on the airwake of a ship. In order to investigate the effects of the freestream turbulence on a helicopter, a high-fidelity CFD approach is used — however, different modeling approaches exist and that is one of the focuses of this work.

Three categories of representing an incoming inflow are further investigated:

Uniform inflow A constant-velocity profile. Straightforward CFD setup.

Steady ABL A profile that contains the appropriate velocity distribution along the height. Not technically an atmospheric boundary layer profile per se.

Unsteady ABL Fully unsteady approach. Representative of an atmospheric condition. Concepts introduced in this chapter are used in the generation of such flowfield. Instantaneous snapshots are highly turbulent.

The three approaches are illustrated in Fig. 2.13.

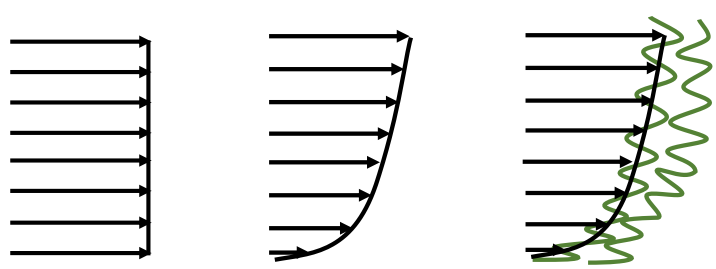

(a) Uniform (b) Steady ABL (c) Unsteady ABL

Figure 2.13: Sketch of the three approaches used when modeling the incoming wind.

In this work, such approaches are described and investigated with respect to the ship airwake problem. The ABL profiles, especially the unsteady ABL, is not straightforward to obtain. Numerical aspects pertinent to the development of the unsteady ABL are the subject of the next chapter.

Chapter 3
Modeling of a Realistic Atmospheric Inflow

In this chapter, the computational modeling aspect of the atmospheric boundary layer is described. Recalling the modeling strategies given at the end of the previous chapter, the unsteady ABL case is the subject of this chapter. The methodology used to achieve the realistic precursor wind fields used to compute the modified airwake is discussed. The numerical setup and solver are described, as well as the evolution and convergence of the atmospheric profiles. After, verification & validation efforts are summarized.

3.1 The ABL Solver in OpenFOAM

One of the main components of this work is the atmospheric boundary-layer (ABL) solver. All of the unsteady ABL simulations presented and discussed throughout this dissertation were preformed in OpenFOAM. OpenFOAM is an open source computational fluid dynamics toolbox [92], based on unstructured grids and a finite volume formulation. It is written in C++, and compared to other commercial CFD packages, OpenFOAM has the advantage of being fully customizable, allowing greater flexibility and control of all stages from code development to post-processing.

In order to simulate the physics present in the ABL, the specific code used derives from the *Simulator for Wind Farm Applications* (SOWFA), developed by the National Renewable Energy Laboratory (NREL) [7]. SOWFA is built on top of the OpenFOAM CFD framework. As the name suggests, the suite of codes within SOWFA was developed with wind energy applications in mind. It is an LES-based solver capable of creating the turbulent wind fields under a variety of atmospheric stability conditions. An overview of the solver and several numerical aspects are discussed in this section.

3.1.1 Governing Equations

In order to simulate the physics present in the ABL, the spatially filtered, incompressible Navier-Stokes equations are solved. The filtered continuity equation reads

$$\frac{\partial \bar{u}_j}{\partial x_j} = 0 \tag{3.1}$$

where the overbar represents filtered quantities, $\bar{u}_j = u_j - u'_j$, is the velocity vector of the resolved scale, being u instantaneous velocity vector and u' the sub-filter scale velocity vector. The filtered momentum equation can be stated as

$$\frac{\partial \bar{u}_i}{\partial t} + \frac{\partial}{\partial x_j}(\bar{u}_j \bar{u}_i) = -\underbrace{2\epsilon_{i3k}\Omega_3\bar{u}_k}_{\text{I}} - \underbrace{\frac{1}{\rho_0}\frac{\partial}{\partial x_i}p_0}_{\text{II}} - \underbrace{\frac{\partial \tilde{p}}{\partial x_i}}_{\text{III}} - \underbrace{\frac{\partial \tau^D_{ij}}{\partial x_j}}_{\text{IV}} + \underbrace{g\left(\frac{\bar{\theta} - \theta_0}{\theta_0}\right)\delta_{i3}}_{\text{V}} + \underbrace{\frac{1}{\rho_0}F_i}_{\text{VI}}. \tag{3.2}$$

The left-hand-side includes the time rate of change and convective transport terms. The terms on the right-hand-side are where the model differs from standard RANS. Term I is the Coriolis force due to planetary rotation where ϵ_{ijk} is the alternating tensor and Ω_j is the rotation rate vector, with $\Omega = \omega\,[0, \cos\phi, \sin\phi]$, where ω is the planetary rotation rate (at the point of interest, which depends on the latitude ϕ). Term II is a constant horizontal-mean, driving pressure gradient, where ρ_0 is the constant reference density. In this work, Term II drives the mean velocity of the ABL and is an input. Term III is the density-normalized gradient of the modified pressure variable, which is a deviation in resolved-scale static pressure from its time-averaged value, lumped together with one-third of the trace of the stress tensor, $\tilde{p} = p/\rho + \tau_{kk}/3$. Term IV is the divergence of the deviatoric part of the stress tensor, $\tau^D_{ij} = \tau_{ij} - \tau_{kk}\delta_{ij}/3$, where δ is the Kronecker delta (note that one third of the trace is lumped into term III). The stress term is composed of a viscous and a sub-filter scale part. Term V represents the buoyancy effects using the Boussinesq approximation, $\bar{\theta}$ is the resolved potential temperature, θ_0 is the reference potential temperature (set to 300 K) and g is the gravity. Term VI represents other momentum sources in the flowfield, such as the immersed boundary method representation of the geometry and/or actuator disk model of a helicopter rotor. Viscous effects in high Reynolds number ABLs are most important near the walls and are primarily handled through the wall boundary condition.

In practice, Term II is directly specified such that a desired horizontal-mean wind vector is achieved at the specified height. We call this location the reference point with the associated reference wind speed.

To solve for the potential temperature in the buoyancy force term, an additional transport equation for the resolved potential temperature has to be solved:

$$\frac{\partial \theta}{\partial t} + \frac{\partial}{\partial x_j}(\bar{u}_j \bar{\theta}) = -\frac{\partial \tau_{\theta i}}{\partial x_i} \tag{3.3}$$

here, $\partial \tau_{\theta i}/\partial x_i$ represents the flux of temperature by viscous and sub-filter scale effects.

In both the momentum and potential temperature equations, the effects of molecular diffusion are not included because the sub-grid scale effects are much more dominant, except very near the surface. Near the surface, LES of the ABL nearly always relies on some sort of surface model in which viscous and sub-grid scale stresses and temperature fluxes are lumped together [93]. At the surface, then, additional model for the stress is used, as will be discussed later. In the rest of the flowfield, the stress is approximated through a linear eddy-viscosity relationship. This relationship reads

$$\tau_{ij}^{D} = -2\nu_t \bar{S}_{ij} \tag{3.4}$$

where, as mentioned, τ_{ij}^{D} is the deviatoric part of the stress tensor and ν_t is the sub-grid scale (turbulent) viscosity, and the resolved strain-rate tensor is given by

$$\bar{S}_{ij} = \frac{1}{2}\left(\frac{\partial \bar{u}_i}{\partial x_j} \frac{\partial \bar{u}_j}{\partial x_i}\right) \ . \tag{3.5}$$

The sub-grid scale temperature flux vector in Eq. (3.3) is approximated in a similar way by the linear relationship given as

$$\tau_{\theta i} = -\frac{\nu_t}{\mathrm{Pr}_t} \frac{\partial \bar{\theta}}{\partial x_i} \tag{3.6}$$

where Pr_t is the turbulent Prandtl number. Here, the sub-grid scale model is based on a partial differential equation for the turbulent kinetic energy. This is the equation that provides closure to the equations presented. The turbulent viscosity that appears in Eq. (3.4) is given as

$$\nu_t = C_k \; l \; k^{1/2} \tag{3.7}$$

where C_k is a model constant, k is the sub-grid scale kinetic energy, and l is a length scale given by

$$l = \frac{0.76 \; k^{1/2}}{\left(\frac{g}{\theta_0} \frac{\partial \bar{\theta}}{\partial z}\right)^{1/2}} \ . \tag{3.8}$$

The equation providing closure, discussed in the work of Moeng [94], reads

$$\frac{\partial k}{\partial t} + u_j \frac{\partial k}{\partial x_j} = \underbrace{\tau_{ij} \frac{\partial u_i}{\partial x_j}}_{\mathcal{P}} + \frac{\partial}{\partial x_j} \left[(\nu + \nu_T) \frac{\partial k}{\partial x_j} \right] - C_k \frac{k^{3/2}}{l}, \tag{3.9}$$

where ν is the molecular viscosity. In stable and unstable ABL cases, however, an extra term is added to the sub-grid scale production due to buoyancy effects, so that the production becomes

$$\mathcal{P} = 2 \frac{1}{\theta_0} g \frac{\nu_T}{\sigma_k} \frac{\partial \theta}{\partial x_j} + \tau_{ij} \frac{\partial u_i}{\partial x_j}. \tag{3.10}$$

This model was selected as it is a commonly used turbulence model in the meteorology community [12, 94, 95]. In uniform inflow cases, the model was maintained the same for a more direct comparison and to avoid the appearance of flow features due to the different approach in the modeling of sub-grid scale effects.

The specification of the turbulent Prandtl number that appears in Eq. (3.6) is important. While sometimes this value is set as a constant, Moeng [94] is followed, which gives it as a function of the grid and the local kinetic energy k. Essentially, in neutral and unstable flow, $\mathrm{Pr}_t = 1/3$, but as the flow comes more stably stratified, the turbulent Prandtl number approaches 1.

3.1.2 Methodology and the Precursor Simulations

In this work, LES is used to generate the turbulent inflow atmospheric winds rather than model them. Here, this method is referred to as unsteady ABL. This method is more realistic than stochastic turbulence-based tools. Its disadvantage is that it requires a large domain to properly capture the ABL, and hours of computing time to arrive at a quasi-equilibrium state.

In order to properly simulate the specific atmospheric conditions, there are several parameters to be considered. A list of the relevant input to SOWFA/OpenFOAM is given in Table 3.1, with typical values. A more in-depth discussion on the convergence of the vertical profiles given a set of parameters is given in section 3.2.

There are a few points worth noting from Table 3.1. The temperature flux can increase or decrease the temperature of the local near-wall region. For example, a negative value creates an unstable scenario, while a positive value will result in a stable scenario. The reference wind speed and reference wind direction are defined at the reference height. These values are defined as reference values because they change over the height — the

Table 3.1: Parameters set on a precursor simulation and typical values used in the simulations performed in this work. Initial conditions of flow quantities and turbulence modeling parameters are not listed.

Parameter	**Typical Values**	
	Neutral	Unstable
x dimension (m)	3000	5000
y dimension (m)	3000	5000
z dimension (m)	1000	3000
grid resolution (m)	10	10
reference height (m)	30 to 100	30 to 150
reference wind speed (m/s)	8 to 20	8 to 20
reference wind direction (deg)	-30 to 30	-30 to 30
capping inversion height (m)	750	1500
inversion width (m)	100	100
$\Delta\theta$ at inversion (K)	5 to 50	5 to 50
$\mathrm{d}\theta/\,\mathrm{d}z$ above inversion (K/m)	0.003	0.003
latitude (deg)	41.3	41.3
surface roughness (m)	0.001 to 1	0.001 to 1
temperature flux (K m/s)	0	0.1 to 0.25

wind speed for obvious reasons and the direction because of the Coriolis force due to the rotation of the Earth. The grid parameters listed in the table are recommended values for wind energy applications. Quantities such as the Obukhov length are not explicitly set, but rather are a result of the development of the precursor based on the initial conditions set.

The target ship coupled with atmospheric turbulence simulations are performed in two steps. In this chapter, the focus is on the first step. To obtain the atmospheric wind fields to be used, the following methodology is used. The LES solver described is used to generate the turbulent atmospheric winds. This is done in a domain that has a periodic type of boundary conditions on the lateral planes. This is what we refer to as the "precursor" simulations. Once the turbulent boundary layer reaches a quasi-equilibrium state, a plane of turbulent data from the most upstream boundary condition is sampled and saved at every time step. The saving of the boundaries occurs for as long as one wishes to perform the second part of the simulation. An illustration of the workflow of this process is given in Fig. 3.1. This approach is the same as used in wind energy applications [96, 97].

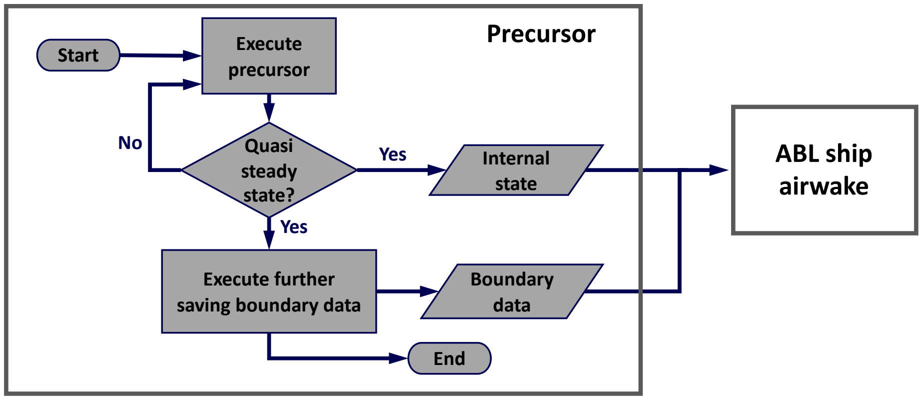

Figure 3.1: General workflow related to the precursor stage and data that is saved to be used in the actual coupled ship simulation.

In the second step, the ship is introduced. The internal state after the ABL reached quasi-steady state is then mapped into the new domain that contains the ship, and the saved planes of inflow data are used as an inlet boundary condition. This second step will be described in depth in the next chapter. We now continue the discussion with aspects that are relevant to the precursor stage only.

Figure 3.2 illustrates typical eddy structures in ABLs at the end of the precursor for different conditions and different stability states. The low surface roughness, neutral case is the most conservative when it comes to the presence of turbulent eddies.

3.1.3 Numerical Setup

Some aspects pertinent to the problem setup and solution methods are described and discussed in this section. These settings are only used in the precursor stage, unless otherwise noted. The numerical aspects of coupling the precursor solution with the ship will be explored in chapter 4, but given the appropriate discussion, a few details are given here.

Computational Domain and Grid Considerations

The large scales present in the atmosphere need a large length and time scale to develop. In this work, recommendations from the literature are followed regarding grid and domain size (for instance, the compilation of studies summarized in Mirocha et al. [98]). The recommendations vary between stability states. Table 3.2 shows typical grid parameters in a few studies that were based on OpenFOAM/SOWFA.

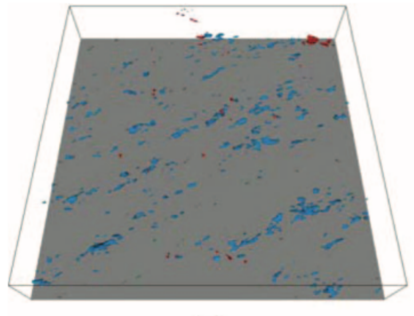

(a) Neutral, low roughness

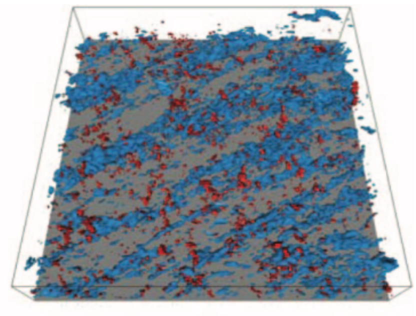

(b) Neutral, high roughness

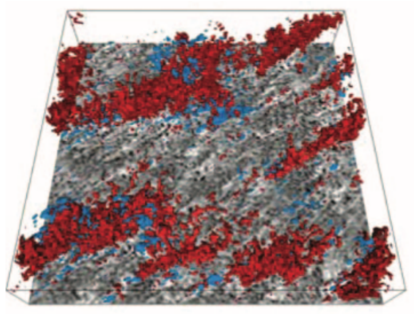

(c) Unstable, low roughness

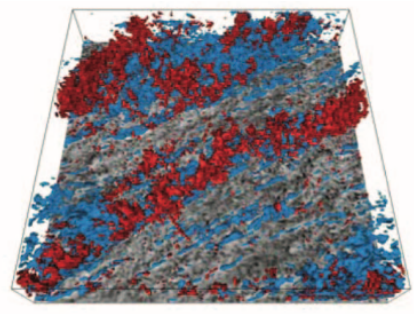

(d) Unstable, high roughness

Figure 3.2: Typical instantaneous flowfield at the end of the precursor, with varying stability state and surface roughness. Shown are isosurfaces of streamwise (blue, -1.25 m/s) and vertical (red,$+1.00$ m/s) velocity fluctuations. All of the domains shown are 3×3 km in the horizontal, and the first 0.5 km of the vertical extent are shown. Figures from Churchfield et al. [7].

The domain recommendations are for the wind energy community where large length scales and associated small time scales are important. Also, note from Table 3.1 that some studies provide the near-blade resolution. For the ship problem under investigation, significantly more resolution will be needed (this aspect will be discussed in detail in the following chapters). The outer domain size is reduced in an attempt to balance the added computational cost due to refinement near the ship.

In order to reduce the outer mesh, two cases are compared by spectral analysis: (i) a relatively large domain, following best practices for grid size and resolution (3 km $\times$ 3 km $\times$ 1 km domain, 10 m uniform resolution); and (ii) a smaller domain, extending outward 4.5 ship lengths and 0.75 ship lengths in height, resulting in a domain roughly 1.2 km in the horizontal and 100 m in the vertical directions. The smaller mesh is similar in size to the ones used in studies such as [25, 26, 63]. The goal of this effort is to show, through spectral analysis, that both domains yield similar results for the large-scale structures with equivalent energy content.

Table 3.2: Typical resolution and domain sizes for precursor simulations using SOWFA for recent wind energy applications. Studies with a 'finest' resolution reported used local refinement around the wind turbine.

Study	**Domain sizes (km)**	**Resolution (m)**	**Finest (m)**
Doubrawa et al. (2018) [99]	$5 \times 5 \times 2$ (unst)	10	0.6
Mirocha et al. (2017) [98]	$2.4 \times 2.4 \times 2$ (neutral)	15	-
	$6 \times 6 \times 3$ (unst)	30 horiz., 10 vertical	-
Jha et al. (2014) [100]	$3 \times 3 \times 1$ (unst, neutral)	10	0.6
Churchfield et al. (2012) [7,96]	$3 \times 3 \times 1$ (unst, neutral)	10	2.5

In order to develop a comparison between these meshes, the velocities associated with the frequencies that both domains are able to capture are first identified. In the context of LES of the ABL, a smaller domain size is expected to potentially affect the ability to capture the largest structures in the ABL. The goal is to ensure that those are still captured in the reduced domain size. This assessment is performed using the following approach: (i) remove the velocities from the large mesh associated with low frequency content that the smaller mesh would not be able to resolve; (ii) remove the velocities from the small mesh associated with high-frequency content that the large mesh would not be able to resolve due to mesh resolution. If the resulting velocity fields and energy from both meshes are comparable, the missed large-scale structure did not affect the smaller-scale structure that the smaller domain could not sufficiently capture. Note that both domains use a precursor-type grid, i.e. no refinement regions and uniform resolution.

A depiction of the process from the aforementioned comparison is provided in Fig. 3.3. Figures 3.3(a) and (d) are snapshots of the predicted velocity fields at 30 m high; Figure 3.3(b) is the low-frequency structure that can only be captured using the larger mesh. The higher frequencies that can only be resolved using the smaller domain are plotted in Fig. 3.3(e). The results suggest that low frequencies missed in the small domain (Fig. 3.3(b)) affect the resulting velocity by roughly 1 m/s, and the time scale

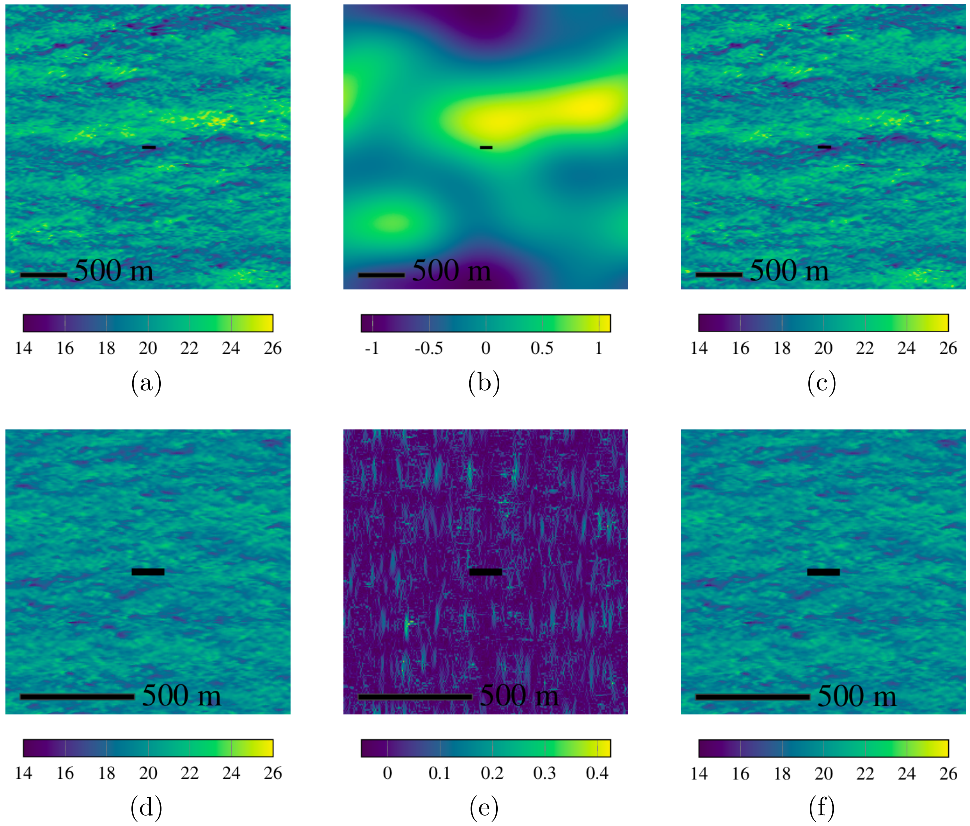

Figure 3.3: Analysis of velocity field in both large (top) and small (bottom) meshes, conducted at 30 m. Domains have different size thus a 500 m scale is shown for reference. Black rectangle in the center of the figures represents the SFS2 dimensions, also only shown for reference. Left-hand-side images show the calculated velocity fields. Center column images show content to be removed in order to compare the large and small domains — velocities associated with low frequency on the large mesh (b), and high frequency on the small mesh (e). Results at the right-hand-side show the final comparable velocity field. Velocity scale shown in m/s.

associated with these structures cause them to be unimportant for the current analysis. The filtered velocity fields for the large and small domains are provided in Figs. 3.3(c) and (f), respectively. In comparing these plots, the resulting velocity fields are quite close. Note that the domain size in the plots are different and can be visually referenced from the size of the ship and auxiliary scale shown.

While it is acknowledged that not all of the velocity scales associated with the neutral ABL are realized, it is found that the low-frequency content that the smaller domain misses does not significantly affect the overall solution for the current analysis as verified through energy content in the subsequent discussion. The grids used for the coupled ship investigations are of similar size to the 1.2 km grid discussed here.

Initial and Boundary Conditions

The cost of high Reynolds LES of wall-bounded flows scales strongly with Reynolds number. At the lower boundary, it is too expensive to resolve the inner layer (including the viscous sublayer), and the grid is also too coarse to resolve the sharp velocity gradients. In a real setting, the planetary surface is covered with roughness elements (rocks, vegetation, waves, etc.) that is not feasible to resolve. It is inappropriate to apply a simple no-slip condition at the surface, so instead a model for surface stress is used. A temperature flux model is also used. Because of that, a constant grid resolution can be maintained, even at lower heights. Outside of the region close to the bottom, the molecular diffusion effects overcome sub-grid scales and thus no model is applied. Assuming the first layer of cells off the bottom surface lie within the surface layer of the ABL, at the surface,

$$\tau_{ij}^D = \begin{bmatrix} 0 & 0 & \tau_{xz}^{\mathrm{tot}} \\ 0 & 0 & \tau_{yz}^{\mathrm{tot}} \\ \tau_{xz}^{\mathrm{tot}} & \tau_{yz}^{\mathrm{tot}} & 0 \end{bmatrix} . \tag{3.11}$$

In this work, Schumann's model [101] is used. The surface stress model predicts the total (viscous and SGS) stress at the surface τ_{xz}^{tot} and τ_{yz}^{tot} as

$$\tau_{xz}^{\mathrm{tot}} = -u_*^2 \frac{\bar{u}_{1/2} - \langle \bar{u}_{1/2} \rangle}{\sqrt{\langle \bar{u}_{1/2} \rangle^2 + \langle \bar{v}_{1/2} \rangle^2}} = -u_*^2 \frac{\bar{u}}{\bar{U}} \tag{3.12}$$

$$\tau_{yz}^{\mathrm{tot}} = -u_*^2 \frac{\bar{v}_{1/2} - \langle \bar{v}_{1/2} \rangle}{\sqrt{\langle \bar{u}_{1/2} \rangle^2 + \langle \bar{v}_{1/2} \rangle^2}} \tag{3.13}$$

where u_* is the friction velocity, the angled brackets denote a horizontal space average and $1/2$ the cell center of the first cell off the surface. To use this model, however, the wall normal velocity gradient at the cell center is needed such that the sub-grid scale has a meaningful gradient. For that, the surface normal velocity gradient at the top of the cell is essentially "copied" to the center of the cell. This is done by specifying a surface-parallel velocity that creates the desired normal gradient at the cell's center. This approach does not create wall normal flow.

Friction velocity can be defined as

$$u_*^2 = \left(\langle \tau_{xz}^{\mathrm{tot}} \rangle^2 + \langle \tau_{yz}^{\mathrm{tot}} \rangle^2 \right)^{1/2} \tag{3.14}$$

and it needs to be approximated. For that, the rough wall log law is used

$$\frac{\sqrt{\langle \bar{u}_{1/2} \rangle^2 + \langle \bar{v}_{1/2} \rangle^2}}{u_*} = \frac{1}{\kappa} \ln \left(\frac{z}{z_0} + f(L) \right) \tag{3.15}$$

For a neutral case, Eq. (3.15), reduces to

$$u_* = \frac{\kappa \langle U \rangle (z)}{\ln z/z_0} \tag{3.16}$$

where $\langle U \rangle (z)$ is the space-averaged velocity at the height z. For convective cases, the solver estimates the stability state using Eq. (2.5), and the solution is obtained using an iterative process. Figure 3.4 shows a typical convergence history of the friction velocity.

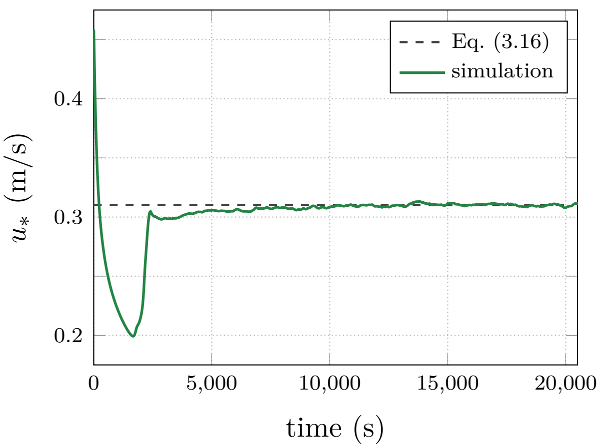

Figure 3.4: A typical convergence history of the friction velocity u_*. The case executed had 8 m/s at 80 m as a reference point, $z_0 = 0.005$ m.

At the upper boundary of the precursor simulations, stress and temperature flux are set to zero. The upper boundary is situated above the capping inversion, such that it is above the turbulence from the ABL and thus such boundary conditions are appropriate. Zero normal velocity is specified at the lower boundary. The boundary conditions for all quantities are periodic/cyclic in the horizontal directions. On both the upstream and downstream boundaries, the gradient of the modified pressure is specified using the momentum equation dotted with the boundary normals [96].

The potential temperature and surface heating characteristics are explicitly set as initial conditions. As discussed earlier, the stability state is a result of the potential temperature variation along the height. A stronger variation of θ around z_i serves as the temperature inversion, or, rather, the capping inversion. Typical values were shown in

Table 3.1. The initial condition for the velocity field is set as a constant velocity. By doing so, rather than specifying a starting profile, bias is avoided in the convergence of the solution. A disadvantage of this approach is that more simulation time is needed to reach a quasi-stationary state.

For the ABL simulations that include the ship, only the side boundaries are periodic. On the upstream boundary, velocity, temperature, and kinetic energy are specified. This time- and space-varying boundary condition comes form the planes of data saved during the precursor step at every time-step. On the downstream boundary, a Neumann type of boundary condition is set for the velocity, temperature, and turbulent kinetic energy, that is, zero gradient. This setup allows the planes generated during the precursor to enter the domain, but the outflow does not recycle. The upper and lower boundary conditions remain the same.

Discretization Schemes and Solution Methods

The equations presented earlier are discretized using an unstructured, collocated, finite-volume formulation. Interpolation of cell-centered quantities to cell faces in order to take derivatives at cell center is done via linear interpolation. This amounts to a second-order central differencing scheme. The velocity fluxes are interpolated using Rhie-Chow interpolation [102], thus avoiding pressure-velocity decoupling. The same second-order accurate scheme is used for all terms.

Advance in time is done by Crank-Nicolson implicit discretization, which is also second-order accurate. Regarding the solution of the coupled pressure-velocity equations, the Pressure Implicit with Splitting of Operators (PISO) algorithm [103] is used. A predictor followed by three correctors are used. In the predictor step, the momentum equations are implicitly solved using the old pressure field. The new velocity may not satisfy the continuity equation, so a correction is applied based on the pressure solved using the velocity field from the predictor, and then the velocity field is corrected. At the end, the momentum predictor and temperature equations are linearized using information from the last time step. The momentum and temperature equations are solved using the diagonal incomplete-lower-upper (LU) preconditioned bi-conjugate gradient iterative solver. The solutions of the pressure equations are the most expensive step. They are solved using a generalized geometric-algebraic multigrid (GAMG) iterative solver with diagonal incomplete Cholesky smoother.

With respect to temporal resolution, the time step is set to be automatically adjusted by the solver based on the maximum Courant-Friedrichs-Lewy (CFL) number. In the simulations performed in this work, a maximum CFL of 0.8 has been set. In practice, that means that the time step will be adjusted based on the region where the flow is locally accelerated, in order to provide the proper temporal resolution. This amounts to a CFL number that is low in regions where the flow has lower velocity. With this approach, the overall average CFL number is quite low. For cases that include the ship and refinement regions, an even lower maximum allowable CFL is set. This is done in order to avoid numerical instabilities and to provide a smoother startup of the wake and the initial transient of the development of the turbulence through the refinement regions.

All of the cases performed in OpenFOAM, that is, both uniform and the different ABLs, use the same numerical schemes and solution methods. A slightly modified scheme for the convective transport terms is used with simulations that include the ship. This aspect will be discussed later.

3.1.4 A Note on Reference Frames

The precursor simulation computes the large scales present in the atmosphere and converges to velocity profiles, such that the velocity magnitude at the reference height is satisfied (this is done by means of term II of Eq. (3.2)). As will be shown in the next section, these profiles can vary depending on the desired velocity. For a typical wind of, say, 8 m/s at around 80 m high, the obtained profile matches relatively well the 1/7 power-law profile, while a higher velocity scenario (say, 16 m/s at 80 m high), will have stronger shear and the overall profile will tend towards the logarithmic profile.

For a scenario where a ship is moving, the flowfield experienced by the ship is a combination of the natural winds and ship movement. Polsky [67] mentions a spiral effect, especially for beam winds (non-zero wind-over-deck). Such spiral effects are due to the combination of the fact that the ship is heading to a direction that is not aligned with the wind, and that the wind velocity changes with height, whereas the ship velocity does not. Considering this discussion, such spiral effects are not accounted for in this work. The spiral effects have the least effect in cases where the ship is aligned with the incoming flow. The reference frame used is such that the ship is stationary, while subject to a relatively high wind speed.

The aerodynamic surface roughness used to represent smooth sea is low. As observed in the parametric study of the analytical curves presented in the previous chapter, a low value for the surface roughness yields a profile with less shear characteristics when compared to a higher surface roughness value. As a consequence, the logarithmic curve approaches the 1/7 power-law as z_0 approaches 0.05 m. High shear can also be obtained by a higher wind speed. This work aims for a very low value of z_0 in an attempt to represent calm sea water — see Table 2.1 and Fig. 2.6. In light of this discussion, the obtained profile with wind speeds at around 8 m/s or below are well-represented by a logarithmic profile, while with higher wind speeds, the increased shear makes the converged profile lean towards a power-law profile with exponent 1/7 — see Fig. 3.5.

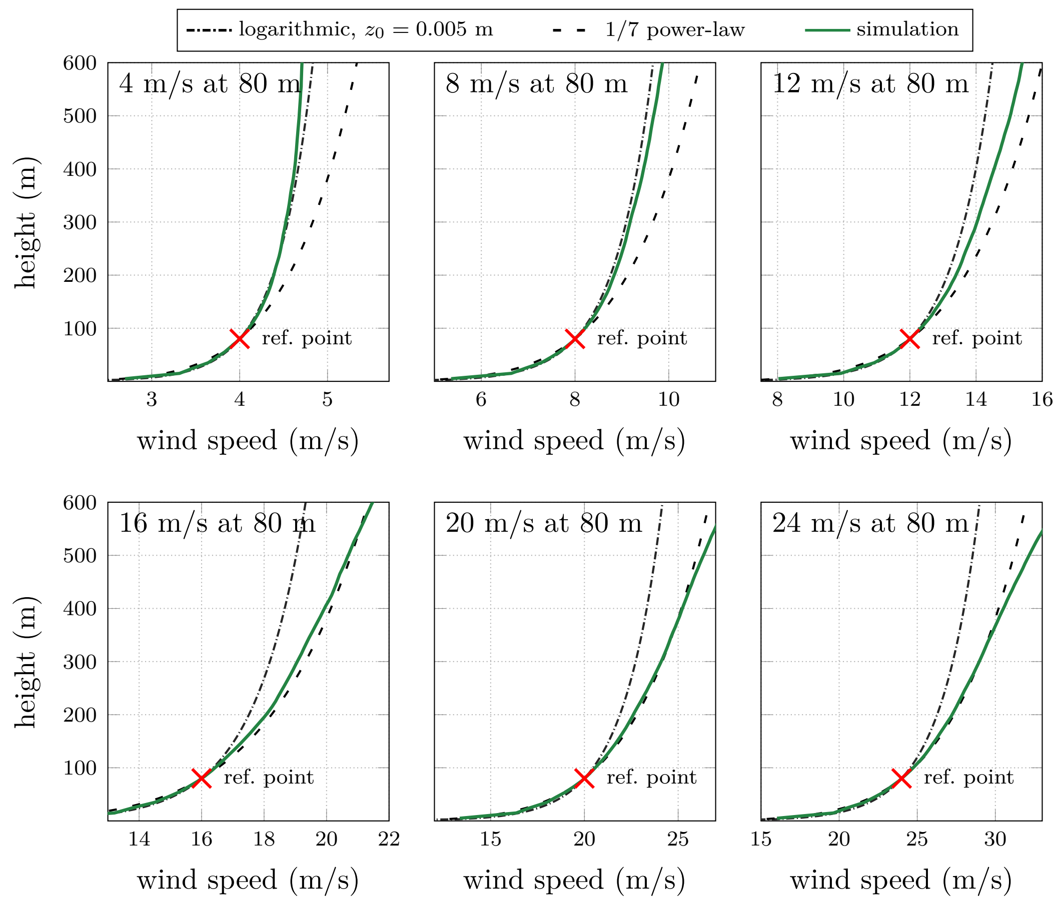

Figure 3.5: Horizontally-averaged velocity magnitude profiles at the end of a precursor simulation for several different wind speeds. Note the shift from a logarithmic match towards a 1/7 power-law match. Only the first 600 m shown; aerodynamic surface roughness kept constant at $z_0 = 0.005$ m. Reference point indicated at the top of each plot.

An aspect to note is that as the wind speed at the reference point increases, the amount of shear observed also increases. While velocities of around 8 m/s are common in the wind energy community for wind farm analyses [98, 100, 104], it is low for a case representing a ship cruising at around 25 knots. As a result, the neutral profiles used in this work will be closer to a 1/7 power-law than a logarithmic profile.

Two extreme scenarios, one that fits the logarithmic curve well — the 8 m/s at 80 m case — and another that will typically be used in this work and follows the power-law profile better — 20 m/s at 80 m — are plotted on a logarithmic scale. Figure 3.6 shows both cases. Note the clear departure from the logarithmic profile at high wind speeds. It is interesting to note, however, that in both Figs. 3.5 and 3.6 the profiles are all close to one another at heights below the reference point. Recalling Fig. 2.9, the shape of the time-averaged velocity profile of a high-shear neutral case at higher altitudes resembles that of an unstable case.

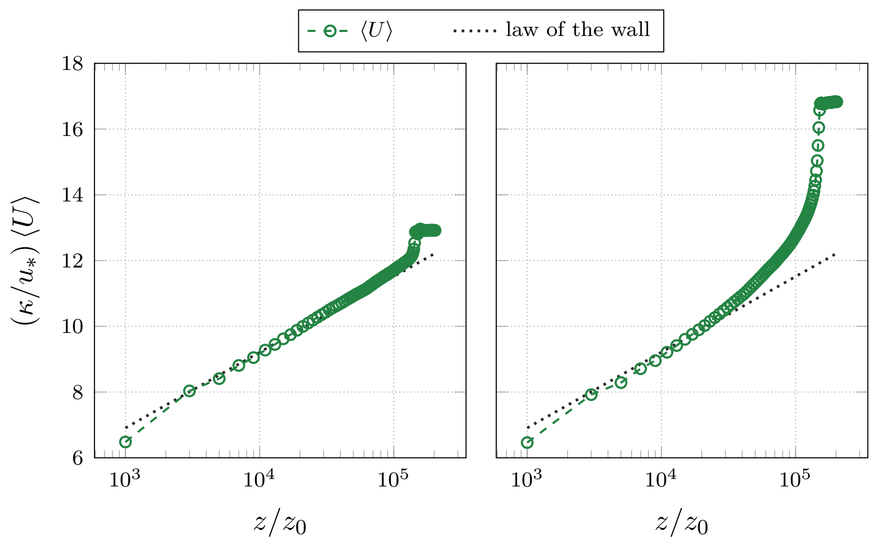

Figure 3.6: Horizontally-averaged velocity profile on a semi-log scale from two neutral, $z_0 = 0.005$ m cases. Left: low shear, $U_{\mathrm{ref}} = 8$ m/s; Right: high shear, $U_{\mathrm{ref}} = 20$ m/s.

The plots in Fig. 3.6 are also known as the law of the wall. In contrast to typical law-of-the-wall plots, however, the meshing strategy employed in these simulations does not aim in capturing neither the linear viscous sublayer part, nor the buffer layer, and thus only the log-law region is shown.

3.2 Development and Evolution of Planar-Averaged Vertical Profiles

The goal is of the precursor is to develop the large scale atmospheric turbulence present in the domain. The general flow structure and turbulent quantities that will be present will depend on the parameters chosen (Table 3.1) as they directly influence stability state, shear level, etc. These parameters will modify the overall flow behavior, affecting the characteristics of the final boundary layer and thus the horizontally-averaged vertical profiles. In this section, the convergence of these profiles for a set of given parameters is explored.

In a neutral, shear-driven boundary layer, turbulent mixing is carried out mainly by smaller eddies structures, mostly through local mixing, and thus a mean vertical gradient is maintained throughout the flowfield [12]. Because of that, this mixing has a long associated time scale, and it takes longer for the final profile to be revealed in a computational setting. This can be observed in the vertical profiles of the velocity magnitude shown in Fig. 3.7. In this figure, a low wind speed is shown on the left, and a high wind speed is shown on the right, following the discussion from the previous section. Many different times are shown. At time $t = 0$ the constant-velocity initial condition mentioned before can be seen. After about 18,000 s, the profiles reach convergence. The capping inversion starts to be effective earlier in the high shear case. At heights lower than the reference point, not much difference is observed.

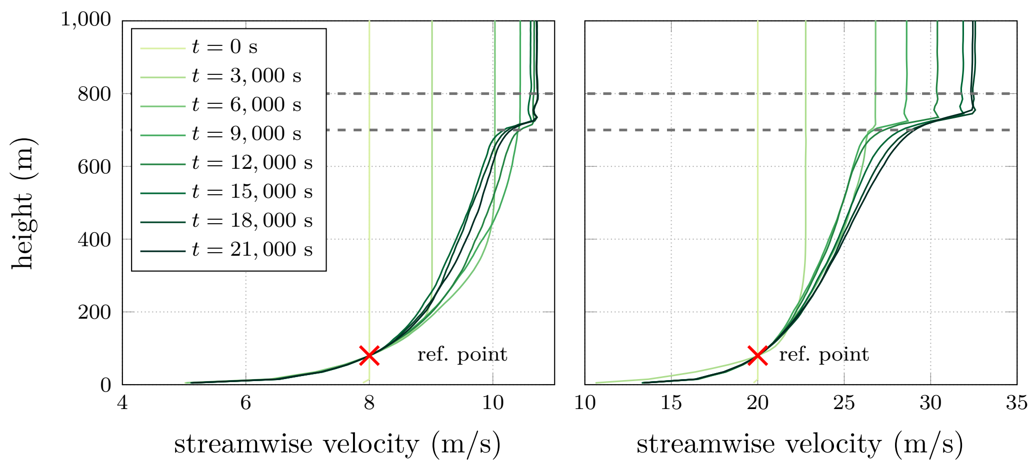

Figure 3.7: Comparison of the time evolution of the streamwise component of the velocity for a low shear (left) and high shear (right) case. The high shear has a much higher velocity gradient (note the different velocity scales involved). The dashed horizontal lines are the limits of the capping inversion.

This is the first plot of this type and there are a few aspects worth noting that relate to previous discussions. All the quantities presented in this section are horizontally-averaged at every height, so the angled bracket notation is dropped. The capping inversion limits are shown by the dashed horizontal lines, and it essentially provides a lid to the flow, not allowing the ABL turbulence to go to the free atmosphere. The wind speed above the capping inversion converges to the geostrophic wind speed. Also indicated in some plots presented in this section is the reference point used to set up the simulation in OpenFOAM/SOWFA.

With low wind speeds, a relatively small (around 5 K) potential temperature difference at the capping inversion is effective in suppressing turbulence to higher altitudes. When increasing the overall wind speed, a larger temperature difference is needed. When such an increase is not set, the result is a higher geostrophic wind and resulting profiles that take longer to converge (if at all). The reason for this behavior is such that at high(er) wind speeds, the amount of shear observed at around z_i can be high when compared to the stableness provided by the thin capping inversion layer and its temperature difference. To circumvent this issue, a stronger temperature variation is used, amounting to an increased inversion strength. A parametric study of the potential temperature difference at the capping inversion is shown in Fig. 3.8. The profiles presented earlier in Fig. 3.7 used a strong capping inversion.

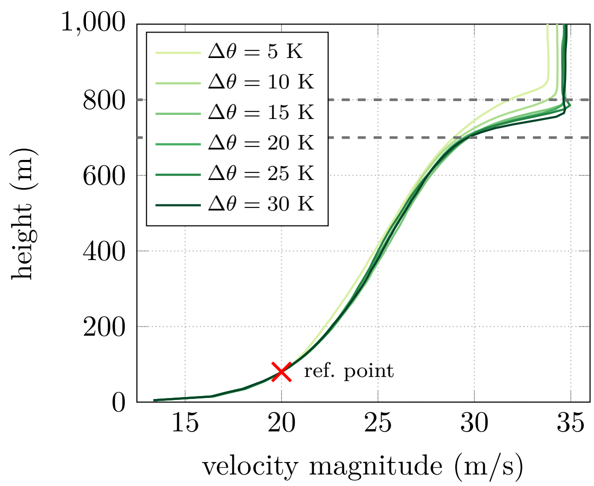

Figure 3.8: Effects of stronger or weaker capping inversion on a high shear flow. The reference point of the specified wind speed is indicated in the plot. All curves shown are at $t = 22,000$ s. The dashed horizontal lines are the limits of the capping inversion.

Next, in Fig. 3.9, the resolved-scale vertical flux of potential temperature is shown. One of the definitions used by some authors for the top of the boundary layer height is where the buoyancy flux has its minimal value. Such quantity increases ever so slightly and the stronger temperature change at the capping inversion provides a reversal in this curve. This results in its lowest value being near the beginning of the capping inversion.

Contrasting the neutral ABL explored in this section, some details of a convective ABL are examined next. Figure 3.10 shows the development of the mean winds over time. Only in the convective type of ABL, the well-mixed feature in the mean profiles

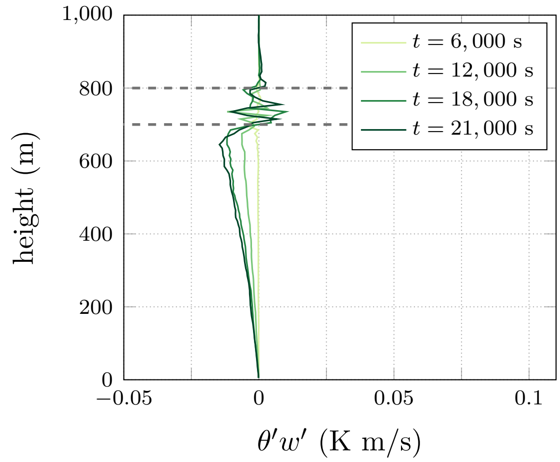

Figure 3.9: Vertical profiles of the resolved-scale potential temperature flux for the neutral case. The minimum of this quantity is one indicator of the boundary layer height.

can be observed. This increased mixing due to buoyancy reflects in a convergence rate that is considerably higher than that of neutral cases. An unstable case usually reaches convergence at around 12,000 s. Times up to 19,000 s are shown here for the sake of comparison. The "flat" nature of the profiles indicate the effectiveness of turbulent mixing by the few strong updrafts present in the convective boundary layer (see Fig. 3.2). The strong updrafts are roughly the size of the depth of the ABL and thus effectively mix the mean fields in a non-local way. Stronger capping inversion is effective in suppressing turbulence into the free atmosphere.

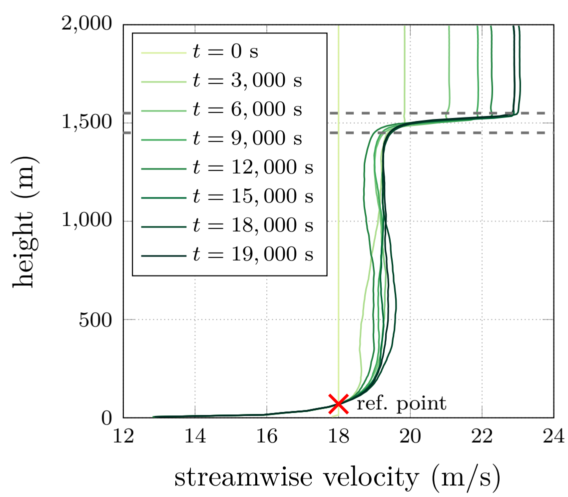

Figure 3.10: Mean wind profile for the convective (unstable) case.

The resolved and sub-grid scale potential temperature flux for the convective case is shown in Fig. 3.11. Similarly to the observations made for the neutral case, the top of the boundary layer can be identified by the minimum of the resolved $\theta' w'$ quantity. Contrasting these curves to the ones from the neutral case, such minimum value is much more evident here. In the neutral case, very little variation is observed, whereas here a more distinctive behavior is present because of the buoyancy effects throughout the domain, a direct effect of the surface heat flux. As expected, the difference in the potential temperature used to enforce the boundary layer top is effective in containing any vertical fluxes. As a consequence, the minimum value is found right at the height where the capping inversion starts. With respect to the sub-grid scale quantity, it really only has a significant magnitude near the ground, where the model is acting. A high-accuracy zone, as discussed by Brasseur & Wei [105], is present near the ground, indicated by the fact that the resolved scale is still higher than the sub-grid scale.

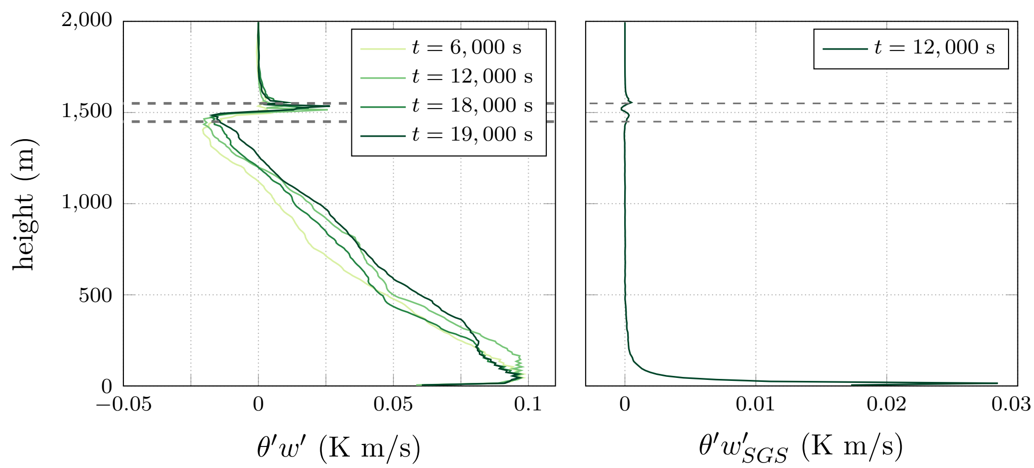

Figure 3.11: Vertical profiles of the resolved-scale (left) and sub-grid scale (right) potential temperature flux for the unstable case. The minimum of the total of this quantity is one indicator of the boundary layer height. Note how model is only relevant at the bottom.

Next, consider a convective case that has reached convergence at 12,000 s. In these cases, surface heating is added by means of the bottom boundary condition. The net effect of the heating is a change in potential temperature. The sub-grid scale has just been shown in Fig. 3.11. The resulting potential temperature profiles are shown in Fig. 3.12. A few more instants are shown for reference. A strong variation of the temperature is set at around 1500 m in order to act as a capping inversion, but most importantly, note the temperature gradient near the very bottom of the domain. The negative slope there is consistent with the schematics shown earlier in Fig. 2.3.

The temperature gradient shown in Fig. 3.12 is a direct effect of the applied surface heating. That temperature variation is responsible for the creation of buoyant forces emanating from the bottom surface. Hence when the heating is strong enough and the large-scale buoyancy effects overcome small-scale shear effects, it is said that the boundary layer is buoyancy dominated. The obtained profile also captured all of the features presented in the sketch provided earlier in Fig. 2.4.

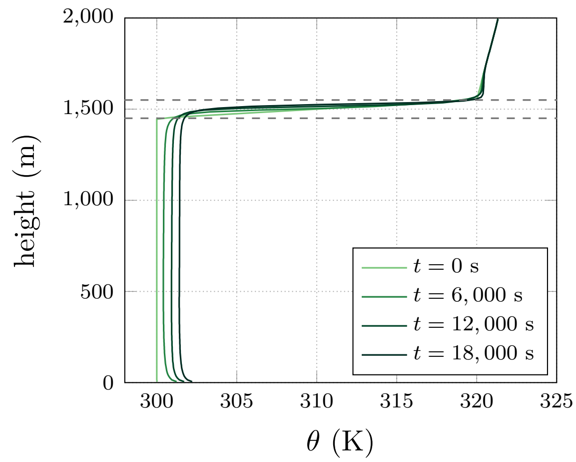

Figure 3.12: Evolution of potential temperature profiles for the unstable case. Convergence is never achieved here because heat flux from the bottom surface is constantly being exerted to the flow. A neutral case has no explicit surface heating and no temperature variation below the capping inversion.

The convergence of several other quantities related to turbulent fluctuations are also observed in the determination of a quasi-steady state. Such state is also identified by the agreement to the $-5/3$ turbulence cascade slope. Some of the vertical profiles will be shown next, comparing with data from the literature.

3.3 Verification & Validation of ABL Data

It is important that the atmospheric data obtained are in fact representative of a real-world setting and that the equations model the appropriate physics. This section discusses some verification and validation efforts conducted with the ABL solver. According to [106], verification is defined as the process of determining if a computational simulation accurately represents the conceptual model, but no claim is made of the relationship of the simulation to the real world. Validation is the process of determining if a computational simulation represents the real world. The data used for validation and verification purposes are the converged ABL, that is, the data obtained at the end of the process described in the previous section.

Availability of such data, however, is limited. For instance, measuring velocity and its fluctuations in a sea environment is not trivial as the sea surface changes height. Also, there is a very high variability in stability state, which can further change the way the profiles present themselves. Four studies have been identified to provide a combination of verification and validation at different heights for the simulations performed here. The studies are as follows:

Moeng and Sullivan (1994) [12] Numerical study based on spectral methods.

Peña et al. (2009) [8] Velocity profile observations at the Horns Rev wind farm.

Anderson et al. (2014) [3] Data acquired at sea by a buoyant platform.

Richard and Hoxey (2012) [9, 107, 108] Pressure data observed on a cube subject to natural winds over a flat terrain (Silsoe cube).

It is important to note that each one of the studies listed focuses on a different height, or rather, range. For instance, the numerical study by Moeng and Sullivan looks at the big picture of these profiles, which includes their characteristics above the capping inversion. The Silsoe cube, on the other hand, looks at the flow at the very bottom of the ABL, over the first few meters off the ground. Peña et al. and Anderson et al. provide insight into the velocity profiles in a sea environment, which is the scenario of most interest in this work.

This section explores the studies highlighted above. Note that the Silsoe Cube comparison will be shown in chapter 4, when the immersed boundary method representation of geometries is described.

3.3.1 Numerical Results by Moeng and Sullivan

Moeng and Sullivan [12] (referred to as MS94 from here on) presented four cases comprised of the following scenarios: shear-driven, buoyancy-driven, and two cases with conditions in between. The two extreme cases — shear- and buoyancy-driven — are used here for comparison. The parameters are selected such that the characteristics of the atmospheric conditions are matched. For instance, the same surface heat flux is specified and an appropriate surface roughness is set such that it matches the friction velocity presented in MS94.

Table 3.3 presents a description of the cases simulated for comparison purposes, alongside values provided by MS94. D_x, D_y, and D_z are the streamwise, spanwise, and vertical dimensions of the domain; q_s is the specified potential temperature flux at the surface (equivalent to $\theta' w'$ at the very bottom). Note the direct relationship between the temperature flux at the surface and the Kansas experiment data shown in Fig. 2.8.

Table 3.3: Numerical parameters of the current simulated cases and those of Moeng and Sullivan [12], denoted by MS94.

	MS94	**OpenFOAM**
	Neutral	
D_x, D_y (km)	3	3
D_z (km)	1	1
z_0 (m)	–	0.4
	Unstable	
D_x, D_y (km)	5	5
D_z (km)	2	2
q (K m/s)	0.24	0.24

Table 3.4 provides a summary of the resulting statistics for both scenarios investigated. Those statistics were gathered after the quasi-equilibrium has been achieved, as indicated by the convergence of profiles. The quantities presented are the friction velocity u_*, the convective velocity w_* (see Eq. (2.10)), the boundary-layer height z_i, the large eddy turnover time τ_* ($\tau_* = z_i/u_*$ for neutral, $\tau_* = z_i/w_*$ for convective), a measure of the stability state by the Obukhov length $-z_i/L$, vertical potential temperature flux $\theta' w'$ at the top of the boundary layer, and velocity at the first grid point of MS94's setup. Attempt has been made in obtaining similar friction velocity, convective velocity, and the stability state. The other quantities were obtained as a consequence.

A series of plots with comparisons between the ABL solver and data from MS94 are explored next. In the plots, the vertical direction is normalized by the boundary-layer height z_i. The absolute value of the boundary-layer height it not critical, but rather how some variables behave near this layer. Angled brackets notation indicates horizontally-averaged values. For each quantity, a set of plots will be first presented for the neutral case, followed by the convective (unstable) case.

Mean wind profiles are shown first in Fig. 3.13 for the neutral case. The velocity magnitude and individual components are shown. It is important to note that MS94's

Table 3.4: Internal parameters of the current simulated cases and those of Moeng and Sullivan [12]. The parameters listed here are at the final simulation times. Quantities at the height z_1 refers to the height of the first grid point in MS94's simulations.

	MS94	**OpenFOAM**	**MS94**	**OpenFOAM**
	Neutral		Unstable	
u_* (m/s)	0.50	0.50	0.56	0.54
w_* (m/s)	0	0	2.02	1.99
z_i (m)	478	678	1030	1470
τ_* (s)	956	1356	510	739
$-z_i/L$	0	0	18	19.1
$\langle\theta' w'\rangle_{z_i}$ (K m/s)	-0.007	-0.0021	-0.040	-0.035
U_{z_1} (m/s)	8.7	4.6	5.1	7.13

specification of the wind speed was given by setting the geostrophic wind speed. In the solver used here, a reference height and the associated wind speed and direction are set. For the sake of comparison, the dimensional data from MS94 was normalized by the speed at a reference height picked to make the datasets comparable. The individual components do not match because of different reference frames.

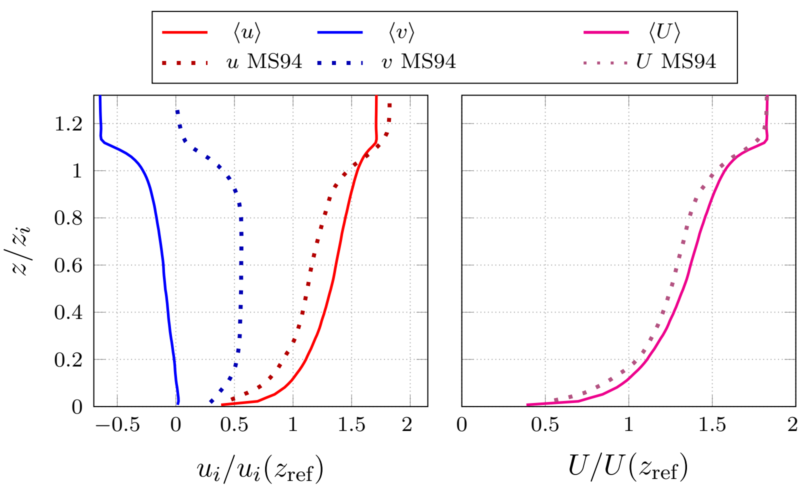

Figure 3.13: Velocity profiles for a neutral case. Left plot shows the components, right plot shows the magnitude. Data normalized by a velocity at a reference height. The solid curves are related to data obtained in this work, while the dashed curves are from Moeng and Sullivan [12], denoted by MS94. The discrepancy observed in the components plot is due to reference frame orientation.

The velocity profile for the unstable case is shown in Fig. 3.14. The nature of a well-mixed profile is present. As discussed, this is due to increased momentum mix and is also well captured in MS94's study.

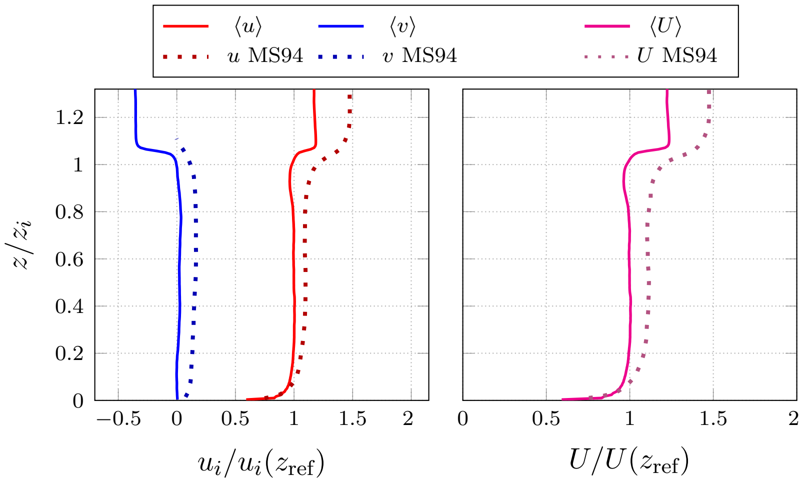

Figure 3.14: Same as Fig. 3.13, but for an unstable case.

The momentum fluxes profiles for the neutral case are shown in Fig. 3.15, while the unstable results are shown in Fig. 3.16. The orientation of our flowfield is slightly different, however, the square root of the square of the quantities can be plotted for a comparison. Note that this is not a turbulent quantity and does not have any physical meaning. The magnitude of the $\langle u'w'\rangle$ quantity, which is related to the flux of flow aligned with the geostrophic winds, decreases linearly with height. The effect of the cross-geostrophic

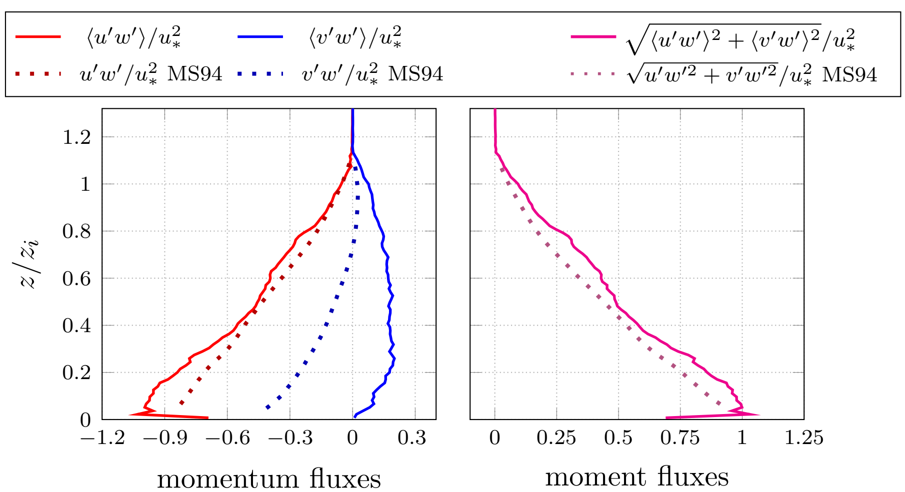

Figure 3.15: Momentum fluxes profiles for a neutral case on the left. The square root of the squared quantities shown on the right. The solid curves are related to data obtained in this work, while the dashed curves are from Moeng and Sullivan [12], denoted by MS94.

wind flux is small (blue curves) such that the quantity shown in magenta is a direct consequence of the along-geostrophic wind flux.

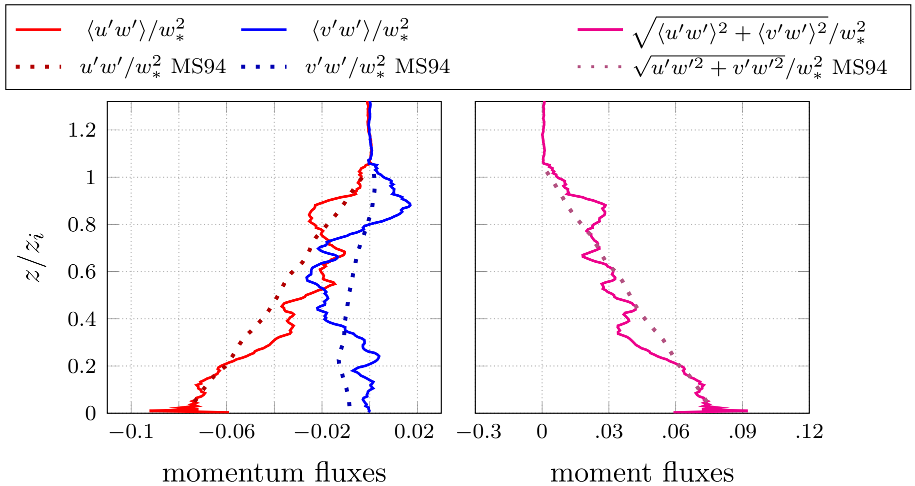

Figure 3.16: Same as Fig. 3.15, but for an unstable case.

The total (resolved scale plus sub-grid scale) velocity variances for the shear and convective types are shown in Fig. 3.17 and 3.18. In these figures, the variances are presented normalized by either u_* or w_*, depending on the ABL type, that is, neutral or convective. In the same figures, is also plotted the analytical curves from Eqs. (2.19)–(2.24). In the neutral ABL, the maximum value occurs near the surface. The ratios of $\langle v^2 \rangle / \langle u^2 \rangle$ and $\langle w^2 \rangle / \langle v^2 \rangle$ are about 0.5 throughout the neutral ABL. Finally, it is noted that these features agree well with observations [109, 110].

In the unstable case, both horizontal velocity variances have roughly the same magnitude and they agree well with MS94. The parabolic shape of the vertical variance is also observed in the simulations performed here. These results also match analytical curves as well as previous observations [111]. From the velocity variances plots presented, one can note that the turbulence has different variances in all three directions, an indication that such a flow is not isotropic.

The vertical fluxes of the three velocity variances are shown in Fig. 3.19 for the shear case (normalized by u_*^3) and in Fig. 3.20 for the convective case (normalized by w_*^3). Only the resolved scales are used to form the fluxes of the velocity variances. However, in the bottom of the surface layer, the sub-grid scale effects are rather large, such that the predictions of these third moments, using only the resolved scales, are either zero or even negative — see heights $z/z_i < 0.2$ in Fig. 3.19. The results found by MS94 are matched here, but note that the same is acknowledged by them for the neutral case. In

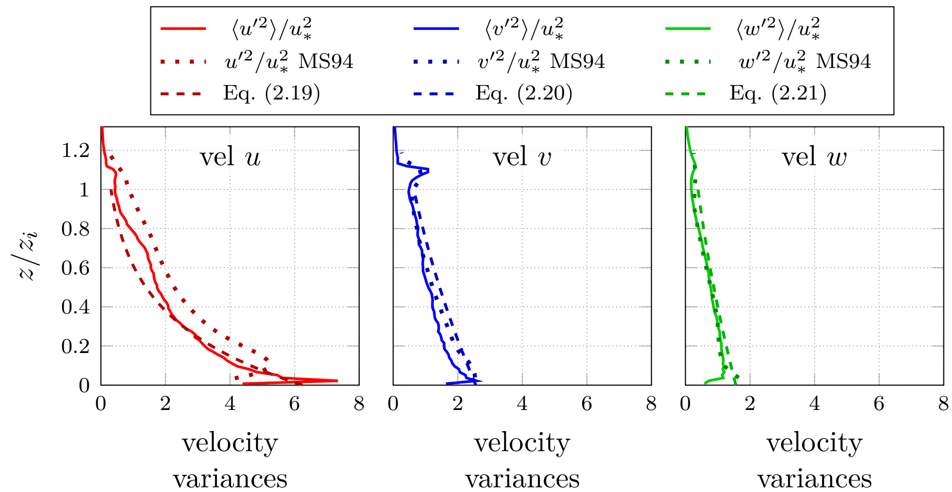

Figure 3.17: Vertical profiles of normalized variances for a neutral case. The solid curves are the results obtained in this work, plotted against analytical equations and numerical results by Moeng and Sullivan [12], denoted by MS94.

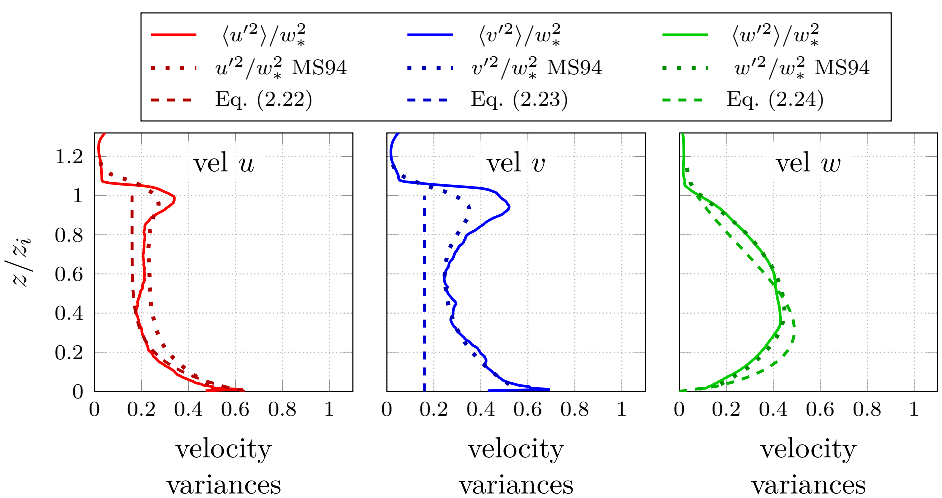

Figure 3.18: Same as Fig. 3.17, but for an unstable case.

fact, they mention that this erroneous behavior is not really representative of the actual third moments [112].

With respect to the convective case, the value of the flux of the vertical velocity variance is much larger than the other two, reaching about $0.3w_*^3$ in the middle of the boundary layer. This value matches observations [112,113], suggesting that the resolution issue from the neutral case is not as severe in the convective case.

The comparisons with MS94 are now finished. OpenFOAM/SOWFA was able to consistently capture all trends and magnitudes observed in both a neutral and a convective

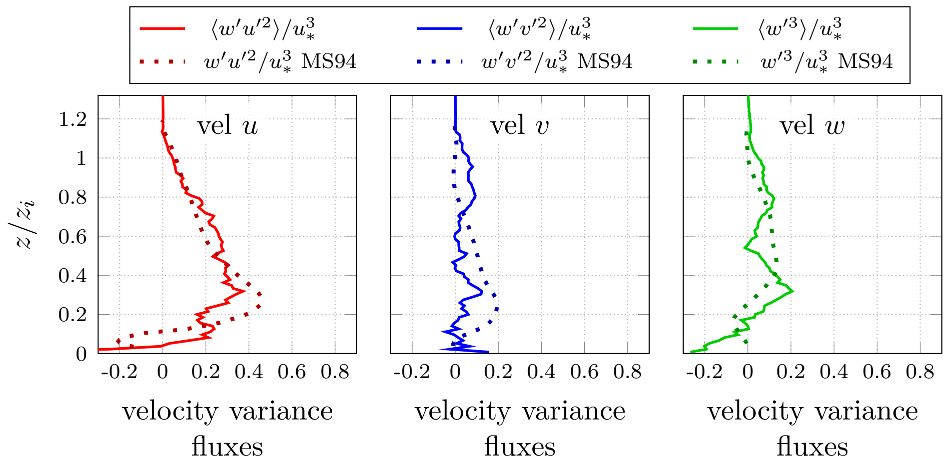

Figure 3.19: Velocity components variance fluxes vertical profiles for a neutral case. The solid curves are the results obtained in this work, plotted against numerical results by Moeng and Sullivan [12], denoted by MS94.

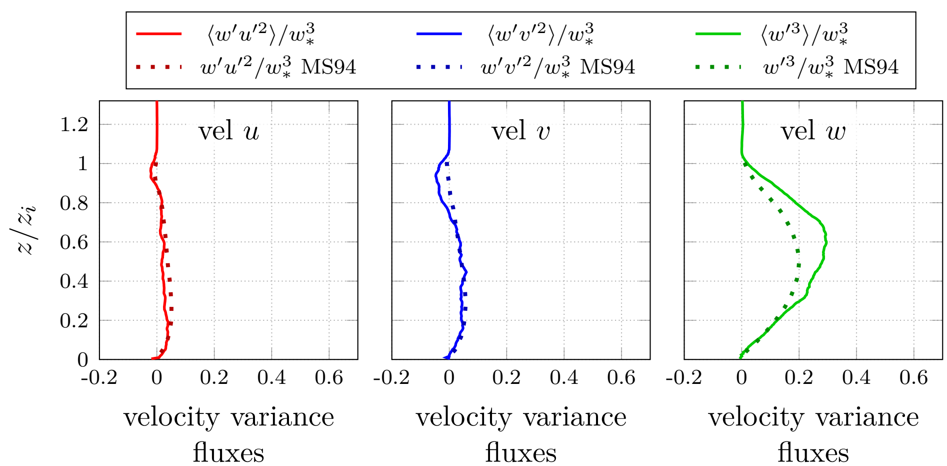

Figure 3.20: Same as Fig. 3.19, but for an unstable case.

(unstable) boundary layer.

3.3.2 At-sea Data by Peña et al.

In the study by Peña et al. [8], the offshore winds and turbulence characteristics were tested during a 6-month campaign at the Horns Rev wind farm, the world's largest wind farm. They used a LiDAR system, which is a ground-based sensing technique that avoids the use of high and costly meteorological masts. Schematics of the experiment are shown in Fig. 3.21.

Three different inflow conditions were clearly observed at the locations where the

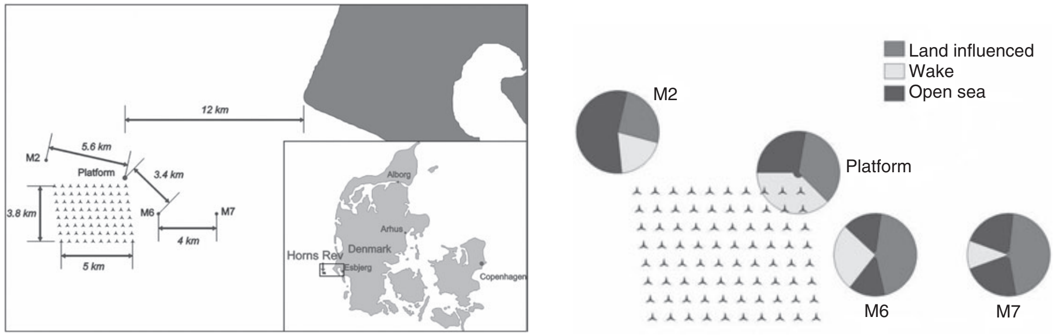

Figure 3.21: Schematics of the experiment conducted by Peña et al. [8]. Data from the three masts were collected and profiles were divided into the three conditions observed.

platforms and masts were installed (Fig. 3.21, right). They are:

- 'Land-influenced': wind coming from the easterly sectors. This is directly influenced by the nearby land.
- 'Open sea': wind coming from the northwesterly sectors, undisturbed, directly from the open sea.
- 'Wake': wind influenced by the farm wake. The direction range depends on the platform/mast position.

Only the velocity data related to 'open sea' are used for comparisons. The details of the experiment and the equipment used are outside of scope here, but a thorough description is given in the original paper by Peña et al. The relevant details are that LiDAR were installed at heights 63, 91, 121 and 161 m above the mean sea level. Lower heights were sampled using cup anemometers. The data have been logged at 2 Hz, and the profiles reported are averages of 2580, 965, and 1948 10-min windows for the mast 2, 6, and 7, respectively. The results for the 'open sea' characterization are shown in Fig. 3.22 on the left.

In order to compare with the numerical data obtained, the profiles are normalized, collapsing them. The conditions reported in the original paper were that the stability was considered "generally unstable" during the campaign. Then, a convective condition is simulated and the normalized results are shown in the right-hand-side of Fig. 3.22.

The trends and magnitude have been captured by the OpenFOAM solver. The results shown are at the end of the precursor simulation. For every height, the results from the solver are within the experimental measurement uncertainty. As a conclusion, the ABL solver is able to capture general characteristics. In a general sense, the challenge

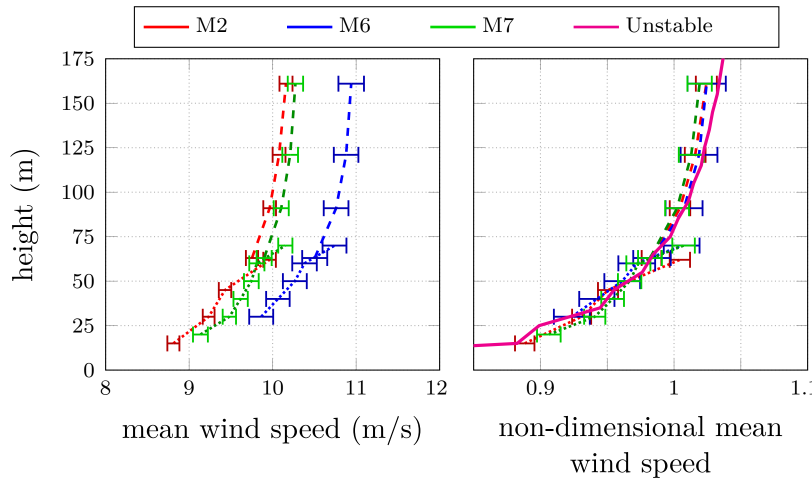

Figure 3.22: Wind speed data collected at-sea near the Horns Rev wind farm. Left: original at-sea data presented in Peña et al. [8] for 'open sea' condition. Right: non-dimensional at-sea data from Peña plotted against time-averaged unstable profile obtained in this work, using OpenFOAM. The same meteorological parameters observed during the experiments have been used in the simulations.

is a matter of knowing what condition to simulate. Upon availability of data and a description of the stability state, the characteristics of the atmospheric turbulence are likely to be captured.

3.3.3 At-sea data by Anderson et al. – The RED Experiment

The rough evaporation duct (RED) [3, 114] experiment was conducted off the Hawaiian island of Oahu in late 2001. The Research Platform Floating Instrument Platform R/P FLIP was moored about 10 km off the northeast coast of Oahu, and served as a host for a variety of meteorological sensors — see Fig. 3.23. The experiment also included two instrumented land sites, two buoys, a small boat, and aircrafts in order to collect the data.

The conditions during the observations are described as consistently slightly unstable, with calm to moderate 4–11 m/s subtropical winds, with relatively calm waves. This study does not provide a lot of data that is directly useful for validation purposes. It does, however, provide observational evidence of some aspects considered previously. For instance, a spectral analysis of the atmospheric turbulence at the 5 probe locations of the platform yielded curves that followed Kolmogorov's $-5/3$ cascade. Such plots are not shown here, but the trend of 156 spectras per probe/sensor followed the cascade.

A few quantities have been derived from turbulent data sampled at the probes. Figure

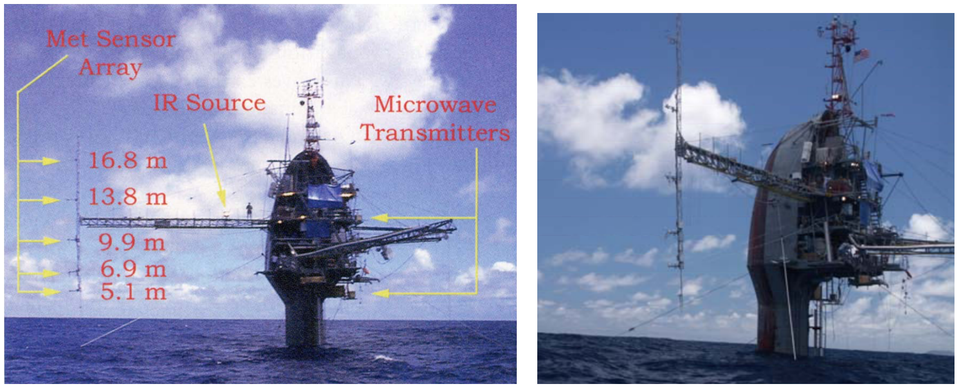

Figure 3.23: The Research Platform Floating Instrument Platform (R/P FLIP) used in the RED study [3]. Data were collected at 5 probes

3.24 shows the average wind speed profile observed. Fitting a logarithmic or a power-lay boundary layer profile on top of this data is troublesome because of the choice of reference point.

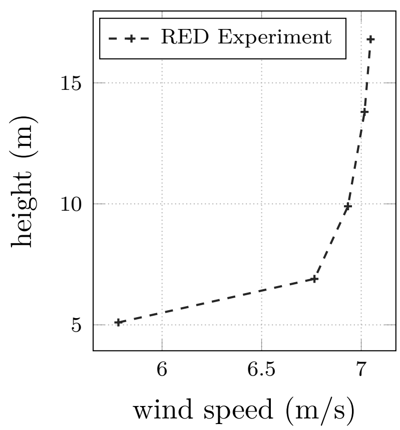

Figure 3.24: Velocity profile observed at the 5 probe locations of the R/P FLIP platform during the RED experiment [3]. The data presented consist of the average of 1650 10-min average samples.

One of the themes of this V&V section is to show how difficult is it to compare data, especially unsteady and turbulent quantities. Data acquired in situ, such as the ones from the RED experiment, are also not of great help in validating the results obtained here. This study was selected because it provides data collected at the first few meters above the sea surface, exactly where it interests us the most. To illustrate the difficulty of obtaining data in such an environment, some of the turbulent fluxes from the RED experiment are shown in Fig. 3.25. The values obtained give an indication of how challenging a sea environment can be, with respect to the fact that variations in the data acquired can yield curves that are not very consistent or of defined shape. In fact, the data presented here was not published in the original RED paper [3], but obtained via private communication with one of the authors of the study. In such communications, it was stated that two of the five probes had not been performing well and were showing signs of failure.

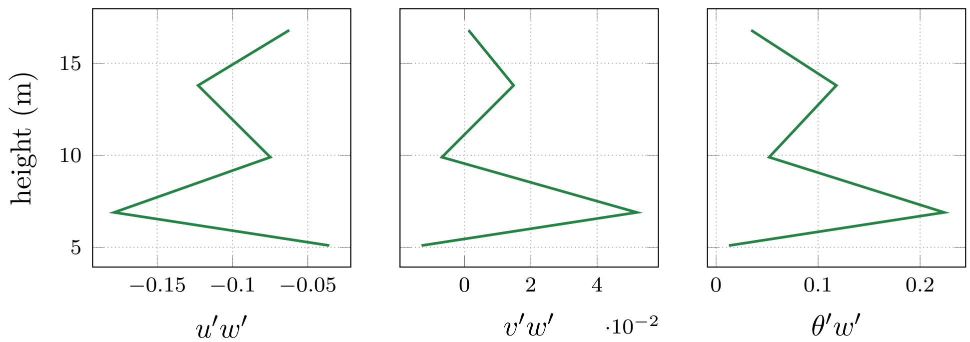

Figure 3.25: Turbulent fluxes observed at the 5 probe locations of the R/P FLIP platform during the RED experiment [3].

Further comparisons are not performed with this study. It served to (i) provided confirmation that real-world at-sea turbulent fluctuations follow Komolgorov's cascade; and (ii) illustrate how challenging it is to acquire data in such an environment. The author did not find any other study that provided validation-quality data in a similar environment.

3.3.4 Other V&V Efforts From the Literature

The suite of codes used in this work has been used by many different authors and several other types of validation can be found in the literature. Since the focus of SOWFA is on wind energy applications, it is more common to find validation from that perspective. The following aspects are pertinent to these studies:

- None of them focus on the very bottom of the surface layer. They tend to focus on the 30–200 m range;
- Verification among codes are more common than validation with observations;
- Several of them validate the ABL aspect by observing power characteristics of a wind turbine immersed in ABL flow.

Among the studies that provide some V&V, the following are worth mentioning: Churchfield et al. [93], Doubrawa et al. [99], Martinez et al. [104, 115], Mirocha at al. [98], Jha et al. [97], Johlas et al. [116], and Quon et al. [117].

Our validation efforts conclude here. Note that the Silsoe cube will be investigated in the next chapter.

3.4 Concluding Remarks

This chapter describes the OpenFOAM solver used to generate the unsteady atmospheric flowfield. The development of the realistic turbulence is achieved by the execution of the precursor simulation. Several aspects have been noted, in particular the evolution and convergence of profiles.

During the execution of many cases and the comparison to different published studies, a few aspects became evident and are worth noting. First, there are not a lot of quality data[1] for validation purposes. Even from a wind engineering perspective, some models lack complete validation because of this. It becomes especially complicated if data is needed over the ocean, rather than over land, adding complexity to an already difficult comparison of unsteady phenomena. Next, from the many validation and comparison exercises investigated throughout the development of this work, the question that arises is not usually whether or not the solver will be able to capture the trends and the magnitude of results, but rather a question of what stability state and conditions are to be met. It is important to highlight this issue, as the stability state and specific conditions can vary greatly.

The results presented in this chapter are, in part, composed of a systematic search for the correct parameters that match a certain condition. Results that match one study, do not usually match others. The variability is quite significant. Once the condition is known, the solver is able to capture the trends and the correct magnitude of the turbulent fluctuations.

The investigation at this point has focused on the ABL as a whole. The goal so far has been to capture the correct physics, to properly model the capping inversion, etc. Results have been compared with data from the meteorology community, establishing confidence that the solver properly captures the main features of the ABL. The results suggest that the stress model is properly generating the shear necessary. For the problem of the coupled atmospheric effects and the ship airwake, however, the interest lies in the

[1] Publicly available

very bottom of the surface layer. The SFS2 geometry investigated in this work is 35 ft high (about 16.7 m), and it is not anticipated that the interaction of the ship airwake with the unsteadiness of the atmosphere spans much higher than 40 m. Because of that, in the next chapter focus is given to the bottom part of the surface layer, with respect to providing more spatial resolution, resolving smaller scales, and account for the SFS2 body.

Chapter 4
Computational Setup of the Coupled Problem & Development of the Atmospheric Boundary Layer Profiles

In the previous chapters, the ABL has been discussed from a meteorological point view, with several theoretical aspects to it. Later, we discussed the computational framework and numerical details of solving the ABL computationally. For the coupled ship airwake and atmospheric turbulence problem, however, the region of interest is the bottom 30 m or so of the surface layer. The interaction of the turbulence present in this region with a ship, the resulting turbulent airwake, and the ultimate effect of the ABL-modified airwake on a flying helicopter are the topics of further investigation of this work. In order to investigate such effects, the attention is focused to this region. In a CFD solver setting, the ship needs to be considered and additional spatial and temporal resolution is needed. This chapter discusses the inclusion of the ship geometry, the steady ABL approach, and some aspects regarding the development of the near-ship atmospheric boundary layer profiles.

4.1 Overview

The setup used for the development of the large-length-scale atmospheric eddies (discussed in chapter 3) is essentially a large domain, with relatively coarse grids, and no geometries. In the simulations performed, the grid has been of uniform spatial resolution. For the coupled problem at hand, it is necessary to resolve the smaller length scales, especially those of the same scale as the ship and/or the helicopter rotor.

Along the lines of the basics of LES models, increased spatial resolution is needed to resolve more of the flowfield. The grid aspect is important to ensure the turbulence cascade is being properly captured as the grid size gets smaller. Additionally, increased resolution is also necessary to properly model the SFS2 geometry — or any geometry. This development of the background atmospheric turbulence into refined portions of the domain is discussed in this chapter.

After a profile and the atmospheric turbulence has been established in a refined region, the goal is then to compare such highly unsteady ABL with the so-called steady profile. For that, OVERFLOW is used and the approach in creating the velocity profile is fundamentally different than that used in OpenFOAM. These aspects are discussed in the rest of this chapter.

4.2 Resolving Smaller Length Scales

In an effort to solve smaller scales, the computational cost of the problem can increase significantly. The coupled helicopter simulations will not span for more than 120 s, such that the effects of very large length scales are not included. Because of that, a compromise has already been made regarding the outer domain size. As previously discussed (see section 3.1.3), the outer domain size has been reduced to a 1-km-by-1-km domain approximately.

This section discusses the approach used in OpenFOAM to refine the mesh around the area of interest, and the procedure to model the geometry. Here, the immersed boundary method is used due to its simplicity and feasibility for the problem at hand.

4.2.1 Gridding Strategy

OpenFOAM is an unstructured solver and thus methods for unstructured grids are used. The grids generated for the precursor simulations, however, are of structured Cartesian nature. This approach is preferred in an effort to maintain grid cells with aspect ratio of approximately one. OpenFOAM offers refinement utilities in which cells are refined by a factor of 2 in each direction. Such utility works by getting information about a sub-domain previously defined, refining it, and writing the new mesh. That is, for every refinement, the number of cells present in a sub-domain increases by 8-fold. Such refinement process is called iteratively for differently-sized sub-domains. We shall call these sub-domains ‘refinement regions’.

These refinement regions around the ship are used to resolve smaller eddies. A diagram of the meshing strategy is provided in Fig. 4.1, where each of the boxes are nested regions with an increased mesh resolution. The resulting grid appears to be of structured nature, however it is treated as unstructured internally.

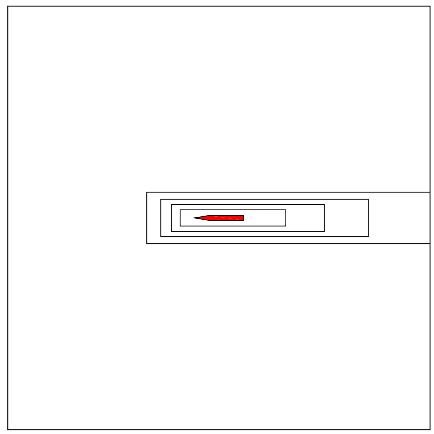

Figure 4.1: Illustration of nested refinement regions. Ship is shown in red.

While the process illustrated in Fig. 4.1 is straightforward, the choice of the size of the regions is not. In a general sense, the proximity of such regions upstream the body of interest is usually not given much importance. That is because in typical CFD, the flow tends to be laminar — or, rather, ’uniform’ in this context. When it comes to the unsteady ABL, however, that is not the case.

The initial precursor solution is mapped onto the new grid that has a few nested refinement regions, similar to the illustration shown in Fig. 4.1. This mapping process amounts to interpolation of quantities. At time $t = 0$, although the near-ship region is fine and has interpolated ABL data, it obviously does not have resolved data up to that grid level. For that to happen, the simulation is started, making use of the boundary condition data saved from the precursor. As the flow moves from the background[1] mesh into the first refinement region, the new grid level needs to be resolved before the flow enters the next refinement level. We call this region in between refinements ‘entry length’.

The entry length should be long enough, allowing the atmospheric turbulence to develop before entering a new level, but not too long as it represents wasted computational resources. In other words, the refinement regions should not be very close to one another.

[1]This is the same resolution as the precursor. It represents the outer-most region, with coarse cells. The term *background* will be used interchangeably.

The resolved aspect is monitored by looking at the spectral content of the flow at various locations within the entry length region, and the drop in resolved content is observed at the right wave number, associated with the length scale of the cell.

As an example of the energy associated with the different regions, Fig. 4.2 shows the energy in the background mesh, and in a refined region. Note that this figure has a close relationship with the grid illustrated in Fig. 4.1. Consider a point in the most refined part of the domain, upstream the ship. The energy content of such a point is shown as the gray curve in Fig. 4.2, whereas the background mesh is shown in black. The energy content of the gray curve was taken from an actual SFS2 immersed in ABL flow simulation, which contains finer regions. The left end of the spectrum in this case is related to the time span this data was taken, and the short simulation time is not able to capture the structures of the same length scale of the domain.

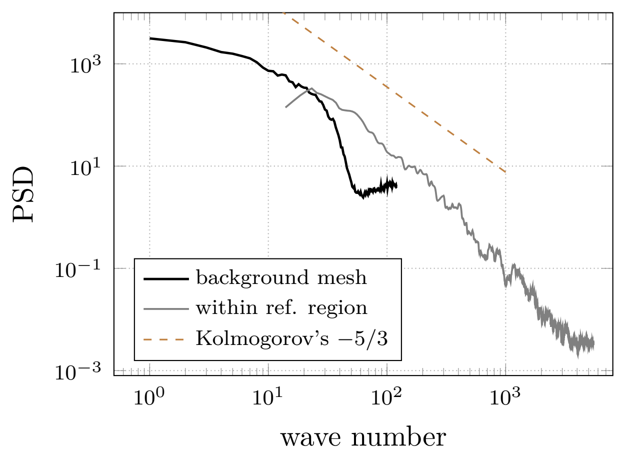

Figure 4.2: Energy spectra of a typical domain. Black curve: average energy spectral density averaged over the entire domain at the end of the precursor level; Gray curve: energy content of a point in a refined region, showing that smaller scales of the ABL eddies are resolved in finer portions of the domain; also shown is Kolmogorov's $-5/3$ slope.

There are 3 characteristics of the curves worth noting:

- The lower bound of the black curve is at a wave number of 1. It corresponds to the largest oscillation able to be resolved in the domain and is a function of the physical domain size. The low-frequency content missed by the smaller domain (for instance, that associated with a velocity field similar to that shown in Fig. 3.3(b)) occurs over time scales larger than what could be captured in a 30–40 s simulation. Therefore, by using a smaller domain with a relatively short simulation time, relevant content is not lost;

- A sharp drop in the resolved content is observed at around 40 to 50 waves that indicates the mesh resolution is not appropriate to capture the eddies of the size such wave numbers represent;

- The upper bound of the curve is at about 120 waves, and is related to the resolution of the grid. It is not possible to capture content related to eddies smaller than the grid cell size, so the resolved quantity spectra end there;

- The gray curve picks up the scale of turbulence and an overall continuation of the scale representing Kolmogorov's $-5/3$ cascade can be seen.

The energy content related to wave numbers below 10 are associated with eddies of the scale of the ship and larger. The region of the plot with wave numbers between 10 and 20 are related to the scale of the ship width and its major components such as the flight deck. This region is the limit of what can be resolved in the background mesh that still follows Kolmogorov's $-5/3$ cascade of turbulence and contains eddies that are expected to interact with the ship and modify the topology of the airwake. The mentioned drop represents a lack of accurately resolved content associated with the length scale of the ship's minor components (chimney and superstructure height, for instance).

As a result, although the base mesh resolution of 10 m is not able to resolve scales of the same order as the SFS2's minor components, the refinement regions resolve them. It was observed that the atmospheric turbulence present in the most refined region is resolved and continues to follow Kolmogorov's $-5/3$ turbulence cascade. The question of how many of these refinement regions are necessary, offering a compromise between accuracy and computational cost, will be investigated later.

Another aspect to note is that in this approach, realistic atmospheric turbulence will only be present after those original large-scale eddies convect down into the refinements. Hence, data is only saved after about 40 s form the start of the simulation. This time varies between simulations as it depends on the freestream velocity. With that respect, this work aims in being conservative and often chooses to let the flow convects a long distance. In conclusion, the process described here is relatively easy to accomplish. After an understanding of the fact that the entry lengths need to be long and that enough time needs to be given to allow the flow to go over the refinements, it is a matter of computational cost.

4.2.2 A Note on Numerical Schemes

It was found that by using the same 2nd order numerical schemes from the precursor (see section 3.1.3) the solution would sometimes exhibit some oscillations in the velocity and pressure. Sometimes these oscillations would appear as "rings" around features of the SFS2. The issue seemed to be coming from the discretization of the convective transport term.

Such behavior has been reported before with respect to the proximity to an actuator line model for wind turbines [97, 118]. The actuator line model works by inserting external forces into the flowfield and thus, as reported, interpolation taking place in close proximity has caused issues. It is believed that the same was observed here because of the immersed boundary method for representation of geometry. A discussion of the method is given later in this chapter, but essentially it also works by exerting forces into the flowfield.

In order to eliminate this numerical issue, scheme recommendations from [7, 97] are followed. To successfully eliminate oscillations caused by the actuator line, they used a blended scheme for the convective transport term, consisting of 90% midpoint/10% upwind upstream of the actuator and 98% midpoint/2% upwind everywhere else with a smooth transition in the blending between these two regions. In the context of this work, some values have been tested and it was found that a much lower portion of upwind was necessary.

Testing shows that spurious numerical issues like these oscillations have been eliminated by using as little as 4% of first-order upwind for the convective transport term in the most refined region. This ensured that the solution would remain mostly second-order accurate. A smooth transition has also been used here. In practice, the schemes were set based on the grid cell size, automatically satisfying the smooth aspect of the blended scheme, while also being easy to set. This approach is similar to a small amount of artificial dissipation common to CFD and is used to ensure boundness of the solution.

In all of the cases that contain an unsteady ABL executed in this work, the blend of numerical schemes is shown in Table 4.1. It shows the amount of second-order, which translates to at most 4% of upwind. At 10 m (and any size greater than 10 m), the blended scheme reduces back to pure second-order.

All of the other numerical schemes and solution method have been kept the same from the precursor stage, discussed previously in section 3.1.3.

Table 4.1: Amount of second-order accurate scheme in the blended scheme used. The amount used in the convective transport term of velocity U and potential temperature θ is shown.

Grid size (m)	U	θ
0.3125	0.96	0.980
0.625	0.96	0.980
1.25	0.97	0.985
2.5	0.98	0.990
5	0.99	0.850
10	1.000	1.000
1E6	1.000	1.000

4.2.3 Methodology

Having discussed some of the individual steps of the process, the methodology use is quickly summarized. At the end of the precursor (as indicated by convergence of profiles, etc. — cf. chapter 3), the case is further executed. In this step, the intent is to save data at the inlet boundaries to serve as prescribed boundary condition to the coupled simulation.

To summarize, the following steps are taken:

1. Precursor is further executed, saving boundary data;
2. State at the end of precursor is mapped to domain of interest (usually smaller, with refined regions);
3. Simulation is started, inlet boundary conditions make use of saved data in step 1;
4. Let the case go through the initial transient (wake development, and, most importantly, the turbulence development between refinements);
5. Start saving data after about 40 s of simulated time.

A general workflow is shown in Fig. 4.3. This workflow builds on top of the precursor block, shown previously in Fig. 3.1. In this workflow, the development of the turbulence through the grids is built into the block checking whether or not the wake is fully developed. The next logical step is to add a body, which is done by means of the immersed boundary method, described next.

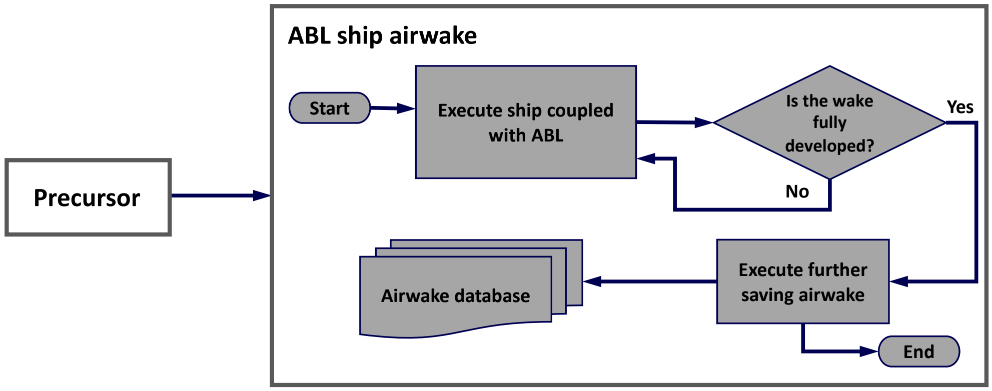

Figure 4.3: General workflow for the airwake solution. This workflow builds on top of the precursor shown in Fig. 3.1. The airwake database aspect will be discussed in chapter 6.

4.3 The Immersed Boundary Method within the ABL Solver

The immersed boundary method (IBM) was first introduced by Peskin [119] and has undergone several improvements over the past few decades. The main feature of this method is that simulation of complex geometries can be conducted on a fixed non-boundary conforming Cartesian grid. In general, IBM can be divided into two categories: (i) "continuous forcing", where the boundary is imposed through a continuous force into the governing equations; and (ii) "discrete forcing", which uses explicit or implicit forcing added to the discretized Navier-Stokes equations. In this work, a discrete forcing-type IBM designed for both structured and unstructured grids has been implemented, following the work of McIntyre et al. [120].

As opposed to body-fitted meshes, IBM enables a mesh generation process that is considerably simpler and easily allows handling of moving boundaries without remeshing. The goal of the IBM is to remove geometrical constraints associated with the computational domain and internal geometry. The IBM introduces an implicit force that replicates solid boundaries. The force is dependent on the velocity field and pressure, and it enters the equation of motion as an extra force term. Our implementation adds the forcing term in a simple and straightforward manner.

The IBM implementation works by modifying the equations of motion to be solved within the body. Thus, it is dependent on the extra terms involved in the equations of motion. For instance, the IBM implemented on the full ABL-resolving Eq. (3.2) is different than an IBM for a regular incompressible momentum equation.

Let the computational domain be Ω, the immersed body β with boundaries $\partial\beta$ and the region occupied by the fluid $\Omega_f = \Omega \setminus \beta$. The direct-forcing method introduces an extra force, F, to Eq. (3.2), given as

$$F \equiv \begin{cases} \begin{array}{c} \dfrac{\partial}{\partial x_j}(u_i u_i) + 2\epsilon_{i3k}\omega_3 u_k + \dfrac{1}{\rho}\dfrac{\partial}{\partial x_i}p_0 + \dfrac{\partial \tilde{p}}{\partial x_i} + \\ \dfrac{\partial \tau_{ij}^D}{\partial x_j} - g\left(\dfrac{\theta-\theta_0}{\theta}\right) + \dfrac{1}{\Delta t}(U_i - u_i) \end{array} & : \; x_i \in \beta \\ 0 & : \; x_i \in \Omega_f \end{cases}, \tag{4.1}$$

that enforces rigid-body motion throughout the immersed body β and hence no-slip conditions at $\partial\beta$ [121]. Introducing $\eta(x,t)$ to mark the location of the immersed body,

$$\eta(x_i,t) = \begin{cases} 1 \; : \; x_i \in \beta, \\ 0 \; : \; x_i \in \Omega_f, \end{cases} \tag{4.2}$$

the forcing term F becomes generalized with

$$F = \eta\left[\frac{\partial}{\partial x_j}(u_i u_i) + 2\epsilon_{i3k}\omega_3 u_k + \frac{1}{\rho}\frac{\partial}{\partial x_i}p_0 + \frac{\partial \tilde{p}}{\partial x_i} + \frac{\partial \tau_{ij}^D}{\partial x_j} - g\left(\frac{\theta-\theta_0}{\theta}\right) + \frac{1}{\Delta t}(U_i - u_i)\right]$$

where U_i is the immersed body velocity and Δt is the time step. For a stationary body, $U_i = 0$. Inside β, F explicitly cancels all fluid forces, so that (3.2) reduces to

$$\frac{\partial u_i}{\partial t} = \frac{1}{\Delta t}(U_i - u_i), \quad \forall x_i \in \beta. \tag{4.3}$$

The immersed boundary forcing enforces boundary conditions at the body surface. Velocity is explicitly forced to the prescribed value throughout the immersed boundary, such that the no-slip boundary condition on $\partial\beta$ is automatically satisfied. How pressure is constrained within the body has not yet been specified, so nothing can be said about the behavior of p approaching $\partial\beta$ from β. Intuitively, the boundary condition will be satisfied approaching $\partial\beta$ from the outside, Ω_f, provided the governing equations are satisfied. Restricting the balance of linear momentum to $\partial\beta$ and taking the inner product with $\hat{\mathbf{n}}$, defined by the induced orientation of β on $\partial\beta$, results in

$$\hat{\mathbf{n}} \cdot \left\{ \frac{\partial \bar{u}_i}{\partial t} + (1-\eta)\left[\frac{\partial}{\partial x_j}\left(\bar{u}_j \bar{u}_i\right) + 2\varepsilon_{i3k}\Omega_3 \bar{u}_k + \frac{\partial \tilde{p}}{\partial x_i} + \frac{1}{\rho_0}\frac{\partial}{\partial x_i}\bar{p}_0\right.\right.$$

$$+\frac{\partial \tau_{ij}^{D}}{\partial x_j} - g\left(\frac{\bar{\theta}-\theta_0}{\theta_0}\delta_{i3}\right)\Bigg] - \eta\left[\frac{1}{\Delta t}\left(U_i - u_i\right)\right]\Bigg\} = 0 \quad (4.4)$$

Now, consider the case that will be explored in this work, that of a stationary immersed body. On $\partial\beta$, $u_i = U_i = 0$ from the IB forcing, so the convective term and the time derivative vanish at the boundary $\partial\beta$. Also, the viscous stress acts only tangent to the plane of a wall, so $\hat{\mathbf{n}} \cdot \left(\frac{\partial \tau_{ij}^{D}}{\partial x_j}\right) = 0$. As a consequence, Eq. (4.4) reduces to $(1-\eta)\frac{\partial \tilde{p}}{\partial x_i} = \hat{\mathbf{n}} \cdot (1-\eta)\, g\left(\frac{\bar{\theta}-\theta_0}{\theta_0}\right)$. Since η is not well defined on $\partial\beta$, the trace operator T_η is used to extend the value of $\eta(x)$ from Ω_f to $\partial\beta$ [120], resulting in

$$\hat{\mathbf{n}} \cdot \frac{\partial \tilde{p}}{\partial x_i} = \hat{\mathbf{n}} \cdot g\left(\frac{\bar{\theta}-\theta_0}{\theta_0}\right) \quad (4.5)$$

Thus, provided momentum balance is satisfied, pressure satisfies the appropriate boundary condition approaching the immersed body surface. Computational agreement to this has been shown in McIntyre et al. [120], but will also be shown later.

The resulting momentum equation, in essence, becomes Eq. (4.3) inside the immersed body and Eq. (3.2) outside, while still satisfying continuity (Eq. (3.1)). A Cartesian-based, computational mesh is used throughout the domain, including regions interior to the solid ship. For regions inside the ship, the gradients remain low; hence, for a stationary geometry, a fine mesh is not required. An illustrative example of different approaches when it comes to stationary immersed boundaries is provided in Figure 4.4. Experimentation with the two types of grids shown have been performed, and while the one with coarse interior is generally better when it comes to computational effort, it was found that by doing so, many cells of bad quality were introduced to the domain — especially at the refinement region boundaries —, hurting the condition number of the system of equations and leading to instabilities and "blow-ups" in the CFD. Because of that, the grid with uniform resolution throughout the immersed boundary has been preferred.

Although in this work ship movement is not explored, the immersed boundary method offers convenience in setting this up. The volume field η can be modified easily and its computational representation allows straightforward user access.

A general difficulty of the IBM is that it tends to be difficult to achieve standard meshing requirements for boundary layers common to aerodynamic CFD models. The present model does not directly resolve boundary layers of the geometry. Shipman et al. [122] performed a detailed study on simplifications that can be made and their impact

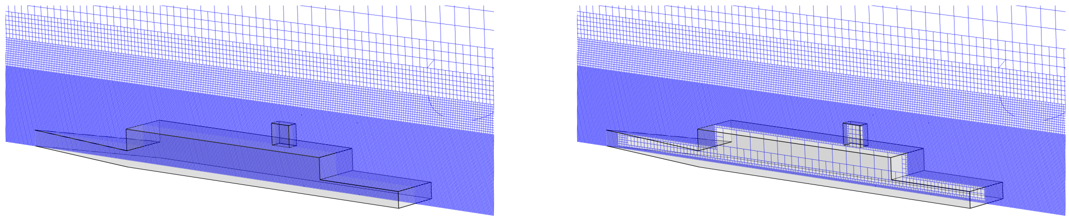

Figure 4.4: Cross section along SFS2's centerline of typical grids around an immersed body. (left) General mesh around an immersed body; (right) Since the body is stationary, the inside does not need to be well discretized. Semi-transparent SFS2 included only for reference.

on the quality of the predicted airwake and concluded boundary-layer resolving grids only marginally improve the solution quality. The region of interest in this work is specifically the wake the helicopter operates in, which is dominated by separated flow. CFD practice for capturing separated flow behind a streamlined aerodynamic body is driven by requirements to capture laminar and turbulent boundary-layer separation in an adverse gradient. In the context of this bluff-body, SFS2 ship, separation and transition tend to initiate from much stronger adverse pressure gradients that form on sharp corners of the ship. Hence, it is not surprising that mesh convention for streamlined aerodynamic bodies need not apply to the bluff bodies of interest.

In light of this discussion, given that the objective is to investigate resolved ABL content in the ship airwake, a no-slip condition on the geometry with an under-resolved boundary-layer profile is considered to be sufficient. The interest is not on the near-wall behavior, thus making the IBM a good candidate for such problems. In fact, body-fitted overset grids are used within OVERFLOW later in chapter 5 and will verify statements made in the work of Shipman [122]. Regarding validation aspects, the Silsoe cube is shown next. Additional validation, however, is given in section 5.3, when the discussion is on the SFS2 airwake and comparisons are made to experimental wind tunnel results.

4.3.1 V&V Revisited: The Silsoe Cube Experiment

The Silsoe cube is a 6 m cube, originally constructed to provide a facility for fundamental studies of the interactions between the wind and a structure. It is located in an 'open country'-exposed location at the Silsoe Research Institute, UK — see Fig. 4.5. Detailed measurements of surface pressure on the cube and of the wind velocities in the region around the cube have been made. The studies around such cube span well over a decade, and some of the relevant references are by Richards and Hoxey [9, 107, 108].

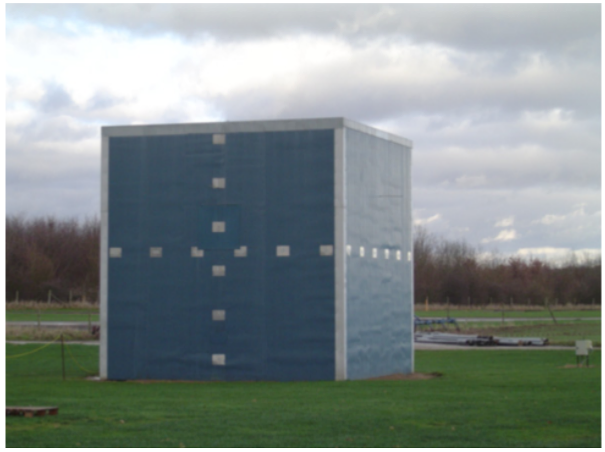

Figure 4.5: The full-scale Silsoe cube. Note the metal plates around each pressure tap. Figure from Richards and Hoxey [9].

Pressure data has been collected at the surface of the cube using 42 pressure taps, aligned vertically and horizontally around the cube (Fig.4.6). The exact location of the pressure taps are available in the paper by Richards and Hoxey [9].

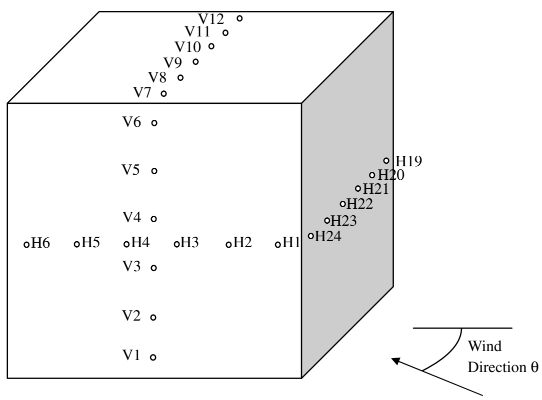

Figure 4.6: Schematics of the pressure taps on the cube and numbering system. In this work, only $\theta = 90$ wind direction is considered. Figure from Richards and Hoxey [9].

The full-scale data has been processed into 12 min non-overlapping record blocks. The beginning of each block was triggered if several wind and calibration conditions were met. The data reported provides a set of mean, maximum, minimum, and standard deviation pressure coefficients. They also presented data at several different angles, although here, only the data related to the flow aligned with the cube is used.

A reference sonic anemometer has been installed on a mast, located upstream of the cube, undisturbed from any building or structure. At the same mast, a pitot tube provided reference dynamic and static pressures utilized to normalize the data. For additional information about the experimental setup, the reader is referred to the work by Richard and Hoxey [9].

It is also important to mention that it was reported that measurements are well matched by a simple logarithmic profile with a roughness length $z_0 = 0.006$–0.01 m — for reference, see Table 2.1 and Fig. 2.6. The typical wind speed measure at the reference point was reported to be around 7 m/s.

Comparisons with the $\theta = 90$ case are made to the simulations. In order to do so, a precursor simulation is executed, where the reference velocity and reference height match the reference sonic readings as well as the specification of the appropriate surface roughness found in the experiment. The actual cube is modeled by the immersed boundary method described in the previous section. It is emphasized that the Silsoe cube experiment looked into the pressure exerted by the wind on the cube, and the reader is reminded that this work uses a relatively simple implementation of the immersed boundary method. One of the acknowledged drawbacks of this method, as mentioned, is the inability to predict accurately the flow very close to the wall, and thus, pressure coefficients. There are no explicit walls and no additional treatment is performed in order to properly capture pressure data. In light of this discussion, the results presented in Fig. 4.7 capture the trends, but not the accurate magnitude of the mean pressure coefficients. The standard deviation, however, is more accurately captured, but still with large associated errors. The standard deviation is associated with the natural fluctuations present in the wind that was captured by the experiment. It is interesting to see that the IBM fails to capture sharp discontinuities, such as those between horizontal probes when changing sides of the cube (H12 to H13, for instance).

The grids used in this case follow the general setup described in section 4.2.1 and the numerical schemes described in section 4.2.2. In doing so, the smaller scales that are needed for this problem are resolved.

4.4 Development of Unsteady ABL Profiles

This section will take a closer look at the mean velocity profiles. For the problem of interest, the focus is on the very bottom part of the surface layer — the first 30 m or so. The previous chapter looked at the profiles as a whole and established confidence that the OpenFOAM/SOWFA solver is able to capture the trends, magnitudes, and

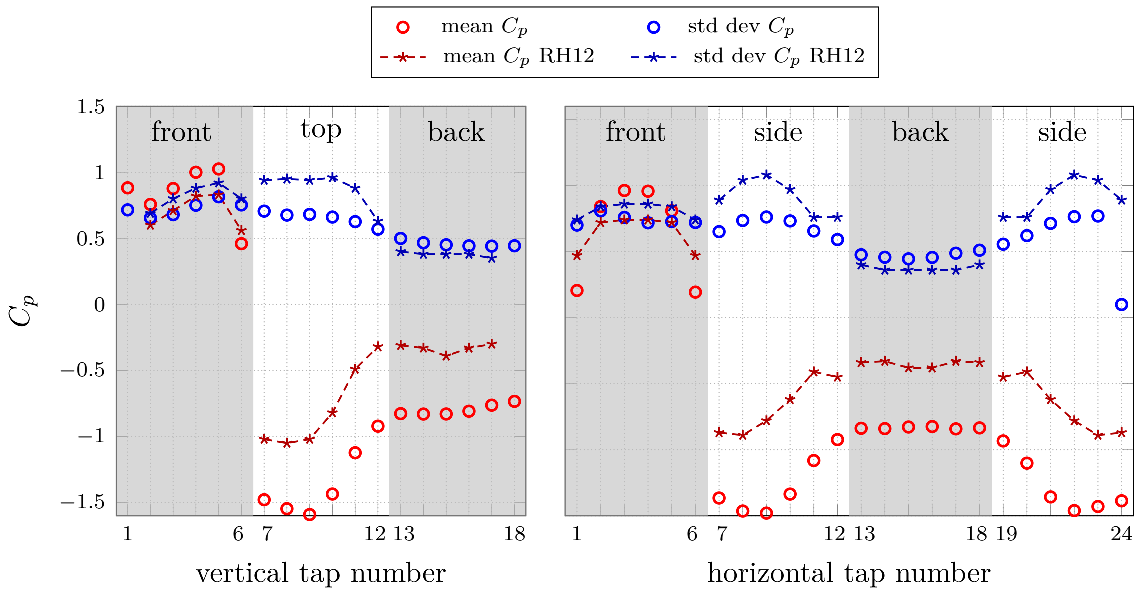

Figure 4.7: Silsoe cube comparison using experimental data from Richards and Hoxey [9] (shown as RH12, star symbols on a curve), and results obtained in this work (circle symbols only). The pressure tap numbering used is shown in Fig. 4.6 ($\theta = 90$). The front and back of the cube are highlighted in gray. The IBM implementation used in this work cannot capture absolute pressure characteristics, but the trends are well captured.

important features.

The obtained profiles at the end of the precursor level go through the meshing procedure outlined in section 4.2.1. However, for now, the ship or any other geometry are not included. By doing so, the profile within the inner-most refinement region is established. The reader is reminded that on a typical 10-m precursor grid, the first (cell-centered) value is at 5 m and the next at 15 m. As stated before, it is clear the precursor background mesh resolution is unable to provide proper spatial resolution for the problem at hand.

The solver is executed for long enough as if the ship was included in the simulation. After the initial transient of the flow convecting into the different refinement levels as explained, time-averaged data start to be recorded. The solver is then executed for at least 120 s and a vertical line is sampled just upstream of where the bow of the ship would be. The velocity data observed at this location is essentially what the SFS2 will experience. This approach allows us to see how the refined profile presents itself, given a specific precursor data. The comparison is shown in Fig. 4.8. Note that in the same figure, the limits of the refinement region in the vertical directions are also shown.

In this region, besides the averaged velocity magnitude profiles, it is also interesting to look at the velocity variances — see Fig. 4.9. This represents a measure of the turbulence

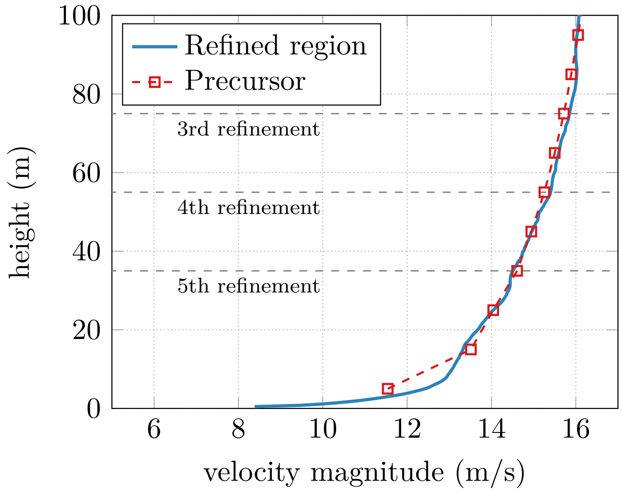

Figure 4.8: Time-averaged velocity magnitude profile obtained at the refined region (small length scales) in comparison to the precursor simulation (large length scales). The height of the refinements regions are shown.

intensity, but they are plotted in such a way that is directly comparable to the earlier V&V plot (Fig. 3.17). The obtained turbulence at the bottom part of the surface layer is of the same order of magnitude as those found in previous studies. Unfortunately, the author did not find any study in which turbulent quantities at this height of interest have been reported (besides those mentioned in this document). Such region, especially in a sea environment, offers tremendous challenges in acquiring data.

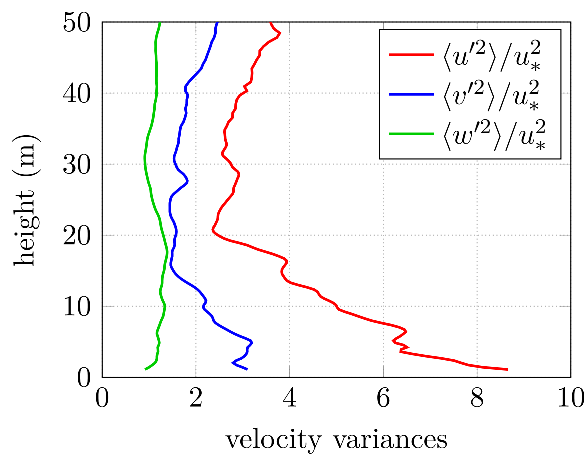

Figure 4.9: Velocity variance profiles obtained at the refined region. Data presented in such a way that is directly comparable to V&V efforts shown previously in Fig. 3.18. The turbulence is of the same magnitude.

In this work, two neutral profiles with different characteristics are explored. They are distinguished by their level of shear, resulting in profiles that are quite different. A characterization of the conditions that were used to generate such profiles is shown in Table 4.2. We shall call them *low shear* and *high shear* profiles and such designation will be used from here on. Their aerodynamic surface roughness values are different (although in a counter-intuitive way), however, the main aspect that drives these profiles to be different is the overall velocity magnitude. A profile with an overall higher velocity will contain more shear and thus it is logical that even though such scenario had a lower surface roughness, the overall levels of shear present are higher.

Table 4.2: Parameters pertinent to the different neutral ABLs investigated.

Parameter	**Value**	
	Low shear	High shear
ref. wind speed (m/s)	15.1	21.5
ref. height (m)	50	80
wind direction (deg)	0	0
z_0 (m)	0.001	0.0002
velocity mag. at $\hat{z} = 1$ (m/s)	13.3	17.1

Figure 4.10 shows these profile in dimensional and non-dimensional form. Normalizing the data by the velocity at the reference height (see Table 4.2) yields comparable results. This is an important aspect to note since these profiles are *scalable*. That is, to go from a low shear to a high shear, a multiplication factor may be used. In a uniform inflow approach, such independency and scalability is present [1, 54] not only on the incoming inflow for obvious reasons, but also on the airwake solution. This aspect will be discussed later, but note that although the velocity profiles are in fact scalable, the airwake solution is not.

When it comes to these profiles and subsequent results, it is important to notice that normalization of data may highlight deficits that are inherent to the velocity profile shape. That is, lower heights experience a lower velocity, and thus a normalization by a "freestream velocity" is not always suitable, or, the definition of the "freestream velocity" should be clearly stated. Hence, for a lot of data related to a sheared profile, preferences are given to dimensional results.

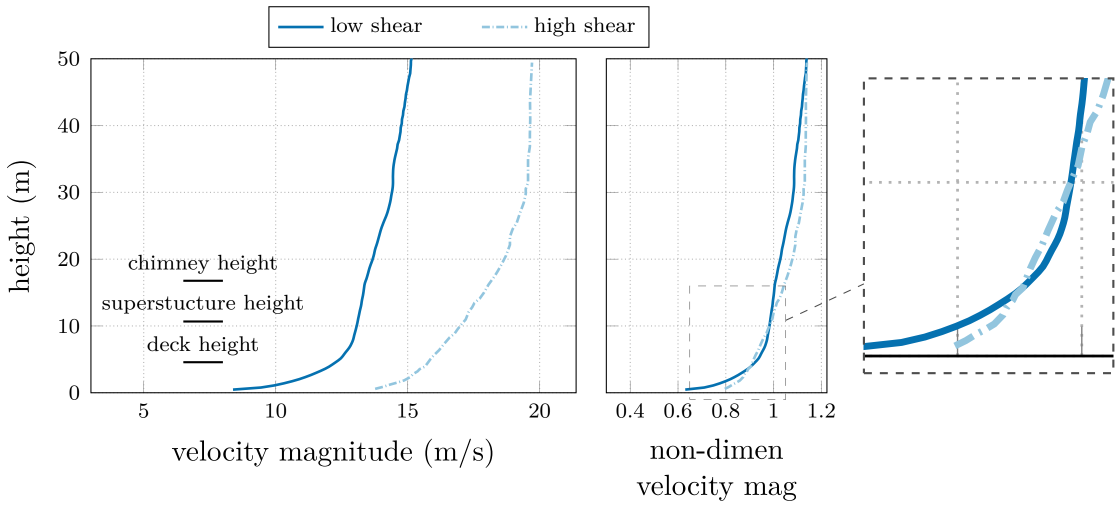

Figure 4.10: Time-averaged profile near the bottom part of the domain, within the inner-most refinement region. The plot shows the two different shear profiles investigated (see Table 4.2). The solid (low shear) curve is the same as the one in Fig. 4.18.

4.5 OVERFLOW and the Steady Velocity Profile

So far, the previous chapters have discussed a real atmospheric boundary layer and how to model it realistically in a numerical framework. The ship airwake community, however, refers to a so-called "steady ABL" approach. Such an approach, briefly described in section 2.8, is an inflow method which does not contain any freestream turbulence — that is, it is a laminar profile. The "ABL" aspect is that its curve resembles or matches a logarithmic profile, and has the general feature of lower heights having lower velocities. The use of quotes here refers to the fact that these are *not* an *atmospheric* boundary layer profile. They have the goal of representing a time-averaged velocity profile, but in a steady sense. The term "steady ABL" continues to be used. Quotes will be dropped from here on, but note the distinction and the fact that the steady ABL is a velocity profile and not a real ABL.

The steady ABL is investigated in an attempt to quantify the differences observed between a fully unsteady, real-world ABL and a turbulence-free ABL. This approach has been investigated using OVERFLOW (version 2.2n) [123], rather than OpenFOAM. The reasons for choosing a second CFD package are:

- It provides overall additional confidence in the results since it is a completely different package;
- Using a body-fitted approach provides further verification of the immersed boundary

method implemented in OpenFOAM;

- Comparison of body-fitted vs. IBM for the walls of the ship investigates findings by Shipman et al. [122], where it was reported that a boundary-layer-resolving grid did not improve results;
- OVERFLOW is a code that has undergone rigorous V&V efforts [124] and it is maintained by NASA;
- The author had access to the code and the opportunity to run very large cases on NASA's supercomputer.

On the downside, OVERFLOW is a compressible code and hence may exhibit numerical instabilities at Mach numbers below 0.2, which is the speed range of interest for this study. In this section, numerical aspects related to OVERFLOW and the development of the steady ABL profile are discussed.

4.5.1 Overview and Governing Equations

OVERFLOW is a finite-difference, three-dimensional time-marching implicit Navier-Stokes code [123]. OVERFLOW uses structured overset grid systems, created using Chimera Grid Tools (CGT) [125]. Similarly to OpenFOAM, OVERFLOW also provides a number of aspects of the computational setup that can be selected and/or adjusted by the user for a given application. These include the turbulence model, temporal discretization and time-stepping schemes, spatial discretization schemes, etc.

OVERFLOW internally only uses non-dimensional quantities. The form in which Navier-Stokes is treated within OVERFLOW is shown next, as at first it looks fairly different from the momentum equations shown for OpenFOAM. Let the Navier-Stokes equations be represented in the following form:

$$\frac{\partial U}{\partial t} = J - \frac{\partial F}{\partial x} - \frac{\partial G}{\partial y} - \frac{\partial H}{\partial z} \tag{4.6}$$

The term on the left-hand-side (LHS) contains the time derivatives, while the right-hand-side (RHS) contains the spatial derivatives. J is a source term (usually zero in the absence of body forces or volumetric heating). U, F, G, H, and J are as follows

$$U = \begin{bmatrix} \rho \\ \rho u \\ \rho v \\ \rho w \\ \rho\left(e + V^2/s\right) \end{bmatrix} \tag{4.7}$$

$$F = \begin{bmatrix} \rho u \\ \rho u^2 + p + \tau_{xx} \\ \rho v u - \tau_{xy} \\ \rho w u - \tau_{xz} \\ \rho\left(e + \frac{V^2}{2}\right) u + p u - k\frac{\partial T}{\partial x} - u\tau_{xx} - v\tau_{xy} - w\tau_{xz} \end{bmatrix} \tag{4.8}$$

$$G = \begin{bmatrix} \rho v \\ \rho u v + \tau_{yx} \\ \rho v^2 + p - \tau_{yy} \\ \rho w v - \tau_{yz} \\ \rho\left(e + \frac{V^2}{2}\right) v + p v - k\frac{\partial T}{\partial y} - u\tau_{yx} - v\tau_{yy} - w\tau_{yz} \end{bmatrix} \tag{4.9}$$

$$H = \begin{bmatrix} \rho w \\ \rho u w + \tau_{zx} \\ \rho w v - \tau_{zy} \\ \rho w^2 + p - \tau_{zz} \\ \rho\left(e + \frac{V^2}{2}\right) w + p w - k\frac{\partial T}{\partial y} - u\tau_{zx} - v\tau_{zy} - w\tau_{zz} \end{bmatrix} \tag{4.10}$$

$$J = \begin{bmatrix} 0 \\ \rho f_x \\ \rho f_y \\ \rho f_z \\ \rho\left(u f_x + v f_y + w f_z\right) + \rho\dot{q} \end{bmatrix} \tag{4.11}$$

In the equations above, u, v, and w are the components of the velocity vector and τ is the shear stress.

The turbulence model is where the two codes differ. In OVERFLOW, the 1-equation Spalart-Allmaras (SA) [126] model is used (in contrast to the k equation used in OpenFOAM).

At low speeds, the eigenvalues of the Navier-Stokes equations become widely separated and the equations become stiff [127]. Preconditioning is then used to scale the eigenvalues to remove this stiffness. Such scaling hurts the time accuracy and thus dual time stepping and additional sub iterations are deemed necessary. It is outside of scope of this dissertation to give the equations and derivations of the preconditioned set of equations and further discussions. More details about OVERFLOW can be found in reference [127].

4.5.2 Numerical Setup

Creating a steady ABL profile is not as trivial as one would think. The velocity gradient usually triggers turbulence and thus the steady aspect is no longer present. In this approach, the goal is to ensure that the velocity field experienced by the tip of the bow is the same as the one at aft portions of the ship. By doing so, effects of the presence of the ship and its airwake are isolated from a space- or time-varying inflow.

This section describes the methodology used to achieve a steady profile. For such, a delayed detached eddy simulation (DDES) framework has been used in the OVERFLOW simulations. DDES is a hybrid method in which RANS is executed in the laminar, attached layer, and LES elsewhere [128].

Computational Domain and Grid Generation Strategy

While the resolution of the grid is manually set in OpenFOAM by means of the refinement regions around the body, the approach is completely different in OVERFLOW. In this section, the strategy will be explained in detail, but essentially, the grids are manually created around the body. The resolution aspect here is not directly comparable. Both the methodology and the resolution aspect are described below.

There are two clear options of domains to be used. One is a relatively short domain, where the incoming inflow is specified as an inlet boundary condition, prescribing the velocity field. Another option is to use a very large domain, where the boundary layer is developed (grown) from a no-slip boundary condition. The second option is used here in this work.

A feature of OVERFLOW is that it only takes overset grids and the whole code is designed to properly handle them. The idea of overset grids arose from the need to model complex multi-component systems where an optimum body-fitted grid is used for each component. Overset grid is also convenient for simulations that include multiple bodies with relative motion (a spinning helicopter blade, for instance). In this work, the grids for the SFS2 have been manually generated using Chimera Grid Tools [125, 129]. By allowing arbitrary overlap between neighboring grids, each grid in an overset system can be generated independently from one another, where the focus can be on maintaining high grid cell quality such as orthogonality and clustering. Another advantage of overset grids is that one can remove a feature from the geometry without the need to regenerate the entire grid system. For instance, a full-configuration aircraft may be simulated and if another simulation without the engine pylons is needed, the task of creating a new grid is straightforward. The grid related to the pylon can be removed and the off-body grids will be appropriately generated to cover the empty space.

The problem examined here, however, does not require relative motion, nor does it have features that need to be removed in subsequent simulations. It is the OVERFLOW default, but, on top of that, it allows for building and modifying the grid system upstream the ship in an easy, independent way.

The grids are created by a `.tcl` script that calls functions within the CGT package. The script approach allows the grid to be re-built in a fast manner, as opposed to an application that resorts to a GUI. It is also convenient to make grid and parametric studies, since several parameters can rely on global variables.

The domain extends around 100 ship lengths into the far field. Six stages of grids surrounding the ship are manually created. Each stage has its own properties such as grid size, stretching ratio, and first cell size. These are the design variables with respect to the velocity profile. The goal is to generate a steady profile, and such sheared conditions usually trigger turbulence to develop. A general direction taken in this approach is that the inflow, up to about two ship heights, is within the boundary layer that grows from the bottom surface. This is achieved by 'tweaking' the cells in the six stages. The grid system developed is shown in Fig. 4.11, alongside the off-body grid automatically created in OVERFLOW.

It is interesting to note that the overset aspect is particularly useful in placing the ship and its near-body grids in the right position. The circular grids around the ship can be independently adjusted. The grids near the ship have higher resolution than the grids further away; however, resolution is not enough to resolve the turbulence and thus the flow is kept laminar. Figure 4.12 shows a detailed view of the overlap of some of the upstream grids. The different grid size can be observed.

The near-body grids were created such that the $y+$ value has been kept below 1. As mentioned, one of the goals of using a body-fitted wall-resolving approach is to further verify a previous study by Shipman et al. [122]. The near-body grids overlapped with automatically-generated off-body grids with two fringe points to ensure proper

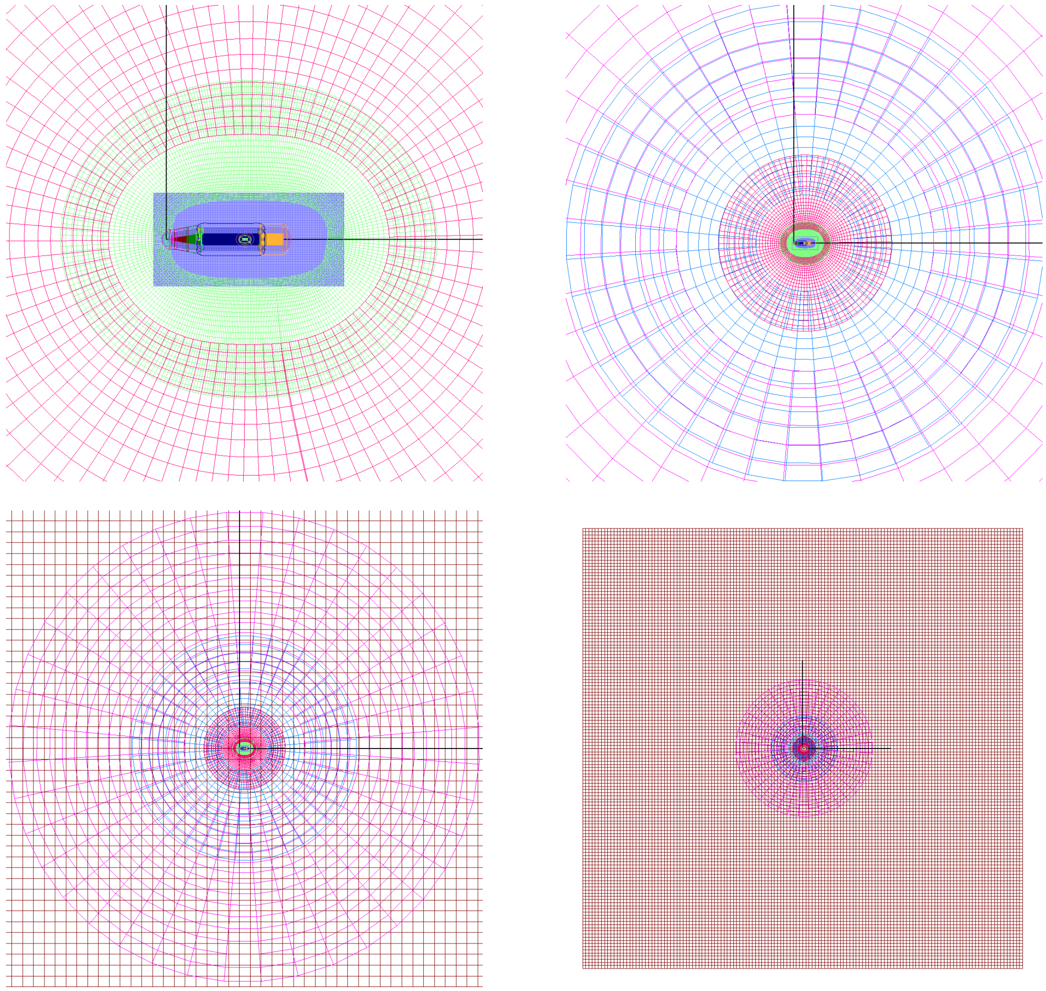

Figure 4.11: Top view of the overset grid system used to generate the steady ABL profile. The domain extends about 100 ship lengths to each direction.

second-order transfer of information. Additional grids have been created around the airwake region itself — see Fig. 4.13. The nature of overset makes this a very easy step.

The grid system near the ship is also manually created within CGT. The total number of near-body grids is 21 — see Fig. 4.14. The very tip of the bow required special attention. The original SFS2 geometry has an infinitely sharp bow, and heavy cell clustering would be necessary to model it without creating a singularity point in the mesh. To circumvent this issue, the tip has been rounded. Note, however, that the length of the bow has only been reduced by 1%. This is also illustrated in Fig. 4.14.

So far, the resolution of the near-body grids are not constant and because of their wall-resolving feature, direct comparisons with OpenFOAM grids cannot be made. However, additional grids are created around the airwake region itself (Fig. 4.13). The nature of

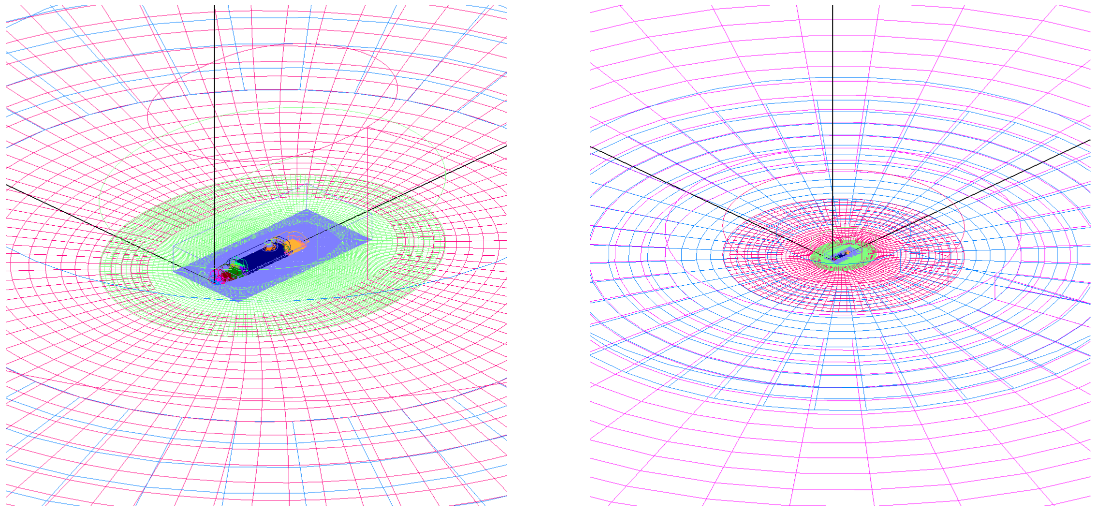

Figure 4.12: Details of the round circular surrounding the ship at two zoom levels.

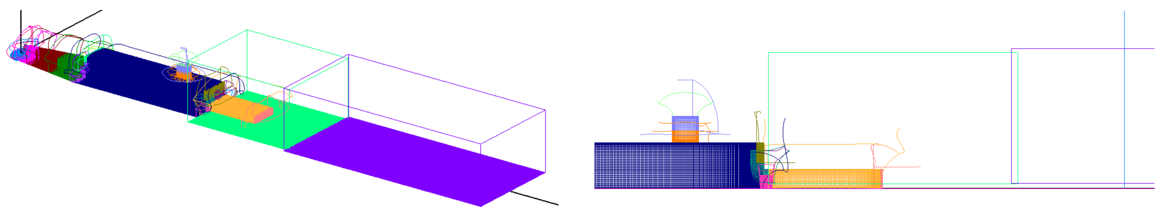

Figure 4.13: Detail of the grids system designed to capture the airwake, shown in green and purple. Another image is shown in Fig. 4.14.

overset grids make this a very straightforward step. These airwake grids are created with uniform resolutions for two reasons: (i) to make sampling of data in OVERFLOW easier; and, most importantly, to have a set constant resolution that is comparable. The resolution of the airwake grid created closest to the ship is twice the resolution of the one used in OpenFOAM. Here, cells are about 0.5 ft in size, whereas in OpenFOAM they are about 1 ft in size (aspect ratio roughly 1 for both codes). A proper grid study has been performed in OpenFOAM and will be presented in section 5.2. There are two reasons for using different grids: (i) grid study in OpenFOAM did not indicate appreciable differences going from 1 ft to 0.5 ft; and (ii) the availability of computational resources.

Initial and Boundary Conditions

The domain strategy described in the previous section was preferred also because of the simplicity encountered in setting the appropriate initial and boundary conditions. As it has been discussed, the profile has been developed by the non-slip boundary condition at

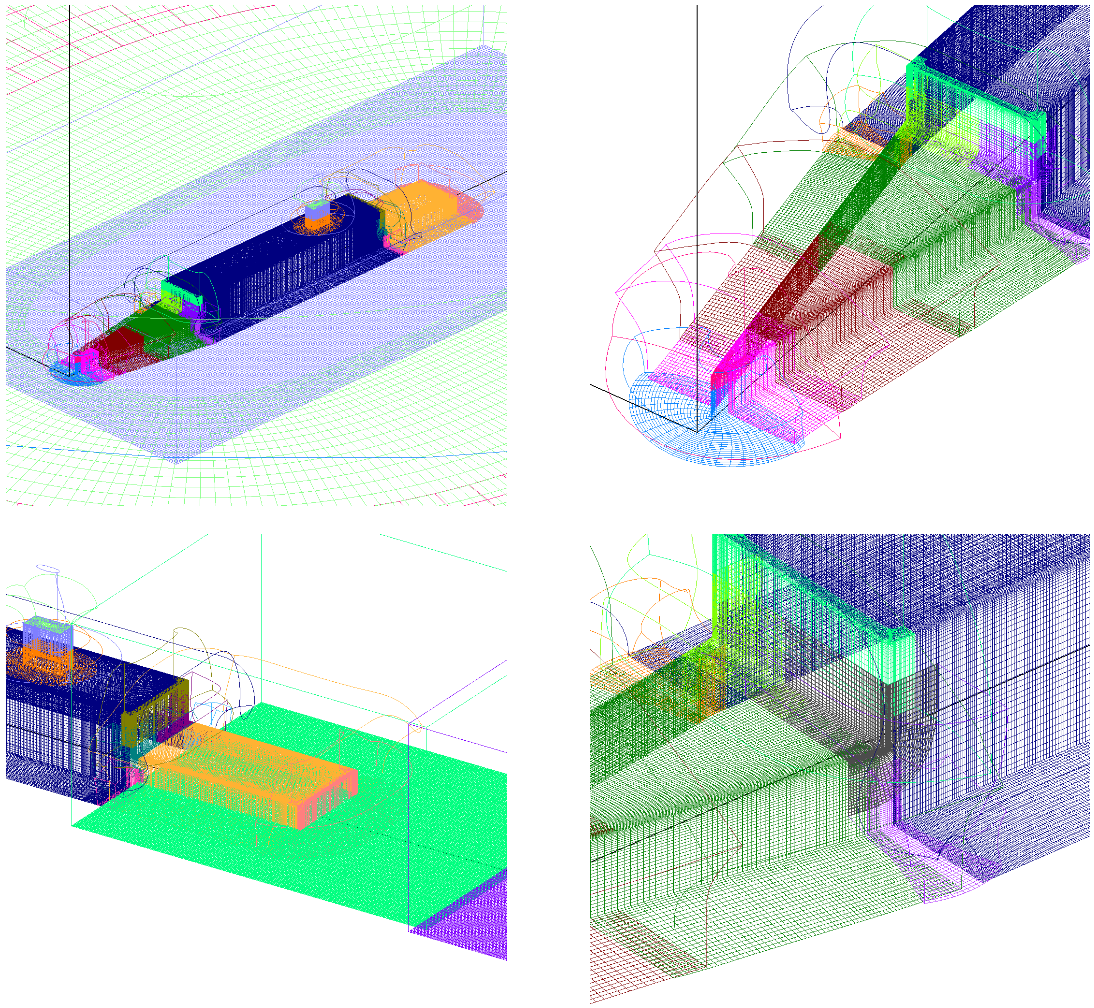

Figure 4.14: SFS2 near-body overset grid system. There are 21 near-body grids. Details shown include the rounded tip of the bow (the original tip was at the origin shown), deck and part of the wake grid, and how extra patches were designed to cover saddle points in the geometry.

the bottom surface, rather than specified as a boundary condition.

The boundary conditions are trivially set. The inlet, outlet, and side walls have a characteristic outflow condition based on Riemann invariants with freestream imposed on incoming characteristics. This boundary condition is the clear choice within OVERFLOW. The freestream Mach number is set in a way such that the desired velocity is obtained at the desired height (more on that in section 4.5.3). The bottom of the domain (the "sea floor") and the SFS2 walls have a no-slip boundary condition (viscous adiabatic wall with pressure extrapolation).

Discretization Schemes and Solution Methods

The numerical schemes are set in OVERFLOW with respect to the RHS and LHS of Eq. (4.7). They are selected as central difference for the right-hand-side terms, and OVERFLOW's default ARC3D diagonalized Beam-Warming scalar pentadiagonal scheme for the left-hand-side. Both schemes amount to second-order accuracy. Second-order time-advance is also set. The overset grids are also designed such that double fringe points overlap are ensured in connections between grids, keeping second-order accuracy in space. In save/restart operations, two steps are also saved, again, to ensure second-order accuracy in time in case of a restart.

As mentioned, OVERFLOW is a compressible code, so that additional care needs to be taken when running a very low Mach number. As the objective was a relatively low velocity at the reference height (the ship height, 35 ft), low-Mach preconditioning needs to be used. low-Mach preconditioning, however, can be tricky as convergence becomes a problem and more iterations are necessary for the residuals to drop, which, in turn, increase the computational cost.

Within each time step, 20 Newton subiterations are used. From experimentation, it was found that 20 was enough for the residuals to drop at least two orders of magnitude. A constant time step is used, as opposed to local time-step scaling, as the latter was found to be overly diffusive and not appropriate for highly unsteady flows. This amounts to a dual time stepping procedure. Dual time stepping is used to improve the accuracy of unsteady simulations, and can also improve the robustness of steady or unsteady simulations. The sub-iterations improve the solution accuracy near interpolated and extrapolated boundaries and also reduce the global solution error at a given time step [127]. Dual-time-step is also recommended for simulations that use low-Mach preconditioning.

OVERFLOW is executed in DDES mode, with no compressibility correction. Such mode is convenient for the current goal as the incoming flow will be within the boundary layer and thus in laminar flow. As far as execution goes, the grid is first executed in RANS mode, that is then used as initial condition for the DDES simulation. The first 40 s of simulated time are not considered due to the start-up and transient of the wake.

4.5.3 Development of Steady ABL Profiles

The approach used in this part of the work is to grow the boundary layer by making use of the grid and different scales involved in the problem. With this approach, the resulting shape of the profile depends quite significantly on the freestream velocity (or, in

OVERFLOW context, the Mach number) and the $y+$ of the grids surrounding the ship model. The aspect of an under-resolved wall boundary layer results in different velocity profile shapes. This section quickly shows some of the design parameters that could be used to achieve the desired profile and how the final profile was obtained. A discussion of the final profile and how it compares with the unsteady OpenFOAM simulations is given in the next section.

OVERFLOW is being executed in DDES mode and upstream the ship, the model switches to RANS. In such region, the entire flow is laminar and thus stays in RANS mode and the lack of proper LES-like grid forces the flow to remain laminar. The overset grid aspect is convenient because the ship can be placed anywhere with respect to the incoming boundary layer.

The shape of the velocity profile can be tweaked by changing some parameters. One of them is the velocity, investigated in Fig. 4.15. The effects of varying the freestream velocity, while keeping the stretching ratio constant, are investigated. This figure shows that the higher the freestream velocity, the more shear the profile presents. In these cases, however, the velocity magnitude at the superstructure height is considerably higher than a realistic ship speed of about 25 kn.

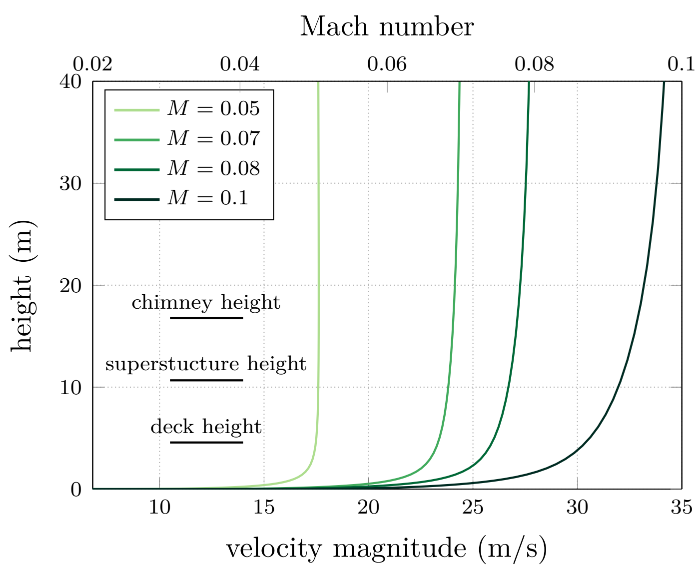

Figure 4.15: Profiles obtained in OVERFLOW with a stretching ratio of 1.2 without low-Mach preconditioning, with different Mach numbers as the freestream velocity. Note how higher levels of shear are present in cases with higher velocities. Also, note the top velocity scale in Mach, and how the profiles converge to the free stream value at higher heights.

The other design variable for obtaining the desired profile is the stretching ratio (SR).

That refers to how fast the RANS-like cells grow from the surface. A stretching ratio of 1.2 is usually recommended. Figure 4.16 shows the effect of increasing the stretching ratio, keeping the freestream Mach number constant.

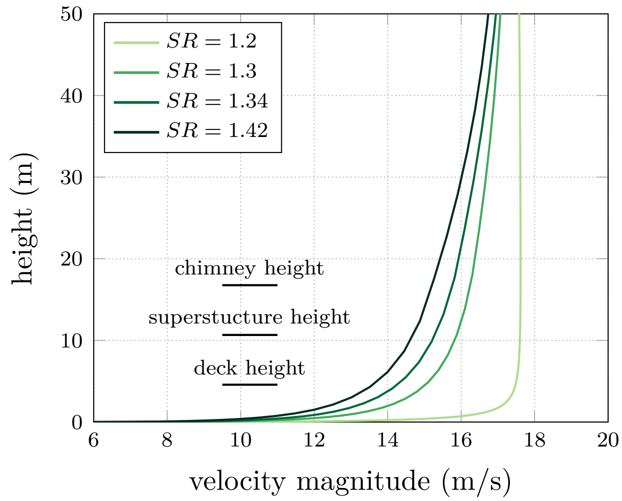

Figure 4.16: Profiles obtained in OVERFLOW with varying stretching ratio for $M = 0.05$.

It is acknowledged that a very large stretching ratio is not a good practice in capturing walls in RANS models. However, here, the interest lies in the shape of the velocity gradient curve. This approach creates the boundary layer by under-resolving the wall.

Analyzing Figs. 4.15 and 4.16, it is evident that a lower velocity is needed (closer to the light green curve of Fig. 4.15), while a higher SR is required, such that the curve approaches the dark green curve from Fig. 4.16. An issue with getting lower velocities has to do with the nature of OVERFLOW. The compressibility aspect of OVERFLOW warrants the use of low-Mach preconditioning for such low Mach numbers. The profiles presented in Figs. 4.15 and 4.16 were obtained without the use of low-Mach preconditioning within OVERFLOW.

It was found that the use of the low-Mach preconditioner modified the shape slightly[2]. Figure 4.17 compares a profile obtained with and without the use of the preconditioner within the solver. It can be noted that the dark green curve ($M = 0.05$, $SR = 2.4$, with low-Mach preconditioning) has a velocity magnitude close to the desired one at the reference height. Finally, the freestream Mach number is adjusted — to $M = 0.048$ — and the curve shown in dashed blue is the final profile. This curve is repeated in Fig. 4.18

[2]It should also be noted that low-Mach preconditioning is necessary in this problem. The investigation of profiles without its use had the purpose of understanding the effect of the design variables on the velocity profiles.

and compared to a analytical logarithmic curve and OpenFOAM results in the following section.

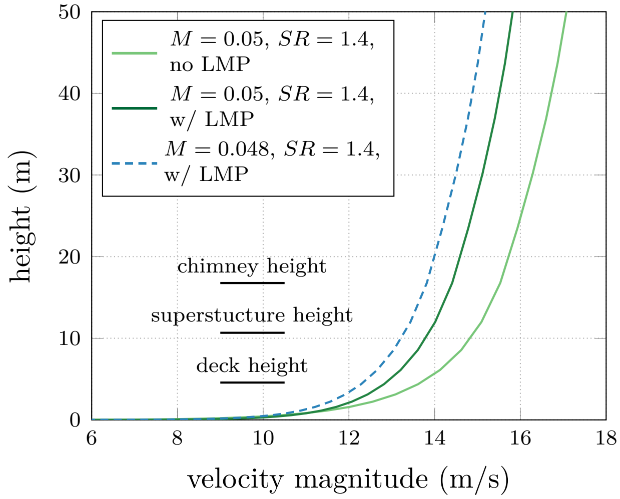

Figure 4.17: Profiles obtained in OVERFLOW, investigating the effect of low-Mach preconditioning (LMP). The final profile used for the rest of this work is shown in dashed blue.

4.6 The Scenarios Investigated and Concluding Remarks

A general difficulty in comparing different codes or even different modeling approaches for the ABL is to make sure they are similar enough to be comparable. On top of that, the profiles have to be similar to an analytical curve, such as a logarithmic with the appropriate $-z_i/L$ and z_0 values, or a power-law.

In this context, given the profile development method in OVERFLOW, there was minimal room to modify the amount of shear present in the steady profile. Thus, the task of having a comparable profile reduces to obtaining a similar shape in OpenFOAM from the one in OVERFLOW. In order to do so, many cases were executed, in the quest for the right surface roughness. Such procedure has been described in section 4.4.

The final profiles that will be investigated further with coupled flight dynamics are shown in Fig. 4.18. The time-averaged velocity profiles shown were sampled at about 0.1 L_{SFS2} upstream of the bow.

A description of the profiles is given below:

Uniform A simple constant-velocity profile, executed in both codes. Used for benchmarking and wind tunnel comparisons.

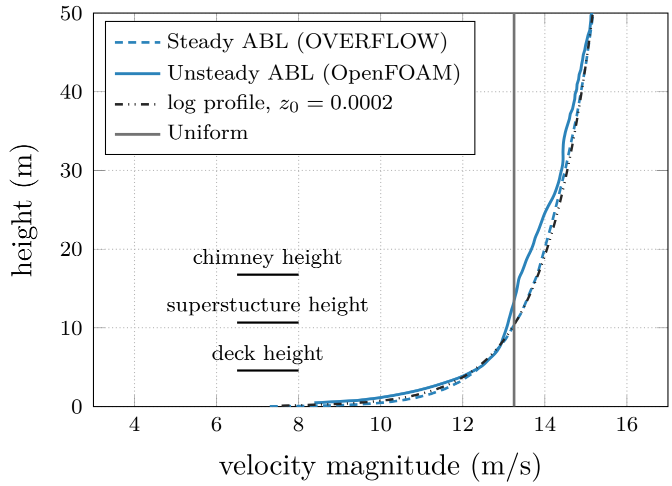

Figure 4.18: Time-averaged velocity profiles for the incoming wind, alongside theoretical logarithmic profile. Height of the ship's main structures shown for reference.

High shear unsteady ABL A fully unsteady ABL simulation, executed in Open-FOAM. High shear is achieved by a high wind speed.

Low shear unsteady ABL A fully unsteady ABL simulation, executed in OpenFOAM. Low shear is achieved by very low aerodynamic surface roughness and moderate wind speed.

Low shear steady ABL A steady velocity profile, executed in OVERFLOW. The flow upstream the ship is completely steady and this scenario does not include freestream turbulence or any shear and buoyant effects from a real atmosphere. Comparable to the unsteady low shear described above.

The wake results for the cases listed above will be explored in the next chapter.

Chapter 5
Characteristics of the Modified Turbulent Airwakes

In this chapter, airwake results are presented and discussed. Here, the results are limited to the airwake flow topology characteristics and unsteadiness. This chapter evaluates the differences between the three categories of inflow investigated: (i) uniform, (ii) unsteady ABL, and (iii) steady ABL. These differences are evaluated from a time-averaged and time-accurate perspective.

With respect to the stability state, although the framework used in this work is general, only neutral cases have been investigated. Such cases represent a conservative approach, since it is the case with the lowest level of turbulence - recall Fig. 3.2. Only flow aligned with the ship has been investigated (zero degrees WOD). These cases are conservative and simple, since the objective is to develop an understanding of the various aspects of a ship airwake in the context of the ABL.

5.1 Overview

Similarly to the discussion in chapter 1, the previous studies can be separated into three major categories: computational, experimental, and in situ. The interest lies in the comparison of results and validation by the execution of similar runs (that is, uniform inflow). In order to do so, the wind tunnel and CFD studies selected follow the obvious choice of those in which the SFS2 geometry was considered. In situ measurements, on the other hand, are obtained with a variety of real-world aircraft carriers and they are used in qualitative comparisons of energy spectral density.

All of the results presented in this work are time-accurate. It is noted that is has been reported that time-averaged time-accurate solutions can exhibit different features as opposed to a pure steady-state RANS solution; also, steady-state solutions do not compare as well with experiments as time-averaged time-resolving results [1].

Results in this section are presented and compared with respect to eight probe $x - y$ locations on the flight deck, designated by A–H — see Fig. 5.1. These locations were originally used in the work of Rosenfeld et al. [38], which is used for CFD model validation.

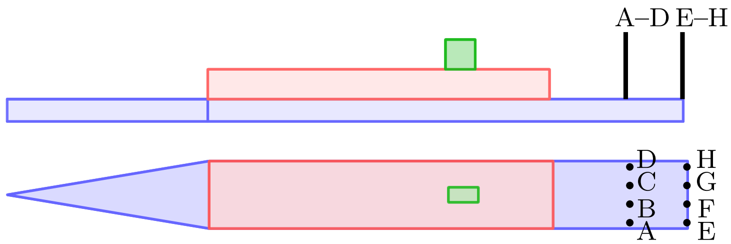

Figure 5.1: Probes A–H location with respect to the SFS2. Exact location of probes, as well as experimental results are available in [38]. This set of probes is investigated in this chapter.

The velocity profiles over the eight probe locations shown in Fig. 5.1 are presented throughout this chapter in terms of a non-dimensional height $\hat{z}$. A non-dimensional height $\hat{z}$ is defined as $\hat{z} = z/H_h$, where z is the height starting from the rear deck floor and H_h is the superstructure height over the rear deck ($H_h = 20$ ft, see Fig. 1.3). By definition, the flight deck surface is at $\hat{z} = 0$, and the top of the superstructure is at $\hat{z} = 1$ — see Fig. 5.2. Velocity is presented in both non-dimensional and dimensional form.

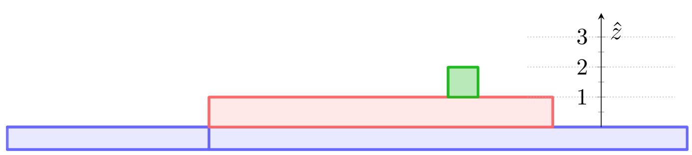

Figure 5.2: Sketch of the non-dimensional scale $\hat{z}$ used for height. The scale starts at the deck floor and is normalized by the height of the superstructure (20 ft).

First, a grid study is presented, following the early grid strategy discussions with respect to the number of refinement regions (section 4.2.1). Next, additional validation of the IBM and general setup used are carried out using uniform-inflow cases, comparing to wind tunnel results and previous CFD efforts. Lastly, comparisons of ABL and uniform inflow cases are performed to develop an understanding of the influence of the ABL on the airwake. Here, power spectral density plots are presented and better agreement with in situ data is observed.

5.2 Grid Resolution Study

The unsteady ABL approach is more complex with respect to domain and grid considerations. Here, a grid study is performed within OpenFOAM. In this study and throughout this section, the meshing strategy described in section 4.2.1 has been adopted. Here, however, the focus is on the grid resolution aspect.

The resolution required near the flight deck to capture essential flow features such as recirculation and turbulent shedding from the ship superstructure is evaluated. Starting with the 10 m resolution background mesh, three different resolutions and nesting options are investigated with respect to their velocity profile at probe locations A–H. These three meshing configurations are shown in Table 5.1.

Table 5.1: Grids investigated within OpenFOAM.

	Grid A	Grid B	Grid C
Refinement zones	6	5	4
Cells per ship beam	88	44	22
Near-deck resolution (m)	0.16	0.31	0.62
Total cell count (millions)	100+	20–30	2–4

The present meshes shown in Table 5.1 are of higher resolution than previous works (e.g. [26]), because (i) the intention is to capture high-frequency content, and (ii) this research is laying out the foundations necessary for fully-coupled methods in which an actuator disk model representation of a helicopter rotor would be included, thus needing more resolution. A related point to consider is that the mesh resolution aspect is often seen as an open problem in the ship airwake community. Many argue that resolutions such as the ones presented in Table 5.1 are not able to capture small scales that are relevant to the problem. The issue is that no high-quality unsteady dataset exists in order to perform an unsteady comparison, and as far as time-average quantities go, relatively coarse grids are able to capture the important features. Perhaps also of importance is that such problems are physically big — ships are often hundreds of feet long —, which results in the need of very large computational resources, often not feasible and/or readily available. Finally, considering the fact that the CFD computations will be used for flight dynamics analysis, quantities are usually integrated over the span of the blade, which can be argued that very small scales are not relevant anymore. This discussion of grid resolution is acknowledged, yet due to the time- and length-scales of interest, resolutions presented in Table 5.1 are considered appropriate.

Results of the grid study are presented in Fig. 5.3. This type of plot will be explored a few times, so it warrants some additional explanation. Each of the sub-plots refer to one of the Profiles A to H. Velocity data is time-averaged and shown normalized by the freestream velocity, while the height starts at the flight deck and is normalized by the height of the superstructure (scale $\hat{z}$). Analyzing the results, it is apparent that all three grids captured the same character, but the near-surface region displays a mesh sensitivity, possibly due to the immersed boundary method. Of perhaps great concern is the recirculation region in the near-wake of the backward-facing step, i.e., $\hat{z} < 0.5$ for Profiles B and C, as they display the largest deficit. The centerline-symmetric pair of profiles A and D exhibited the largest sensitivity to mesh resolution. Note that, similarly, wind tunnel experiments at the same WOD but varying Reynolds number also showed increased sensitivity with this pair [38] as will be shown in the next section. It is hypothesized that the Profiles A and D sensitivities observed both experimentally and numerically are due to flow asymmetries (reported by [20, 26] and also identified in this study as will be shown later). In terms of comparing results from Grid B and Grid C, Grid C exhibited too much deficit at heights $\hat{z} < 0.3$, even though it captured contents well at higher heights. In grid C, one of the drawbacks of the IBM can be seen at the lower values of $\hat{z}$. When it comes to Grid A and Grid B, even though Grid A has a significant increase in computational cost, its impact on the solution was minor,

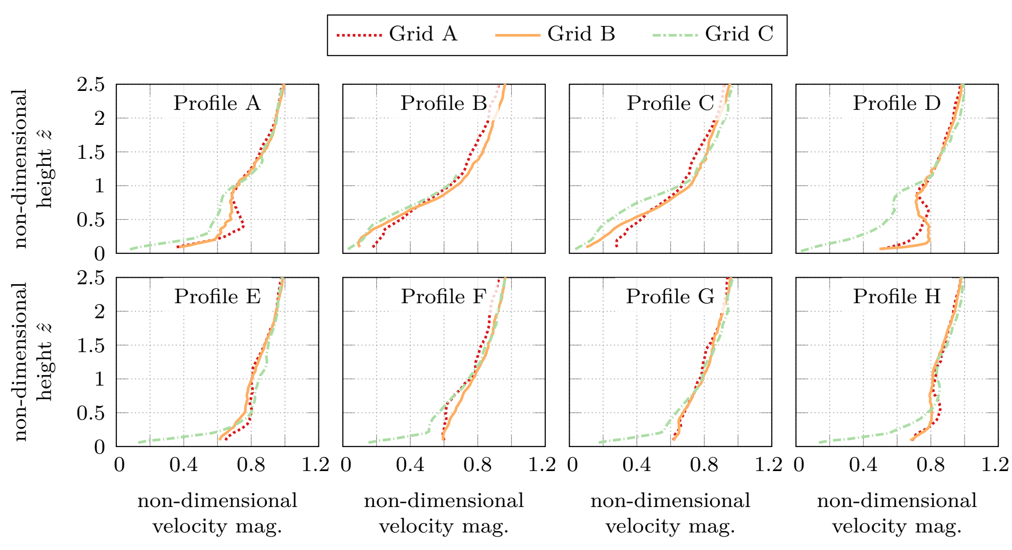

Figure 5.3: Time-averaged velocity magnitude profile on the deck (see Fig. 5.1) for three different near-deck resolutions: Grid A, 0.16 m; Grid B, 0.31 m; Grid C, 0.62 m. Uniform inflow at $Re_L = 1.6 \times 10^8$.

reaching a mesh insensitivity stage. For the remaining analyses, Grid B is used. Grid B captures high-frequency content that Grid C lacks, though at a much lower computational cost than Grid A. Thus, Grid B was selected and will be used for all of the subsequent OpenFOAM simulations — it provides adequate spatial resolution and allows reasonable turn-around time, while maintaining sufficient temporal resolution.

As previously mentioned, the initial transient of the wake has not been considered in the time-averaged computations. For uniform inflow applications, such time is shorter than ABL inflow, since only the wake start-up is disregarded, as opposed to the atmospheric development through new grid-resolving resolutions. All of the presented results considered similar convective time scales for proper time-averaging of the data. In terms of choosing a freestream velocity for these studies, a velocity that represents the Reynolds number of a full-scale aircraft carrier with wind speeds of roughly 33 kts was used — the result is a full-scale SFS2 with a Reynolds number of $Re_L = 1.6 \times 10^8$, where the subscript L represents a Reynolds number based on the ship length.

Moving forward, the general setup for all of the OpenFOAM cases presented from here on are based on grid type B. Numerical schemes and setup numerical parameters are used as described in section 4.2. A Reynolds number investigation is shown next.

5.3 Reynolds Number Study & Initial Model Validation

It has been noted before in references [1, 54] that the airwake flowfield structure does not change much when varying the wind speed. This statement was made for the LHA ship, under a uniform-inflow condition and with wind speeds of 15 and 30 kts. The flowfield at 15 kts has been reported to be essentially the same flowfield at 30 kts, except that it is moving at half the speed. Zero degrees WOD scenario was also investigated, observing flow reattachment and near-field wake characteristics. These studies concluded that based on this Reynolds independency, the solutions could be scaled. It was noted, however, if the speed is scaled too high, compressibility effects will corrupt the solution. Similarly, as the speed approaches zero, the flow will look very different from that at 15 kts.

In this section, a similar study to that of the references mentioned is performed. The idea is to further verify such finding for the SFS2 geometry, but also to be able to scale experimental data in order to compare to simulations performed here. Regarding the experimental data used to validate uniform inflow, results were acquired by the U.S. Navy at the Naval Surface Warfare Center — Carderock Division (NSWCCD) [38].

The NSWCCD 8' × 10' ft. subsonic wind tunnel is a general-purpose, continuous-flow, closed-circuit facility. The experiment investigated impacts of Reynolds number, blockage, and wall effects on wind loads and airwake in the context of experimental practices.

This experiment is of interest as the effort investigated a range of conditions useful for validation. Specifically, the experiments investigated a number of different conditions resulting in different Reynolds numbers with respect to the ship length. Particularly, they investigated three SFS2 models, a number of wind speeds, and relative wind heading. In this work, data associated with a headwind, 1:50 scale model at 60 knots wind speed case, is used. Considering that the full-size SFS2 geometry is used in the simulations, this case is selected as it provides the highest Reynolds number among the cases investigated, i.e. $Re_L = 5.9 \times 10^6$.

These experiments collected velocity data at several points in the aft portion of the ship. Flow data were measured using Aeroprobe five-hole Fast Response Probes (FRP) with 2.4 mm tips. The FRPs were mounted on a vertical traverse and were oriented with the tunnel freestream. Data were recorded at 2 kHz over 8 s and averaged at the eight locations illustrated in Fig. 5.1. Such data are to be used for validation of the details of the velocity field prediction.

A summary of the cases investigated as a initial model validation is shown in Table 5.2. For a more direct comparison, a case matching the experiment's Reynolds number of $Re_L = 5.9 \times 10^6$ (Case 1) is executed. Then, a full-scale Reynolds number of $Re_L = 1.6 \times 10^8$ is executed using both uniform and ABL approaches — this Reynolds

Table 5.2: Summary of the cases executed and the NSWCCD experiment [38] used for comparison.

	Previous study	**Present effort**		
	NSWCCD	Case 1	Case 2	Case 3
Type	Experim.	CFD (LES)	CFD (LES)	CFD (LES)
Inflow	Uniform	Uniform	Uniform	ABL
$\mathbf{Re_L}$	5.9×10^6	5.9×10^6	1.6×10^8	1.6×10^8
WOD	0 deg	0 deg	0 deg	0 deg
Scale	1:50	Full-scale	Full-scale	Full-scale

number represents a full-scale ship moving at around 33 kts. Results from the uniform inflow solutions are shown in Fig. 5.4.

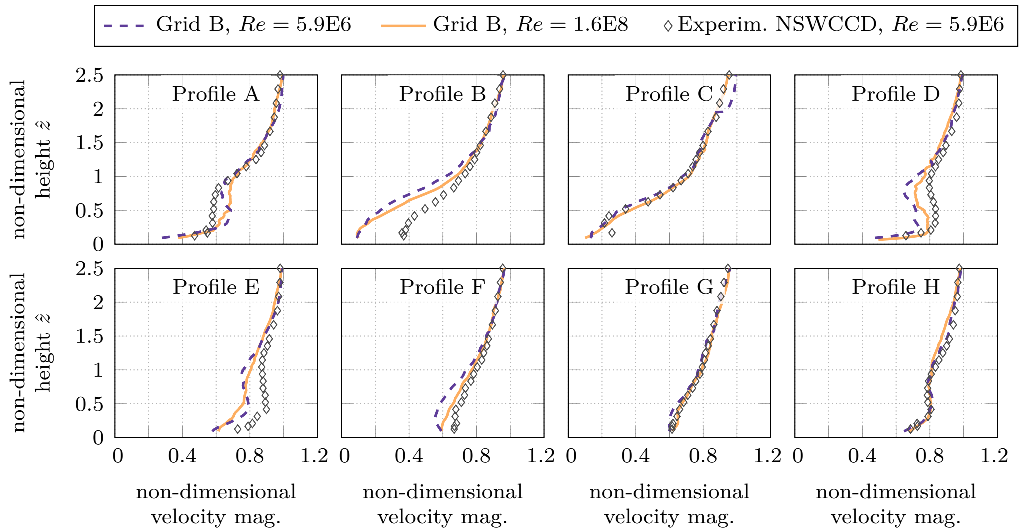

Figure 5.4: Mean velocity magnitude profile comparison at different Reynolds numbers and NSWCCD wind tunnel data for uniform inflow. For probe locations and non-dimensional height see Fig. 5.1 and 5.2.

With respect to the comparison shown in Fig. 5.4, general trends have been captured. Again, the pair of profiles A and D showed the large deviations from the experiment and also the largest deviations from one Reynolds to another (although small). In Profile B, the same can be observed; however, note that the results captured on Profile B match well experimental results from the centerline-symmetric Profile C. The same can be said about Profile E, and experimental results from Profile H. The results are considered acceptable because the deviations found for each individual profile are within the deviations observed in the experimental centerline-symmetric profiles. This aspect indicates that although the flow seems to be symmetric, some asymmetry is being observed and the profiles seem to be sensitive to it.

It is noted that the velocity in profiles A–H shown up to here were presented in non-dimensional form. This also allowed for the investigation of the Reynolds number independency by varying the flow velocity in the CFD setup and present it in a compact way. Moving forward, results will be shown in dimensional form. The scaling analysis enables the scaling of the experimental results to the freestream velocity desired for comparison purposes. Presenting the velocity in a dimensional form is a preferred choice because of the underlying profile. We will come back to this discussion soon. Next, after establishing this independency for the velocity investigated, uniform inflow solutions from OpenFOAM and OVERFLOW are compared. The general setup of the OVERFLOW simulations has been described in section 4.5.2. The dimensional results are presented in Fig. 5.5. The freestream velocity used for the cases presented in this figure is around 26 kts (about 13.3 m/s), which represents yet another Reynolds number. This velocity matches the velocity of the ABL at the reference height and thus it was selected (recall Fig. 4.18).

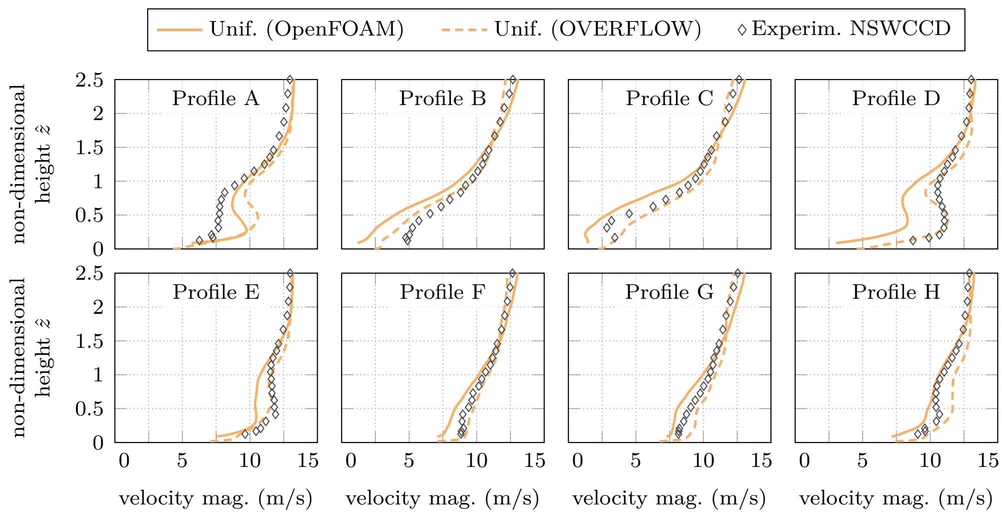

Figure 5.5: Time-averaged velocity magnitude on the deck (locations A–H, see Fig. 5.1) when subject to uniform inflow scenarios. The non-dimensional height scale is such that it is zero on the flight deck and is normalized by the height of the superstructure (20 ft).

Considering results from Figs. 5.4 and 5.5, there are a few conclusions that can be drawn. First, considering the two sets of plots, the CFD findings for the three different Reynolds numbers investigated are similar. Such a finding is consistent with the findings of Polsky [1, 54] and Buchholz et al. [47] discussed earlier, but also with those of Forrest et al. [20], where it was mentioned that the flow over bluff-body structures consisting of rectangular surfaces and sharp edges is insensitive to Reynolds number in this Re range. According to the findings shown, within a Reynolds number range of 5–200 million, the wake in a time-averaged sense appears to be Reynolds number independent, at least on a uniform-inflow setting. When it comes to Fig. 5.5, the largest deviations are found for the mid-deck profiles A–D, with the largest being, again, on the pair A and D.

Next, the asymmetry present in the flowfield should be noted. Upon closer inspection, experimental profiles that should be perfectly symmetric are not — compare results from profile pairs A/D, B/C, and E/H. The deviation of uniform-inflow results observed between OVERFLOW and OpenFOAM are within the experimental deviation of symmetric profiles. The differences observed between OpenFOAM and OVERFLOW may be due to the turbulence model and how it treats the dissipation of sub-grid scale quantities. Lastly, an additional aspect of the differences that is found at very low $\hat{z}$ is that the approach taken by both OVERFLOW and OpenFOAM is different with respect to resolving the wall. The OVERFLOW body-fitted approach is expected to better resolve the flow in that region as opposed to the immersed boundary implementation on OpenFOAM. However, such region is not critical for the accurate representation of the airwake [122]. The reader is reminded that the flow is already highly turbulent and separated at the deck. In view of the arguments presented, the uniform inflow scenarios are considered adequately resolved, as all profiles present good general agreement with experimental data.

At this point, qualitative comparisons of the overall flowfield are discussed with respect to the particle image velocimetry (PIV) measurements of the flow over the SFS2 model in a uniform inflow. In the context of ship airwakes, similar comparisons had been previously performed by Polsky [1]. As mentioned, in this study it was found that steady-state solutions do not give the same results as time-averaged time-resolving solutions, and also that steady-state results do not compare nearly as well to experiments as time-averaged time-resolving results. In light of that, consider flow visualization of the time-average of a time-accurate quantity, where results are compared to the experiment in Figs. 5.6 and 5.7. The CFD solutions and experimental measurements have several features in common that include (i) the bubble on the top of the superstructure and its size; (ii) the size of the recirculating region behind the funnel; (iii) and the flow around the flight deck.

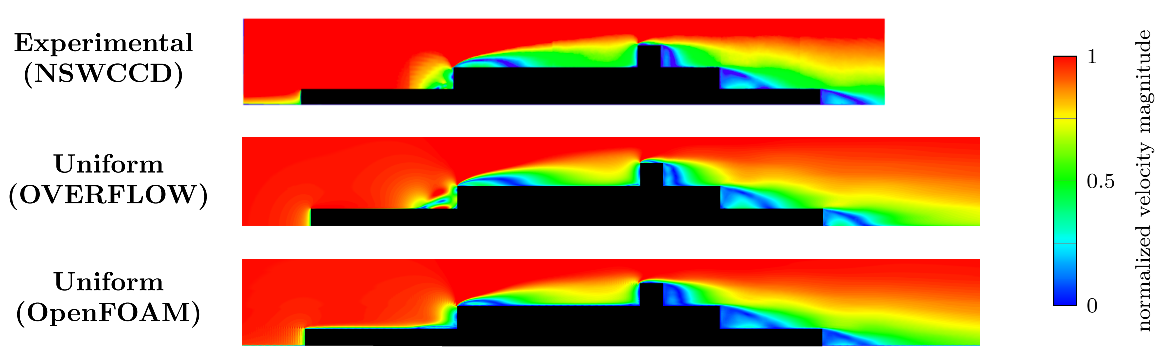

Figure 5.6: Time-averaged time-accurate uniform inflow solutions from OpenFOAM and OVERFLOW in comparison to experimental data from NSWCCD [38] along the centerline of the SFS2. Note the non-dimensional velocity scale.

In Figure 5.7, the comparison of the time-accurate CFD solutions and experimental PIV measurement (both time-averaged) is extended to a plane perpendicular to the flow and halfway through the deck. In this figure, the flow asymmetry pointed out earlier is clearly apparent for the OpenFOAM case. Such flow asymmetries were also previously observed in experimental results reproduced here from [130] and other CFD approaches [20, 26]. Despite the symmetric configuration of the experimental and numerical setup, it is not clear what triggers such asymmetry. Although only a single wind-over-deck angle was benchmarked, which is not sufficient for complete validation, the results do give confidence to extend to the ABL for similar geometric conditions.

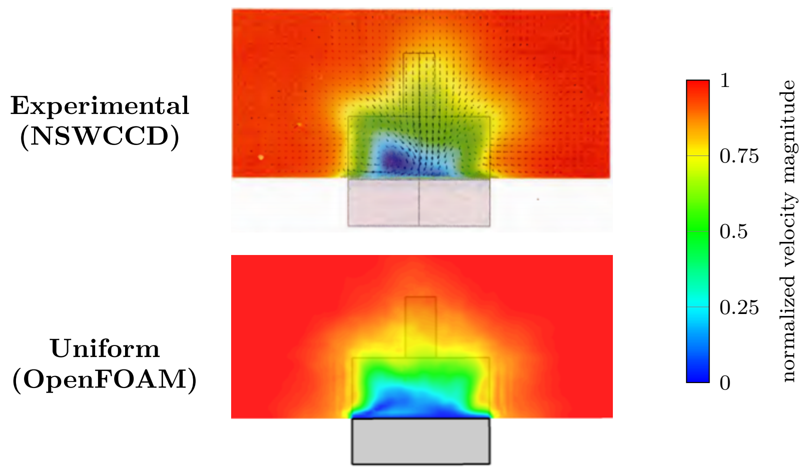

Figure 5.7: Time-averaged time-accurate uniform inflow solution from OpenFOAM in comparison to experimental data from NSWCCD [38] at mid-deck. Note the non-dimensional velocity scale.

This section is finished by pointing out the additional validation on the IBM method. Although the IBM method has its drawbacks when it comes to resolving walls and capturing forces or pressure distributions, it is nonetheless a good choice for a problem where the interest lies in the wake. Comparisons with body-fitted grids created in OVERFLOW did not show appreciable differences.

5.4 Uniform Inflow vs. Unsteady Atmospheric Inflow

The study is now directed towards the understanding of the influence of the ABL. Specifically, this is evaluated through time-accurate simulations by comparing the wake topology and flow characteristics of the SFS2 under uniform and fully-resolved turbulent ABL inflow conditions.

5.4.1 Quantitative Comparison

Following the discussions in section 4.4 about the two levels of shear, this section looks at the results obtained with the two profiles shown in Fig. 4.10. The resultant dimensional time-averaged velocities at the same A–H profiles are shown in Fig. 5.8.

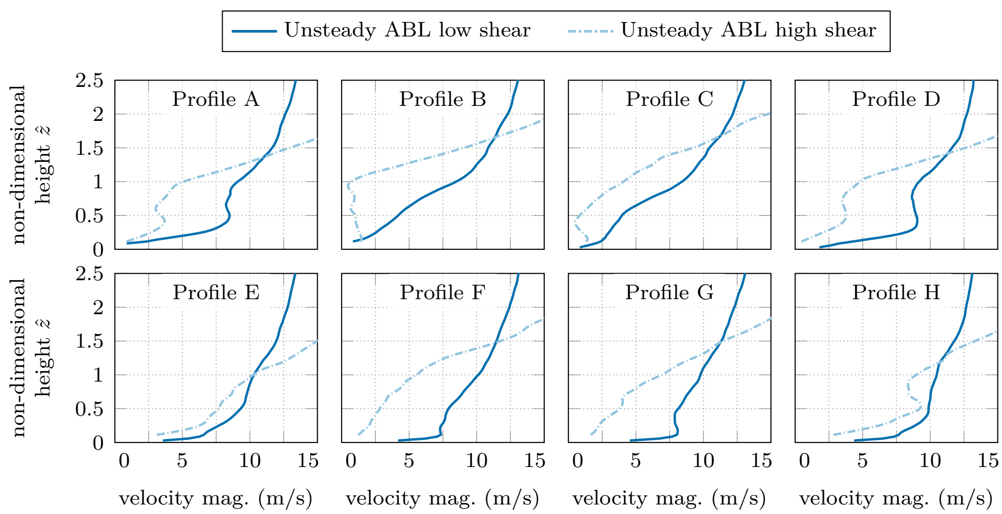

Figure 5.8: Comparison of profiles when subject to ABLs with different levels of shear.

Figure 5.8 shows two very different airwake velocities. The fundamental difference for that is because the underlying profile is quite different — see Fig. 4.10. The desire to show these differences lead to the choice of the dimensional velocity. It should be noted that in previous published work by the author — Journal of the AHS, reference [131] — the data related to what it is being called 'low shear' here was presented in non-dimensional form. The choice of the height selected for normalization, $\hat{z} = 3.5$, resulted in a profile that had an apparent large deficit in the wake. The results presented are the same as the ones presented here, but it is important to acknowledge that the normalization presented in [131] accentuated the deficit in the wake. In light of this and the previous discussion on such normalization, the comparisons are shown in dimensional form to make it clear to the reader that the underlying profiles are different and will yield different airwake characteristics. It is reminded that both scenarios are realistic — it is a matter of the situation one wishes to simulate.

An important aspect of Fig. 5.8 is the lack of scaling. Despite the discussion of velocity scaling (or, Reynolds number) in uniform inflows, this is not observed under resolved ABL inflows. The underlying profiles have different velocity magnitudes (recall Fig. 4.10), but they are within the range mentioned by Polsky [1] and are confirmed by the current analyses. Perhaps of even more relevance to this discussion is that the non-dimensional comparison of the ABL profiles (left-hand-side of Fig. 4.10) seems comparable, and scaling would be expected. Because of this, it is concluded that the scaling may *not* occur for ABL flows, in particular those highly unsteady shear-driven flows.

Next, consider the velocity along a lateral line, passing through probes A–D at a height of $\hat{z} = 1$. Time-averaged velocity components across this line are plotted in Fig. 5.9. The two extra datasets used in this comparison are:

- A DES study from Forrest and Owen [20]. Uniform inflow, 0 degrees WOD, and full-scale model, resulting in Reynolds number $Re_L = 2.3 \times 10^8$;
- Wind tunnel measurements from the 2 $\times$ 3 m, low-speed wind tunnel at the Aerodynamic Laboratory of the National Research Council (NRC), Canada (as reported by [20]). Uniform inflow (the experiment had suction on the bottom wall), 0 degrees WOD, and 1:100 scale model, resulting in Reynolds number $Re_L = 6.6 \times 10^5$.

In this comparison, the Re_L is of the same order of magnitude among the CFD studies and thus the results are expected to be comparable, based on the aforementioned assessment of Re_L sensitivity. It is acknowledged that the Reynolds number of the NRC experiment may not be within the valid range of scaling anymore. The experiment is compared with the uniform inflow solution to establish a common ground, and with two neutral ABL scenarios - one containing little shear and another with high shear (see Fig. 4.18). There are a few points worth noting. First, a uniform inflow solution shows good general agreement with other CFD and wind tunnel studies, both for the mean velocities and turbulence intensity (with the exception of turbulence intensities at around $y/b = -0.25$). Second, a high shear imposes a large velocity deficit on the wake, reflected mostly in the streamwise direction. The low shear case has mean velocities comparable to uniform solutions; note that these results are at $\hat{z} = 1$, which is also the reference height, thus it is not surprising that a low shear case matches the observed mean velocities. The high shear case, however, shows larger differences, and part of that is due to the normalization aspect. The ABL case shows higher levels of turbulence, as measured by the turbulence intensity. In the wake directly above the ship ($-0.5 < y/b < 0.5$), the turbulence levels are not very different, however, the atmospheric turbulence is clear at the extreme values of y/b. While this may not affect a 0 degrees WOD wake solution, it is extremely important for case scenarios where the ship is not aligned with the wind (and thus a vehicle would experience the increased levels of turbulence).

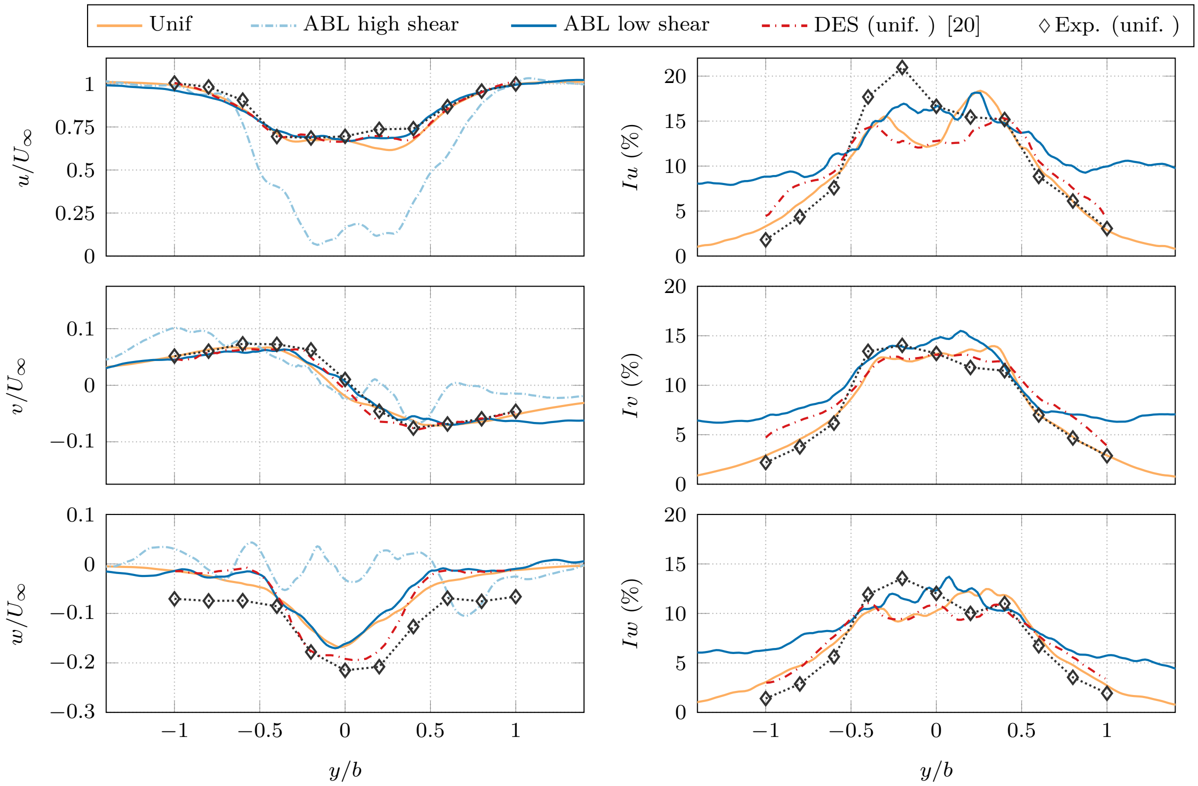

Figure 5.9: Comparison of velocity components (left) and turbulence intensity (right) along profiles A–D at $\hat{z} = 1$ with previous uniform inflow DES and experimental (wind tunnel) data (both from [20]). Values normalized by the averaged freestream velocity at the ship height, and lateral position normalized the ship beam width.

5.4.2 Airwake Flowfield Visualization

These differences observed so far become more apparent by comparing the actual flowfield. In Fig. 5.6, time-averaged solution has been shown. An important aspect of this work is that time-accuracy is relevant when the unsteady atmospheric turbulence is used as an inflow. Figure 5.10 shows instantaneous streamwise and vertical velocity contours on slices at different heights taken at 30 s for the high shear and equivalent uniform inflow case. Following, Fig. 5.11 shows the same contours on a vertical slice across the ship's centerline.

The wake downstream of the ship is quite different. The data presented strongly suggest very different airwake shedding characteristics between uniform inflow and fully-resolved ABL inflow. Specifically, in the case of the ABL present, the wake extends for substantially longer distances. The region dominated by high-frequency, small-scale eddies extends about half a ship length downstream. The longer wake may possibly be due

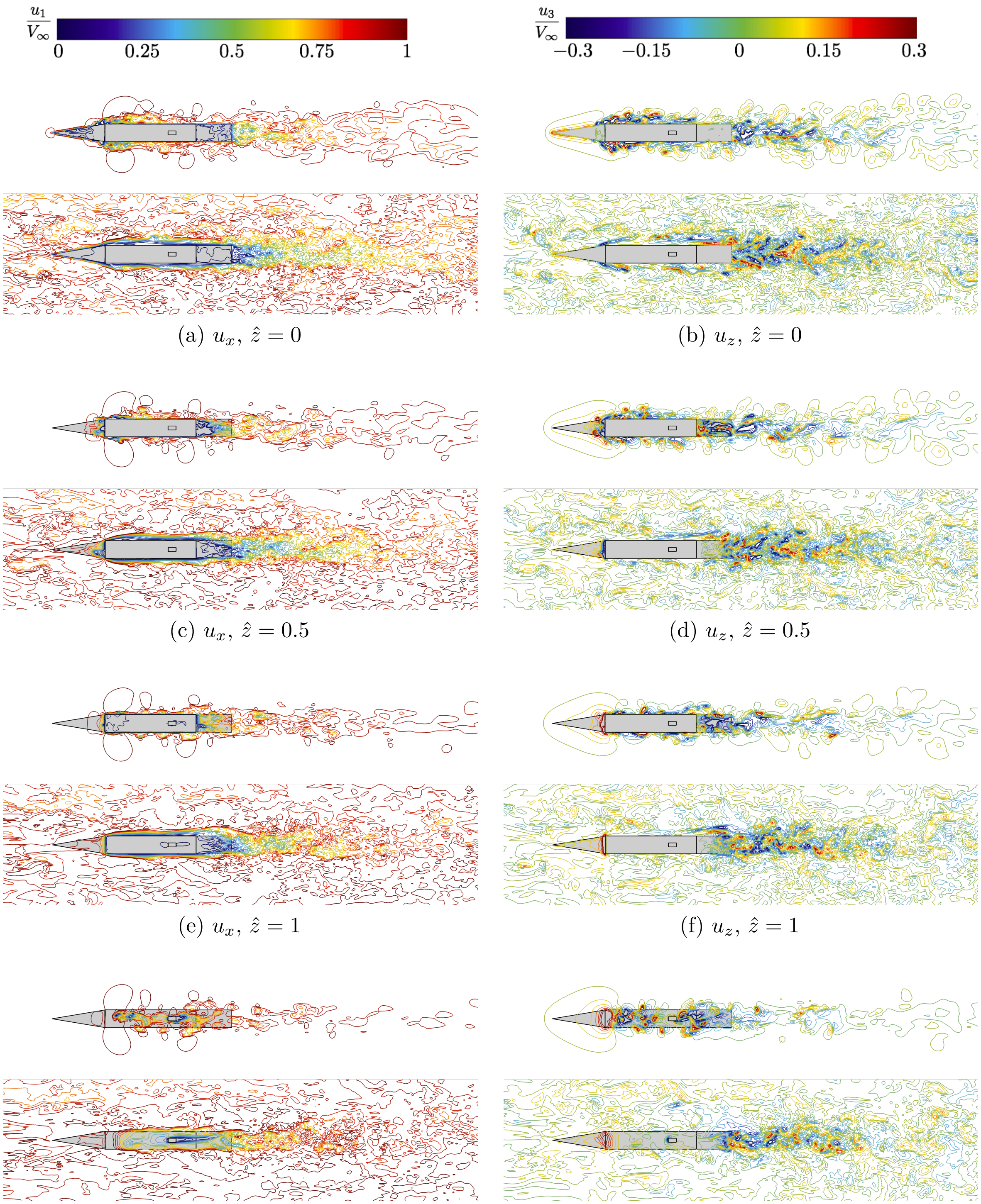

(a) u_x, $\hat{z} = 0$

(b) u_z, $\hat{z} = 0$

(c) u_x, $\hat{z} = 0.5$

(d) u_z, $\hat{z} = 0.5$

(e) u_x, $\hat{z} = 1$

(f) u_z, $\hat{z} = 1$

(g) u_x, $\hat{z} = 1.5$

(h) u_z, $\hat{z} = 1.5$

Figure 5.10: Instantaneous horizontal slices at different heights showing contours of velocity components. Left: streamwise velocity, right: vertical velocity. For each item, top is uniform inflow and bottom is ABL inflow. High shear unsteady ABL case shown.

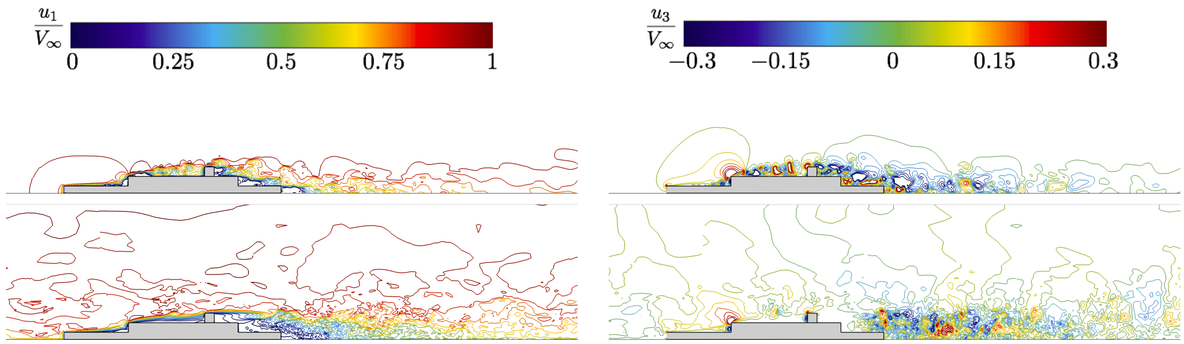

(a) u_x (b) u_z

Figure 5.11: Instantaneous vertical slices through centerline showing contours of (a) streamwise velocity; and (b) vertical velocity. High shear unsteady ABL case shown.

to the increased momentum exchange with the turbulent incoming flow. The atmospheric eddies are clearly present here. Such flow features are not seen in time-averaged quantities and it is somehow difficult to visualize just by inspecting isosurfaces from the plain large-scale atmospheric solution from Fig. 3.2. This unsteady content indicates that time-accurate effects may be relevant for shipboard operations of helicopters. Because of that, the energy related to the airwake is now looked at and then compared with a completely steady ABL inflow.

5.4.3 Energy Spectra

The aforementioned time-averaged results suggest that the ABL affects the airwake size. In particular, depending on the level of shear, the underlying profile can be quite different. This difference can result in lower velocity at lower heights, which, in turn, can impose a deficit on the wake. This deficit makes the wake extend for longer and just present itself differently. This does not, however, yet directly address the shedding characteristics that relate to pilot workload. In general, it is known that the airwakes are accompanied by a highly unsteady behavior with characteristic frequencies less than 2 Hz [21]. In this section, the impact of the high-frequency small-scale eddies associated with the ABL-modified airwake region is evaluated.

Before continuing with the present analysis, consider previous studies of the energy content in a ship airwake. As mentioned in chapter 1 when discussing the motivations, in general, past CFD efforts indicated difficulty capturing frequencies higher than 3 Hz. As apparent in Fig. 5.12[1], the at-sea data presented in [13] (possibly reformatted data

[1]This figure has been presented earlier, but it is reproduced here for convenience

from [1]) show energy content that continues to follow the $-5/3$ slope, as opposed to the sharp decay observed in CFD at 3 Hz. Similar behavior is observed for data presented in Fig. 5.13. Interestingly, the same pattern is observed in the more recent CFD effort of Polsky et al. [67]. In addition, other sets of full-scale, at-sea, experiments from Kang et al. [52] also measured a $-5/3$ trend that extended to higher frequencies. In general, past CFD efforts indicated difficulty capturing frequencies higher than 3 Hz. Also, Thornber et al. [25] noticed a distinctive "kink" at 3 Hz, where the spectra no longer followed Kolmogorov's $-5/3$ slope, but rather started following a -4 slope. Note that the energy content captured by CFD studies (e.g. [61, 66]) frequently exhibit a spectral pattern similar to wind-tunnel experiments; however, the wind-tunnel experiments also neglect real-world ABL effects. Hence, CFD consistently predicts a discrepancy with full-scale, at-sea measurements in the mid-to-high-frequency energy. It is noted that such behavior was observed in several CFD studies, which all used different approaches, conditions, and solver settings, supporting the idea that something beyond the solver and user settings is affecting high-frequency energy content prediction.

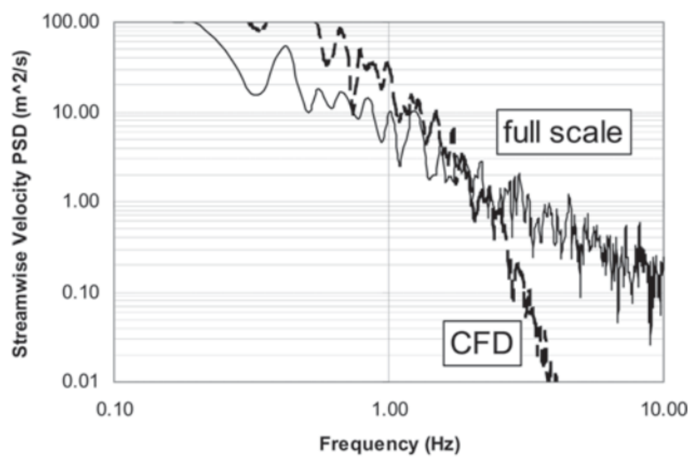

Figure 5.12: Typical velocity spectra from data collected at a real carrier, in comparison with typical CFD calculation. Note the drop in resolved content at higher frequencies that usually happens in typical CFD calculations. Figure from [13], with data from Polsky [1].

In terms of the present analysis, consider a helicopter approach in the context of the turbulent wake forming in a 0 degrees WOD condition. Such an approach can involve a number of scenarios, hence, the frequency analyses are performed at various points that include heights and locations where the helicopter could be descending or hovering. Specifically, the focus is on all of the mid-deck and deck-edge probe locations at $\hat{z} = 2$ as

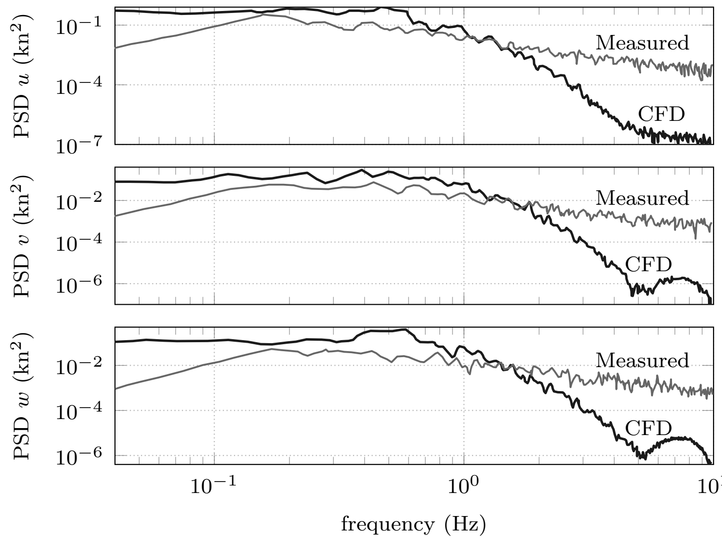

Figure 5.13: Same as 5.12. Data from Wilkinson et al. [10].

well as the deck-edge probes E–H at $\hat{z} = 1$ for energy-content analysis. It is argued that the energy content is a reasonable way to quantify pilot workload, hence, sensitivity to the energy content directly relate to physical character important to develop a physically accurate dynamic interface simulation.

Results are presented in Fig. 5.14. These PSDs are processed using data extracted from the deck-edge probe lines E–H at $\hat{z} = 2$. Although only results at these points are presented, the data were processed at several other locations. It is emphasized that, in general, the behavior and trends were consistent for all locations investigated, hence why only a few are shown.

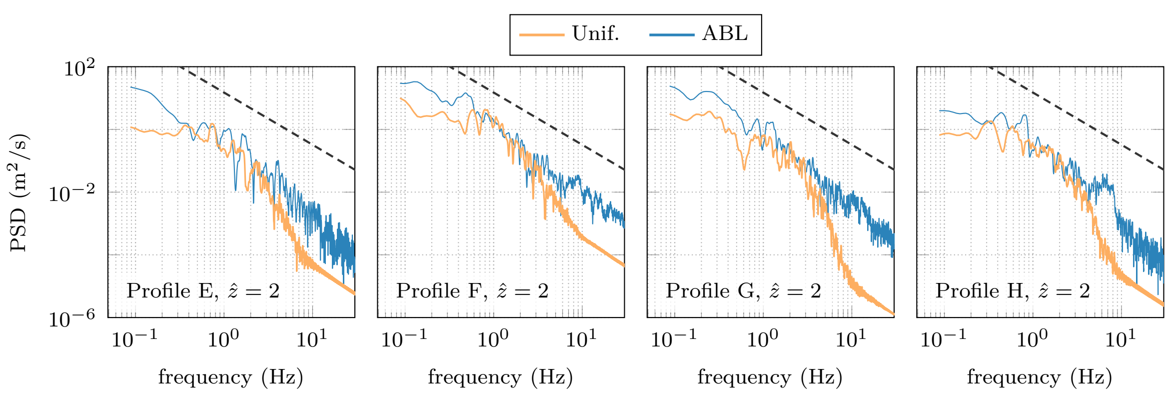

Figure 5.14: Power spectral density analysis of the streamwise velocity component for points located at Profiles E–H, at $\hat{z} = 2$. Under ABL inflow, the trend can better follow the $-5/3$ cascade (dashed line). Plots clipped at 30 Hz.

From Fig. 5.14, several conclusions can be drawn. For the frequency range investigated, ranging from 0.1 Hz to 25 Hz, the energy present in the airwake modified by the ABL is comparable or higher. A higher energy content for ABL cases is clear in the low-frequency range of about 0.1–0.8 Hz, in comparison to uniform inflow. It is speculated that this additional energy present in the low frequencies cascades down to the high-frequency range of about 4–25 Hz, resulting also in increased content in the high-frequency range. An increased high-frequency content can be visually observed in several of the slices shown in Figs. 5.10 and 5.11 in which small-scale high-frequency content can be seen convecting downstream.

The increased energy in both the low- and high-frequency range makes the overall energy spectra follow Kolmogorov's $-5/3$ slope better. Kolmogorov's cascade was captured for frequencies spanning two orders of magnitude. This behavior was observed in the ABL cases, whereas, on the other hand, the uniform-inflow solutions presented the same behavior observed in different studies described above, where a drop in resolved content occurs around the 3–4 Hz range. This finding supports the fact that uniform-inflow CFD is usually unable to capture the correct slope at frequencies higher than 4 Hz.

One can argue that the high-frequency content may not be important for pilot workload because it is well into the vibratory frequency range. The authors acknowledge that but stress that the increased high-frequency content is also due to energy cascading from a more realistic low-frequency content. The low-frequency content in the ABL case is likely to be related to the large coherent structures present in the neutral atmospheric boundary layer and was already seen in Fig. 4.2.

The energy content captured in the high-frequency range for an ABL case is consistently at least one order of magnitude higher than that captured in a uniform-inflow case. It is worth noting the spike in energy at around 7–8 Hz in the H profile. Spikes in some profiles may be due to the shedding characteristics of the funnel. With respect to general trends, these initial results indicate better agreement with typical energy slopes seen in full-scale at-sea data.

Considering a typical helicopter with a rotor speed of about 300 rpm, its wake has contents in the frequency range of 5 Hz for 1/rev content and 20 Hz for 4/rev content (for a 4-bladed rotor). The presence of the ABL increases the energy content in the airwake in this frequency range. Thus, the increased content observed at these frequencies has potential to impact pilot workload, hence, may be important for flight dynamics simulation and dynamic interface modeling.

5.5 Steady Velocity Profile vs. Unsteady Atmospheric Inflow

So far, results indicated that time-accurate features present in the airwake appear to be important. The ship airwake community frequently mentions the so-called steady ABL approach, in which no turbulence is present in the incoming inflow. In this section, results comparing the steady ABL and unsteady ABL are shown in an attempt to investigate such effects. The incoming wind profiles have been discussed in sections 4.4 and 4.5.3, and summarized in section 4.6. The low-shear profiles are the subject of interest in this section.

Similarly to the previous uniform vs. ABL inflow investigation, this section is divided into flowfield visualization, where time-accurate effects are qualitatively investigated, and then perform some quantitative comparisons, using time-averaged velocity data at the eight A–H deck profiles.

5.5.1 Airwake Flowfield Visualization

Here qualitative comparisons between all four cases investigated — uniform for both codes, steady ABL (OVERFLOW), and unsteady ABL (OpenFOAM) — are shown. The images are shown in Fig. 5.15 and present a visual representation of the differences in the modeling approach. The left-hand-side figures show instantaneous snapshots of the velocity magnitude, while the right-hand-side images show time-averaged velocity magnitude. Two slices are shown: one along the centerline of the ship, and another horizontal, at the superstructure height.

The images in Fig. 5.15 are dimensional, and the reader can note the color gradient, representing the profile shown earlier in Fig. 4.18. There are several aspects to note. Uniform inflow cases are considered first. Their time-averaged results look very similar, as observed earlier in Fig. 5.6 — here the same snapshots are presented, but on a different scale for easier comparison. The instantaneous snapshot appears to show resolved eddies of the same length scale in the associated airwake.

For the ABL cases, upon inspection of time-averaged data, both modeling approaches result in what seems to be a very similar airwake structure. As mentioned in this work, an ABL is considered to be comparable to a uniform inflow case if their time-averaged velocity magnitude matches at the superstructure height. Hence, it is not surprising that the horizontal slices shown at that height all look similar. The shade of yellow seen

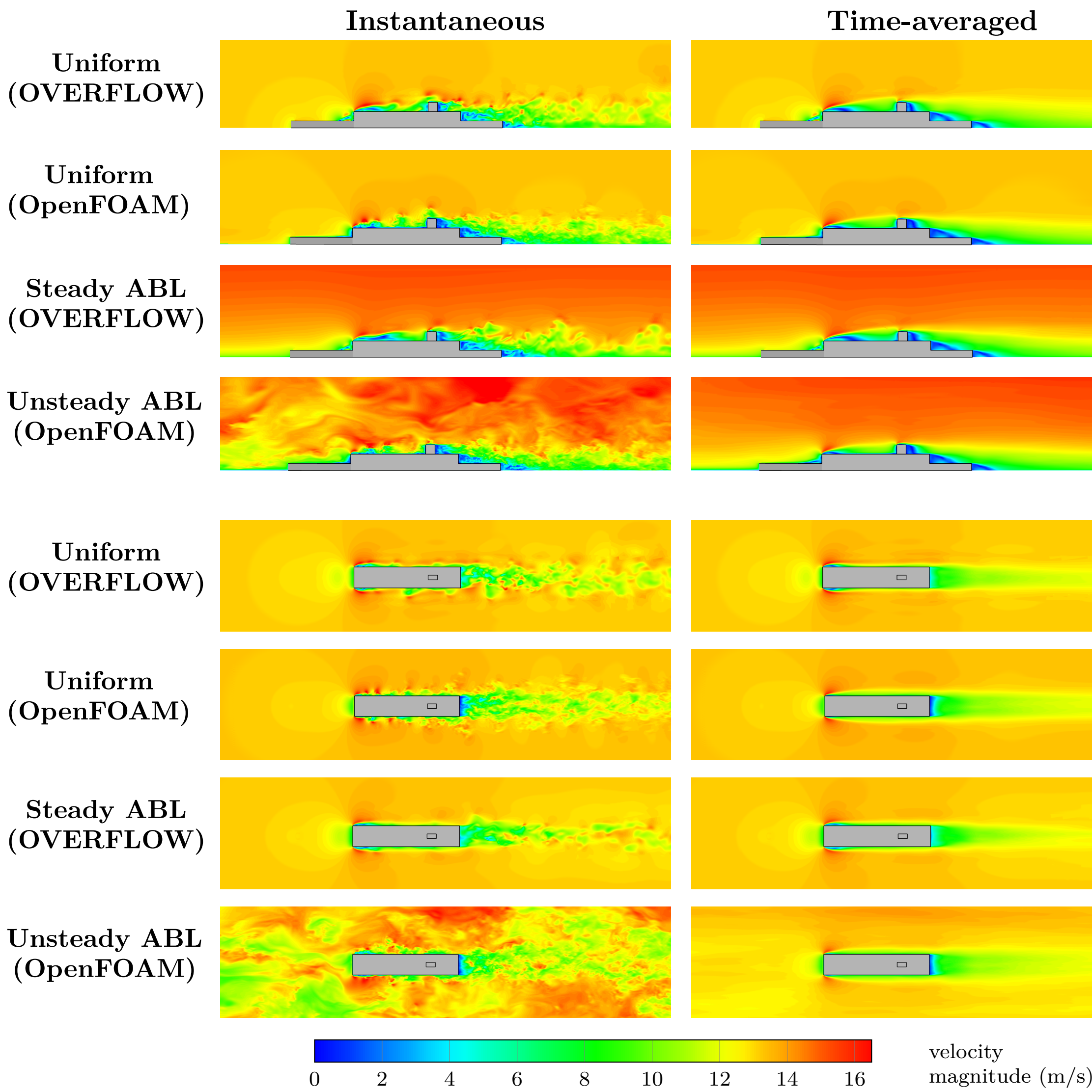

Figure 5.15: Instantaneous and time-averaged snapshots of the velocity magnitude along the centerline of the SFS2 and at the top of the ship for the various cases investigated. The same scale is used in all of the figures. Note that the freestream velocity of the uniform inflow case matches the time-average velocity at the superstructure height for the cases with the ABL. This aspect is evident on the horizontal slices. For the steady ABL, the instantaneous and time-averaged flowfield upstream of the ship are the same.

corresponds to a velocity of about 13.3 m/s, or ~ 26 knots, and is the freestream velocity set for the uniform inflow CFD runs.

The steady ABL (OVERFLOW) case displays a completely steady upstream flowfield, with the instantaneous slice matching the time-averaged. The reader is reminded that although we refer to steady ABL, these simulations are time-accurate DDES. Since a steady ABL case is similar to a uniform inflow, but with a sheared velocity gradient, the eddies present in the back of the ship for both cases are comparable upon visual inspection. By definition, no freestream turbulence exists in this case.

The most striking difference is seen for the unsteady ABL scenario. This is the case where the coherent structures and the unsteadiness present in the atmosphere can be seen. To make the difference more evident, Fig. 5.16 shows the vertical velocity field of the same slices for both ABL approaches. The updrafts and downdrafts that are naturally present in real ABLs are evident there. It can be seen that some eddies are of large scale and get broken down by the ship's structure, resulting in smaller length-scale eddies at the rear of the ship. This interaction of the incoming turbulence with the ship results in a flowfield that has been shown to directly affect the helicopter controls and thus pilot workload, as it will be shown in the next chapter.

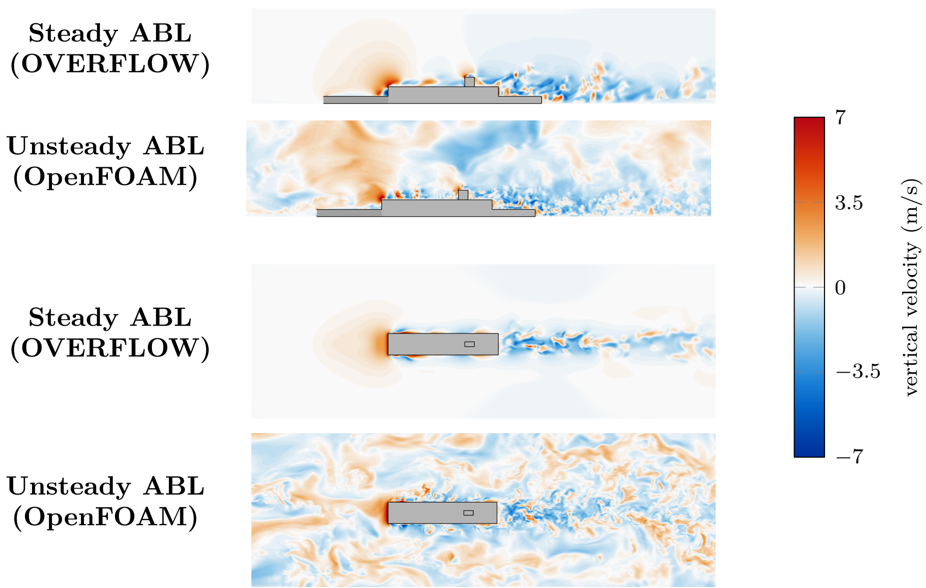

Figure 5.16: Instantaneous snapshot of the vertical component of the velocity, showing updrafts and downdrafts. The scale is such that blue means negative velocity (downdrafts) and red means positive velocity (updrafts). The disturbances present in the incoming flow due to a realistic fully-unsteady ABL is likely to be the source of the extra stick workload on the helicopter.

It is acknowledged that the coherent structures seen at higher heights are not well resolved. Upon inspection of the horizontal slice, at a lower height, the coherent structures can be better seen. The reason for that is a balance of resolution and runtime. The unsteady ABL cases have cell-count of around 50 million, and thus obtaining a time-averaged profile that matched OVERFLOW's steady one was a tedious task. The purpose of this effort is to show that time-dependent flow features are important and they can be of significant impact to a vehicle and time-dependent wake structure.

5.5.2 Quantitative Comparison

Following the uniform inflow validation, the same set of eight probes — Fig. 5.1 — are used to compare between both ABL approaches. The results are presented in Fig. 5.17.

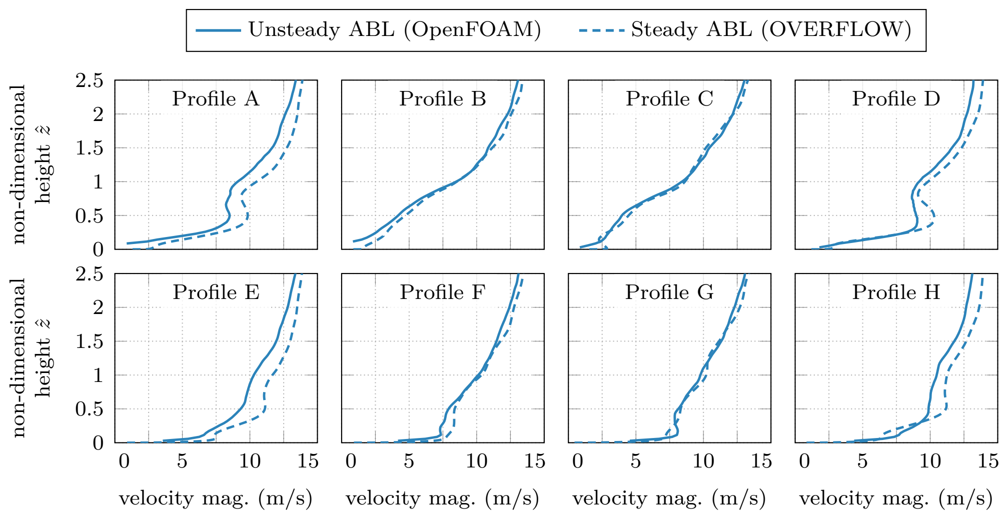

Figure 5.17: Time-averaged velocity magnitude on the deck (locations A–H, see Fig. 5.1), when subject to ABL-modified inflow scenarios.

There are a few interesting points worth highlighting from Fig. 5.17. The probe profiles indicate the final flowfield is also asymmetric, although less than in the uniform inflow cases. Inboard profiles' behavior are similar to the uniform inflow case. The wake re-attachment point is similar for inboard probes B, C, F, and G. The outboard probes at the back (E, H) showcase one of the differences when subject to unsteady ABL inflow. The probes do not converge to the same value at high values of $\hat{z}$ and this is especially clear for the outboard probes. This is a direct result of the profiles not being exactly the same at that height (see Fig. 4.18, $\hat{z} = 2$ corresponds to about 16.8 m). The deviations seen at outboard probes are also likely due to the fact that those locations are at the edge of the deck and thus more subject to the larger scales atmospheric eddies (this is a scenario where the flow is aligned with the ship). The mismatch at very low values of $\hat{z}$ is likely due to the fact that the OVERFLOW case properly resolved the walls — however, for helicopter simulation practices, such values are not relevant. Finally, it is not surprising that the general averaged results are comparable; in fact, the goal was to create two types of ABLs that were comparable in a time-averaged sense. The unsteady features that are present in the unsteady ABL, but not in the steady ABL will be investigated next, in a coupled helicopter dynamics setting.

5.6 Concluding Remarks

In this chapter, an investigation on the flow topology of the wake of the SFS2 under uniform inflow and turbulent atmospheric inflow has been performed. This part of the work used two frameworks: one based on LES with geometries modeled by the IBM; and another based on DDES, with body-fitted grids. The IBM implementation was validated for ship airwakes by exhibiting good overall agreement with experimental data for the uniform inflow case and matching findings based on a body-fitted DDES approach. The model was then used to develop an understanding of various aspects of a ship airwake in the context of an ABL. As previously mentioned, the cases investigated are representative of strong winds on a stationary ship, rather than a ship moving into a calm ABL (recall discussion in section 3.1.4).

The findings can be summarized as follows:

- The airwake topology depends on the nature of the incoming wind, and more importantly, the physical characteristics of the current conditions (aerodynamic surface roughness, heat flux from the surface, etc.);

- The amount of shear (and possibly buoyancy) can modify the airwake, as the underlying profile can be substantially different;

- The scaling commonly performed in uniform inflow cases (also referred to as Reynolds independency in the literature) does not appear to be valid in comparing ABLs with different characteristics;

- Spectral analysis on the wake revealed higher energy content at the low-frequency range of 0.1–0.8 Hz and high-frequency range of 4–25 Hz for the ABL cases. This increased content amounted to a better agreement to the $-5/3$ slope observed at-sea (provided all uncertainties when comparison to a different setup at-sea). The increased content in the low-frequency range is likely due to the coherent structures present in the resolved ABL field, which is lacking in modeled ABLs, uniform-inflow CFD solutions, and wind tunnel experiments;

- Time-averaged quantities can be matched; however, unsteadiness sets the airwakes apart as time-accurate effects become important.

The time-accurate aspect seems to be relevant and in the next chapter, the airwakes are coupled with a flight dynamics software and those effects are analyzed from a flight dynamics perspective.

Chapter 6
Coupling Airwake Solutions with Helicopter Flight Dynamics

In this chapter, the airwake solutions previously described are used to perform coupled dynamic interface simulations. Here, several baseline cases are shown, representing the traditional approach of modeling the incoming wind as a constant, uniform inflow. Comparisons between the ABL-resolved solutions and the baseline simulations are performed for several different scenarios.

In a broad sense, the unsteady computational fluid dynamics solution is saved as a database and used as external disturbances for flight dynamics analysis. Such an approach is common in piloted flight simulation. This work evaluates pilot workload by a frequency-domain investigation of the stick usage. The methodology of the coupling is described first, followed by a description of the rotorcraft flight dynamics codes used. Next, the analysis is divided into initially understanding the effect of the pure atmospheric inflow, and then looking at the dynamic response of the vehicle when subject to inflows generated by different ABL modeling strategies. The chapter finishes with some concluding remarks.

6.1 Coupling Methodology

Using CFD to solve for the flowfield and another code to solve the equations of motion of the vehicle is inherently a coupled problem. Generally speaking, coupling between a flight simulation code and CFD can be classified into two major categories: one-way and two-way coupling. Coupling methodologies can be described as follows:

One-way coupling In one-way coupling, the flight dynamics code receives information about the flowfield from the CFD. Then, flight simulation is carried out using the

CFD inflow data as additional disturbances (on top of the induced inflow model, for instance), which is obtained at every time step. In this mode, inflow data can be obtained "offline", indicating the CFD does not need to be running concurrently with flight dynamics, and thus is used as a look-up database. Additional interference effects are usually modeled. This method is typically used for real-time piloted flight simulation.

Two-way coupling In two-way coupling, information about the presence of the helicopter is passed back to the CFD for more realistic wake computations. In this mode, the CFD and flight dynamics have to be running concurrently. Wake calculations by the CFD code take into account helicopter features that alter the flowfield; and the flight dynamics component gets airwake data that has been modified by the presence of the helicopter itself. The CFD is responsible for accounting all of the interference effects. Real-time piloted two-way coupling is still a challenge from a computational power perspective.

In this work, only one-coupled simulations are performed. The coupling methodology utilized is illustrated in Fig. 6.1. Note that in the context of this work, the airwake solution component can be either executed in OpenFOAM or OVERFLOW.

The "offline" aspect of the airwake-saving approach means that the CFD is executed *a priori*. Velocity data in the airwake region is saved to files that are easily read into the computer memory when performing coupled simulations. The region saved is indicated by the gray box in Fig. 6.2. Starting at the flight deck, right behind the backward-facing step, the region spans 435 ft in the streamwise direction, 85 ft high and 150 ft in the spanwise direction. This airwake box size is large enough to perform an approach trajectory and multiple hover locations (inside and outside ground effect, inside and outside of the wake, etc.).

With respect to temporal resolution of the airwake, an instantaneous snapshot is saved at every 0.1 s into a separate text file. A saved scenario, or rather, a database, is composed of many of these files. For instance, a 60 s long airwake database is composed of 600 files (plus an additional file for grid considerations). Speaking of grid, regarding spatial resolution, the airwake is saved as a structured Cartesian grid with a resolution of 5 ft in all directions. Although this represents a considerably coarser grid than that of the CFD, it is nonetheless sufficient. On the helicopter dynamics side, the blade is discretized and the velocity data from the CFD is sampled at the blade control points. Ten points per blade are used and the quantities are integrated over the span of the

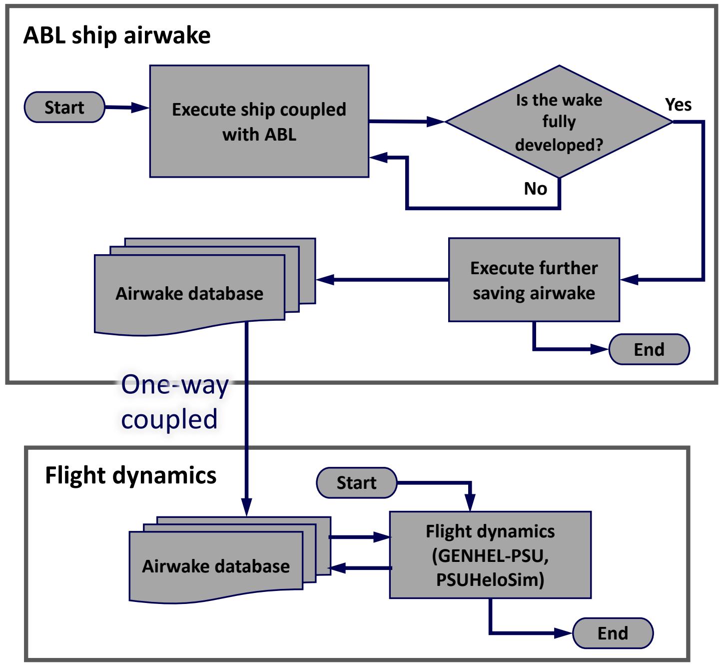

Figure 6.1: One-way coupling methodology used in this work. Note that both components usually are executed independently. This workflow builds on top of the precursor block previously shown in Fig. 3.1.

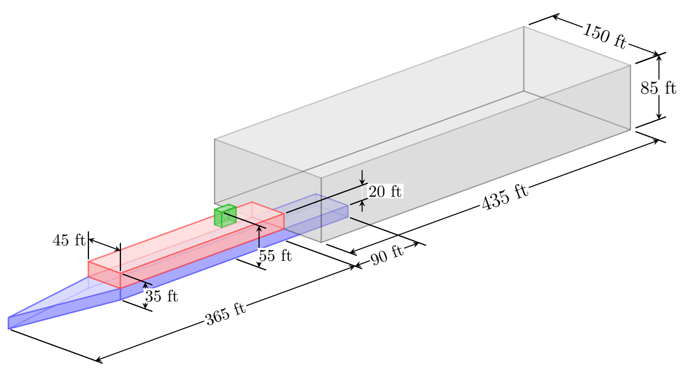

Figure 6.2: The SFS2 and the region where the airwake is saved for one-way coupled analysis. Figure to scale.

blade, which means a higher resolution on the airwake database is not warranted.

6.2 GENHEL-PSU and PSUHeloSim Simulation Models

The helicopter dynamics computations carried out in this work were executed using two modeling softwares, namely, GENHEL-PSU and PSUHeloSim. Both have been the subject of many studies at Penn State, and hence carry the PSU acronym in their names.

PSUHeloSim has been under development and during the progress of the current work it was validated and became the tool of choice. Nevertheless, earlier results obtained with GENHEL-PSU are also shown and discussed. The controller used in both is the same, and thus, the results obtained with GENHEL-PSU were reproducible in PSUHeloSim, and vice-versa. In this section, general aspects that are relevant to both codes are discussed.

In general, GENHEL-PSU and PSUHeloSim are quite similar. In a broad sense, they are both based on the GENeral HELicopter (GENHEL) simulation model. GENHEL-PSU is written in Fortran, while PSUHeloSim, is a C++ wrapper code that is designed to interface with different simulation models developed in MATLAB/Simulink. The advantage of PSUHeloSim is that it has been re-written into a modular format, using a library of functions that model the aircraft's main components (main rotor, fuselage, etc.). The simulation model is developed in Simulink and then auto-coded to C that links with the PSUHeloSim wrapper. Both softwares handle interface with external modeling tools and aerodynamic data. Both can be integrated with a flight simulation facility, and executed in real time (if feasible), while interfacing with visuals, pilot control inceptors, and other simulator hardware. Alternatively, the codes can be executed in non-real-time batch simulations for engineering analysis (as it is done in this work).

The GENHEL simulation model was initially developed by Sikorsky for the U.S. Army, and is currently well established and has been validated with flight-test data [53]. It is a real-time capable simulation library that includes a mathematical model of the flight dynamics of a utility helicopter representative of a UH-60A (see Fig. 6.3). The model has a level of sophistication considered necessary for handling qualities evaluation. The model includes a total force, non-linear, large angle representation of the six rigid-body degrees of freedom. Also included are rotor blade flapping, lagging, and hub rotational degrees of freedom, rotor and engine revolutions dynamics, alongside a three-state Pitt-Peters dynamic inflow model. It uses a blade-element representation of the main rotor by means of look-up tables for blade section lift and drag as a function of the angle of attack α and Mach number. A block diagram representation of GENHEL is shown in Fig. 6.4.

This model uses a blade-element rotor model, so that the effects of induced velocity as a result of the ship airwake can be easily achieved. Rotorcraft distributed inflow, downwash, and sidewash aerodynamics are affected by the ship airwake flowfield [55]. Because of the one-way coupled nature, however, the rotor wake does not affect the airwake.

The fuselage is represented by six components of aerodynamic characteristics — forces and moments — that are derived from wind tunnel experiments. Wind tunnel data up to

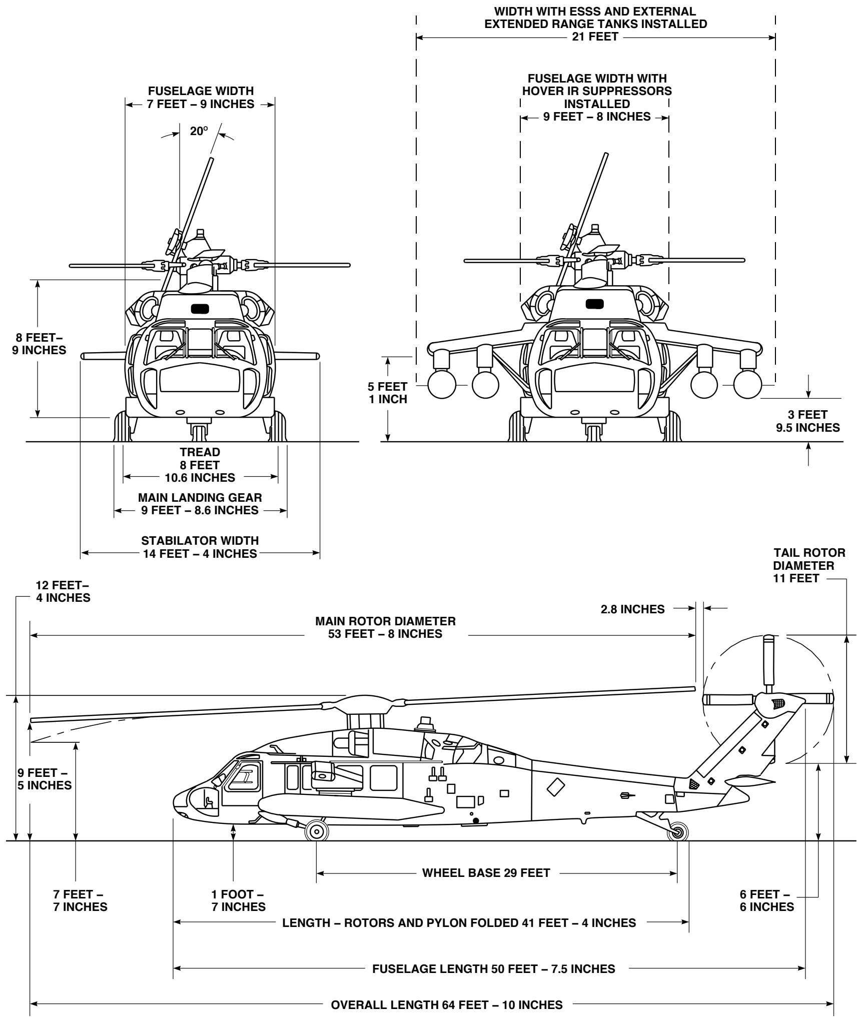

Figure 6.3: UH-60A Black Hawk general dimensions. A vehicle representative of the UH-60A is used in this work. Figure from [132].

post-stall conditions are extended to ±90° in order to cover for low-speed flight conditions. Near hover, however, the vertical drag and side forces are the most relevant ones. The angle of attack of the fuselage is defined by the freestream with added interference effects from the main rotor, which, in turn are based on rotor loading and rotor wake skew angle.

The tail rotor is represented as a simplified, closed-form Bailey theory solution. The induced inflow is calculated using simple momentum theory. The aerodynamics of the empennage are treated separately from the fuselage. The angle of attack of the empennage and tail rotor, for instance, is obtained from the freestream velocity plus rotor and airwake wash. Similarly, dynamic pressure effects on empennage and tail rotor

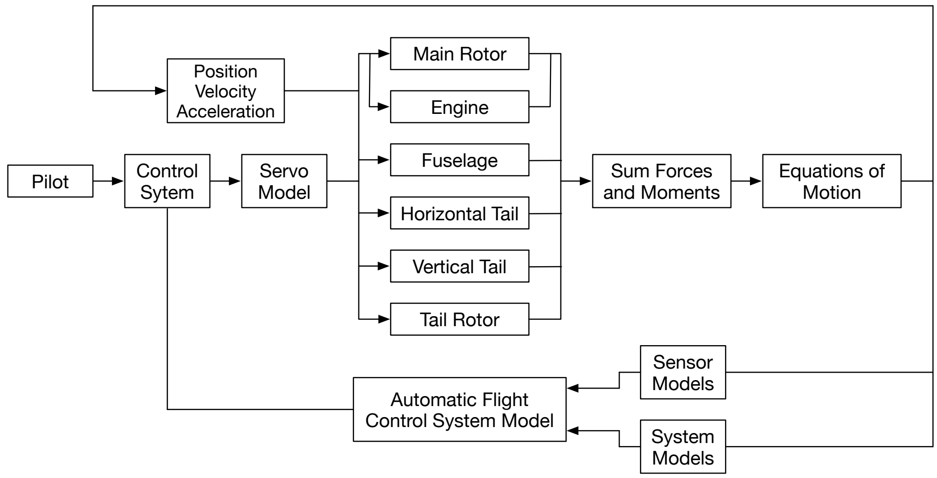

Figure 6.4: Block diagram of the flight dynamics model in GENHEL. Adapted from Howlett [53].

are calculated by factoring the freestream velocity components [53].

GENHEL-PSU or PSUHeloSim, when used on its own (batch analysis, no airwake model), relies on inflow models to account for the incoming flowfield. As mentioned, a three-state Pitt-Peters model is used here. It also makes use of low-order models to represent conditions such as ground effect and rotor/airframe interactions. In coupled simulations, the idea is to replace such models with high-accuracy CFD-resolved inflow data, thus improving the fidelity of the simulation.

In this study, the external inputs to the simulation model are used for the injection of gust velocities as interpolated from the ship airwake databases generated by CFD. These gust velocities are transformed into appropriate local coordinate systems of the various aerodynamic components of the simulation model and summed with the local velocity vector. Airwake velocities are distributed to the 10 blade elements on each rotor blade, as well as to the aerodynamic control points of the fuselage, horizontal stabilator, vertical stabilizer, and tail rotor. Such control points are illustrated in Fig. 6.5. Advance in time is given as 0.01 s increments, and the airwake solution is interpolated in time from the saved 0.1 s interval.

It is noted, however, that the Pitt-Peters inflow model is used only during the initial transient of the simulation. This is done in order to initialize and trim the rotor. During this stage, no inflow data are gathered from the CFD and GENHEL is executed in a decoupled manner, allowing the simulation to start smoothly. Data related to such initial transient is not considered in the hover analysis shown later.

Regarding non-real-time simulations, some sort of "pilot model" is useful in coupled

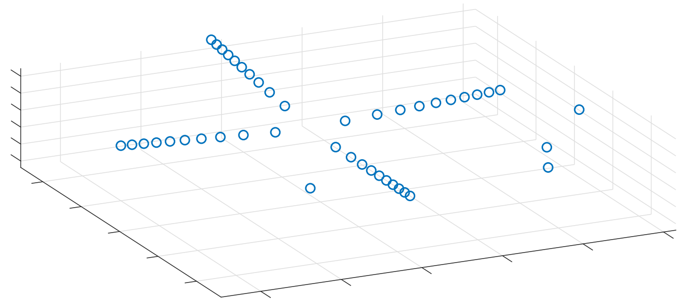

Figure 6.5: The 44 control points used to represent the vehicle. Ten points per blade are used plus additional control points for the fuselage, horizontal and vertical stabilizer, and tail rotor.

simulations in order to regulate the helicopter and keep it in a fixed location and/or to be able to fly a predefined flight trajectory while subject to external disturbances present in the flowfield. For this, a nonlinear dynamic inversion (NLDI) control law developed by Soneson et al. [11] is used within GENHEL-PSU and also PSUHeloSim. This controller achieves high-precision closed-loop control of the vehicle and is able to maintain tolerances lower than 5 ft with respect to the predefined position or trajectory. A description of the NLDI controller is given next. The modularity of the code allows relatively straightforward implementation of different controllers and response types.

6.2.1 Non-Linear Dynamic Inversion Controller

The Non-Linear Dynamic Inversion (NLDI) is used in both GENHEL-PSU and PSUHeloSim. This is especially important since it ensures a direct and fair comparison between results. It is reinforced that the results executed first with GENHEL-PSU are reproducible in PSUHeloSim. For the sake of completeness, the NLDI controller is described in this section. More information and theoretical aspects can be found in the original work by Soneson et al. [11], and a more general derivation in [133].

The NLDI controller is designed around a simple 6-DOF non-linear dynamic model of the helicopter. The controller uses full state feedback (all rigid body states) to track the ideal response dictated by the command filters (that is, the ideal response models). The non-linear flight model uses a stability and control derivatives representation of aerodynamic loads extracted from GENHEL using a perturbation method at different airspeeds. It uses, however, an exact representation of the non-linear dynamics and kinematics. The rigid body equations of motion are given in Eqs. (6.1)–(6.3):

$$
\begin{aligned}
\dot{u} &= \frac{X}{m} - g\sin\theta - qw + rv \\
\dot{v} &= \frac{Y}{m} + g\cos\theta\sin\phi - ru + pw \\
\dot{w} &= \frac{Z}{m} + g\cos\theta\cos\phi - pv + qu
\end{aligned}
\tag{6.1}
$$

$$
\begin{aligned}
\dot{p} =& \frac{1}{I_x I_z - I_{xz}^2}\left[I_z L + I_{xz} N + I_{xz}\left(I_x - I_y + I_z\right) pq \right.\\
&\left. - \left(I_z^2 - I_z I_y + I_{xz}^2\right) qr\right] \\
\dot{q} =& \frac{1}{I_y}\left[M - \left(I_x - I_z\right) rp - I_{xz}\left(p^2 - r^2\right)\right] \\
\dot{r} =& \frac{1}{I_x I_z - I_{xz}^2}\left[I_x N + I_{xz} L + I_{xz}\left(I_x - I_y + I_z\right) qr \right.\\
&\left. + \left(I_x^2 - I_x I_y + I_{xz}^2\right) pq\right]
\end{aligned}
\tag{6.2}
$$

$$
\begin{aligned}
\dot{\phi} &= p + q\sin\phi\tan\theta + r\cos\theta\tan\theta \\
\dot{\theta} &= q\cos\phi - r\sin\phi \\
\dot{\psi} &= \frac{q\sin\phi}{\cos\theta} + \frac{r\cos\phi}{\cos\theta}
\end{aligned}
\tag{6.3}
$$

The trim states, stability and control derivatives, controls, and forces are scheduled with airspeed. The non-linear state-space model is of the form

$$\dot{x} = f(x) + g(x)u \tag{6.4}$$

and the state and control vectors, x and u are given in Eqs. (6.5) and (6.6) below

$$x = [u\ v\ w\ p\ q\ r\ \phi\ \theta\ \psi]^T \tag{6.5}$$

$$u = [\delta_{\text{lat}}\ \delta_{\text{long}}\ \delta_{\text{col}}\ \delta_{\text{ped}}]^T \tag{6.6}$$

The aircraft forces and moments are calculated and are then coupled with the full non-linear equations of motion shown.

A controlled variable per input channel is required for a NLDI controller. These variables are tied directly to the pilot inceptors and the command filter. In this particular application, the controlled variables for the inner loop control law are defined by roll attitude $\dot{\phi}$, pitch attitude $\dot{\theta}$, vertical speed V_z, and yaw rate r as follows

$$y = \left[\dot{\phi}\ \dot{\theta}\ V_z\ r\right]^T \tag{6.7}$$

where y is the output vector. The output function as a function of the aircraft states x is defined by

$$y = h(x) = \begin{bmatrix} p + q\sin\phi\tan\theta + r\cos\phi\tan\theta \\ q\cos\phi - r\sin\phi \\ u\sin\theta - v\sin\phi\cos\theta - w\cos\phi\cos\theta \\ r \end{bmatrix} \tag{6.8}$$

The time derivative of the output vector can be determined by simple chain rule and plugging in Eq. (6.4) results in

$$\dot{y} = \frac{\partial h(x)}{\partial x}\dot{x} = \frac{\partial h(x)}{\partial x}f(x) + \frac{\partial h(x)}{\partial x}g(x)u = F(x) + G(x)u \tag{6.9}$$

where F and G can be derived.

In order for the system to track desired values y_{cmd}, the tracking error is defined as $e(t) = y_{\text{cmd}}(t) - y(t)$ and its time derivative $\dot{e}(t) = \dot{y}_{\text{cmd}}(t) - \dot{y}(t)$. Plugging the latter into (6.9), an alternate form of the time derivative of the controlled variables can be obtained:

$$F(x) + G(x)u = \dot{y}_{\text{cmd}} - \dot{e}\,. \tag{6.10}$$

Defining a vector of auxiliary inputs, or, "pseudo commands" as $\nu(t) = -\dot{e}$, and solving for u, results in a control law in the form

$$u = G^{-1} \cdot [\dot{y}_{\text{cmd}} + \nu - F(x)] \tag{6.11}$$

A simple proportional-integral (PI) type of compensator can be used to satisfy the error dynamics, $\dot{e} = -\nu$, thus $\nu = K_{\text{PI}}(s) \cdot e$.

The final non-linear dynamic inversion control law is then given as:

$$u = G^{-1} \cdot [\dot{y}_{\text{cmd}} + K_{\text{PI}} \cdot e - F(x)] \tag{6.12}$$

In summary, the command filters in the inner loop of the controller yield the desired response of the controlled variables y_{cmd} and their first derivative $\dot{y}_{\text{cmd}}$.

Given no disturbance and no model error, the aircraft will follow the ideal response perfectly. In practice, the feedback compensation will help account for both disturbances and modeling error. In a scenario without an airwake model, the controller resorts to the mentioned ideal response — this scenario will be shown as *no airwake* in the plots that follow. A diagram of the structure of the NLDI controller is shown in Fig. 6.6.

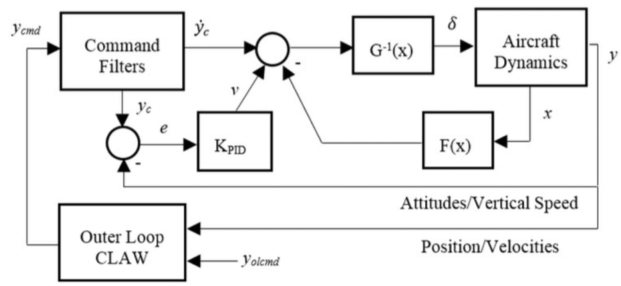

Figure 6.6: Non-Linear Dynamic Inversion Controller architecture. Figure from [11].

This section finishes by noting that neither the flight dynamics simulation models nor the controller used are the subject of further studies and/or detailed investigations. That is, they are used as a tool, rather than being improved upon. The use of GENHEL-PSU and PSUHeloSim allows for the study of time-accurate airwakes from a dynamic interface perspective and quantify aspects related to the operation of helicopters in such environments.

6.3 Uniform vs. Unsteady ABL

Recalling the workflow presented earlier in this chapter, the execution of the CFD generates the database based on text files. The stored CFD airwake database is used to provide velocity perturbations that affect the local velocity vector on the various rotorcraft components. This, in turn, results in external disturbances that alter the vehicle motion.

The dynamics of the vehicle when subject to the ABL-modified inflow are investigated by means of the analysis of hover on different locations and an approach trajectory. This section presents some results of an approaching trajectory and two hover locations using GENHEL-PSU. The cases evaluated are:

Trajectory An approach trajectory which represents a typical helicopter approach. Final position is in the center of the flight deck, at (45, 0, 30) ft.

Hover 1 Hover outside of the wake, subject only to the incoming wind, at 20 ft above the sea, (335, 45, 20) ft;

Hover 2 Hover outside of the wake, subject only to the incoming wind, at 85 ft above the sea, (335, 45, 85) ft.

The cases are schematically shown in Figs. 6.7 — hover cases —, and 6.8 — trajectory. The coordinates are given with respect to the reference frame shown in the figures.

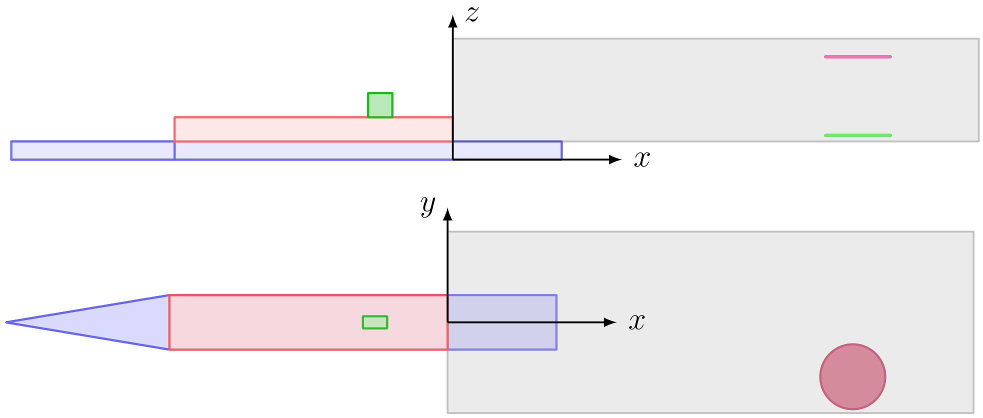

Figure 6.7: The two hover locations investigated with respect to the incoming inflow modeling, ABL or uniform. Figure to scale, including size of rotor.

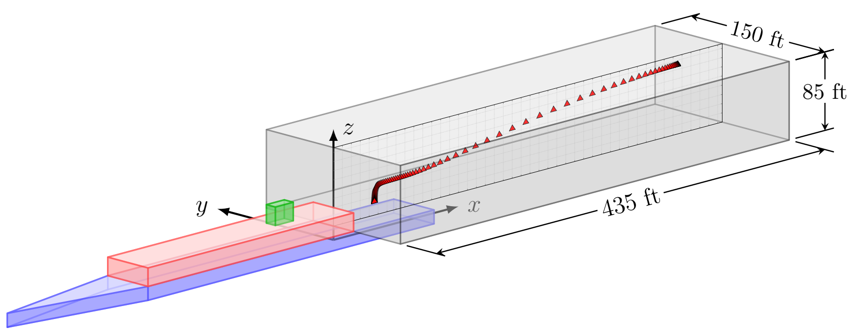

Figure 6.8: The approach trajectory investigated. Every symbol is spaced by 2 s — clusters of symbols means lower velocity and symbols spaced out means high speed. Figure to scale.

Regarding the hover cases, due to the nature of the coupling strategy, it is anticipated that no significant disturbances will be seen under uniform inflow. Such cases are evaluated to understand how the incoming atmospheric turbulence, by itself, affects the handling qualities of the helicopter, both in and outside of ground effect. The position chosen is such that the vehicle should experience very little turbulence from the airwake and thus the goal is the isolation of the effects of the freestream turbulence. The rotor presence is not accounted for in the CFD calculations. In light of that, ground effect is modeled within GENHEL-PSU. All cases presented here were executed for 120 s, allowing the helicopter to perform the desired trajectory smoothly, hover, and also allowing for the aircraft to trim. For hover cases, however, only the last 60 s are shown for ease of presentation.

As previously mentioned, an aspect concerning the ABL that is fundamentally different from a uniform inflow is that it does not have a *single* freestream velocity. In this approach, the ABL is unsteady and highly turbulent, making instantaneous comparisons inappropriate. After the initial transient is discarded, horizontally-averaged quantities are sampled within the most refined region. Thus, for comparison purposes, the horizontally-averaged velocity obtained at the superstructure height is matched for simulations with uniform inflow. The high shear case is compared here. The reader is reminded of the previous discussion of reference frames and the concept of a strong wind blowing over the ship, rather than the ship moving into the wind.

6.3.1 A Landing Approach Trajectory

The approach position over time is shown in Fig. 6.9 (Fig. 6.8 shows the spatial trajectory). Once the trajectory path is set, kinematically consistent velocities and accelerations are obtained. As can be observed, for the first several seconds, the path of the aircraft is at a fixed location for trimming purposes. The final descent is performed at the center of the flight deck. The approach can be broken down into several segments (times are approximate): (i) 0–20 s trimming and hover; (ii) 20–40 s smooth start; (iii) 40–80 s approach; (iv) 80–88 s high hover; (v) 88–105 s descent; (vi) 105–120 s station keeping/low hover.

Let us start by showing in Fig. 6.10 the positions the aircraft maintains during the trajectory. Due to the scale of the plot, the deviation from the original trajectory is shown on an auxiliary plot in the same figure. Looking at the deviations in y and z, a clear low-frequency content of about 0.1–0.2 Hz can be seen during the first 40 s. It is interesting to note the expected behavior, i.e. uniform inflow exerts little effect on the aircraft until it reaches a region of the airwake. From these plots, especially during the first 30 s, the large length-scale, small time-scale atmospheric eddies passing through and disturbing the helicopter can be observed. In these plots, as in the rest of the results presented, the 'no airwake' solution presents only what would be necessary for the aircraft to perform the approach or hover, with no external disturbance present whatsoever. The

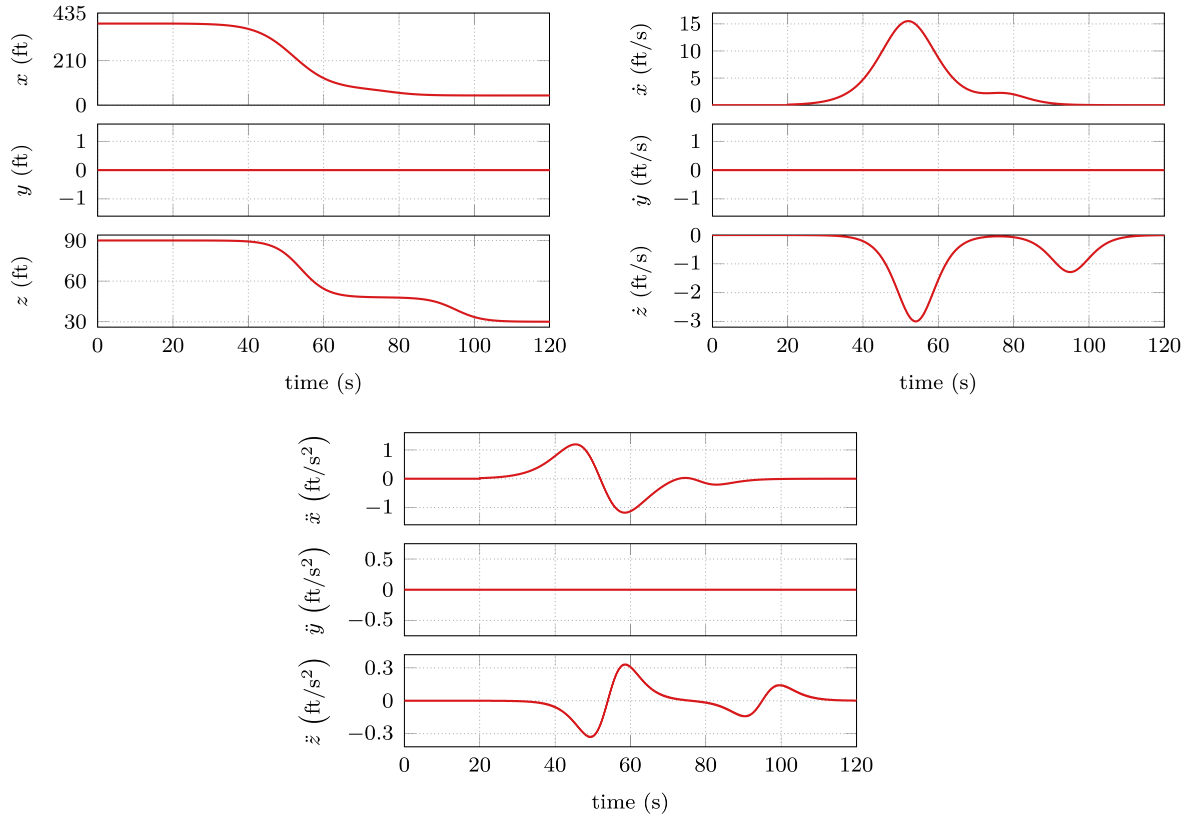

Figure 6.9: Specified positions, and associated velocities and accelerations over time for the trajectory approach investigated.

'no airwake' solution uses Pitt-Peters inflow model.

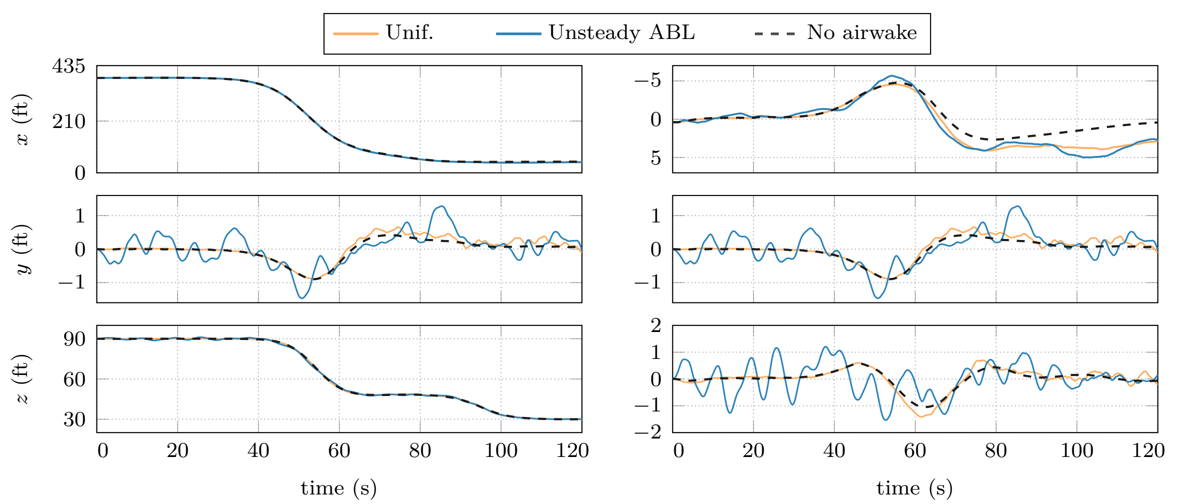

Figure 6.10: Trajectory: position over time for the approach. Left: positions; right: deviation from the original trajectory shown in Fig. 6.9.

The eddies related to the atmospheric turbulence are more visible by looking at the airwake data that is actually read by GENHEL-PSU at the location where the aircraft is at a certain time. The disturbances in the velocity encountered by the vehicle in the y and z directions are shown in Fig. 6.11. In this figure, it is evident that outside of the wake the aircraft experiences significant low-frequency disturbances that are not present in 'uniform inflow' cases. Vertical eddies are known to directly interact with the rotor. On the other hand, as the aircraft approaches the ship, and thus is in its wake, the disturbances become stronger (higher amplitude) under both ABL and uniform inflow, perhaps of comparable intensity. The 'no airwake' case presents no disturbances, by definition. The values shown for the ABL case are deficits from a horizontally-averaged velocity at that specific height.

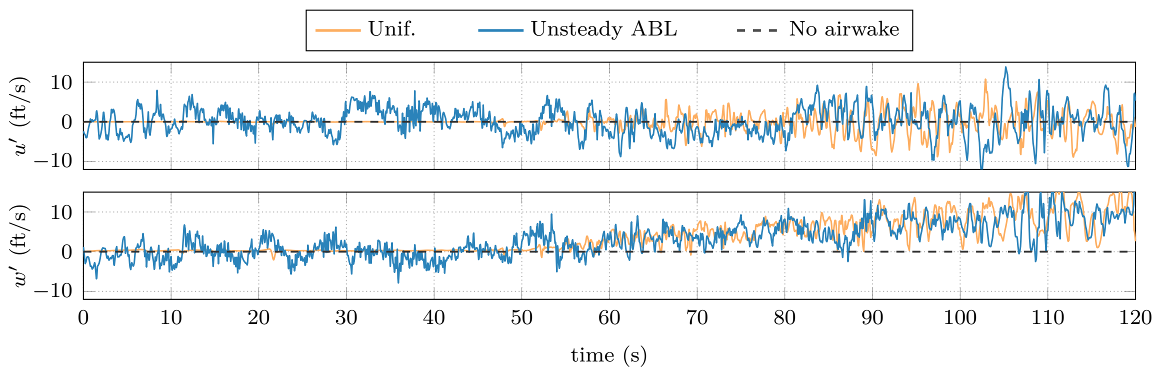

Figure 6.11: Trajectory: velocity disturbances in y and z encountered by the vehicle.

When subject to the disturbances shown in Fig. 6.11, the helicopter controller responds to keep the aircraft on the desired path. The time history of the position of the control sticks is shown in Fig. 6.12. The plots are given in terms of percentage of the total allowable physical movement of the control on the helicopter. The physical controls movement, both their frequency and magnitude, are translated into pilot workload. The reader is reminded that the analyses of the impact of resolved ABL data rather than uniform inflow is performed from the perspective of pilot workload and what important features should be considered when designing a high-fidelity training platform. There are several aspects that can be noted in Fig. 6.12. First, it can be seen that a considerable amount of stick movement is present far from the airwake under ABL inflow when compared to a uniform inflow. Both inflows require more from the pilot than a no-airwake scenario. Near the ship, overall collective is higher and that directly affects the power requirements — Fig. 6.14. During the descent and station keeping stages, an increasing amount of stick movement can be observed under both inflows.

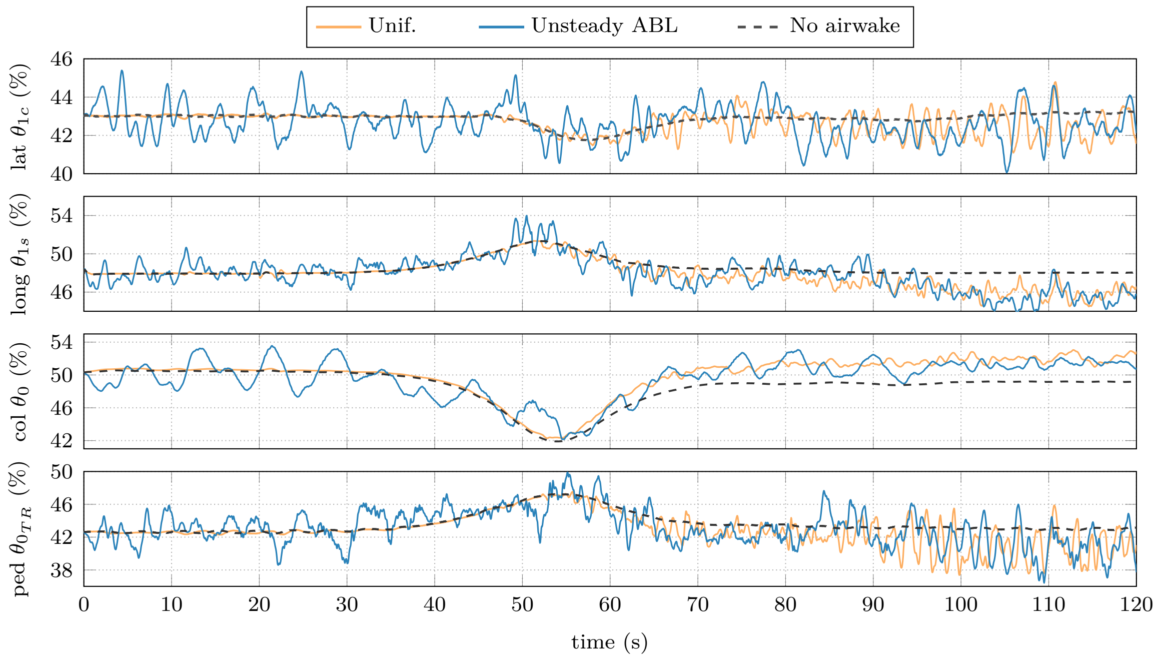

Figure 6.12: Trajectory: Control stick inputs during the approach. From top to bottom: lateral, longitudinal, collective, and pedal.

The response of the helicopter to the control inputs is given in terms of roll, pitch, and yaw, as shown in Fig. 6.13. It is easy to note that these responses in time are all linked to the controls, that in turn, are linked to the airwake disturbances. Once again, disturbances on the aircraft position are observed while the vehicle is under the effects

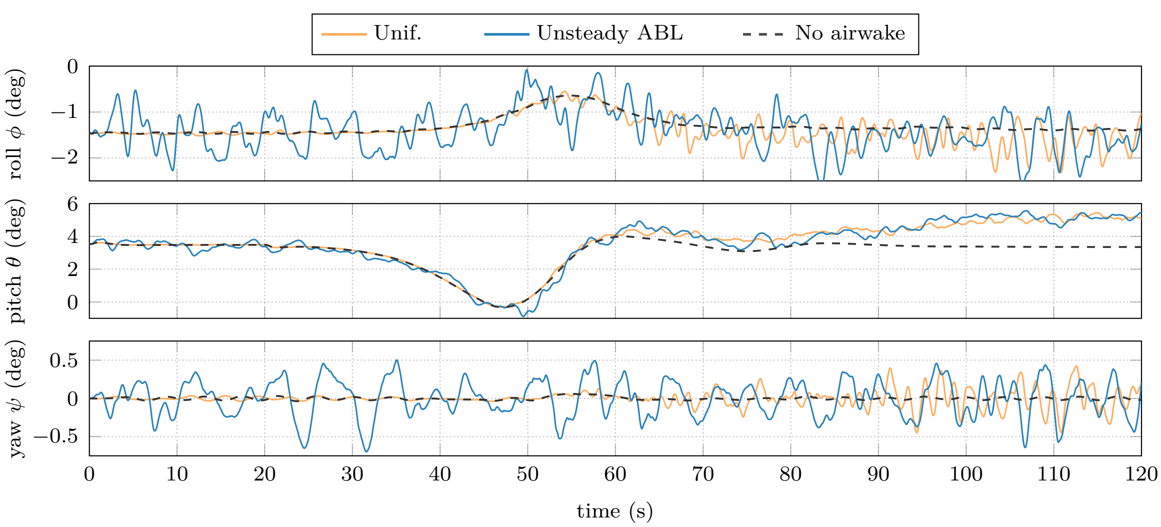

Figure 6.13: Trajectory: attitudes during approach. From top to bottom: roll, pitch, and yaw.

of the pure atmospheric turbulence (that is, not modified by the ship). The aircraft attitudes near the deck are also different, exhibiting higher amplitude and clear difference in frequency when subject to ABL inflow.

Within the airwake (last 20 s or so), for the ABL case, the magnitude of the attitudes seems to continue to remain the same, however, with lower frequency. Very close to the flight deck, from a time-domain perspective, no significant difference can be observed between both inflows.

Due to the much higher variation of stick usage under ABL inflow, the power required fluctuates significantly more — see Fig. 6.14. The power history is driven mainly by the collective use, resulting in a very similar time-history. The power required for the 'no airwake' case when the vehicle is in proximity to the flight deck is about 150 hp lower, which is expected since no disturbance is present, thus resulting in considerably less use of the commands. Similarly, the thrust is shown in Fig. 6.15.

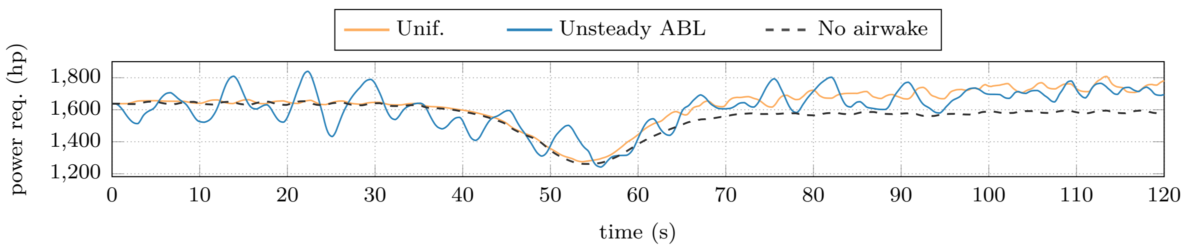

Figure 6.14: Trajectory: Power required.

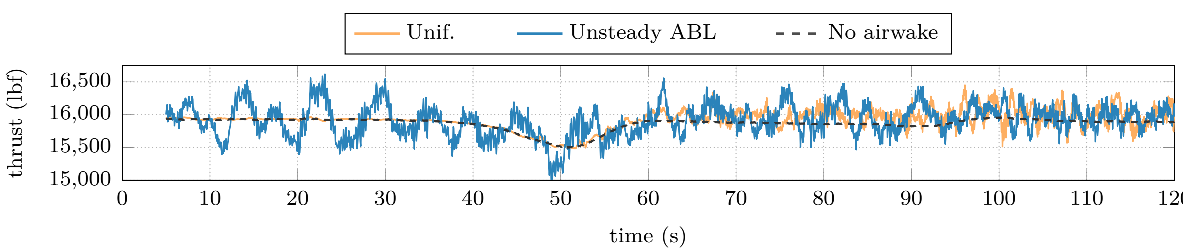

Figure 6.15: Trajectory: Main rotor thrust.

Overall, within the airwake, both ABL and uniform inflow scenarios seem comparable from a qualitative time-domain perspective. Outside of the airwake, however, the ABL case shows clear differences. That difference is due to the unsteadiness present in the incoming wind, since the flowfield is essentially laminar under the uniform inflow modeling approach. A logical next step for these results is to investigate them in the frequency domain. A frequency-domain analysis is not performed on the trajectory approach because there are different scenarios (as in inside and outside the wake) that would make it complicated to isolate the effects. The approach case shown served more as a qualitative investigation rather than quantitative one, and allowed for confirmatory conclusions to be performed. Moving forward, with the goal of looking at the energy content, hover maneuvers are performed. A vehicle performing a single maneuver for 120 s provides enough data to execute a frequency analysis on the stick positions. It is also an appropriate time scale such that the aircraft experiences a wide range of turbulence time scales.

6.3.2 Hover Cases

In this section, the results of the two hover locations are presented and compared. The results are given in the same order as the trajectory. The figures are arranged such that there is a figure for each group of quantities: deviation from hover point, disturbance present in the airwake, each control stick inputs, attitudes, power, and thrust. Two hover locations shown in Fig. 6.7 are investigated. Within each figure, the left-hand-side plots refer to the case where the vehicle is hovering closer to the ground, at 20 ft. (Hover 1, green disk), while the right-hand-side plots are related to the case where the hover location is at an altitude of 85 ft. (Hover 2, magenta disk). Note that special attention has been given to the axis for easy comparison of every quantity across the three hover cases.

All of the plots previously presented are in the time domain, which sometimes hides valuable information. The occasional periodic nature of the approach results strongly suggest a frequency analysis should be performed on the data. However, the trajectory included many different stages making that data unsuitable for a proper frequency analysis. Alternatively, a single maneuver is performed for 120 s — hover. Therefore, the control inputs of the hover cases presented in this section are now suitable for frequency-domain analysis. In the results shown in the time domain for the rest of this section, only the last 60 s are shown, rather than the full 120 s. This was preferred due to space limitations and the desire to keep the plots as compact and readable as possible

The relative deviation of the vehicle's center of gravity from the hover point is shown first in Fig. 6.16. In both hover scenarios investigated, ABL cases present significantly increased disturbances, in all 3 directions. Although the differences are of the order of 1 ft, they can still be important for precise operations and/or landings, especially when paired with ship motion, which is not accounted for in the present work.

The magnitude of the deviation is directly influenced by the controller used. In this work, the NLDI controller was set to keep the vehicle on the specified hover location by a tight tolerance. Note that although the magnitude of the disturbances might change

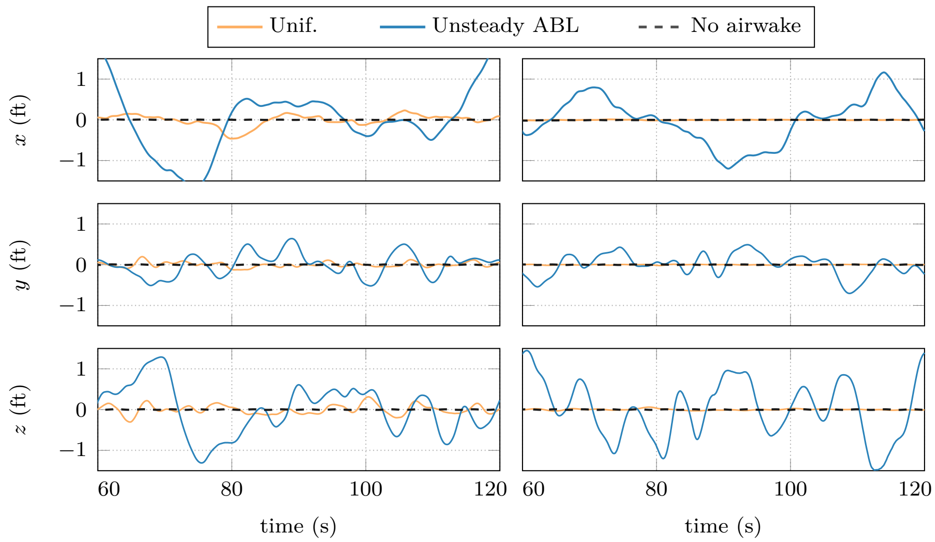

Figure 6.16: Hover: Deviation from the specified hover position. Negative x means closer to the ship. Left: *Hover 1*; Right: *Hover 2*.

depending on the controller used, the general trend is unlikely to change.

The disturbances the helicopter experiences while hovering are shown in Fig. 6.17. Once again, confirming what has been observed in the approach trajectory, the disturbances are significantly higher under the ABL inflow for positions far from the airwake. In such locations, most of the airwake content is from the pure background inflow. The uniform inflow case exhibits non-zero disturbances that are due to the ship airwake.

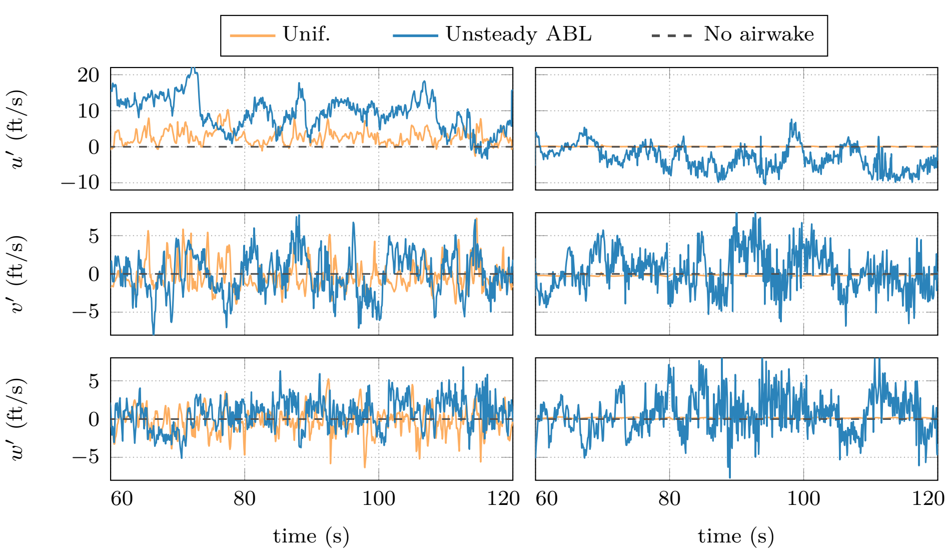

Figure 6.17: Hover: Disturbances present in the airwake at the hover location. Left: *Hover 1*; Right: *Hover 2*.

Next, the control stick activity for the two cases is investigated. The same data will be shown in both the time and frequency domains. With respect to the frequency domain, ultimately, the interest lies in observing differences in energy content in the frequency range that influences the pilot and increases the workload. Again, such a range is known to be 0.2–2 Hz [2, 73]. Power spectral density (PSD) plots are used to evaluate the energy content associated with the stick inputs needed, representing a preliminary quantification method to investigate the increase in pilot workload. To obtain the PSD plots presented hereafter, Welch's algorithm [134] is used with 110 s of data (discarding the first 10 s used for trimming purposes). The window size is an important parameter to choose, as it directly affects the low-frequency end of the curves. A small window provides smoother averaged data, but can compromise the accuracy of the low-frequency end of the spectrum. A very large window, on the other hand, results in few overall sampling windows and may not provide smooth data over the frequency range of interest. In these analyses, the focus is on the difference in the energy content, but perhaps most importantly, on the trend of the differences. With that in mind, a window size investigation is provided in Fig. 6.18. In such figure, a sample lateral cyclic and collective result dataset is investigated under different window sizes.

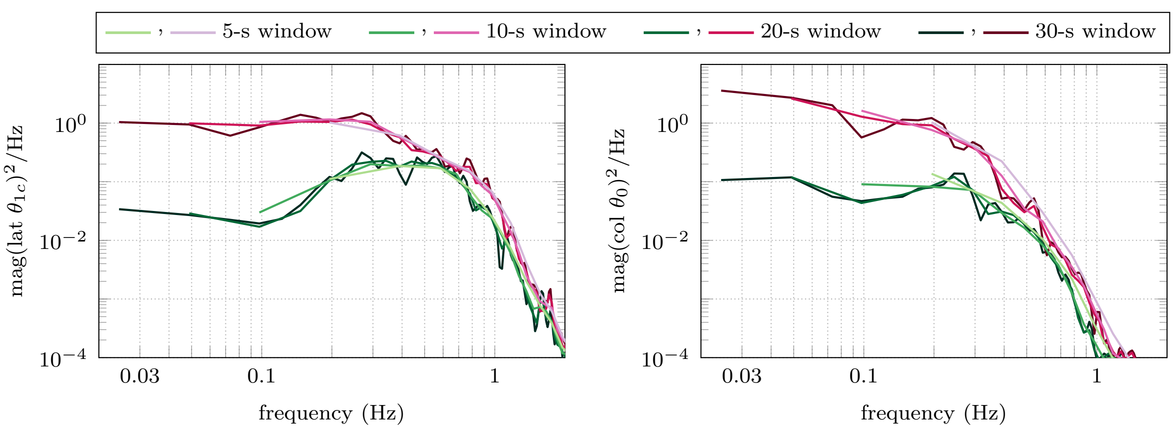

Figure 6.18: Window size investigation for Welch's PSD algorithm. Green curves are from a typical uniform inflow scenario, whereas purple curves are from a typical ABL case. The range of interest is 0.2–2 Hz.

The quantities picked to show in Fig. 6.18 is from a case that will be investigated in the next section and are representative of the overall trends observed. The smallest window shown, 5 seconds, yields 0.2 Hz as the lowest frequency. As a consequence, the data at this frequency is not reliable — since this is part of the range of interest (0.2–2 Hz), it is decided that such window is too small. On the end of the windows investigated, a 30-second window yields a lowest frequency of about 0.03 Hz. While the lowest frequency is more than adequate, such window size results in very few sampling windows and thus averaging does not result in a smooth curve, as can be seen by the dark curves of Fig. 6.18. Two intermediate window sizes are also shown.

Given the trends observed in Fig. 6.18 and the frequency range of interest, a 10-second Hanning window with 50% overlap was selected. Such window yields the lowest frequency of 0.1 Hz. It was decided to compromise the 0.1 Hz data point in favor of smoother data within the range of interest. Note that with a 10-second window, Nyquist is satisfied. In all of the PSD plots from here on, a 10-second window is used.

The cyclic controls both in time and frequency domains are shown in Fig. 6.19, collective in Fig. 6.20, and the pedals/directional in Fig. 6.21. Regarding time-domain data, overall, the magnitude of the controls necessary was larger for both cases under ABL inflow than under uniform inflow, while the frequency also appears to have changed. The increased magnitude, which represents an increase in the used physical range of the controls, by themselves, represents additional pilot workload.

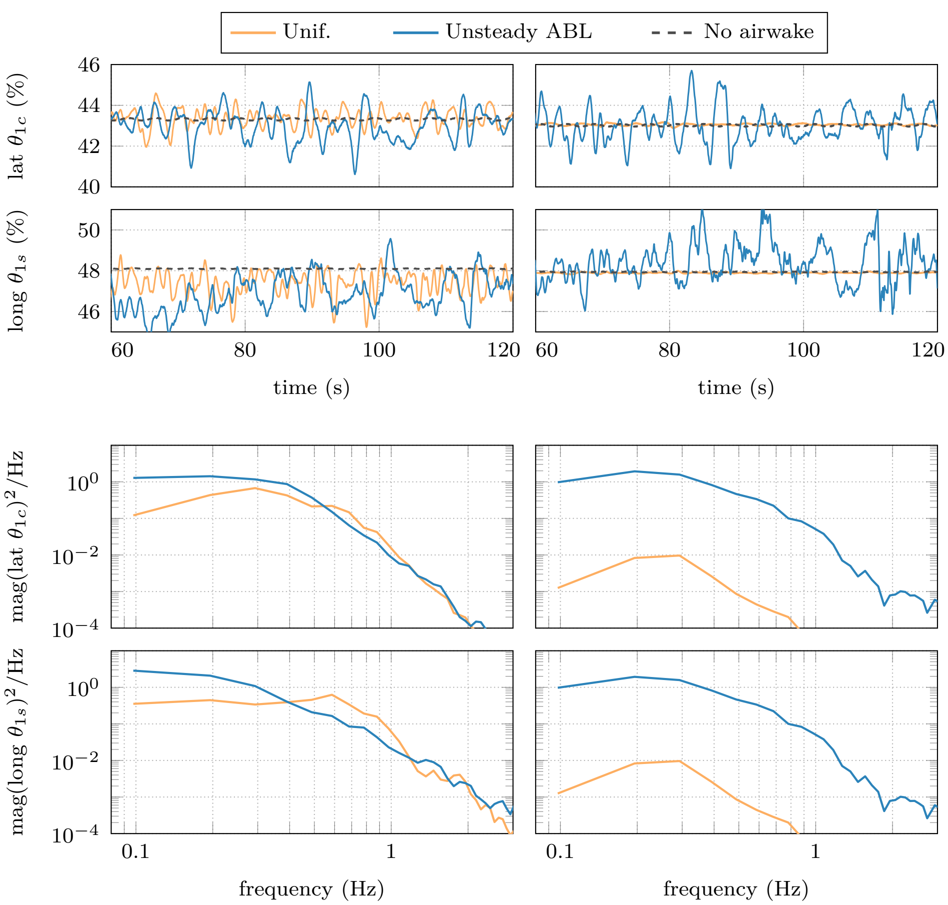

Figure 6.19: Hover: Cyclic stick inputs, lateral and longitudinal. Top two: time domain; bottom two: frequency domain. Left: *Hover 1*; Right: *Hover 2*.

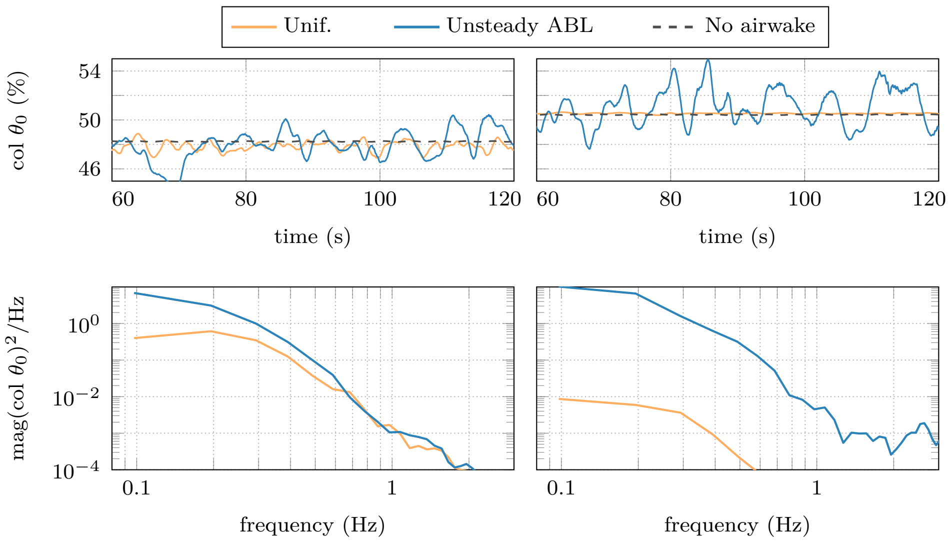

Figure 6.20: Hover: Collective stick inputs. Top: time domain; bottom: frequency domain. Left: *Hover 1*; Right: *Hover 2*.

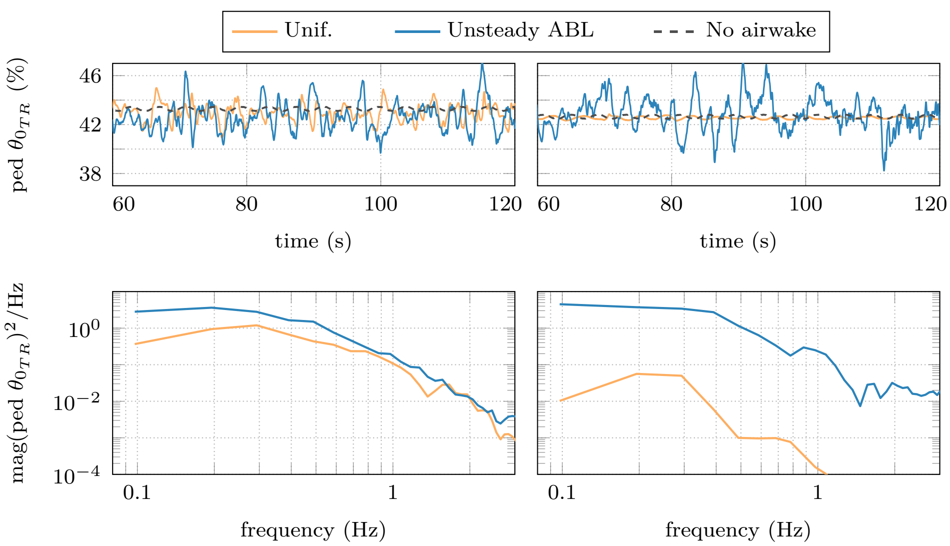

Figure 6.21: Hover: Pedal inputs. Top: time domain; bottom: frequency domain. Left: *Hover 1*; Right: *Hover 2*.

Regarding the energy content, in all cases presented (Figs. 6.19–6.21), the energy from the lowest frequency investigated, 0.1 Hz, all the way to around 0.6 Hz, is consistently higher when the helicopter is subject to the unsteady ABL inflow. In the range 0.6–2 Hz, the ABL appears to be of comparable magnitude. Under ABL inflow, the sticks also exhibited higher energy content above 2 Hz, however, that range is not relevant anymore for pilot workload so the presented data is clipped at 3 Hz. Overall, hover maneuvers under atmospheric inflow impose higher fluctuations on the vehicle which is reflected in additional controls. The ground effect can be seen in the collective-usage time-history, as the *Hover 1* case presented lower mean values of collective. These are expected behaviors captured in the one-way coupled simulations. The *Hover 2* case shows the effect of the pure unsteady ABL inflow, outside of the wake and subject to the large-scale atmospheric eddies. As expected, a uniform inflow model was not effective there, as the experienced disturbance is due to the atmospheric turbulence.

The aircraft attitudes maintained by the controller are shown in Fig. 6.22. The observations that can me made about these results are similar to the hover stages of the approach trajectory. In the low altitude case (*Hover 1*) pitch is mostly above the value seen in the 'no airwake' case, which is not observed in the high altitude case *Hover 2*. This is explained through a closer look at the airwake disturbances plots: there is a higher average disturbance at higher altitudes, such that the aircraft needs to maintain nose-up behavior most of the time. This can be explained from a turbulence perspective — the size of eddies scale with the distance from the wall (ground), such that the eddies present in high altitudes are larger than those present in lower altitudes. Attitudes under ABL inflow present higher amplitude and different frequency behavior. The differences are evidenced in the results of translational positions of the aircraft (discussed earlier — see Fig. 6.10 and 6.16), with considerably higher amplitude and different frequency observed under ABL inflow, at every location investigated. Lastly, the 'no airwake' condition has almost no effect on the helicopter attitudes.

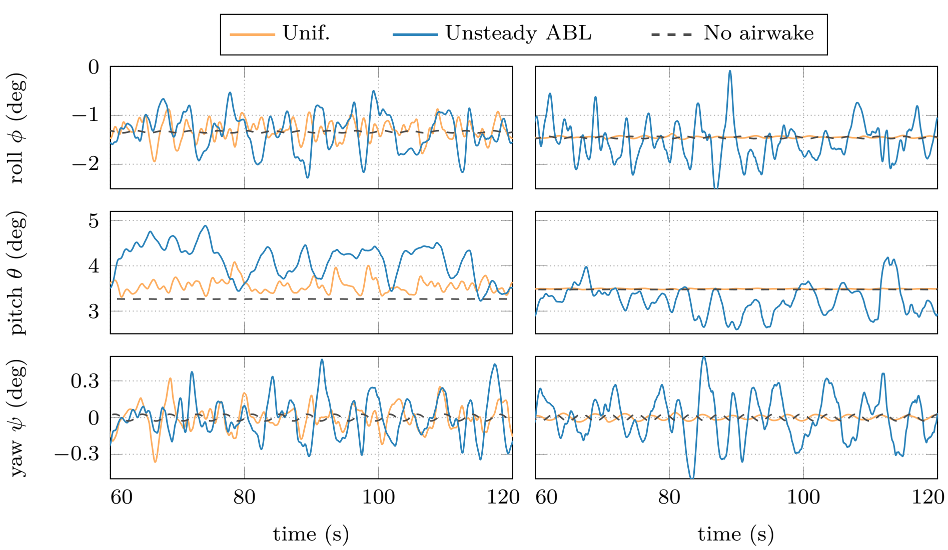

Figure 6.22: Hover: Attitudes during hover. From top to bottom: roll, pitch, and yaw. Left: *Hover 1*; Right: *Hover 2*.

Regarding the power, the scenario where the vehicle is in lower altitude resulted in lower power requirements, as expected — see Fig. 6.23. Fluctuations in power can be observed in both hover positions and under both inflows. With respect to uniform inflow, stronger fluctuations are observed on the Hover 1 case. Under unsteady ABL inflow, however, the fluctuations are much stronger, with the *Hover 2* case having a larger valley-to-peak difference. Similar behavior can be observed for the thrust in Fig. 6.24. The scenario where the vehicle is hovering at a lower altitude required slightly lower thrust, and uniform inflow did not result in nearly the same fluctuation levels found in the ABL case.

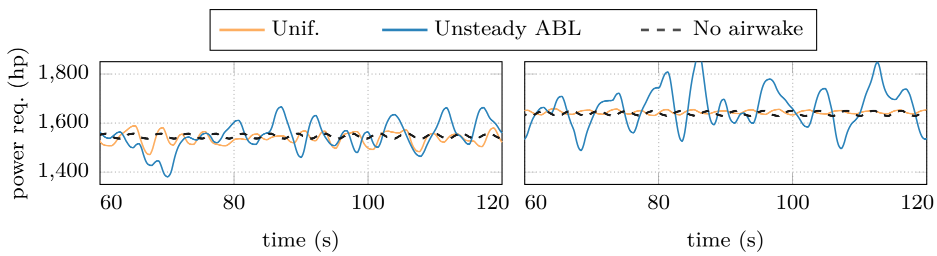

Figure 6.23: Hover: power required. Left: *Hover 1*; Right: *Hover 2*.

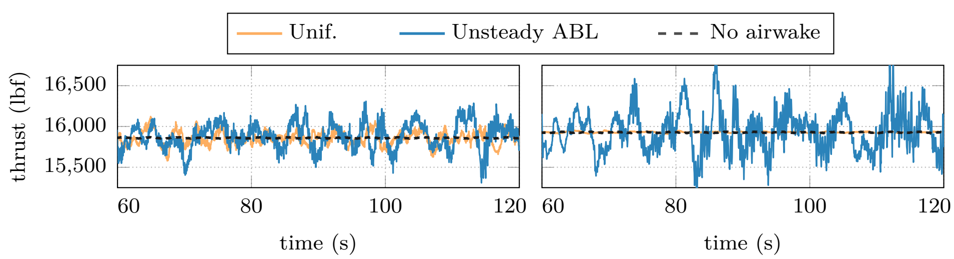

Figure 6.24: Hover: Thrust. Left: *Hover 1*; Right: *Hover 2*.

6.4 Unsteady vs. Steady ABL

Attention is now turned to the comparison of unsteady vs. steady ABL approach. This section presents the results obtained with PSUHeloSim. With respect to the CFD, both OpenFOAM and OVERFLOW were used and the airwakes used here were thoroughly described in the previous chapter. Following the discussion presented earlier, analyzing the results in the time domain do not offer much insight and were of similar behavior as the ones shown in the previous section. Therefore, the focus of the discussions is on the frequency-domain analysis of the controls.

Similarly, two hover locations are executed here, now considering the vehicle subject to the airwake. The scenarios investigated here correspond to a helicopter representative of the UH-60 hovering above the flight deck. This region is of interest because (i) is highly turbulent, and likely to be affected by the incoming atmospheric turbulence, and (ii) is it a reasonable location to perform station keeping in a real-world setting, while waiting for the right time to land. The two hover locations investigated are:

Hover 1 hover at the center of the deck, aligned with the centerline of the ship, 35 ft above the deck.

Hover 2 hover at 75% of the deck, aligned with the centerline of the ship, 45 ft above the deck.

The hover locations are shown in Fig. 6.25. The yellow disk represents the *Hover 1* location, while the red disk represents the *Hover 2*. The plots shown in this section follow a different structure. A set of figures is presented for each hover position. The left-hand-side plots are related to the cases executed in OpenFOAM, whereas the right-hand-side plots relate to OVERFLOW cases. The uniform inflow case is executed in both codes and serves as a baseline for comparison. Again, comparisons are only performed within the same code.

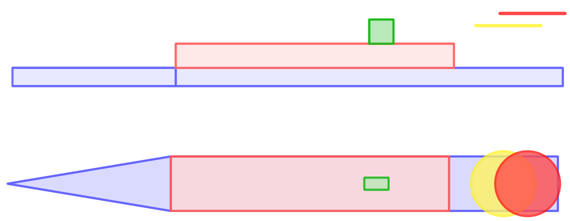

Figure 6.25: The two hover locations investigated with respect to the unsteadiness of ABL inflow modeling. Figure to scale, including size of rotor.

6.4.1 Hover Cases

The results from the two hover locations listed above as now presented. The helicopter control usage in the *Hover 1* location is shown first. Figure 6.26 shows a frequency-domain analysis of the cyclic commands. Results in the time-domain are not shown in this section. The PSD plots presented here were processed in a similar manner — Welch's algorithm, 10-second Hanning window, etc.

From Fig. 6.26, it is apparent that there is a larger difference in the OpenFOAM cases than in OVERFLOW ones. Upon close inspection, however, it can be noted that

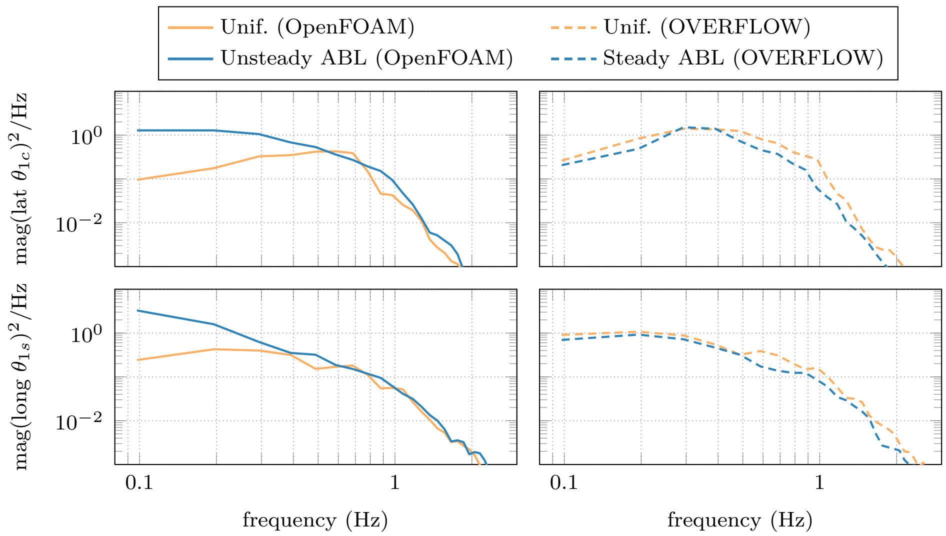

Figure 6.26: Cyclic commands in the frequency domain for the *Hover 1* case. Top is lateral, bottom is longitudinal.

the uniform inflow solution from OVERFLOW resulted in slightly higher energy content. The behavior of both longitudinal and lateral commands is similar. Figure 6.27 shows the results from the collective command.

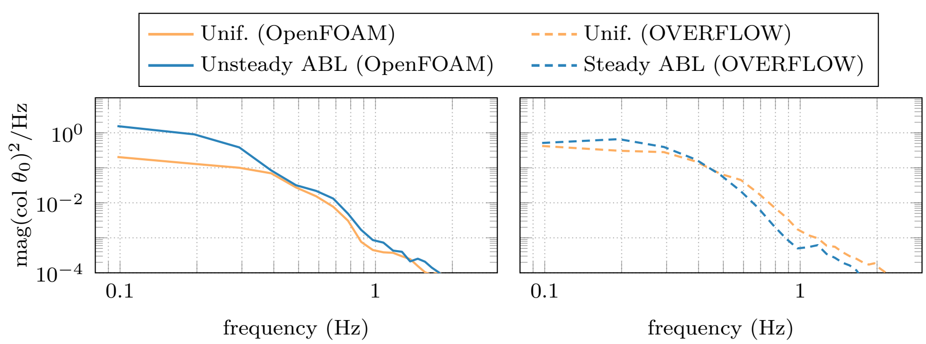

Figure 6.27: Collective command in the frequency domain for the *Hover 1* case.

The collective exhibited similar trends. Low frequencies around 0.2–0.4 Hz have an increase under unsteady ABL conditions. Higher frequencies, still in the range of interest, do not appear to have significant effect. For the steady ABL scenario, both curves have been close to each other, which indicates they have similar unsteady features. Interestingly, OVERFLOW's uniform inflow still has a higher energy content (although small).

The directional control of the vehicle is obtained through the pedals, and their usage is shown in Fig. 6.28.

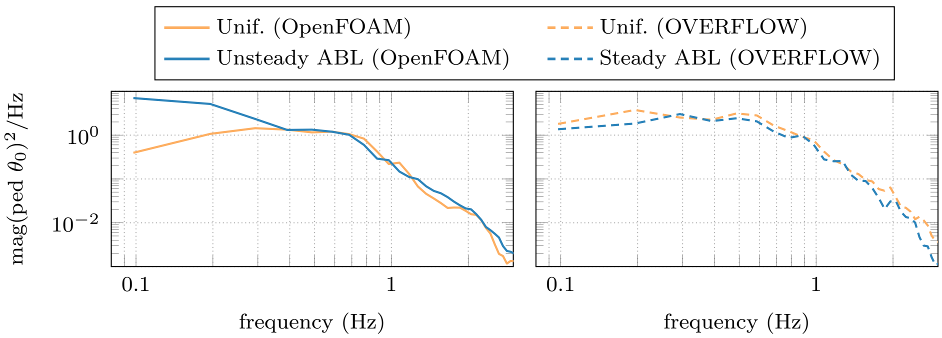

Figure 6.28: Directional (pedals) command in the frequency domain for the *Hover 1* case.

The common aspect in all of the results is that the energy related to the stick usage in the lower frequencies is increased when under the effect of the resolved unsteady ABL. Lateral and collective show the largest increase. The increase in the collective is likely due to the smaller-scale vertical disturbances that are present in the unsteady ABL (OpenFOAM) case — see Fig. 5.16. Above 0.5 Hz, however, the unsteady ABL does not seem to play a major role. Lateral flow, on the other hand, results in increased lateral cyclic command. Flow shedding off the chimney and the wake downstream the superstructure contribute to increased lateral cyclic use; however, the turbulence present in the unsteady ABL further accentuates the disturbances and it results in increased stick usage.

Several different locations have been analyzed in this work, but for the sake of simplicity only one more location is shown — *Hover 2*. Shown next are the PSD of the same four controls for the *Hover 2* case. Figure 6.29 shows the cyclic commands, Fig. 6.30 the collective, and Fig. 6.31 the pedals.

Some trends can be observed. The gap between the curves contrasting uniform and ABL inflow for the OpenFOAM cases are larger, indicating that the higher the aircraft is, the more disturbances from the ABL are experienced. These disturbances are also reflected on the controls. Such findings are consistent with previous studies by some of the authors [135] where it was shown that an aircraft subject to an atmospheric flow only (no wake) exerts a substantial amount of extra workload to the pilot, when compared to a uniform-inflow modeling approach. Regarding the OVERFLOW solutions, one aspect stands out: the stick usage under uniform inflow has consistently exhibited higher energy content for the frequency range investigated. An interesting result that has been consistent with many locations investigated near the flight deck is that, in OVERFLOW, the energy under the steady ABL has usually been lower than the uniform inflow. It

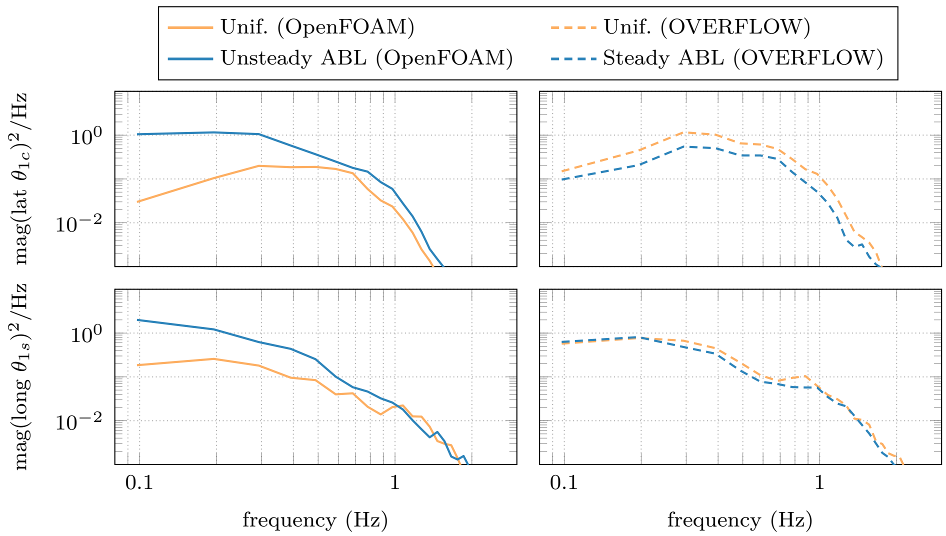

Figure 6.29: Cyclic commands in the frequency domain for the *Hover 2* case. Top is lateral, bottom is longitudinal.

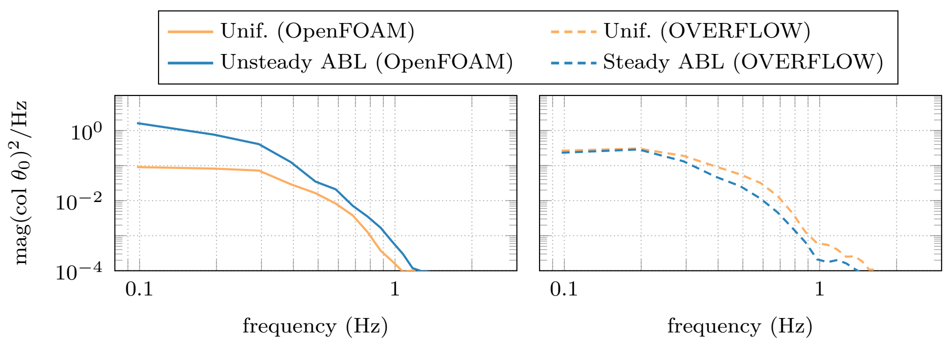

Figure 6.30: Collective command in the frequency domain for the *Hover 2* case.

appears that the velocity gradient is damping some of the unsteady phenomena and that is reflected on the helicopter. Nonetheless, the uniform inflow when compared to a steady ABL approach appears more conservative as it predicts a higher energy content and thus a higher pilot workload.

The common theme of the results presented is that in OpenFOAM, the difference between the uniform and the unsteady ABL is larger than the difference between the approaches executed in OVERFLOW. In general, direct comparisons of the two uniform inflow cases, or even the two ABL approaches, cannot be made. They were executed under very different setups, i.e., solver, turbulence model, and wall treatment are some of the differences. Spalart-Allmaras, used in OVERFLOW, can overdamp some unsteady features, and the use of low Mach preconditioning can further accentuate it. It is hypothesized that some of the differences observed are due to the turbulence model, with

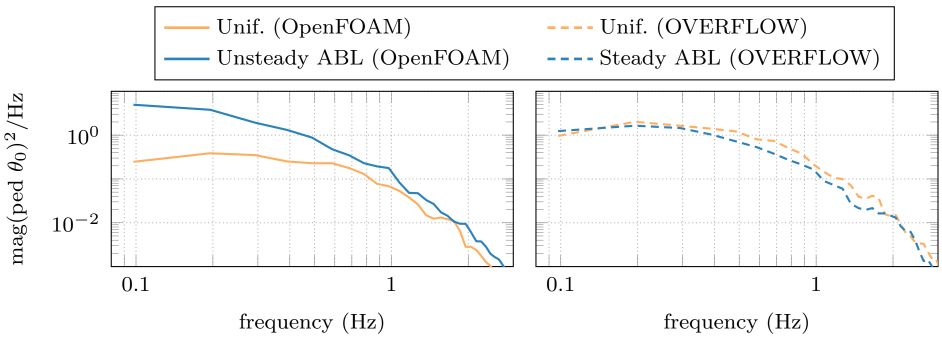

Figure 6.31: Directional (pedals) command in the frequency domain for the *Hover 2* case.

the k equation in OpenFOAM being more diffusive than SA. Only the cases within the same code are compared.

Looking closely at the increase of energy across the cases, there are several noteworthy aspects. The unsteady ABL has consistently exerted 2–3 times the energy of the uniform inflow scenario (both executed in OpenFOAM) for frequencies below 0.4 Hz for the *Hover 1* case. At 0.2 Hz, for instance, it experienced at least a 4-fold increase in the energy content, with the collective and lateral controls showing the highest differences. No significant differences were noted for frequencies above 0.5 Hz. For the *Hover 2* case, however, the increase was higher. A 6-fold increase is seen in ABL cases for frequencies below 0.3 Hz for the lateral, collective, and pedals command. Differently than the first hover case, there was an increase at frequencies higher than 0.5 Hz. Regarding the steady ABL (executed in OVERFLOW), no significant differences were observed between the two hover cases, with the exception of the consistently lower energy related to the lateral command under *Hover 2*.

In summary, comparing the positions *Hover 1* to *Hover 2*, the differences observed in the energy content become larger for the unsteady ABL case (OpenFOAM) and smaller for the steady ABL case (OVERFLOW), indicating the higher the aircraft is, the more significant the atmospheric effects are. The reason for this is that the aircraft is then flying less in the wake of the deck, and more in the wake of the chimney and subject more to the effects of the incoming unsteady ABL flow turbulence and its interaction with the chimney. That is an important aspect to consider for ships where the flight deck is flat and thus the incoming atmospheric turbulence is expected to interact more with the aircraft and reflect on the pilot workload. This aspect is also very relevant when the wind-over-deck is not zero, as more of the deck is exposed to the incoming flow.

It is important to note, however, that on a real-world setting, a significant increase in pilot workload is observed when comparing a hover outside of the wake and inside of the wake. For instance, on a ship such as the LHA, a landing in the wake of the island is considerably more challenging than a landing on a spot subject only to the incoming inflow. In this work, an increase *between* the two modeling approaches has been identified, which is not the same as an increase across different hover locations. In fact, upon close inspection of the last two hover cases presented, the energy for hover in the airwake is larger than outside, for the uniform inflow cases.

6.5 Conclusions

In this chapter, the unsteady aspects of the incoming inflow have been assessed from a flight dynamics perspective. At first, an analysis of the aircraft flying purely in the turbulent atmospheric inflow was performed. Next, a comparison of the different modeling approaches with respect to a hovering vehicle near the deck was performed. The time-accurate CFD solutions have been one-way coupled with flight dynamics.

The following conclusions can be drawn from this work

- Uniform inflow cases executed in both OpenFOAM and OVERFLOW match results from wind tunnel experiments. This also constitutes further verification of the immersed boundary method used in OpenFOAM. The uniform inflow cases serve as a baseline to analyze the increase in pilot workload for each code;

- Regarding the differences between unsteady ABL and uniform executed in OpenFOAM, increase in energy content across all frequencies known to affect pilot workload have been found. The largest increases, however, are present in the lower frequencies of the spectrum (approximately 0.1–0.5 Hz);

- For the steady ABL case, executed in OVERFLOW, no significant change has been captured when comparing to the uniform inflow baseline of the same code. In fact, a decrease in content has been experienced. The results suggest that, for the level of sheared inflow investigated (Fig. 4.18), not much is gained with the additional fidelity of modeling the sheared profile;

- For hover locations subject less to the wake of a backward-facing step and more to the atmospheric turbulence, more significant differences between the modeling strategies have been observed. This increase may be important when simulating aircraft carriers that have a flat flight deck;

- Finally, from the analysis of helicopter stick usage when hovering in the turbulent airwake, results suggest that when modeling the ABL, a fully unsteady approach is preferred. The so-called “steady ABL” can be deceiving or not add relevant information for zero WOD conditions

It is worth noting that a single condition has been explored in this effort. A single flow velocity, a single atmospheric stability state with very little shear, and a single wind-over-deck angle have been investigated. In a scenario of 30 degrees wind-over-deck, for instance, the flowfield will present itself very differently. It is important to realize that this is one particular scenario that may not represent a generalized real-world setting. Much more atmospheric effects may be present if the wind is blowing from a different direction than that of the heading of ship, and thus results closer to *Hover 2* may be expected. It is also important to recall the discussion that the results presented in this work indicate an increase in energy content when comparing different modeling strategies. Such perspective is different than that of a real-world setting where it is known that the vehicle flying in the wake of an island imposes more workload on the pilot than when it is hovering outside of the wake.

In conclusion, the differences observed in this work may be relevant for piloted workload under a flight simulation setting. Future work consists of further analysis of the airwake data obtained via the different approaches, further quantifying the unsteadiness present. Piloted flight simulation with the obtained airwake databases is also anticipated. The response of a human pilot is likely to be different than that of a controller. Large eddies and correspondent large deviations may require extra workload. Those effects were not quantified in the current effort.

Chapter 7 Conclusion and Future Work

The dynamic interface between a ship and a helicopter is a complex, dynamic, and hazardous environment, presenting a unique set of challenges to pilots. Some of these challenges are degraded visual cues (especially at night), increased turbulence from the airwake, restricted landing site, and ship movement (pithing, heaving, yawing). Added to the airwake turbulence is the turbulent fluctuations present in the freestream. These difficulties, as well as the level of workload required from the pilot, are considered when a ship-helicopter operating limits diagram is constructed for a given ship/helicopter combination.

Understanding of the physical phenomena that occurs in this dynamic and unsteady environment allows the use of modeling and simulation to improve sea trials. Simulation tools have the potential to provide a controllable environment, which can result in safer and cheaper alternatives to pilot training. Model fidelity requirements of each component present in a dynamic interface vary between the purpose of the tool. Here, the focus has been on the airwake, which is known to contribute to an increase in pilot workload in shipboard launch and especially recovery operations.

This dissertation investigates the effects of fully-resolved atmospheric turbulence on a ship airwake. The handling impact on a helicopter flying in an ABL-augmented wake has been assessed. The ultimate goal of the project is to enhance simulator fidelity and therefore improve pilot training. This section begins by listing the conclusions and findings of this work. Next, the specific contributions are discussed. Limitations of the tool developed are presented and some suggestions for future research are offered.

7.1 Conclusions

A ship airwake is formed as a combination of wind and ship motion, and it is influenced by elements of the ship superstructure. When considering the wind, the unsteadiness of the turbulent atmosphere needs to be accounted for. In this work, the effects of the turbulence present in the atmospheric boundary layer on a ship airwake are studied in detail. The subsequent effect of the modified airwake on the dynamics of a helicopter is assessed by means of coupled CFD and flight dynamics analysis. Pilot workload is then quantified by the control stick usage from a frequency-domain perspective.

For the fluid dynamics component of this work, the CFD codes OpenFOAM [92] and OVERFLOW [123, 127] were used. Scenarios that include the realistic, unsteady ABL were all executed in OpenFOAM, while the steady ABL cases were obtained using OVERFLOW. The helicopter dynamics calculations, on the other hand, were performed by GENHEL-PSU and PSUHeloSim. A one-way coupling methodology was used, similar to those used in real training flight simulators.

The main findings and conclusions drawn are summarized and briefly below.

IBM suitability The immersed boundary method has been implemented. It has been shown that it is a suitable approach for ship airwake problems. The usual drawbacks associated with the method do not apply if the interest is on the highly separated flow. The immersed boundary method implemented for this work has been validated through uniform-inflow solutions compared to wind tunnel results and other body-fitted CFD simulations.

Precursor data The ABL solver has been validated with data from the wind energy literature. At a precursor level, quantities such as mean wind speed, momentum fluxes, velocity variances and velocity variance fluxes have all been matched for different stability states. Studies that focus in different heights have been explored and the CFD solver routinely captured the relevant trends. Neutral cases with low wind speeds, around 8 m/s are shown to match well a logarithmic profile; however, with higher wind speeds, the obtained profile shifts towards a 1/7 power-law curve.

Domain size requirements When including the ship, it has been shown that the domain size recommendations from the wind energy community do not necessarily apply. In the problem explored, the associated time scales of interest have to be taken into account and thus the large length scales that have a small time scale need not to be captured. Different requirements exist for different applications.

ABL-modified airwake Neutral cases with two levels of shear are investigated and compared to uniform inflow solutions. Analysis of velocity distributions along probe lines at the deck revealed that the presence of an ABL modifies the recirculation region and delays the reattachment point. Different levels of shear yields different characteristics (see Fig. 5.8). For airwakes modified by unsteady ABL inflow, spectral analysis at locations near the ship's flight deck indicated that higher energy content at frequencies above 3 Hz, with better agreement to Kolmogorov's $-5/3$ cascade, have been captured. Increased content has also been observed in the 0.1–0.3 Hz range. This represents an important finding, as the trend observed matches that also seen during at-sea observations, which are usually not captured in standard CFD simulations (see Figs. 5.12 and 5.13).

Solution scalability An aspect pertinent to airwake solutions obtained with uniform inflow modeling is that they are usually scalable. Such scaling has been reported in the literature and is also observed here. For ABL-modified airwakes, however, this scaling is not present. The airwake can present itself quite differently depending on the level of shear present and they are not related by a one-to-one relationship. It is also suggested that comparisons of airwake data that include an ABL are performed using dimensional data. It was found that normalization of data may either introduce artificial deficit increased, or may hide the underlying profile.

Asymmetry Asymmetric flow features reported by some authors have also been found in OpenFOAM simulations, but not on OVERFLOW ones. For cases subject to ABL inflow, no asymmetry was observed, likely because of the increased mix of momentum due to the turbulence present on the freestream.

Steady ABL This research also explored the so-called steady ABL. This part of the work was executed using OVERFLOW. This inflow type is often mentioned in the literature as a "higher fidelity" alternative to uniform inflow, although no actual evidence is given. Here, the airwake solution obtained via this method is used in helicopter dynamics computations. The steady ABL solution is contrasted by a low-shear neutral case, in which a time-averaged profile matches the profile of the steady ABL simulation. This way, the time-accurate effects can be assessed. While these two scenarios are very similar in a time-averaged sense, they differ greatly when a snapshot of the flowfield is analyzed — see Figs. 5.15 and 5.16.

Flight dynamics, hover outside the wake The airwake generated under uniform inflow, steady ABL, and unsteady ABL are then used as databases for the execution of an approach scenario and hover cases using GENHEL-PSU and PSUHeloSim. By means of one-way coupled simulations, the frequency-domain use of the control sticks is analyzed. Pilot workload is quantified by the energy associated with the stick usage. At first, two hover locations outside of the airwake are considered, subject only to the turbulence present in the inflow, at two different heights. Uniform inflow approaches in this case had essentially laminar flow. The ABL turbulence had a substantial effect on the vehicle, resulting in significantly more disturbances, considerably more power fluctuations, and fluctuations on the vehicle's attitudes. While this was observed on both cases, it was much more prominent in the case of higher altitude. The fluctuations were reflected on the stick usage. The uniform inflow case barely exerted any effect and had comparable results to a case where no external disturbances were provided (Pitt-Peters inflow model only). Analysis of the energy related to the stick usage showed that substantially more energy was found for the ABL case across all of the frequency range investigated for high altitude case, and a lower increase for the low altitude case, found in the range of approximately 0.1–0.6 Hz. These results suggested that the large length-scale eddies that are present in the atmosphere seems to affect the vehicle, and that a higher altitude contains potentially larger structures that affect the vehicle in a more significant way.

Flight dynamics, steady vs. unsteady ABL Finally, two hover locations at the flight deck have been investigated. Here, the steady and unsteady ABL have been compared. Direct comparisons between OpenFOAM and OVERFLOW are not performed. They have slightly different numerical setup, and thus it was preferred to execute a baseline case using uniform inflow and then look at the difference between the ABL and uniform flow case for each code, separately. One hover location is at the center of deck, at 35 ft high, while the other is about 20 ft downstream at 45 ft high. These locations were selected in order to check whether or not the effects from the atmospheric turbulence observed previously would apply here. For the unsteady ABL case, the results indicated that when the airwake turbulence dominates, an increase in the energy associated with frequencies in the range of 0.1–0.3 Hz has been observed. For frequencies above 0.5 Hz, not many differences are observed at the energy associated with the stick use. However, one of the main findings of this work is that when the aircraft was hovering only 10 ft higher, in a flowfield that was a mix of airwake and atmospheric turbulence, the energy associated with the unsteady ABL was higher than that associated with the uniform inflow for all of the 0.2–2 Hz spectrum. Now, with respect to the OVERFLOW's steady ABL case, no appreciable differences have been captured, in neither of the hover locations. The steady ABL approach did not affect the vehicle nearly as much as the unsteady ABL did. In fact, the uniform inflow consistently exhibited higher energy (although very small) than that seen under the steady ABL. It is hypothesized that the velocity gradient present on the steady ABL may be dampening some of the relevant frequencies.

The results indicate that when the aircraft is flying at a location that is subject to more of the atmospheric eddies, the vehicle tends to react to the unsteadiness present. This is especially relevant for a ship with a flat deck (similar to the LHA class). If the vehicle is solely in the wake of (e.g.) the superstructure, no relevant differences were observed.

In summary, while it is known that the airwakes are often dominated by vortex flows and unsteady features that are known to adversely affect helicopter flight operations, in this work, it was shown that the presence of the ABL can have an increased impact on the vehicle, especially if the landing spot is not directly in the wake of a superstructure component. Extra disturbances on the vehicle results in more control activity, which is likely to increase pilot workload.

7.2 Contributions

The contributions of this work can be summarized by the published material. The investigation can be separated into three distinct stages and they are listed below. Following, a summary of the findings is given.

- The coupling of the precursor ABL data into a domain with the ship. Implementation and validation of the IBM, validation of ABL data, airwake comparisons.

  Presentations, proceedings, papers:

  1. AHS Forum 73 (2017), reference [136], "High-Fidelity Simulations of the Interaction of Atmospheric Turbulence with Ship Airwakes".
  2. APS DFD Presentation (2017), "Numerical study of ship airwake characteristics immersed in atmospheric boundary-layer flow".

3. Journal of the AHS (2018), reference [131], "An Evaluation of the Effects of Resolved Shear-Driven Atmospheric Turbulence on Ship Airwakes".

- Coupling with GENHEL, investigation of approach and hover trajectories. Hover outside of the wake and subject to the ABL turbulence only. Pilot workload evaluation

  Presentations, proceedings, papers:

  1. AHS Forum 74 (2018), reference [137], "Simulation of a Helicopter-Ship Dynamic Interface Using Offline Database of Atmospheric Turbulence-Modified Airwake".
  2. Journal of Aircraft (2019), reference [135], "Coupled Simulations of Atmospheric Turbulence-Modified Ship Airwakes and Helicopter Flight Dynamics".

- Setup of OVERFLOW scenario, development of the steady ABL and comparison with an unsteady ABL. Multiple hover scenarios investigated, pilot workload evaluation.

  Presentations, proceedings, papers:

  1. AIAA Aviation (2019), reference [138], "On the unsteadiness of ship airwakes subject to atmospheric boundary-layer inflow from a helicopter operation perspective".
  2. Journal of Aircraft (submitted, under review, 2019), reference [139], "Effects of Atmospheric Turbulence Unsteadiness on Ship Airwakes and Helicopter Dynamics" (title subject to change).

The conclusions of this work have been outlined in the previous section, and the specific contributions can be summarized below:

- Confirmed previous findings from Shipman et al. [122] about capturing the ship's boundary layer and supported the simple and easy choice of the immersed boundary method for such problems;
- Showed that an ABL-modified airwake can be substantially different than that of an uniform inflow, and that different levels of shear can result in different airwake characteristics;
- Performed one-way coupled helicopter flight simulation under ABL inflow, quantifying differences observed in the flight controls by means of power spectral density;

- Showed that control activity has increased energy content when the vehicle is subject to atmospheric turbulence;
- Showed evidence for the need of ABL modeling in scenarios where the ship is not aligned with the incoming flow (WOD different than zero) and/or ships with a flat top.

Additionally, it has been suggested that comparisons of velocity data in which an underlying ABL is included is performed in dimensional form. Although uniform-inflow cases have a clear choice of a freestream velocity, an ABL does not have *one* characteristic freestream value. Presentation of normalized ABL data may introduce deficits that are not present and may hide information about the actual underlying profile.

7.3 Limitations

The framework developed and explored in this work had the goal of providing a better understanding of the effects of the atmospheric turbulence in the wake and then on the helicopter dynamics. The tool, however, has a few clear limitations. Some of them are discussed below. Note that the framework allows some of these limitations to be overcome in a relatively simple manner in future research.

Ship model Only the SFS2 has been explored. Results indicated that ABL effects may be more relevant for ships with geometries similar to the LHA. The SFS2, however, offers the largest number of publicly available results that are used for validation and comparison purposes.

Few conditions This work has explored in more detail two levels of shear present in a neutral ABL. Also, only one ship heading has been considered. This limitation is acknowledged, but the tool developed is ready to handle the investigation of these other scenarios.

Ship motion This work does not explore ship heaving or any general motion. Because of the IBM representation of geometries, however, provided a fine enough grid along the boundaries to the geometry, this is an aspect that the current framework could handle in a relatively straightforward way. The body representation by means of the η variable means this field can be changed at every time step. It is noted, however, that studies by Dooley et al. [48] concluded that turbulent fluctuations did not change much with ship motion, suggesting a linearized addition of motions may be possible. Additionally, another limitation described earlier is that in the cases investigated in this work, the ship is stationary, while subject to a strong wind. While such an approach is acceptable for winds aligned with the ship, it may not be representative of yawed cases.

Sea modeling The sea is modeled as a flat wall with a low aerodynamic surface roughness value. No waves or multiphase flow has been considered. This was one of the simplifications made in order to investigate the problem. Note that when considering modeling the ocean surface, the complexity is increased if consideration is given to wind-induced waves and wave-induced winds.

Occurrence of rare events In a real-world setting, there is the possibility of occurrence of perhaps rare atmospheric events that may have major consequences. For instance, a stronger gust may occur at the right time that may be of crucial importance. These stronger prescribed gusts are not implemented in the current tool.

Piloted flight simulations The flight simulation analysis presented were executed using a controller in a batch engineering analysis. Although this work provides a readily available database for piloted simulations, this aspect is not formally addressed in this work. This aspect is also suggested as a future work below.

7.4 Suggestions for Future Research

The insights and understanding gained in this work motivate the investigation of many different aspects. Some of them are discussed below.

Flight dynamics validation Additional validation of the coupled atmospheric turbulence and flight dynamics is currently being performed. One of the datasets being used is that used during the development of the Control Equivalent Turbulence Input (CETI) turbulence model by Jeff Lusardi [140–142]. The model was developed by the U.S. Army Aeroflightdynamics Directorate (AFDD) by collecting flight data from a UH-60 hovering within the airwake of a large cube-shaped hangar and extracting the control inputs required to replicate the aircraft's response to the atmospheric disturbances. The time histories of the control inputs are summed with the controller's commanded control inputs and are scalable for different turbulence levels. Use of this model for ship airwakes has been investigated in the work of

Soneson et al. [11], for instance. Currently, the unsteady ABL framework described in this work is undergoing further validation by using the flight data form the CETI model development. The goal is to compare the levels of control inputs used in both the actual flight and the simulation model.

Different scenarios Following the conclusions from this work, different wind-over-deck and different stability states may be of importance. The aspect of the more the aircraft flies into the atmospheric eddies, the more control activity is warranted may be intensified in different scenarios. For instance, a case of a ship with a wind-over-deck of 30 degrees heading can result in landing spots subject to undisturbed atmospheric winds, or lightly disturbed. Also, the interaction of the shear layers created at the corners of the ship may result in a considerably different flowfield.

Different helicopter-ship combinations This work only looked at the dynamic interface of SFS2 and a vehicle representative of the UH-60 combination. Although the availability and feasibility of further studies on different ship and helicopter models are the subject matter of a different discussion, different carriers may present different challenges to pilots. The results presented in this work indicated that ships with geometries similar to that of the LHA carrier may produce considerably different airwakes. In a general sense, ship carriers with flat top will be more susceptible to the incoming wind turbulence and the effects are likely to be greater than those found in the SFS2 with 0 degrees WOD.

Piloted flight simulation The airwake databases obtained for the development of this work are readily available to be used in a real-time piloted flight simulation setting (one-way coupled). Early and preliminary tests of this nature have been conducted at Penn State in 2018. The steady and unsteady solutions can be tested in such a setting. These simulations depend upon the availability of skilled pilots and thus are not always feasible.

Reduced-order modeling The simulations presented here are very expensive and not suitable for routine engineering design and analysis. With further investigations of different scenarios, one can develop a better understanding of the problem and the effects of different levels of shear, buoyancy, and a combination of both. The use of reduced-order modeling seems promising in this area, since not all scales are known to affect the vehicle. Using only the eigenvectors of the eigenvalues related to the important scales (those with high associated energy), the order of the problem can be greatly reduced. This can amount to a model of a new scenario, without the need to resorting to expensive CFD computations. The proper orthogonal decomposition (POD) method seems suitable, but also note the spectral POD (SPOD). SPOD [77] is the frequency-domain equivalent of the POD and may have higher suitability for this work, since the interest is heavily skewed towards time-accurate effects and frequencies of interest.

Fully-coupled model One-way coupled approaches neglect any feedback loop of the vehicle on the flowfield, and it is not known how the atmospheric turbulence will affect the vehicle and/or the pilot in a fully-coupled manner. It is acknowledged that real-time fully-coupled methods are not feasible with today's computing power, but with the use of controllers properly designed to mimic a human, some insight into the problem may be gained. Due to the nature of OpenFOAM and how the solver handles external momentum sources, such a coupling may not be too far into the future. For instance, The extra force in the momentum equation might be used to include an actuator disk model of a helicopter rotor. The author notes that several steps have already been taken towards a fully-coupled model, including the initial parallel communication between two codes, the sampling of velocity at arbitrary points in the CFD (including across processor boundaries) and the exchange of dummy data back and forth via the message-passing interface (MPI) protocol.

Bibliography

[1] Polsky, S. (2002) "Computational study of unsteady ship airwake," in *AIAA Aerospace Sciences Meeting & Exhibit*, Reno, NV, paper no. 2002-1022.

[2] Brownell, C. J., L. Luznik, M. R. Snyder, H. S. Kang, and C. H. Wilkinson (2012) "In situ velocity measurements in the near-wake of a ship superstructure," *Journal of Aircraft*, **49**(5), pp. 1440–1450.

[3] Anderson, K., B. Brooks, P. Caffrey, A. Clarke, L. Cohen, K. Crahan, K. Davidson, A. De Jong, G. De Leeuw, D. Dion, et al. (2004) "The RED Experiment: An assessment of boundary layer effects in a trade winds regime on microwave and infrared propagation over the sea," *Bulletin of the American Meteorological Society*, **85**(9), pp. 1355–1366.

[4] Businger, J. A., J. C. Wyngaard, Y. Izumi, and E. F. Bradley (1971) "Flux-profile relationships in the atmospheric surface layer," *Journal of the atmospheric Sciences*, **28**(2), pp. 181–189.

[5] Wyngaard, J. C. (2010) *Turbulence in the Atmosphere*, Cambridge University Press.

[6] Charnock, H. (1955) "Wind stress on a water surface," *Quarterly Journal of the Royal Meteorological Society*, **81**(350), pp. 639–640.

[7] Churchfield, M. J., S. Lee, J. Michalakes, and P. J. Moriarty (2012) "A numerical study of the effects of atmospheric and wake turbulence on wind turbine dynamics," *Journal of Turbulence*, **13**(14), pp. 1–32.

[8] Peña, A., C. B. Hasager, S.-E. Gryning, M. Courtney, I. Antoniou, and T. Mikkelsen (2009) "Offshore wind profiling using light detection and ranging measurements," *Wind Energy*, **12**(2), pp. 105–124.

[9] Richards, P. and R. Hoxey (2012) "Pressures on a cubic building–Part 1: Full-scale results," *Journal of Wind Engineering and Industrial Aerodynamics*, **102**, pp. 72–86.

[10] Wilkinson, C., M. Roscoe, and G. VanderVliet (2001) "Determining fidelity standards for the shipboard launch and recovery task," in *AIAA Modeling and*

Simulation Technologies Conference and Exhibit, Montreal, Canada, paper no. 2001-4062.

[11] Soneson, G. L., J. F. Horn, and A. Zheng (2016) "Simulation Testing of Advanced Response Types for Ship-Based Rotorcraft," *Journal of the American Helicopter Society*, **61**(3), pp. 1–13.

[12] Moeng, C.-H. and P. P. Sullivan (1994) "A comparison of shear-and buoyancy-driven planetary boundary layer flows," *Journal of the Atmospheric Sciences*, **51**(7), pp. 999–1022.

[13] Zan, S. (2005) "On aerodynamic modelling and simulation of the dynamic interface," *Proceedings of the Institution of Mechanical Engineers, Part G: Journal of Aerospace Engineering*, **219**(5), pp. 393–410.

[14] Azuma, A., S. Saito, and K. Kawachi (1987) "Response of a helicopter penetrating the tip vortices of a large airplane," *VERTICA*, **11**(1), pp. 65–76.

[15] Healey, J. V. (1991) "The aerodynamics of ship superstructures," in *In AGARD, Aircraft Ship Operations 14 p (SEE N92-21951 12-05)*.

[16] Wakefield, N., S. Newman, and P. Wilson (2002) "Helicopter flight around a ship's superstructure," *Proceedings of the Institution of Mechanical Engineers, Part G: Journal of Aerospace Engineering*, **216**(1), pp. 13–28.

[17] Forrest, J. S., I. Owen, G. D. Padfield, S. J. Hodge, et al. (2012) "Ship-helicopter operating limits prediction using piloted flight simulation and time-accurate airwakes," *Journal of Aircraft*, **49**(4), pp. 1020–1031.

[18] Advani, S. and C. Wilkinson (2001) "Dynamic interface modelling and simulation — A unique challenge," in *Royal Aeronautical Society Conference on Helicopter Flight Simulation, London*.

[19] Hodge, S. J., J. S. Forrest, G. D. Padfield, and I. Owen (2012) "Simulating the environment at the helicopter-ship dynamic interface: research, development and application," *Aeronautical Journal*, **116**(1185), p. 1155.

[20] Forrest, J. S. and I. Owen (2010) "An investigation of ship airwakes using Detached-Eddy Simulation," *Computers & Fluids*, **39**(4), pp. 656–673.

[21] Crozon, C., R. Steijl, and G. N. Barakos (2014) "Numerical Study of Helicopter Rotors in a Ship Airwake," *Journal of Aircraft*, **51**(6), pp. 1813–1832.

[22] Lumsden, B., C. Wilkinson, and G. Padfield (1998) "Challenges at the helicopter-ship dynamic interface," in *24th European Rotorcraft Forum*, Marseilles, France.

[23] Polsky, S. (2003) "CFD prediction of airwake flowfields for ships experiencing beam winds," in *21st AIAA Applied Aerodynamics Conference*, Orlando, FL, paper no. 2003-3657.

[24] Snyder, M. R., H. S. Kang, C. J. Brownell, and J. S. Burks (2013) "Validation of ship air wake simulations and investigation of ship air wake impact on rotary wing aircraft," *Naval Engineers Journal*, **125**(1), pp. 49–50.

[25] Thornber, B., M. Starr, and D. Drikakis (2010) "Implicit large eddy simulation of ship airwakes," *The Aeronautical Journal*, **114**(1162), pp. 715–736.

[26] Quon, E. W., P. A. Cross, M. J. Smith, N. C. Rosenfeld, and G. R. Whitehouse (2014) "Investigation of Ship Airwakes Using a Hybrid Computational Methodology," in *American Helicopter Society 70th Annual Forum*, Montreal, Canada.

[27] Gool, P. C. A. v. (1997) *Rotorcraft responses to atmospheric turbulence*, Ph.D. thesis, Delft University of Technology.

[28] Jha, P. K., E. P. Duque, J. L. Bashioum, and S. Schmitz (2015) "Unraveling the Mysteries of Turbulence Transport in a Wind Farm," *Energies*, **8**(7), pp. 6468–6496.

[29] Wilkinson, C., S. Zan, N. Gilbert, and J. Funk (1998) "Modelling and simulation of ship air wakes for helicopter operations — A collaborative venture," in *RTO AVT Symposium*, The Netherlands.

[30] Cheney, B. and S. Zan (1999) *CFD code validation data and flow topology for the technical co-operation program AER-TP2 simple frigate shape*, National Research Council Canada, Institute for Aerospace Research.

[31] Zan, S. (2001) "Surface flow topology for a simple frigate shape," *Canadian Aeronautics and Space Journal*, **47**(1), pp. 33–43.

[32] Reddy, K., R. Toffoletto, and K. Jones (2000) "Numerical simulation of ship airwake," *Computers & Fluids*, **29**(4), pp. 451–465.

[33] Tinney, C. and L. Ukeiley (2009) "A study of a 3-D double backward-facing step," *Experiments in Fluids*, **47**(3), pp. 427–438.

[34] Driver, D., H. Seegmiller, and J. Marvin (1987) "Time-dependent behavior of a reattaching shear layer," *AIAA Journal*, **25**(7), pp. 914–919.

[35] Zan, S., G. Syms, and B. Cheney (1998) "Analysis of patrol frigate air wakes," in *Proceedings of the RTO AVT Symposium on Fluid Dynamics Problems of Vehicles Operating near or in the Air-Sea Interface*, Amsterdan, The Netherlands, pp. 7–1–7–14.

[36] Syms, G. (2004) "Numerical simulation of frigate airwakes," *International Journal of Computational Fluid Dynamics*, **18**(2), pp. 199–207.

[37] Lee, R. (2003) "SFS 2 Code Validation Data Update," in *TTCP AER TP 2 Dynamic Interface Workshop, Patuxent River, USA*.

[38] Rosenfeld, N. C., K. R. Kimmel, and A. J. Sydney (2015) "Investigation of Ship Topside Modeling Practices for Wind Tunnel Experiments," in *53rd AIAA Aerospace Sciences Meeting, AIAA SciTech Forum*, Kissimmee, FL, paper no. 2015-0245.

[39] Nacakli, Y. and D. Landman (2011) "Helicopter downwash/frigate airwake interaction flowfield PIV surveys in a low speed wind tunnel," in *AHS 67th annual forum*, Virgiana Beach, VA, pp. 1–11.

[40] Gilooly, S. and G. Taylor-Power (2016) *Physical Modeling of the Atmospheric Boundary Layer in the University of New Hampshire's Flow Physics Facility*, *Tech. rep.*, Honors Theses and Capstones, University of New Hampshire.

[41] Zan, S. (2002) "Experimental determination of rotor thrust in a ship airwake," *Journal of the American Helicopter Society*, **47**(2), pp. 100–108.

[42] Lee, R. G. and S. J. Zan (2005) "Wind tunnel testing of a helicopter fuselage and rotor in a ship airwake," *Journal of the American Helicopter Society*, **50**(4), pp. 326–337.

[43] Rajagopalan, G., S. Niazi, A. Wadcock, G. Yamauchi, and M. Silva (2005) "Experimental and computational study of the interaction between a tandem-rotor helicopter and a ship," in *Proceedings of the 61st Annual Forum of the American Helicopter Society*, Grapevine, TX, pp. 729–750.

[44] Silva, M. J., G. K. Yamauchi, A. J. Wadcock, and K. R. Long (2004) "Wind tunnel investigation of the aerodynamic interactions between helicopters and tiltrotors in a shipboard environment," in *American Helicopter Society 4th Decennial Specialist's Conference on Aeromechanics*, San Francisco, CA.

[45] Kääriä, C. H., Y. Wang, M. D. White, and I. Owen (2013) "An experimental technique for evaluating the aerodynamic impact of ship superstructures on helicopter operations," *Ocean Engineering*, **61**, pp. 97–108.

[46] Rahimpour, M. and P. Oshkai (2016) "Experimental investigation of airflow over the helicopter platform of a polar icebreaker," *Ocean Engineering*, **121**, pp. 98–111.

[47] Buchholz, J., J. Martin, A. F. Krebill, G. M. Dooley, and P. Carrica (2018) "Structure of a Ship Airwake at Model and Full Scale," in *2018 AIAA Aerospace Sciences Meeting*, p. 1263.

[48] Dooley, G. M., P. Carrica, J. Martin, A. Krebill, and J. Buchholz (2019) "Effects of Waves, Motions and Atmospheric Turbulence on Ship Airwakes," in *AIAA Scitech 2019 Forum*, p. 1328.

[49] Watson, N. A., M. White, and I. Owen (2019) "Experimental Validation of the Unsteady CFD-generated Airwake of the HMS Queen Elizabeth Aircraft Carrier," in *AIAA Aviation 2019 Forum*, p. 3029.

[50] Watson, N. A., M. F. Kelly, I. Owen, S. J. Hodge, and M. D. White (2019) "Computational and experimental modelling study of the unsteady airflow over the aircraft carrier HMS Queen Elizabeth," *Ocean Engineering*, **172**, pp. 562–574.

[51] Metzger, J. D. (2012) *Measurement of Ship Air Wake Impact on a Remotely Piloted Vehicle*, *Tech. rep.*, No. USNA-TSPR-406. Naval Academy Annapolis MD.

[52] Kang, H. S., M. R. Snyder, D. S. Miklosovic, and C. Friedman (2016) "Comparisons of In Situ Ship Air Wakes with Wind Tunnel Measurements and Computational Fluid Dynamics Simulations," *Journal of the American Helicopter Society*, **61**(2), pp. 1–16.

[53] Howlett, J. J. (1981) *UH-60A Black Hawk engineering simulation program. Volume 1: Mathematical model*, *Tech. rep.*, NASA Technical Report CR-166309.

[54] Polsky, S. and C. Bruner (2000) "Time-accurate computational simulations of an LHA ship airwake," in *18th AIAA Applied Aerodynamics Conference*, Denver, CO, paper no. 2000-4126.

[55] Lee, D., N. Sezer-Uzol, J. F. Horn, and L. N. Long (2005) "Simulation of helicopter shipboard launch and recovery with time-accurate airwakes," *Journal of Aircraft*, **42**(2), pp. 448–461.

[56] Lee, D., J. F. Horn, N. Sezer-Uzol, and L. N. Long (2003) "Simulation of pilot control activity during helicopter shipboard operations," in *Proceedings of the AIAA Atmospheric Flight Mechanics Conference, Austin, TX*.

[57] Roper, D., I. Owen, G. Padfield, and S. Hodge (2006) "Integrating CFD and piloted simulation to quantify ship-helicopter operating limits," *The Aeronautical Journal*, **110**(1109), pp. 419–428.

[58] Yesilel, H. and F. Edis (2007) "Ship airwake analysis by CFD methods," in *AIP Conference Proceedings*, vol. 936, AIP, pp. 674–677.

[59] Keller, J. D., G. R. Whitehouse, A. H. Boschitsch, J. Nadal, J. Jeffords, and M. Quire (2007) "Computational fluid dynamics for flight simulator ship airwake modeling," in *Interservice/Industry Training, Simulation, and Education Conference (I/ITSEC) 2007*, Orlando, FL, paper no. 7320.

[60] Syms, G. (2008) "Simulation of simplified-frigate airwakes using a lattice-Boltzmann method," *Journal of Wind Engineering and Industrial Aerodynamics*, **96**(6), pp. 1197–1206.

[61] Zhang, F., H. Xu, and N. Ball (2009) "Numerical simulation of unsteady flow over SFS 2 ship model," in *47th AIAA Aerospace Sciences Meeting including The New Horizons Forum and Aerospace Exposition*, Orlando, FL.

[62] van Muijden, J., O. Boelens, J. van der Vorst, and J. Gooden (2013) "Computational ship airwake determination to support helicopter-ship dynamic interface assessment," in *21st AIAA Computational Fluid Dynamics Conference*, paper no. 2013-3078.

[63] Kelly, M. F., M. D. White, I. Owen, and S. J. Hodge (2016) "The Queen Elizabeth Class Aircraft Carriers: Airwake Modelling and Validation for ASTOVL Flight Simulation," in *American Society of Naval Engineers, Launch and Recovery Symposium*, Baltimore, MD.

[64] Mann, J. (1994) "The spatial structure of neutral atmospheric surface-layer turbulence," *Journal of Fluid Mechanics*, **273**, p. 141–168.

[65] Forsythe, J. R., C. E. Lynch, S. Polsky, and P. Spalart (2015) "Coupled Flight Simulator and CFD Calculations of Ship Airwake using HPCMP CREATE-AV Kestrel," in *53th AIAA Aerospace Sciences Meeting, SciTech*, pp. 1–18.

[66] Rajmohan, N. and C. He (2016) "A VPM/CFD Coupling Methodology to Study Rotor/Ship Aerodynamic Interaction," in *AIAA Modeling and Simulation Technologies Conference*, San Diego, CA, paper no. 2016-1915.

[67] Polsky, S. A., C. Wilkinson, J. Nichols, D. Ayers, J. Mercado-Perez, and T. S. Davis (2016) "Development and Application of the SAFEDI Tool for Virtual Dynamic Interface Ship Airwake Analysis," in *54th AIAA Aerospace Sciences Meeting*, San Diego, CA, paper no. 2016-1771.

[68] Oruc, I., J. F. Horn, and J. Shipman (2017) "Coupled Flight Dynamics and Computational Fluid Dynamics Simulations of Rotorcraft/Terrain Interactions," *Journal of Aircraft*, pp. 1–15.

[69] Oruc, I., J. F. Horn, J. Shipman, and S. Polsky (2017) "Towards real-time pilot-in-the-loop CFD simulations of helicopter/ship dynamic interface," *International Journal of Modeling, Simulation, and Scientific Computing*, **8**(04), p. 1743005.

[70] Sharma, A., J. Xu, A. K. Padthe, P. P. Friedmann, and K. Duraisamy (2019) "Simulation of Maritime Helicopter Dynamics During Approach to Landing With Time-Accurate Wind-Over-Deck," in *AIAA Scitech 2019 Forum*, p. 0861.

[71] Leishman, J. G. (2006) *Principles of Helicopter Aerodynamics*, Cambridge university press.

[72] Kääriä, C. H., Y. Wang, G. D. Padfield, J. S. Forrest, and I. Owen (2012) "Aerodynamic Loading Characteristics of a Model-Scale Helicopter in a Ship's Airwake," *Journal of Aircraft*, **49**(5), pp. 1271–1278.

[73] McRuer, D. T. (1994) "Interdisciplinary interactions and dynamic systems integration," *International Journal of Control*, **59**(1), pp. 3–12.

[74] Tulin, M. (1998) "Technical evaluation report," in *Proceedings of the RTO AVT Symposium of Fluid Dynamics Problems of Vehicles Operating Near or in the Air-Sea Interface, RTO MP-15, Amsterdam*.

[75] Castillo, L., J. Dabiri, J. Naughton, and C. Meneveau (2013) "Foreword: a special issue on turbulence and wind energy," *Journal of Turbulence*, **14**(4), pp. 53–54.

[76] Oruc, I., R. Shenoy, J. Shipman, and J. F. Horn (2016) "Towards Real-Time Fully Coupled Flight Dynamics and CFD Simulations of the Helicopter/Ship Dynamic Interface," in *Proceedings of the 72nd Annual Forum of the American Helicopter Society*, West Palm Beach, FL.

[77] Towne, A., O. T. Schmidt, and T. Colonius (2018) "Spectral proper orthogonal decomposition and its relationship to dynamic mode decomposition and resolvent analysis," *Journal of Fluid Mechanics*, **847**, pp. 821–867.

[78] Wang, X., D. Sarhaddi, Z. Wang, M. Mignolet, and P. Chen (2019) "Modeling-based hyper reduction of multidimensional cfd data: Application to ship airwake data," in *AIAA Scitech Forum, 2019*, American Institute of Aeronautics and Astronautics Inc, AIAA.

[79] Stull, R. B. (2000) *Meteorology for scientists and engineers*, Brooks/Cole.

[80] ——— (2012) *An introduction to boundary layer meteorology*, vol. 13, Springer Science & Business Media.

[81] ——— (2017) *Practical meteorology: an algebra-based survey of atmospheric science*, Univ. of British Columbia.

[82] Deardorff, J. W. (1972) "Numerical investigation of neutral and unstable planetary boundary layers," *Journal of the Atmospheric Sciences*, **29**(1), pp. 91–115.

[83] Garratt, J. (1977) "Review of drag coefficients over oceans and continents," *Monthly weather review*, **105**(7), pp. 915–929.

[84] Smedman-Högström, A.-S. and U. Högström (1978) "A practical method for determining wind frequency distributions for the lowest 200 m from routine meteorological data," *Journal of Applied Meteorology*, **17**(7), pp. 942–954.

[85] Kondo, J. and H. Yamazawa (1986) "Aerodynamic roughness over an inhomogeneous ground surface," *Boundary-Layer Meteorology*, **35**(4), pp. 331–348.

[86] Thompson, R. S. (1978) "Note on the aerodynamic roughness length for complex terrain," *Journal of Applied Meteorology*, **17**(9), pp. 1402–1403.

[87] Nappo Jr, C. (1977) "Mesoscale flow over complex terrain during the Eastern Tennessee Trajectory Experiment (ETTEX)," *Journal of Applied Meteorology*, **16**(11), pp. 1186–1196.

[88] Dyer, A. J. (1974) "A review of flux-profile relationships," *Boundary-Layer Meteorology*, **7**(3), pp. 363–372.

[89] Basu, S. and A. Lacser (2017) "A cautionary note on the use of Monin–Obukhov similarity theory in very high-resolution large-eddy simulations," *Boundary-Layer Meteorology*, **163**(2), pp. 351–355.

[90] Edson, J. B., C. J. Zappa, J. Ware, W. R. McGillis, and J. E. Hare (2004) "Scalar flux profile relationships over the open ocean," *Journal of Geophysical Research: Oceans*, **109**(C8).

[91] Bauer, E. (1996) *The Lowest Atmosphere: Atmospheric Boundary Layer Including Atmospheric Surface Layer.*, *Tech. rep.*, Institute for Defense Analyses, Alexandria VA.

[92] Free Software Foundation (2015), "OpenFOAM. The Open Source CFD Toolbox," Available at `http://www.openfoam.com/`.

[93] Churchfield, M. J., L. Sang, and P. J. Moriarty (2013) *Adding complex terrain and stable atmospheric condition capability to the OpenFOAM-based flow solver of the simulator for on/offshore wind farm applications (SOWFA)*, *Tech. rep.*, National Renewable Energy Lab.(NREL), Golden, CO (United States).

[94] Moeng, C.-H. (1984) "A large-eddy-simulation model for the study of planetary boundary-layer turbulence," *Journal of the Atmospheric Sciences*, **41**(13), pp. 2052–2062.

[95] Deardorff, J. W. (1980) "Stratocumulus-capped mixed layers derived from a three-dimensional model," *Boundary-Layer Meteorology*, **18**(4), pp. 495–527.

[96] Churchfield, M., S. Lee, P. Moriarty, L. Martinez, S. Leonardi, G. Vijayakumar, and J. Brasseur "A large-eddy simulation of wind-plant aerodynamics," in *50th AIAA Aerospace Sciences Meeting including the New Horizons Forum and Aerospace Exposition*, p. 537.

[97] Jha, P., M. Churchfield, P. Moriarty, and S. Schmitz (2013) "Accuracy of state-of-the-art actuator-line modeling for wind turbine wakes," in *51st AIAA Aerospace Sciences Meeting including the New Horizons Forum and Aerospace Exposition*, p. 608.

[98] Mirocha, J. D., M. J. Churchfield, D. Muñoz-Esparza, R. K. Rai, Y. Feng, B. Kosovic, S. E. Haupt, B. Brown, B. L. Ennis, C. Draxl, et al. (2017) *Large-eddy simulation sensitivities to variations of configuration and forcing parameters in canonical boundary-layer flows for wind energy applications*, *Tech. rep.*, National Renewable Energy Lab.(NREL), Golden, CO (United States).

[99] Doubrawa, P., L. A. Martinez-Tossas, E. Quon, P. Moriarty, and M. J. Churchfield (2018) "Comparison of Mean and Dynamic Wake Characteristics between Research-Scale and Full-Scale Wind Turbines," in *Journal of Physics: Conference Series*, vol. 1037, IOP Publishing, p. 072053.

[100] Jha, P. K., M. J. Churchfield, P. J. Moriarty, and S. Schmitz (2014) "Guidelines for volume force distributions within actuator line modeling of wind turbines on large-eddy simulation-type grids," *Journal of Solar Energy Engineering*, **136**(3), p. 031003.

[101] Schumann, U. (1975) "Subgrid scale model for finite difference simulations of turbulent flows in plane channels and annuli," *Journal of Computational Physics*, **18**(4), pp. 376–404.

[102] Rhie, C. and W. L. Chow (1983) "Numerical study of the turbulent flow past an airfoil with trailing edge separation," *AIAA journal*, **21**(11), pp. 1525–1532.

[103] Issa, R. I. (1986) "Solution of the implicitly discretised fluid flow equations by operator-splitting," *Journal of Computational Physics*, **62**(1), pp. 40–65.

[104] Martínez-Tossas, L. A., M. J. Churchfield, and C. Meneveau (2015) "Large eddy simulation of wind turbine wakes: detailed comparisons of two codes focusing on effects of numerics and subgrid modeling," in *Journal of Physics: Conference Series*, vol. 625, IOP Publishing, p. 012024.

[105] Brasseur, J. G. and T. Wei (2010) "Designing large-eddy simulation of the turbulent boundary layer to capture law-of-the-wall scaling," *Physics of Fluids*, **22**(2), p. 021303.

[106] American Institute of Aeronautics and Astronautics (1998) *AIAA guide for the verification and validation of computational fluid dynamics simulations*, American Institute of Aeronautics and Astronautics.

[107] Richards, P., R. Hoxey, and L. Short (2001) "Wind pressures on a 6 m cube," *Journal of Wind Engineering and Industrial Aerodynamics*, **89**(14-15), pp. 1553–1564.

[108] Richards, P. and R. Hoxey (2012) "Pressures on a cubic building–Part 2: Quasi-steady and other processes," *Journal of Wind Engineering and Industrial Aerodynamics*, **102**, pp. 87–96.

[109] Nicholls, S. and C. J. Readings (1979) "Aircraft observations of the structure of the lower boundary layer over the sea," *Quarterly Journal of the Royal Meteorological Society*, **105**(446), pp. 785–802.

[110] Drobinski, P., P. Carlotti, R. K. Newsom, R. M. Banta, R. C. Foster, and J.-L. Redelsperger (2004) "The structure of the near-neutral atmospheric surface layer," *Journal of the atmospheric sciences*, **61**(6), pp. 699–714.

[111] Lenschow, D., J. C. Wyngaard, and W. T. Pennell (1980) "Mean-field and second-moment budgets in a baroclinic, convective boundary layer," *Journal of the Atmospheric Sciences*, **37**(6), pp. 1313–1326.

[112] Hunt, J. C. R., J. C. Kaimal, and J. E. Gaynor (1988) "Eddy structure in the convective boundary layer – new measurements and new concepts," *Quarterly Journal of the Royal Meteorological Society*, **114**(482), pp. 827–858.

[113] Lemone, M. A. (1973) "The structure and dynamics of horizontal roll vortices in the planetary boundary layer," *Journal of the Atmospheric Sciences*, **30**(6), pp. 1077–1091.

[114] Friehe, C. A. and T. Hristov (2003) "Flux-profile relations over the open ocean," in *Preprints, 12th Conf. on Interactions of the Sea and Atmosphere, Long Beach, CA, Amer. Meteor. Soc., CD-ROM*, vol. 6.

[115] Martinez-Tossas, L. A., M. J. Churchfield, A. E. Yilmaz, H. Sarlak, P. L. Johnson, J. N. Sørensen, J. Meyers, and C. Meneveau (2018) "Comparison of four large-eddy simulation research codes and effects of model coefficient and inflow turbulence in actuator-line-based wind turbine modeling," *Journal of Renewable and Sustainable Energy*, **10**(3), p. 033301.

[116] Johlas, H., L. Martínez-Tossas, D. Schmidt, M. Lackner, and M. Churchfield (2019) "Large eddy simulations of floating offshore wind turbine wakes with coupled platform motion," in *Journal of Physics: Conference Series*, vol. 1256, IOP Publishing, p. 012018.

[117] Quon, E. W., P. Doubrawa, J. Annoni, N. Hamilton, and M. J. Churchfield (2019) "Validation of Wind Power Plant Modeling Approaches in Complex Terrain," in *AIAA Scitech 2019 Forum*, p. 2085.

[118] Troldborg, N. (2008) *Actuator line modeling of wind turbine wakes*, Ph.D. thesis, PhD thesis, Technical University of Denmark.

[119] Peskin, C. S. (1972) "Flow patterns around heart valves: a numerical method," *Journal of Computational Physics*, **10**(2), pp. 252–271.

[120] McIntyre, S., M. Kinzel, S. Miller, E. Paterson, J. Lindau, and R. Kunz (2011) "The Immersed Boundary Method for Water Entry Simulation," in *49th AIAA Aerospace Sciences Meeting including the New Horizons Forum and Aerospace Exposition, Aerospace Sciences Meetings*, Orlando, FL, paper no. 2011-759.

[121] Fadlun, E., R. Verzicco, P. Orlandi, and J. Mohd-Yusof (2000) "Combined immersed-boundary finite-difference methods for three-dimensional complex flow simulations," *Journal of Computational Physics*, **161**(1), pp. 35–60.

[122] Shipman, J., S. Arunajatesan, C. Menchini, and N. Sinha (2005) "Ship airwake sensitivities to modeling parameters," in *43rd AIAA Aerospace Sciences Meeting and Exhibit*, p. 1105.

[123] Nichols, R., R. Tramel, and P. Buning (2006) "Solver and turbulence model upgrades to OVERFLOW 2 for unsteady and high-speed applications," in *24th AIAA Applied Aerodynamics Conference*, p. 2824.

[124] Jespersen, D. C., T. H. Pulliam, and M. L. Childs (2016) "OVERFLOW turbulence modeling resource validation results," .

[125] Chan, W. (2011) "Developments in Strategies and Software Tools for Overset Structured Grid Generation and Connectivity," in *20th AIAA Computational Fluid Dynamics Conference*, p. 3051.

[126] Spalart, P. R. and S. R. Allmaras (1992) "A one equation turbulence model for aerodinamic flows," *AIAA Journal*, **94**.

[127] Nichols, R. H. and P. G. Buning (2008) "User's Manual for OVERFLOW 2.1," *University of Alabama and NASA Langley Research Center*.

[128] Sagaut, P., S. Deck, and M. Terracol (2013) *Multiscale and multiresolution approaches in turbulence: LES, DES and hybrid RANS/LES methods: applications and guidelines*, World Scientific.

[129] Chan, W. M. (2009) "Overset grid technology development at NASA Ames Research Center," *Computers & Fluids*, **38**(3), pp. 496–503.

[130] Kimmel, K., P. Atsavapranee, A. Sydney, J. Ramsey, M. Marquardt, and E. Harrison (2014) *Implementation of a Particle Image Velocimetry System for Wind Tunnel Flowfield Measurements*, *Tech. rep.*, No. NSWCCD-80-TR-2014/045. Naval Surface Warfare Center Carderock Div Bathesda, MD. Naval Architecture and Engineering Dept.

[131] Thedin, R., M. P. Kinzel, and S. Schmitz (2018) "An Evaluation of the Effects of Resolved Shear-Driven Atmospheric Turbulence on Ship Airwakes," *Journal of the American Helicopter Society*, **63**(2), pp. 1–16.

[132] (1996) *Operator's Manual for UH-60A Helicopter, UH60L Helicopter, EH-60A Helicopter*, *Tech. rep.*, TM 1-1520-237-10. U.S. Army.

[133] Stevens, B. L., F. L. Lewis, and E. N. Johnson (2015) *Aircraft control and simulation: dynamics, controls design, and autonomous systems*, John Wiley & Sons.

[134] Welch, P. (1967) "The use of fast Fourier transform for the estimation of power spectra: a method based on time averaging over short, modified periodograms," *IEEE Transactions on audio and electroacoustics*, **15**(2), pp. 70–73.

[135] Thedin, R., M. P. Kinzel, J. F. Horn, and S. Schmitz (2019) "Coupled Simulations of Atmospheric Turbulence-Modified Ship Airwakes and Helicopter Flight Dynamics," *Journal of Aircraft*, **56**(2), pp. 812–824.

[136] Thedin, R., M. P. Kinzel, and S. Schmitz (2017) "High-Fidelity Simulations of the Interaction of Atmospheric Turbulence with Ship Airwakes," in *Proceedings of the 73rd Annual Forum of the American Helicopter Society*, Forth Worth, TX.

[137] ——— (2018) "Simulation of a Helicopter-Ship Dynamic Interface Using Offline Database of Atmospheric Turbulence-Modified Airwake," in *Proceedings of the 74th Annual Forum of the American Helicopter Society*, Phoenix, AZ.

[138] Thedin, R., S. M. Murman, J. Horn, and S. Schmitz (2019) "On the unsteadiness of ship airwakes subject to atmospheric boundary-layer inflow from a helicopter operation perspective," in *AIAA Aviation 2019 Forum*, Dallas, TX, paper no. 2019-3032.

[139] Thedin, R., S. M. Murman, J. F. Horn, and S. Schmitz (2019) "Effects of Atmospheric Turbulence Unsteadiness on Ship Airwakes and Helicopter Dynamics," *Under review, Journal of Aircraft.*

[140] Lusardi, J. A., C. L. Blanken, and M. B. Tischeler (2002) "Piloted evaluation of a UH-60 mixer equivalent turbulence simulation model," .

[141] Lusardi, J. (2004) *Control equivalent turbulence input model for the UH-60 helicopter*, Ph.D. thesis, University of California, Davis.

[142] Lusardi, J. A., M. B. Tischler, C. L. Blanken, and S. J. Labows (2004) "Empirically derived helicopter response model and control system requirements for flight in turbulence," *Journal of the American Helicopter Society*, **49**(3), pp. 340–349.

Vita

Regis Santos Thedin

Regis is from the small town of Nova Friburgo, in the state of Rio de Janeiro, Brazil. He moved to Rio de Janeiro to attend the Pontifical Catholic University of Rio de Janeiro (PUC-Rio), majoring in mechanical engineering. During his undergraduate studies, he spent a semester abroad at the University of Illinois at Urbana-Champaign. His interet in aerospace sciences spur after participating for many years in the SAE Aero Design competition, winning two times in the advanced class. He continued at PUC-Rio for his masters, which focused on topology optimization. He started his PhD in aerospace engineering at Penn State right after he obtained his masters.